Towards a Point-of-Care Optical Waveguide Biosensor for Enabling Judicious Use of Antibiotics

by

Hazel Jade Dixon

UNIVERSITY OF BIRMINGHAM

A thesis submitted to the

University of Birmingham

For the degree of

Doctor of Philosophy

School of Chemistry

College of Engineering and Physical Sciences

University of Birmingham

September 2022

Abstract

Leaky waveguide (LW) films prepared from cheap and readily available hydrogel materials have the potential to produce affordable, sensitive, and label-free biosensors for use in point-of-care (POC) settings. Specifically, this project focuses on the development of a LW biosensor which, when combined with a 3D printed portable instrument, presents the opportunity to carry out testing for biomarkers at POC.

Overuse of antibiotics is a major health concern and is leading to increased antibiotic resistance and the emergence of new antibiotic-resistant bacteria. The motivation of this project is to work towards a POC biosensor which can distinguish between bacterial and viral infections, thus allowing for more informed treatments and a reduction in overprescription of antibiotics. Consequently, the reduction in antibiotic use should serve to slow down antibiotic resistance. The POC aspect is of vital importance to this as portability and a simplistic design will allow for the device to be used in various settings rather than in dedicated laboratories, leading to quicker results and earlier patient treatment.

A crucial element of POC sensing is the requirement for an internal referencing system. To meet this requirement, two different techniques were studied. These comprised of two-channel systems and stacked systems. The two-channel system allows for direct removal of common mode effects and non-specific adsorption (NSA) *via* a referencing channel running parallel to the sensing channel, while the stacked approach simplifies the system and reduces the opportunity for channel-to-channel variance by vertically stacking the reference and sensor layers and interrogating *via* a single channel flow cell.

This thesis is broken down into eight chapters covering the following content:

Chapter 1 – Introduction. This chapter offers a review of current antibiotic usage and an overview of some of the different biosensors currently available.

Chapter 2 – Instrumentation and Techniques. This chapter covers the instrumentation and techniques used throughout the project. Optical biosensing was selected as the focus for this work, allowing for use of LWs to detect analytes *via* the changes in refractive index (RI) caused when an analyte binds to the LW. The simplistic sensing technique combined with the high sensitivity of LWs offers excellent potential for quick and real-time results.

Chapter 3 – Single Layer Waveguides. To achieve the desired sensitivity and reactivity of the LWs multiple different polymers were investigated. This included assessing the sensitivity, longevity, and cost of the polymers, along with storage requirements and batch-to-batch reproducibility. These polymers included both natural and synthetic polymers. Overall, the material which fulfilled most of the requirements was found to be chitosan (CS), a natural polymer derived from crustacean shells.

Chapter 4 – Stacked Waveguides. This chapter discusses the potential for LWs produced from an inert reference LW and a functionalised sensor LW in a stacked conformation as an internally referenced biosensor. While the inert (reference) LW should only react to environmental changes and NSA, the functionalised (sensor) LW should react to these and the analyte of interest. A differential response can then be taken between the two layers, providing a final response caused only by the analyte. The chapter firstly covers different inert hydrogel films as potential reference layers and tests these in the same way as the single layer LWs. The most suitable reference LW was found to be a synthetic hydrogel

produced from poly(ethylene glycol) (PEG)-aldehyde and PEG-hydrazide polymer units. Using these reference layers and the sensor layers developed in Chapter 3, the films are then combined into the stacked conformation and characterised.

Chapter 5 – Protein Detection. After development of the LWs in Chapters 3 and 4, the most promising LWs were tested for their protein detection abilities. As part of this, NSA was investigated and blocking strategies applied to reduce this. Multiple different protein immobilisation strategies were developed and tested on different LWs to assess the reproducibility and sensitivity of the techniques. Finally, protein detection was attempted in different solutions: buffers, synthetic urine, and human serum. Using 1% CS LWs we were able to detect down to 5 nM lactoferrin (LF) in buffer samples which offers an improvement over a surface plasmon resonance (SPR)-based LF sensor which was able to detect down to 10^{-8} M [1]. We were also able to detect 25 nM anti-biotin antibody (ABA) in 10% (v:v) human serum, which has been detected in this quantity in the literature in buffer but not in human serum [2].

Chapter 6 – Portability. In this chapter a portable waveguiding device, produced and provided by a collaborator, was used to interrogate different LWs and protein immobilisation strategies. The results of these are compared directly with the equivalent results produced on the laboratory-based instrumentation, allowing for assessment of the portable device and comparison of the advantages and limitations of both the laboratory-based and portable devices.

Chapter 7 – Conclusion and Future Outlook. This chapter provides a brief summary of the entire work, compiling information into tables for simplicity and ease of comparison. Future work is also discussed.

Chapter 8 – Experimental. This details the experimental methods used throughout the work.

Overall, this work has developed various LW films and protein detection strategies and proven their ability to detect proteins on both laboratory-based and portable instruments. It has also assessed the advantages and limitations of stacked LWs, providing a basis for future development into a reliable POC biosensor for enabling judicious use of antibiotics.

Dedication

I would like to dedicate this thesis to Mr. Simon Martindale for inspiring me to follow my dreams in chemistry and offering his unconditional support and unwavering belief. R.I.P. and thank you, this would not have been possible without you.

Acknowledgements

Thank you to my supervisor Dr Gupta and the Gupta group for their assistance. This project would not have been possible without the funding generously provided by the EPSRC and GCRF.

Particular gratitude is extended to Fern for being my personal therapist and cheerleader, and for answering all my silly maths questions with minimal judgement. Equally, I would like to thank Nicola and Jake for keeping me sane and providing support, expertise, and rationality. Thank you to Elisabetta for helping me to understand physics slightly more than I could before I started this endeavour, and for being an excellent source of knowledge, entertainment, and motivation. And thank you to William, for being a source of resolute optimism and fun. Additional thanks must be extended to Trevor for all the technical support and knowledge provided throughout this project.

I am also unequivocally thankful to my parents Jon and Pauline and my sister Fiona for their consistent encouragement and steadfast support throughout everything, and to Momo, Flynn, Max, Buffy, and Al for putting up with my need for attention and hugs to help me recharge.

Table of Contents

List of Figures

List of Tables

List of Equations

Abbreviations

2-MAL	2-arm-$PEG_{20,000}$-maleimide
2-SH	2-arm-$PEG_{20,000}$-thiol
4-CHO	4-arm-$PEG_{20,000}$-aldehyde
4-HZ	4-arm-$PEG_{2,000}$-hydrazide
4-MAL	4-arm-$PEG_{40,000}$-maleimide
4-SH	4-arm-$PEG_{20,000}$-thiol
3D	Three-dimensional
AAm	Acrylamide
ABA	Anti-biotin antibody
AIP	2,2'-Azobis[2-(2-imidazolin-2-yl)propane] dihydrochloride
APMA	N-(3-aminopropyl)methacrylamide
APR	Acute phase reactant
APS	Ammonium persulfate
APTES	(3-aminopropyl)triethoxysilane
ARI	Acute respiratory infection
BAAm	N,N'-methylenebisacrylamide
Biotin A-IgG	Biotin anti-IgG

BPM	Biotin-PEG_6-maleimide
BSA	Bovine serum albumin
CDC	United States Centers for Disease Control and Prevention
CDMVS	Chloro(dimethyl)vinyl silane
CF-PLA	Carbon fibre-filled polylactic acid
CFU	Colony forming unit
CNC	Computer numerical control
CRP	C-reactive protein
CS	Chitosan
CT	Computerised tomography
CXR	Chest X-ray
DBCO	Dibenzocyclooctyne
DDLW	Dye-doped leaky waveguide
DI	Deionised
DMSO	Dimethylsulfoxide
ECDC	European Centre for Disease Prevention and Control
ELISA	Enzyme-linked immunosorbent assay
E waves	Transverse magnetic waves

F5M	N-(5-Fluoresceinyl)maleimide
FDA	United States Food and Drug Administration
FITC	Fluorescein isothiocyanate
GA	Glutaraldehyde
HEPES	4-(2-hydroxyethyl)piperazine-1-ethanesulfonic acid
HI	Hartman interferometer
HIV	Human immunodeficiency virus
HMDS	Hexamethyldisilazane
HMW	High molecular weight
HPMA	N-(2-hydroxypropyl)methacrylamide
H waves	Transverse electric waves
IgG	Immunoglobulin G
IRRM	Internally referenced resonant mirror
LED	Light emitting diode
LF	Lactoferrin
LMW	Low molecular weight
LSCM	Laser scanning confocal microscopy
LW	Leaky waveguide

MAA	Methacrylic acid
MCLW	Metal clad leaky waveguide
Mn	Molecular number
MPTMS	(3-mercaptopropyl)trimethoxysilane
MRI	Magnetic resonance imaging
MS	Mass spectrometry
MW	Molecular weight
MZI	Mach-Zehnder interferometer
m/z	Mass-to-charge ratio
NA	Numerical aperture
NMR	Nuclear magnetic resonance
NPB	NHS-PEG_{12}-biotin
NSA	Non-specific adsorption
PAAm	Poly(acrylamide)
PAAm-Ac	Poly(acrylamide-*co*-acrylic acid)
PAB	Protein A biotin
PAGE	Poly(acrylamide) gel electrophoresis
PBS	Phosphate buffered saline

PCT	Procalcitonin
PEG	Poly(ethylene glycol)/poly(ethylene oxide)
PEGDA	Poly(ethylene glycol) diacrylate
PEGDGE	Poly(ethylene glycol) diglycidyl ether
PEGDMA	Poly(ethylene glycol) dimethacrylate
PEGMEA	Poly(ethylene glycol) methyl ether acrylate
PMMA	Poly(methyl methacrylate)
POC	Point-of-care
PVDF	Polyvinylidene difluoride
PWR	Plasmon waveguide resonance
QCM	Quartz crystal microbalance
RB4	Reactive Blue 4
RI	Refractive index
RIS	Refractive index sensitivity
RIU	Refractive index units
RM	Resonant mirror
SDS-PAGE	Sodium dodecyl sulfate-polyacrylamide gel electrophoresis
SEM	Scanning electron microscopy

SNA	Sulfo NHS acetate
SPAAC	Strain-promoted alkyne-azide cycloaddition
SPD	Surface plasmon diffraction
SPR	Surface plasmon resonance
TB	Tuberculosis
TCEP	Tris(2-carboxyethylphosphine)
TEM	Transmission electron microscopy
TEMED	N,N,N',N'-tetramethylethylenediamine
TIR	Total internal reflection
TMTFS	Trimethoxy-(3,3,3-trifluoropropyl)silane
Trypsin EDTA	Trypsin-ethylenediaminetetraacetic acid
UTI	Urinary tract infection
UV-Vis	Ultraviolet-visible spectroscopy
WB	Western blot
WHO	World Health Organisation
YI	Young interferometer

Publications

3D Printed Instrumentation for Point-of-Use Leaky Waveguide (LW) Biochemical Sensor. Nicholas J. Goddard, Hazel J. Dixon, Nicola Toole, Ruchi Gupta. IEEE Transactions on Instrumentation and Measurement, 2020. **69**(9): p. 6390-6398; https://doi.org/10.1109/TIM.2020.2969036

A Self-Referenced Diffraction-Based Optical Leaky Waveguide Biosensor Using Photofunctionalised Hydrogels. Anil K. Pal, Nicholas J. Goddard, Hazel J. Dixon, Ruchi Gupta. Biosensors, 2020. **10**(10): p. 134; https://doi.org/10.3390/bios10100134

Conferences

Towards a Point-of-Care Optical Waveguide Biosensor for Enabling Judicious Use of Antibiotics. University of Birmingham Research Poster Conference, Birmingham, UK. June 2019. Poster presentation.

Point-of-Care Biosensor for Judicious Use of Antibiotics. Bright Spark Symposium, Brighton, UK. September 2019. Oral presentation.

Towards a Point-of-Care Optical Waveguide Biosensor for Enabling Judicious Use of Antibiotics. University of Birmingham Postgraduate Symposium, Birmingham, UK (online). July 2020. Poster presentation.

Two-Layer Internally Referenced Leaky Waveguide Optical Biosensor for Detection of Biological Analytes. Royal Society of Chemistry Tokyo International Conference 2020 (RSC-TIC2020): Optical Biosensing and Devices, Tokyo, Japan (online). December 2020. Poster presentation.

Internally Referenced Two-Layer Polymer Leaky Waveguide for Optical Sensing of Biomolecules. Europtrode, Warsaw, Poland (online). November 2021. Poster presentation.

Towards a Point-of-Care Optical Waveguide Biosensor for Enabling Judicious Use of Antibiotics. University of Birmingham Postgraduate Symposium, Birmingham, UK (online). June 2021. Oral presentation.

References

1. Gupta, R. and N.J. Goddard, A study of diffraction-based chitosan leaky waveguide (LW) biosensors. Analyst, 2021. 146(15): p. 4964-4971.
2. Tomassetti, M., et al., Lactoferrin determination using flow or batch immunosensor surface plasmon resonance: Comparison with amperometric and screen-printed immunosensor methods. Sensors and Actuators B Chemical, 2013. 179: p. 215-225.

1 Chapter 1 – Introduction

1.1 Antibiotic resistance

Acute respiratory infections (ARIs) can be broadly classified as either bacterial or viral; unfortunately, both bacterial and viral ARIs present with very similar symptoms in patients [1]. This makes determining the correct nature of an infection a challenge and can lead to misdiagnosis. Approximately 40-60% of ARIs are viral [2, 3], and yet the prescription of antibiotics for ARIs exceeds 70% [4]. It is therefore easy to conclude that antibiotics are being overprescribed for ARIs when a portion of these are likely to be viral in nature. Ultimately, this will lead to an antibiotic crisis in which antibiotics will no longer be efficacious enough to treat genuine bacterial infections due to an increase in bacterial resistance [5]. According to a 2019 report by the United States Centers for Disease Control and Prevention (CDC), antimicrobial-resistant infections (comprising of infections both bacterial and fungal in nature) exceed 2.8 million in the U.S. per year [5]. The World Health Organisation (WHO) and European Centre for Disease Prevention and Control (ECDC) estimate that around 670,000 infections in Europe were caused by antibiotic-resistant bacteria which consequently led to around 33,000 deaths in 2020 [6]. While there appears to be a much higher infection rate in the U.S., it is important to recognise that the data provided by the CDC encompasses both bacterial and fungal infections, while the ECDC data only reports infections caused by 8 bacterial species of concern.

Antibiotic resistance can be split into two broad categories: intrinsic resistance and acquired resistance [7]. Intrinsic resistance is a natural resistance to drugs *via* the limitation of drug uptake and can take the form of poor permeability of the bacterial cell membranes and

active drug efflux which pumps the drug out of the bacterium. Acquired resistance refers to any form of resistance gained through horizontal gene transfer (HGT) or mutations, which occur on average as 1 mutation per 10^6 to 10^9 bacterial cell divisions [7]. Any mutation which is beneficial to the survival and growth of the bacterium is likely to enhance the robustness and lifetime of that cell, allowing for further replications with the same mutation. These bacterial strains will then possess resistance to certain antibiotic classes and will continue to proliferate and cause the infection to worsen.

Ensuring that patients who require antibiotics can receive them quickly is a priority to reduce the chance of serious complications or mortality from dangerous bacterial infections, but unnecessary prescription of antibiotics for viral illnesses must be significantly reduced to prevent bacterial resistance increasing. It is estimated that 40 million people are prescribed antibiotics for ARIs in the U.S. annually, while only 13 million actually need them [8]. The reduction of unnecessary antibiotic usage is called antibiotic stewardship, and is a vital measure involved in reducing morbidity due to antibiotic resistance [9].

In 2018 the CDC produced a list of 5 main measures required to combat the issues associated with antibiotic resistance (**Figure 1.1**). From the figure we can see that antibiotic stewardship is an important part of these measures but is not enough on its own.

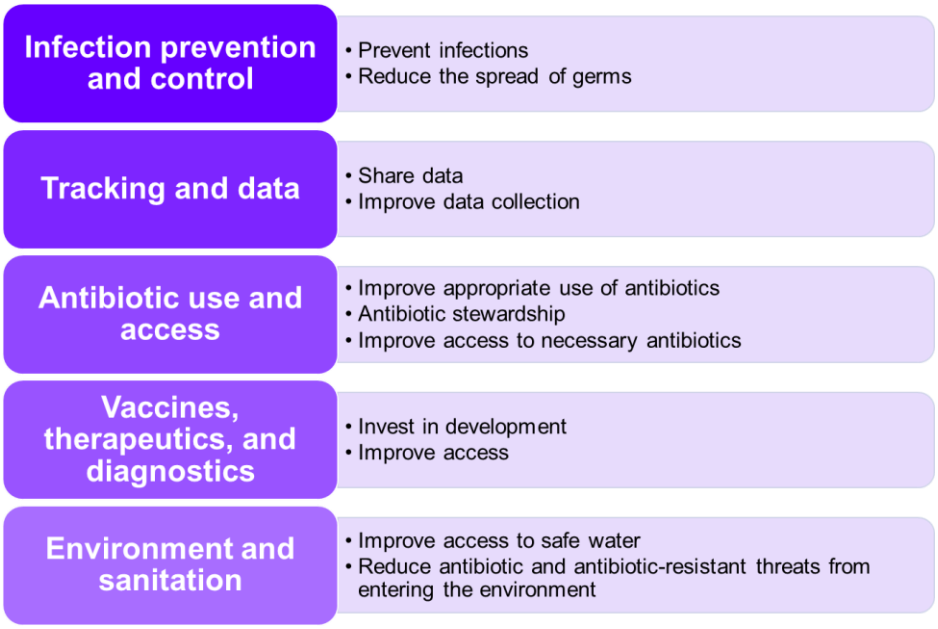

Figure 1.1. CDC list of measures to combat antibiotic resistance. Adapted from [9].

Not only does antibiotic stewardship include limiting unnecessary usage, but also includes using the correct class of antibiotic. For example, predominantly using newer antibiotics where older antibiotics would have sufficed will likely lead to antibiotic resistance developing for the newer drugs quicker than otherwise expected [8]. Tuberculosis (TB) is commonly treated with rifampicin, an ansamycin approved for use in the U.S. in 1971 [10]; drug-resistant TB can be treated with pretomanid, a nitroimidazole approved for use in 2019 [11]. If less resistant strains of TB are immediately treated with pretomanid, drug resistance to this is likely to rapidly develop. This will reduce the long-term usage of newer drugs such as pretomanid as they will become obsolete.

It is important to note that antibiotic resistance does not come entirely from use and misuse of antibiotics in humans; it can also develop from use in veterinary applications and agriculture, and even occur spontaneously *via* mutation and evolution of bacteria. Resistant

bacteria can transfer to the environment through general use, misuse, and mishandling, and rapidly spread, including transferring the resistant genes to other bacteria [9, 12].

Antibiotic resistance is just one form of antimicrobial resistance. Antimicrobial resistance encompasses antibiotic, antiparasitic, antiviral, and antifungal resistance. While antibiotic resistance is the focus of this work, it is important to recognise the difference between these terms. **Table 1.1** is adapted from The Review on Antimicrobial Resistance, a commissioned report from the UK government published in 2016, and projects the mortality rates caused by antimicrobial resistance by 2050.

Table 1.1. Projected mortality rates from antimicrobial resistance by 2050, based on the assumption that infection rates double then remain constant. Adapted from The Review on Antimicrobial Resistance 2016 [13].

REGION	MORTALITY
ASIA	4,730,000
AFRICA	4,150,000
LATIN AMERICA	392,000
EUROPE	390,000
NORTH AMERICA	317,000
OCEANIA	22,000

These mortality rates are based on the assumption that antimicrobial infections will double, then remain consistent. As of 2016, antimicrobial resistance was estimated to cause the deaths of 700,000 people, while the projection for 2050 increases this value to a staggering 10 million. While this is a projection and cannot account for unexpected developments, it does show an alarmingly high mortality rate and indicates that antimicrobial resistance is soon going to become one of the biggest killers of the human population; this will include antibiotic resistance.

Antibiotic stewardship is going to be vital in reducing this mortality projection. The WHO has classified 53 European countries according to their optimisation of antimicrobial use in humans (**Figure 1.2**). This is based on 2020 data and shows that only 7 European countries are classed as "excellent" in this regard. The majority of countries are categorised as "very good", but a total of 13 countries are "fair", worse, or did not provide data. This indicates that 24% of the European countries included are below ideal and this will have a significant impact on improving antibiotic stewardship and antimicrobial resistance. Antibiotic resistance is a worldwide issue and must be approached as such.

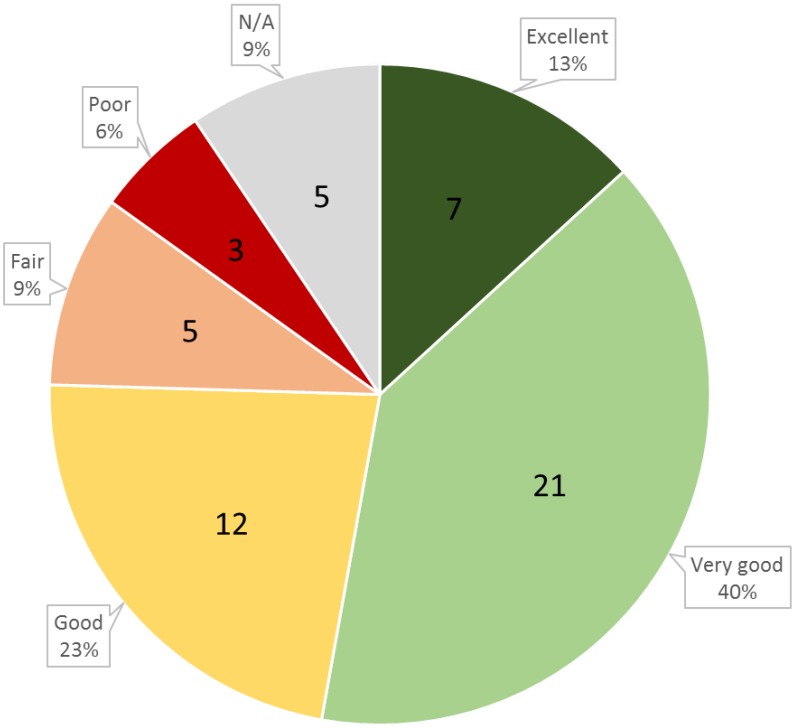

Figure 1.2. A pie chart depicting 53 European countries and their rating in optimisation of antimicrobial use in humans according to WHO 2020 data [6].

From this data we can extrapolate that antimicrobial resistance, including antibiotic resistance, is going to continue increasing and with this morbidity and mortality rates will also climb. Without a global commitment to tackling this issue antimicrobial resistance will

continue to grow. It is likely that antibiotic stewardship in some countries will slow down the rate of this growth, but ultimately every country needs to implement the same measures for maximum effect.

The development of new antibiotics to combat the resistant strains is not quick enough to be the sole focus of a strategy to reduce these mortality rates. As of June 2019, 42 antibiotics were in development and just 4 had applied for approval from the United States Food and Drug Administration (FDA) [9, 14]. Unfortunately, antibiotic research is not a profitable business and has seen a reduction in large pharmaceutical companies pursuing this in favour of more lucrative ventures, with 95% of antibiotics currently in development led by small companies [15]. Wellcome estimate it can take 10-15 years to develop a single new antibiotic, costing over $1 billion [16]. Additionally, the use of next-generation antibiotics must be carefully controlled and monitored, further reducing monetary profits.

It is also important to consider the cost of antibiotic over-prescription. One study estimates that over $12 million was spent between 2008-2011 in 505 U.S. hospitals on unnecessary antimicrobial treatment [17]. This wasted money could be put to better use in countless other ways, including further scientific research and drug development.

Misconceptions on the nature of antibiotic resistance are rife, with a 2015 WHO survey revealing that 32% of respondents believed that stopping a course of antibiotics is the right thing to do once their symptoms have cleared, and 64% believed antibiotics will effectively treat viral infections such as colds and flu [18]. Stopping a course of antibiotics before an infection is fully treated can lead to increased opportunity for the development of antibiotic resistance and cause an even more serious infection which is significantly more difficult to

treat, while mis-prescription of antibiotics for viral infections will have no benefit on the recovery of the patient other than a costly placebo effect as it will likely lead to further antibiotic resistance.

1.2 Biosensors

Oxford Languages defines a biosensor as "*a device which uses a living organism or biological molecules, especially enzymes or antibodies, to detect the presence of chemicals*" [19]. This involves the combination of a biological element with a physical transducer capable of converting the biological change into a signal. A general outline of the components and process of a biosensor is depicted in **Figure 1.3**.

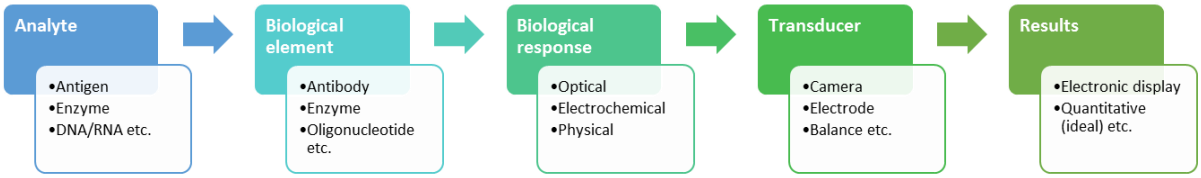

Figure 1.3. A simplified flow chart describing the process of a biosensor [20-22].

Selective detection of specific molecules within a solution is required in a range of different industries, from healthcare to environmental to industrial samples [23]. Not only must the target be detected, but in many cases it must also be quantified [24]. A large downfall of many point-of-care (POC) tests currently available is the lack of quantification. A range of techniques have been developed to combat this challenge including, but not limited to, electrochemical, optical, physical, nanomaterial, and thermal [25].

Throughout the development of a biosensor intended for commercialised use the following essential criteria must be considered:

- High specificity, accuracy, and reproducibility
- Stable under storage conditions
- Independent of pre-treatment processes
- Free from transducer-induced noise

- Real-time analysis
- User-friendly

To meet these demands there are a large number of biosensors currently available and in development, and these can generally be grouped into various categories, for example based on transducers, technology, detection type, receptors etc. [26]. For the sake of this thesis, we will refer to the following three main categories: optical, electrochemical, and physical. Optical biosensors are the most prevalent form of biosensor and rely on the interaction between a biorecognition element and an optical field, converting the response into a measurable signal. Optical biosensors are the focus of this work, and as such they are discussed in more detail later in **Section 1.2.3**.

Within these broad categories there are many different branches, with some reported in **Figure 1.4**. There can also be overlap between different branches with biosensors combining two or more types of sensing mechanism to obtain the final results. For example, electro-optical biosensing can be achieved in electrochemical surface plasmon resonance (EC-SPR), a combination of electrochemical and optical techniques [27].

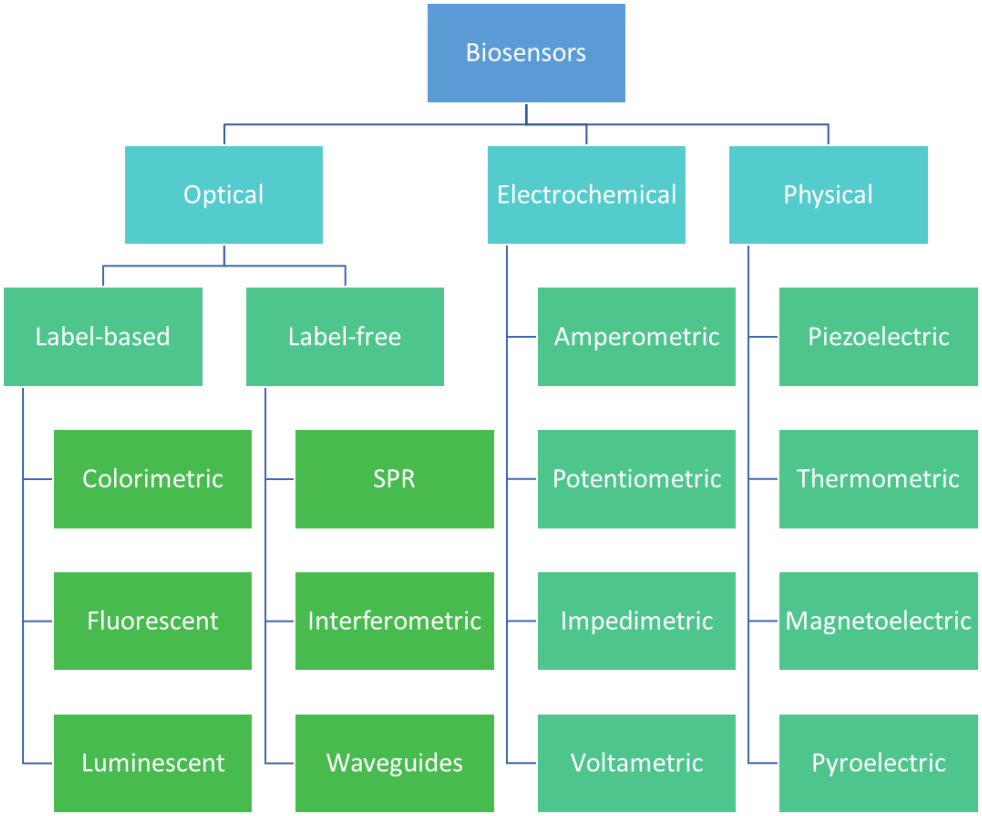

Figure 1.4. The three main biosensor categories with non-exhaustive examples of each type [20-22].

As of 2021 the biosensor market is valued at $25.5 billion. This is predicted to grow to $36.7 billion by 2026, owing in part to the prevalent COVID-19 pandemic, but also due to ongoing technological advancements, a rise in government funding, and the increasing demand for wearable biosensors for continuous monitoring [28].

With such a wide range of biosensors available, it is easy to become overwhelmed when selecting the best biosensor. In reality there is no single “best” biosensor, and when considering the merits and failings of each sensor these points must be correlated to their intended use. For example, it is not pragmatic to compare a quantitative biosensor to a qualitative lateral flow test except in cases where an improvement has been made, but both types of sensor have their own applications.

Additionally, most biosensors are developed to detect a single analyte and provide excellent results for this but may be entirely useless when applied to a different analyte. For these reasons, the research into multiple different types of biosensors is an important and ongoing process.

1.2.1 Electrochemical biosensors

Electrochemical biosensors use electrodes to quantitatively convert a biochemical signal into an electric signal via an electrochemical transducer, and can be used to detect biomolecules such as glucose, DNA, cholesterol etc. [29]. The electrode is the transducer, and a receptor molecule (i.e. antigen, antibody, DNA, protein) is immobilised onto the surface of the electrode. When exposed to a solution containing the analyte, the analyte will bind with the receptor and induce a measurable change. The most well-known example of this is the glucometer, a test to determine glucose levels first reported in 1962 [30]. Unfortunately, due to the technological constraints of the time these instruments were large and cumbersome. Over the years this bulky instrumentation has been streamlined and portable versions of these glucose sensors are now commonly used at home by diabetic patients (**Figure 1.5**).

Figure 1.5. A portable mylife Pura X blood glucose meter [31].

Research into such sensors is continuously expanding, such as the report of an amperometric glucose biosensor developed by Li *et al.* with the ability to detect 0.05 M of glucose with a linear response range spanning from 0 – 10 mM [32]. To achieve this, glucose oxidase was covalently immobilised onto the surface of indium-tin oxide. As the glucose reacts with the glucose oxidase it produces hydrogen peroxide which can be detected at a Pt electrode.

1.2.2 Physical biosensors

Physical biosensors rely on physical changes such as mass, temperature, resonance frequency etc., and use the comparative transducer to measure this such as in the quartz crystal microbalance (QCM). A piezoelectric biosensor such as the QCM is comprised of a disc of quartz to which electrodes are attached on either side. The quartz can oscillate at a particular frequency upon application of the correct voltage *via* the electrodes. Any change in mass at the surface of the electrode will impact the oscillation of the quartz, and produce a measurable signal due to the change in frequency of the quartz resonance [33]. This makes the QCM a highly sensitive instrument for measuring mass changes, typically down to nanogram levels [34].

Thermometric biosensors are well-known in serum cholesterol testing. Such sensors can measure the change in temperature which occurs as a response to enzyme-catalysed reactions. This change in temperature can then be converted to a quantitative value corresponding to the concentration of the substrate [35].

1.2.3 Optical biosensors

Currently, optical biosensors are the most prevalent branch of biosensors reported [21]. In comparison to culture-based analytics, optical biosensors offer numerous advantages in a range of areas, including faster results, lower costs, and higher accuracy [21, 36]. These properties make optical biosensors an excellent choice for further development into POC devices.

1.2.3.1 Interferometry

Interferometry is a versatile optical sensing technique and has been used in many fields varying from astronomy to biosensing. Interference patterns are produced through the convergence of two light beams which originated from the same source. This typically involves a light source with a high degree of coherence such as a laser, which is split into two equal beams. The beams pass through the sample parallel to each other and recombine to form the interference pattern; any change in refractive index (RI) causes a phase shift which is consequently detected by the instrument. The interference pattern forms due to constructive and destructive interference, which is where the beams are either in phase (constructive) or out of phase (destructive) when they combine [37]. There are different configurations of the interferometer, including the Mach-Zehnder interferometer (MZI), Young interferometer (YI) and the Hartman interferometer (HI) [38]. A YI biosensor has been reported to detect RI changes of 0.9×10^{-6}, with the successful detection of a 50 nM 21-mer DNA dilution and resolution expected to be in the picomolar range after further optimisation [39]. In fact, interferometers are regularly reported to detect in the picomolar range [40].

The interferometer can be combined with different instruments such as the waveguide. Kristensen *et al.* explored this technique by combining a YI with two slab waveguides containing nano-filters, allowing for simultaneous measurement of refraction and absorption alongside size exclusion from 100 – 500 nm [41].

While interferometry instrumentation is extremely sensitive to analytes, it also tends to be very sensitive to mechanical fluctuations and vibrations. This can make the miniaturisation and portability of the equipment difficult as it requires a stable and ideally isolated environment. To reduce the impact of noisy environments, some interferometers can be set up to collect data within a very short time-span, but this often comes with a reduction in sensitivity [37]. Interferometer instruments are also usually expensive, requiring high quality lasers, beam splitters, prisms, and cameras. This makes them unsuited for use outside of research.

1.2.3.2 Surface plasmon resonance

The phenomenon of surface plasmon resonance (SPR) was first discovered and investigated between 1902 and 1912 by R.M. Wood [42, 43] and Lord Rayleigh [44], but was not developed into the technique we use today until the 1960s by Kretschmann [45] and Otto [46], and further developed in the 1980s for applications in biosensing on thin films [47].

Kretschmann SPR sensors are the most dominant type of label-free optical sensors, and involve the binding of a molecule (ligand) onto a thin dielectric metal film, usually gold, which is then detected by a different molecule (analyte) flowing over the film and bonding to it (**Figure 1.6**) [48-50]. This changes the RI of the film which can be measured in real-time. The presence of the metal film is important to the SPR technique as the free electrons within this

metal allow for the resonance. The light is introduced to the metal layer *via* a prism where it is totally internally reflected, leading to resonance between the free electrons and the photons [51]. This resonance is in the form of oscillations, which subsequently causes an electromagnetic field to occur within the metal layer. This field is called the evanescent wave, and decays exponentially with distance from the metal film. Any changes in RI that occur within this field will cause a difference in the resonance angle, and consequently change the output. This is a very powerful quantitative technique but is hindered by the small penetration depth of the evanescent wave.

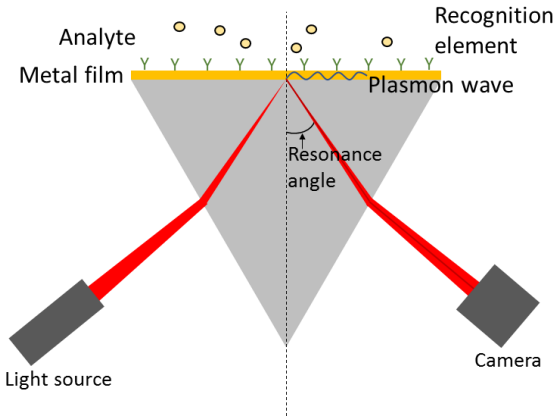

Figure 1.6. Schematic of an SPR setup.

Unfortunately, the SPR technique has some inherent properties that make it expensive and unsuitable for certain uses such as techniques requiring electro-focusing. The initial and maintenance costs of such sensors is often high, due to the need for highly specialised and delicate instrumentation, expensive and fragile metal films, and low penetration depth (<300 nm) [52-54].

Optical leaky waveguides (LWs) can overcome the issues presented above for interferometer and SPR sensors and will be discussed in depth in **Chapter 2**.

1.2.4 Label-based versus label-free

Detection of biomarkers can be broadly split into two groups: label-based and label-free (**Figure 1.7**).

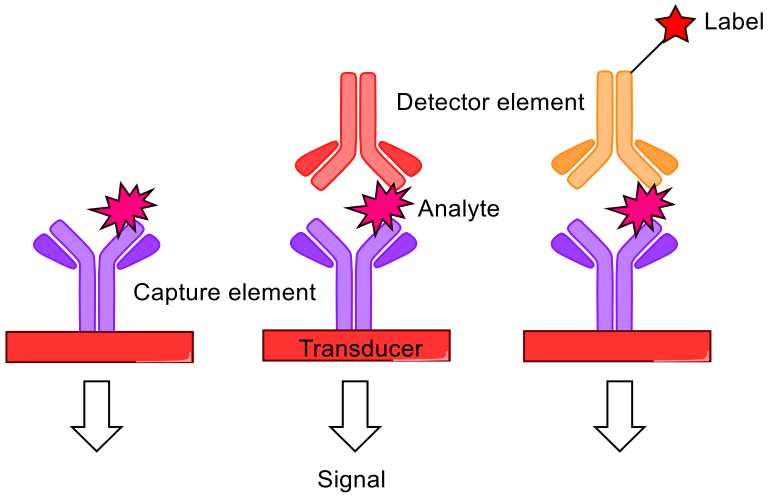

Figure 1.7. Label-free (left) versus label-based (middle and right) sensing. Label-based sensing can involve a detector element that is naturally labelled (middle), or a detector element with an added label (right) [55].

Traditionally, label-based detection involves the use of a dye or tag which changes colour or intensity when it binds to a target molecule for subsequent detection by optical methods involving colorimetric, fluorescent, or luminescent phenomena [21]. Such techniques have high sensitivity and well-developed methods, and fluorescent probes are used extensively throughout the biosensing community owing to their simplicity and sensitivity. Such probes can be used to tag analytes or detector moieties, or even to assist and amplify techniques such as microscopy [56]. The enzyme-linked immunosorbent assay (ELISA) is a classic example of a label-based technique. Optical label-based biosensors include a fluorescent swelling polymer gel reported by McCurley [57]. In this instance, a hydrogel was functionalised with a fluorophore, a free amine functional group, and glucose oxidase. When exposed to glucose the hydrogel would swell due to protonation of the amine functional group by the reaction product gluconic acid, while the concentration of fluorophore present

remained constant but would spread throughout the swollen gel. This is an indirect way to monitor glucose concentration.

Swanson *et al.* reported a waveguide-based optical biosensor which was used to detect biomarkers of breast cancer [58], anthrax [59], influenza [60], and TB [61, 62]. Analytes were detected down to 1 pM using the evanescent wave, and the addition of excitable fluorophores increased sensitivity and reduced background fluorescence in unclean samples.

While label-based biosensors certainly have a well-defined and important role to play in sensing, they are not without flaws. Often the labelling technique will lead to lengthy sample preparation and analysis which often need to be conducted separately rather than easily within one device [63], and by experienced technicians. Also, the label can potentially interact with the surface of the target molecule and permanently alter it which causes problems if the molecule is still needed to react with yet another molecule [64]. In a similar manner, labels can cause false-positives by interacting with non-targeted molecules, particularly in unprocessed samples [65].

Conversely, label-free biosensors adopt the use of various techniques to detect the desired analytes and monitor changes by interacting directly with the analyte; no label is needed. Instead, the response is due to inherent properties of the analyte such as optical, electrochemical, or physical changes. Raman Spectroscopy, SPR, Piezoelectric detection, and Optical Interferometry are all examples of label-free biosensing techniques [24].

1.3 Protein detection methods

There are many protein detection methods available in modern testing laboratories, and some of the most common methods are based on the techniques described in this section. These techniques typically have high sensitivity and specificity, but long processing times (from a few hours to multiple days) and require a highly trained technician to complete.

Perhaps the best-known technique used to study the presence and concentration of soluble substances including antibodies, antigens, and proteins is the quantitative ELISA. Sandwich ELISA, the most common type of ELISA, is depicted in **Figure 1.8** and occurs firstly by the immobilisation of a capture antibody to a microplate. The plate is then treated with a blocking agent. The sample containing the target antigen is applied to the microplate, where it will bind with the capture antibody. A detection antibody is then added, which also binds to the antigen *via* a different epitope and contains an enzyme [66]. Finally, the substrate is added, which reacts with the enzyme and produces a measurable colorimetric response. This response can be chemiluminescent, chromogenic or chemifluorescent, and can be measured by using the appropriate corresponding instrument i.e. a fluorometer for chemifluorescent phenomena [66].

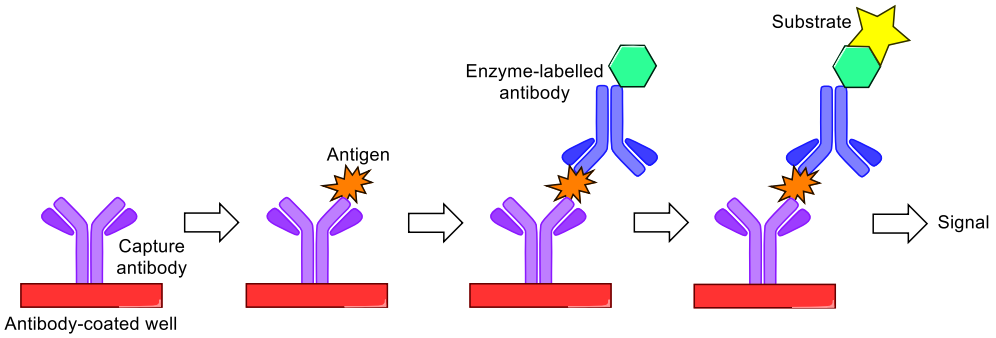

Figure 1.8. Sandwich ELISA.

Due to the high specificity of an antigen-antibody complex this is a very powerful and accurate technique that is capable of detecting antigens in a multicomponent sample, provided that the correct antibody and antigens are chosen. Unfortunately, this does come at a price, as ELISA is a labour-intensive technique requiring multiple incubation and washing steps and hence can take multiple days to run [67]. The optimisation of the technique for different antibody-antigen complexes can also take a significant amount of time and costly chemicals, with GenWay Biotech quoting an average of two months to develop a sandwich ELISA [68]. Finally, there is a high risk of false positives/negatives if not carried out correctly [69].

Western blot (WB) tests are commonly seen in biological laboratories and are often used to confirm a positive ELISA result for human immunodeficiency virus (HIV) or Lyme disease [70]. Again, this is a powerful technique capable of identifying specific proteins from within a complex sample. Before the WB can be carried out the sample must be separated based on protein size. To achieve this the sample is first treated with sodium dodecyl sulfate (SDS) to unfold the proteins, and polyacrylamide (PAAm) gel electrophoresis is used to separate the linear proteins *via* size; this particular technique is called sodium dodecyl sulfate-polyacrylamide gel electrophoresis (SDS-PAGE) (**Figure 1.9**). When the electric field is applied the linear proteins migrate through the PAAm mesh *via* electrophoresis to the positive electrode at differing speeds based on their mass. A size marker is often run alongside the samples to allow for a direct comparison.

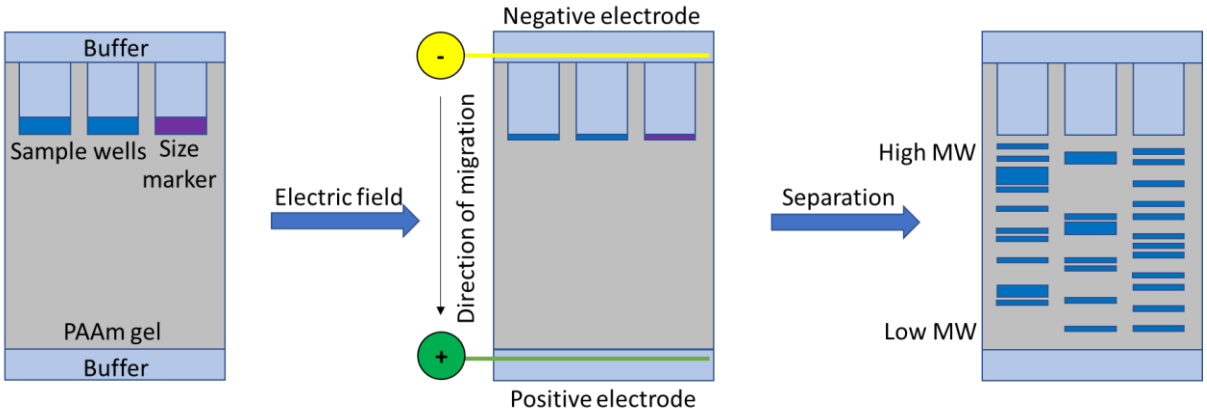

Figure 1.9. SDS-PAGE [71].

Once separation is complete the samples are transferred *via* further electrophoresis to the blotting membrane, which is typically nitrocellulose or polyvinylidene difluoride (PVDF). The membrane is then blocked to prevent non-specific binding, followed by incubation with the antibody corresponding to the protein of interest. The membrane is washed, then again incubated with a second antibody containing an enzyme label; this binds to the first antibody and a complementary substrate is added which binds with the immobilised enzyme and produces a positive response if the protein is present [72]. This is shown in **Figure 1.10.** As is apparent, there are many steps involved in a WB test which increases the length of processing time. They are also more expensive than ELISA, and only provide qualitative/semi-quantitative results [72].

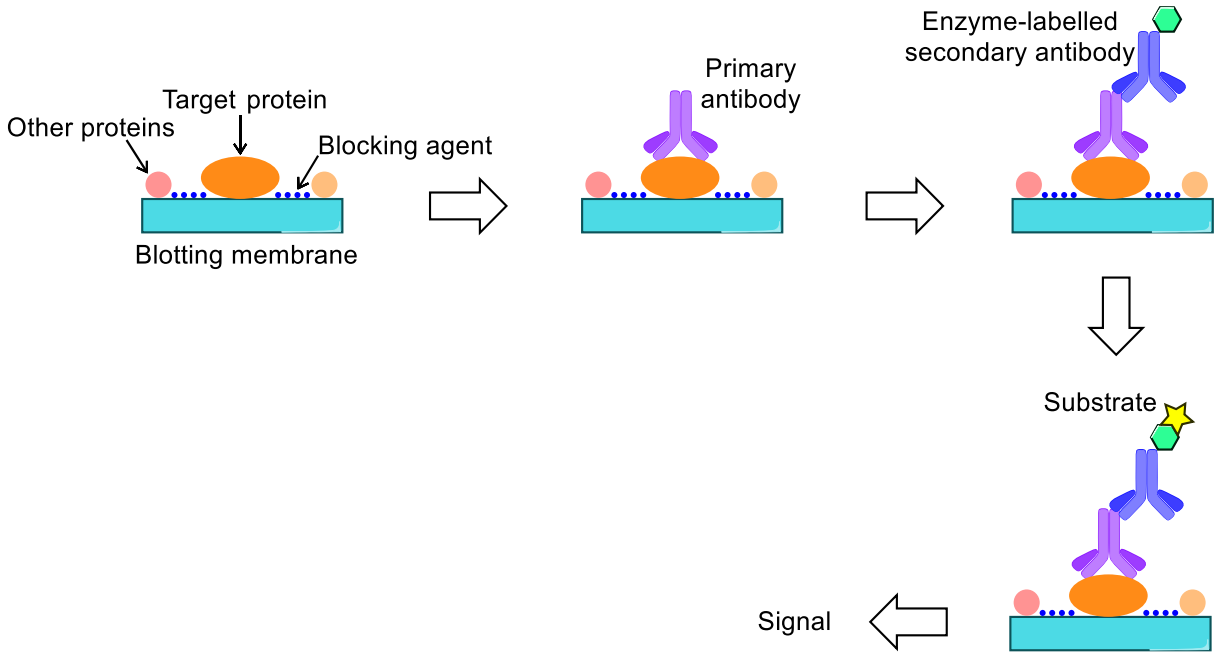

Figure 1.10. Western blot [73].

Mass spectrometry (MS) is a widely used separation and analysis technique, allowing for semi-quantitative detection and subsequent identification of proteins. The sample can be liquid, gas, or solid, and will be both vaporised and ionised by an ion source. The ions are accelerated through the MS column where they are subjected to a magnetic field which separates the ions based on their mass-to-charge (m/z) ratio. Smaller and highly charged ions are deflected by the magnetic field to a higher degree than larger and less charged ions, causing the separation. The sensitivity of modern MS instruments can detect analytes down to a concentration of 10^{-18} [74]. MS is not a quantitative technique by nature, as a portion of ions will be lost during the analysis and not all species ionise in the same proportion as others. However, combination of MS with reference standards can account for this issue. Unlike ELISA and WB, some sample preparation is necessary for MS, particularly when a quantitative result is required. The preparation steps can add lengthy and expensive steps to the technique, such as sample pre-concentration/enrichment and clean-up [74].

It is clear that we have the techniques available to detect very small quantities of analytes, but none of these are the “perfect” test. Long processing times, moderate- to high-intensity labour, and high costs are all problems faced by these techniques, showing why research is ongoing into development of new or modified techniques which address these issues.

1.4 Procalcitonin and C-reactive protein

Procalcitonin (PCT) is a known acute phase reactant (APR) biomarker which can be particularly useful in determining whether a patient requires antibiotics or not. The presence of increased PCT levels in the blood is indicative of bacterial inflammation, and has been studied with particular interest into sepsis and pneumonia treatment [75]. After infection by bacteria, elevated PCT levels in the body can be detected within 2 hours, increase rapidly within 6-12 hours, and peak at 24 hours [76]. These raised levels are sustained whilst bacterial infection persists and drop by approximately 50% each day as the bacterial infection clears [3, 76].

Conveniently, PCT levels do not change significantly in response to viral infection [3, 77], maintaining the normal levels of below 0.05 ng/mL compared with up to 1000 ng/mL for severe bacterial infection [78]. This makes PCT an inherently strong marker for distinguishing between bacterial and viral infection.

As PCT levels remain stable when exposed to viral infection, monitoring PCT levels can indicate whether antibiotics need to be prescribed within early onset of symptoms, indicate whether a treatment is working, and once PCT levels have dropped below a threshold amount the antibiotic treatment can be deescalated and safely stopped. Also, PCT levels can be conveniently monitored through simple blood samples rather than anything more invasive [79]. These characteristic features make PCT an excellent choice for further study as a biomarker.

Unfortunately, the low concentrations of PCT present in blood samples incurs an additional challenge in development of accurate biosensors, and C-reactive protein (CRP) is

often used as the gold standard test to detect inflammation. CRP is an APR synthesised in the liver with typical levels remaining below 0.01 mg/mL in a healthy adult which increase significantly in response to inflammation [80]. These larger values make CRP much easier to accurately detect than PCT, but CRP is a non-specific biomarker, meaning it cannot be used to distinguish between bacterial and viral infection and can only provide an indication as to whether the patient is suffering from some form of inflammatory infection [81]. Chronic inflammation such as that seen in rheumatoid arthritis will lead to persistently elevated CRP levels and make CRP testing in such individuals for suspected bacterial infection less useful, while moderate CRP levels can have other explanations such as poor sleep [82]. Additionally CRP levels take 48 to 72 hours to peak after infection by bacteria; this is significantly longer than the 24 hours seen in PCT and could delay treatment [76].

Therefore, the motivation behind this project is the beginning of the development of an optical biosensor capable of detecting clinically relevant levels of PCT at POC level, with the aim of allowing judicious use of antibiotics. To do this, other relevant analytes have been carefully selected to allow for the development and fine tuning of the sensing platform which will then be refined to detect PCT in the future.

1.5 Point-of-Care testing

Many of the well-known diagnostic tools used on a day-to-day basis in hospitals require an experienced and dedicated technician, physical space, and a large investment. For example, TB diagnosis may rely on a combination of tests, including but not limited to: X-ray, computerised tomography (CT), magnetic resonance imaging (MRI), and ultrasound scans [83]. All of these methods require expensive and bulky instrumentation and careful handling. Each scan must be carried out by a qualified and highly trained technician and can in some cases take a few hours to complete for a single patient, making them low-throughput devices. Such scans do typically give excellent results, allowing medical staff to accurately pinpoint areas of concern and rule out other potential causes, but most cannot be used as quick (<20 minutes) and portable tests. Other standard tests carried out in hospitals and doctors' offices include blood, phlegm, sputum, and urine cultures. Again, these typically have high specificity and selectivity, but can take days to weeks to provide results and some patients do not have the luxury of this waiting time based on the severity of the infection. For any infection, timely diagnosis and treatment is vital for the best outcome.

One method to help increase correct diagnosis and reduce antibiotic over-prescription is through POC devices. Testing for bacterial infections during an appointment would give definitive answers on whether antibiotics should be prescribed or not within an acceptable waiting time, compared to laboratory testing which will lead to significant delays in treatment. This should prevent over-prescription of antibiotics as the medical professional will not need to guess whether the patient is suffering from a viral or bacterial infection, which in many cases leads to prescription of antibiotics "just in case" [8]. A study by the European Commission in 2009 showed that 53% of EU citizens agreed with the statement "Antibiotics

kill viruses", while 11% did not know the answer; this lack of understanding from the general population can add to the pressure doctors' face from their patients to prescribe antibiotics [84], and it is often safer for a doctor to prescribe antibiotics at the request of their patient than to refuse and risk their symptoms becoming worse. A conclusive result that can be discussed with the patient during the appointment would be much more beneficial to both parties.

It will also allow for the swift treatment of dangerous bacterial infections much quicker, both in doctors' offices and in hospitals. What classes as an acceptable waiting time is up for debate and will rely on the suspected cause of infection, specific type of test performed along with the ease of the sample collection and instrumentation, and the competency of the technician in operating the device and interpreting results. There are certain guidelines for some tests, for example the National Academy of Clinical Biochemistry suggest cardiac troponins should be detected and treated within less than 60 minutes [85]. Ideally, POC devices should offer results within a practical timeframe, i.e., before the patient leaves the doctors' surgery, or within an hour of admittance to the emergency room.

To achieve this, samples are tested as "whole samples" with minimal/no pre-processing. Additionally, the sample does not need to be sent to a testing laboratory, with sample analysis and results occurring within the device itself.

Figure 1.11 shows a simplified diagnostic flow chart for patient diagnosis *via* standard methods and POC methods. The POC method provides a quicker turnaround, ideally removing the need for sending off and pre-processing the initial sample. Additionally, in POC techniques the sample analysis and results often occur simultaneously without input from the technician,

such as with lateral flow tests where a simple positive or negative result is provided. This is in direct comparison to laboratory-based techniques which often require the expertise of a specialised practitioner to interpret the results and feed these back to the doctor who ordered the test.

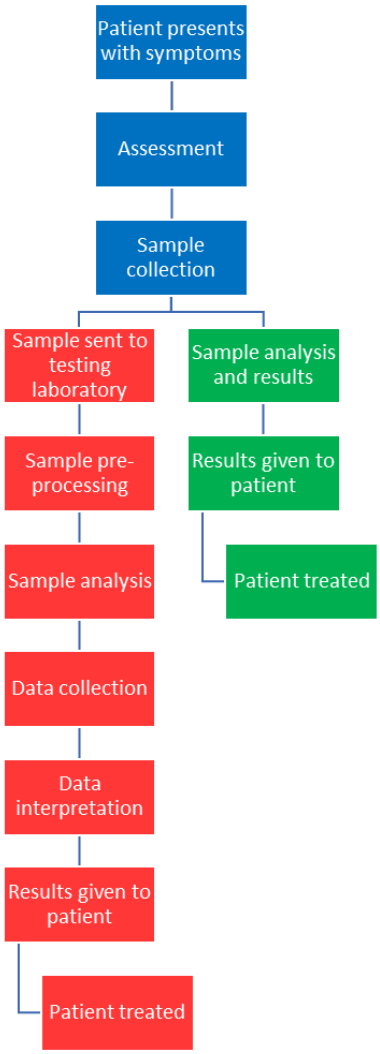

Figure 1.11. Flow chart comparing a standard diagnostic procedure (red) to a POC diagnostic procedure (green) [86].

POC testing has been known for decades, for example in the form of home glucose monitoring for diabetic patients [24], self-test pregnancy strips [87], and more recently the widespread use of lateral flow tests for COVID-19. However, the increasing demand for healthcare solutions worldwide has put a huge strain on the budget of various Governments,

leading to a need for cheaper and more practical solutions [88-90], including improved diagnostics and homecare as opposed to expensive hospitalisation and treatment. This issue is faced across the world including third-world countries where abundant poverty and disease only adds to the increased need for affordable and portable POC devices. POC testing can be applied in wide range of settings, such as [91]:

- Doctors' surgeries
- Pharmacies
- Health clinics
- Schools
- Care facilities and nursing homes
- Temporary testing sites
- Urgent care and walk-in centres
- Hospitals
- Home

POC systems come in many different forms, from small portable devices up to benchtop machinery (sometimes referred to as near-patient devices). These include devices designed to measure heartrate and oxygen saturation [92], but have also been developed to include bio-recognition systems. They have been designed to measure a range of different biomarkers from different types of specimens, such as those collected from blood, sputum, urine, and breath. POC devices have several desirable features, including those mentioned below in **Table 1.2**.

Table 1.2. A non-exhaustive collection of ideal properties for a POC device.

Fast results	Accurate	Specific	Selective
Accessible	Easy to use	Low cost	Minimally invasive
Portable	Durable	Reusable	Long-lived

Realistically, achieving all these desired qualities within one device is not feasible, but certain features are more important than others. Essentially, POC devices must be designed to achieve a good turnaround in both time and accuracy, at the lowest cost possible whilst remaining portable. This will make it accessible to a range of different healthcare services across the world. Currently the cost of antibiotic prescription is typically cheaper than the tests used to identify the source of the infection, which makes it more economical for antibiotics to be prescribed without a conclusive test [8]. It is therefore of vital importance that new tests can be developed that are cheaper than the antibiotics themselves and are consequently worthwhile to run on both a cost and time basis.

While in first-world countries antibiotics are strictly controlled and regulated, in developing countries antibiotics are much easier to access and are heavily over-prescribed. A 2012 report suggested that 44-97% of patients in hospitals are prescribed antibiotics in developing countries despite not always being necessary [93]. The author also noted uninformed self-medication with antibiotics is prevalent in such countries, further increasing the risk of an increase in bacterial resistance. Thus, the need for a quick and reliable POC test is high in all countries to ensure better chances of survival, both imminently from antibiotic infections, and long-term from antibiotic resistance and the emergence of superbugs.

There are a number of POC tests available that target CRP, such as the QuikRead go CRP, which boasts quantitative results within 2 minutes of sample application, and requires only 20 µL of blood sample and no pre-processing [94]. The NycoCard CRP test combined with the NycoCard READER II is able to quantitatively measure CRP levels in a 5 µL whole blood sample within 3 minutes [95]. Both these tests feature detection limits between 5 and 200 mg/L and are highly suitable for POC testing inside and outside of hospitals, with low sample volumes and quick turnaround, and no training required. But as each test is single use, they could quickly become a costly and environmentally damaging method if used regularly. Additionally, both tests must be stored at 2-8 °C which could pose storage and transportation issues.

Current methods of PCT detection vary, from laboratory-based culture tests to those branded as POC. Biopanda reagents have developed the Biopanda PCT Rapid Test, a lateral flow immunoassay which provides results in 15 minutes [96]. Patient blood samples are required, anywhere from 25 mL for serum or plasma samples, up to 50 mL for whole blood samples. This can be placed into a pre-packaged test cassette, alongside a buffer, to provide results within 15 minutes with an accuracy of 98.8% (**Figure 1.12**).

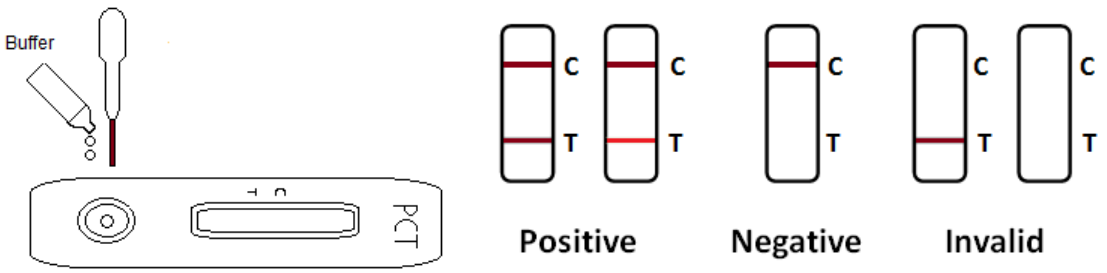

Figure 1.12. Biopanda PCT Rapid Test [96].

This is a good example of a simple and practical POC test, but only provides qualitative results; there is no indication as to the concentration of PCT, therefore making it difficult to diagnose the severity of the infection. Additionally, 50 mL of blood sample is a significant volume for a POC and qualitative test.

Radiometer also offer a rapid PCT test, working in 21 minutes and providing quantitative results [97]. Usefully, this device also does not require prior sample handling. The major disadvantage of this technique is expensive specialised instrumentation requiring a significant investment.

There is a gap in the market for a quantitative, reliable, quick, and affordable POC test for PCT. While CRP levels are useful for diagnosis, PCT is more specific and will offer more precise information for treatment.

Table 1.3 provides a comparison of common infections and the current methods used to diagnose them.

Table 1.3. A summary of some of the currently available methods used to diagnose certain respiratory illnesses. Waiting times are based on outpatient diagnosis.

INFECTION	TEST	POC	TIME		ADVANTAGES	DISADVANTAGES
			Collection	Results		
TUBERCULOSIS (TB)	X-ray [83, 98]	No	<10 min	Same day to 2 weeks	High quality imaging. Painless.	Radiographer required to read results.
	CT, MRI, ultrasound [83, 99-101]	No	10 min to 2 h	2-4 weeks	High quality imaging. Painless.	Radiographer required to read results. Patients suffering from claustrophobia or issues with loud sounds may struggle. Expensive and bulky instrumentation.
	Endoscopy, laparoscopy [83, 102, 103]	No	30 min to 2 h	2-3 weeks	Allows for investigation and diagnosis that may not be possible from non-invasive methods.	Invasive. Uncomfortable and/or painful for the patient. May require local or general anaesthetic.
	Phlegm culture tests, smear microscopy	No	<10 min	Up to 6 weeks	Well-developed. Reliable results.	Long waiting times can reduce treatment effectiveness. Unsuitable for severe infections.
	Lumbar puncture [83, 104]	No	20 min to 1 h	48 h	Useful for detection of specific analytes in spinal fluid. Can determine whether the TB has spread to the central nervous system.	Uncomfortable and/or painful for the patient. Requires a skilled practitioner to reduce risk to patient.
	Urine and blood tests [83, 105]	No	<10 min	Up to 6 weeks	Well-developed and suited to a large range of different tests.	Long waiting times can reduce treatment effectiveness.
	Mantoux test [83]	No	<10 min	48-72 h	Very simple test with visible result. Detects latent and active TB.	May provide false-positives in patients who have previously received the BCG vaccine.
	Interferon-Gamma Release Assays [83, 106]	No	<10 min	16-24 h	Quantitative.	Not recommended for patients under 5 years. Requires chest x-ray to confirm.

					Suitable for patients who have previously received the BCG vaccine.	
	Xpert MTB/RIF [107] (sputum sample)	Yes	<10 min	2-4 h	Can detect TB and resistance to common TB drugs simultaneously. Can be carried out in a doctors' office.	Susceptible to false-positives in patients who previously had TB. Expensive instrumentation. Requires ambient temperature. 2 h processing time reduces POC usability.
	GeneXpert OMNI [108]	Yes	<10 min	2 h	4 h battery life allows for use without a consistent power supply. Can be used with the Xpert MTB/RIF cartridges.	Expensive cartridges. Commercialisation has been suspended at the time of writing.
	Portable digital chest X-ray (CXR) [109]	Yes	<10 min	Same day to 2 weeks	High sensitivity, same day diagnosis.	Low specificity. Requires a van to transport.
PNEUMONIA	X-ray [110]	No	<10 min	Same day to 2 weeks	See TB.	See TB.
	Blood and sputum tests [105, 110]	No	<10 min	Up to 6 weeks	Well-developed and suited to a large range of different tests.	Long waiting times can reduce treatment effectiveness.
	Physical examination [110]	Yes	<20 min	Same day	Cheap, usually the first point of contact for a patient.	Not quantitative. Subject to bias.
	mariPOC [111, 112] (nasopharynx swab)	Yes	<10 min	20 min preliminary 2 h full	Quantitative detection of viral pneumonia. Can run multiple samples at once. Easy sample collection.	Low sensitivity. Does not rule out additional bacterial infection.
	Portable digital CXR [108]	Yes	<10 min	Same day to 2 weeks	See TB.	See TB.

PHARYNGITIS OR TONSILLITIS/STREP-A	Throat culture [113]	No	<10 min	Up to 6 weeks	Well-developed. Reliable results.	Long waiting times can reduce treatment effectiveness. Unsuitable for severe infections.
	Blood test [105]	No	<10 min	Up to 6 weeks	See TB.	See TB.
	Physical examination [114]	Yes	<20 min	Same day	See pneumonia.	See pneumonia.
	QuikRead Go Strep A test [113, 115]	Yes	<10 min	10 min	Qualitative. Quick positive/negative response. High specificity.	Not quantitative. Single use.
	Clearview exact Strep A cassette/dipstick [113, 116]	Yes	<10 min	5 min	Qualitative. Quick positive/negative response. High specificity and sensitivity.	Not quantitative. Single use. Cannot distinguish between asymptomatic carriers and infected patients.
	BD Veritor plus system group A Strep [113, 117]	Yes	<10 min	5 min	Qualitative. Quick positive/negative response. High specificity and sensitivity.	Not quantitative. Single use.
	Molecular tests [113]	Yes	<10 min	<20 min	Qualitative.	Usually not quantitative.
LARYNGITIS	Throat culture [118]	No	<10 min	Up to 6 weeks	See pharyngitis.	See pharyngitis.
	Blood test [105, 118]	No	<10 min	Up to 6 weeks	See TB.	See TB.
	Biopsy [119, 120]	No	<30 min	3-10 days	Allows for direct testing of the sample.	Invasive. Uncomfortable and/or painful for the patient. Requires a skilled practitioner to reduce risk to patient.

						May require local or general anaesthetic.
	Laryngoscopy [119]	No	<30 min	3-10 days	Allows direct visualisation of the area.	Invasive. Uncomfortable and/or painful for the patient. Requires a skilled practitioner to reduce risk to patient. May require local or general anaesthetic.
	Physical examination [118]	Yes	<20 min	Same day	See pneumonia.	See pneumonia.
INFLUENZA	Nasal swab [121]	No	<10 min	24 h	Viral culturing with high specificity.	Unsuitable for doctors' offices.
	Lateral flow immunoassays [121]	Yes	<10 min	15 min	Quick results. Suitable as a guide for further investigation.	Low sensitivity. Low specificity. Narrow target range.
	Molecular assays [121]	Yes	<10 min	30-60 min	High sensitivity. High specificity. Wide target range.	Longer waiting time.
UNSPECIFIED RESPIRATORY INFECTIONS (CRP TESTS)	Blood tests [122]	No	<10 min	Up to 6 weeks	See TB.	See TB.
	QuickRead go CRP [94, 123, 124]	Yes	<10 min	2 min	20 µL sample. Whole blood, plasma, or serum samples.	Instrument costs £1050. 50 single-use tests cost £215. Storage must be between 2-8°C.
	NycoCard CRP and NycoCard READER II [95, 125]	Yes	<10 min	3 min	5 µL sample. Battery powered. Quantitative. Whole blood, plasma, or serum samples. Reader has cross-compatibility with other NycoCard tests.	Instrument costs £540. 48 single-use tests cost £160. Storage must be between 2-8°C.

1.6 Project specification and objectives

The motivation behind this project is to work towards the development of a POC biosensor capable of detecting PCT, with the inclusion of an internal referencing system.

The objectives of the project at this stage are as follows:

1. Study different hydrogel materials and their suitability as LWs. Covered in Chapters 3 and 4.
2. Investigate a stacked LW system to incorporate the required internal referencing. Covered in Chapter 4.
3. Develop an appropriate protein immobilisation method based on the chosen hydrogels. Covered in Chapter 5.
4. Detect clinically relevant levels of a chosen analyte in buffer and in the presence of interferents. Covered in Chapter 5.
5. Assess the use of a portable instrument for point-of-care testing. Covered in Chapter 6.

1.7 Thesis outline

Chapter 1: Introduction. This will cover the project outline and aims, with information on current methods and techniques for biosensing.

Chapter 2: Instrumentation and Techniques. The instrumentation used throughout this thesis will be introduced, and the optical sensing technique will be covered.

Chapter 3: Single Layer Waveguides. This chapter covers the characterisation and optimisation of all the various hydrogels investigated for use as a sensor leaky waveguide.

Chapter 4: Stacked Waveguides. This covers the fabrication and testing of reference leaky waveguides, along with stacked leaky waveguides to aid internal referencing.

Chapter 5: Protein Detection. Immunoglobulin G and lactoferrin are detected in this chapter by using both single and stacked leaky waveguides, and the effect of human serum and synthetic urine on the films is investigated.

Chapter 6: Portability. A portable instrument is introduced in this chapter and results presented in comparison to the laboratory-based instrument.

Chapter 7: Conclusion and Future Outlook. A conclusion of the project and scope of future work.

Chapter 8: Experimental. A record of all the experimental methods and instrumentation used.

1.8 References

1. Health Direct. *Differences between bacterial and viral infection*. 2018 [cited 19-10-2018]; Available from: https://www.healthdirect.gov.au/bacterial-vs-viral-infection.
2. Swamy, M.A., et al., *Profile of respiratory pathogens causing acute respiratory infections in hospitalised children at Rajasthan a 4 year's study.* Indian Journal of Medical Microbiology, 2018. **36**(2): p. 163-171.
3. Schuetz, P., et al., *Effect of procalcitonin-guided antibiotic treatment on mortality in acute respiratory infections: a patient level meta-analysis.* Lancet Infect Dis, 2018. **18**(1): p. 95-107.
4. Meili, M., et al., *Infection biomarkers in primary care patients with acute respiratory tract infections-comparison of Procalcitonin and C-reactive protein.* BMC pulmonary medicine, 2016. **16**: p. 43-43.
5. Centers for Disease Control and Prevention. *About Antibiotic Resistance*. 2021 [cited 12-05-2022]; Available from: https://www.cdc.gov/drugresistance/about.html#:~:text=Antibiotic%20resistance%20happens%20when%20germs,in%20the%20U.S.%20each%20year.
6. European Centre for Disease Prevention and Control and World Health Organization, *Antimicrobial resistance surveillance in Europe*. 2020.
7. Reygaert, W.C., *An overview of the antimicrobial resistance mechanisms of bacteria.* AIMS microbiology, 2018. **4**(3): p. 482-501.
8. O'Neill, J., *Tackling drug-resistant infections globally: final report and recommendations*. 2016: Government of the United Kingdom.
9. Centers for Disease Control and Prevention, *Antibiotic resistance threats in the United States, 2019.* 2019.
10. van Ingen, J., et al., *Why Do We Use 600 mg of Rifampicin in Tuberculosis Treatment?* Clinical Infectious Diseases, 2011. **52**(9): p. e194-e199.
11. TB Alliance. *FDA Approves New Treatment for Highly Drug-Resistant Forms of Tuberculosis*. 2019 [cited 12-08-2022]; Available from: https://www.tballiance.org/news/fda-approves-new-treatment-highly-drug-resistant-forms-tuberculosis.
12. Dadgostar, P., *Antimicrobial Resistance: Implications and Costs.* Infection and drug resistance, 2019. **12**: p. 3903-3910.
13. The Review on Antimicrobial Resistance, *Antimicrobial Resistance: Tackling a crisis for the health and wealth of nations*. UK Government commissioned report, 2014.
14. World Health Organization. *Antimicrobial resistance*. 2021 [cited 12-05-2022]; Available from: https://www.who.int/news-room/fact-sheets/detail/antimicrobial-resistance.
15. The Pew Charitable Trusts. *Tracking the Global Pipeline of Antibiotics in Development, March 2021*. 2021 [cited 12-08-2022]; Available from: https://www.pewtrusts.org/en/research-and-analysis/issue-briefs/2021/03/tracking-the-global-pipeline-of-antibiotics-in-development.
16. Wellcome. *Why is it so hard to develop new antibiotics?* 2020 [cited 12-08-2022]; Available from: https://wellcome.org/news/why-is-it-so-hard-develop-new-antibiotics.
17. Schultz, L., et al., *Economic Impact of Redundant Antimicrobial Therapy in US Hospitals.* Infection Control & Hospital Epidemiology, 2014. **35**(10): p. 1229-1235.
18. World Health Organization. *WHO multi-country survey reveals widespread public misunderstanding about antibiotic resistance*. 2015 [cited 27-05-2022]; Available from: https://www.who.int/news/item/16-11-2015-who-multi-country-survey-reveals-widespread-public-misunderstanding-about-antibiotic-resistance#:~:text=More%20than%20half%20(53%25),can%20be%20treated%20by%20antibiotics.
19. Oxford Languages. *Biosensor*. 2022 [cited 08-06-2022].

20. Shavanova, K., et al., *Application of 2D Non-Graphene Materials and 2D Oxide Nanostructures for Biosensing Technology.* Sensors, 2016. **16**(2): p. 223.
21. Damborský, P., J. Švitel, and J. Katrlík, *Optical biosensors.* Essays in Biochemistry, 2016. **60**(1): p. 91-100.
22. Electronics Hub. *What are Biosensors? Principle, Working, Types and Applications*. 2019 [cited 08-06-2022]; Available from: https://www.electronicshub.org/types-of-biosensors/.
23. Zanchetta, G., et al., *Emerging applications of label-free optical biosensors.* Nanophotonics, 2017. **6**(4): p. 627.
24. Khansili, N., G. Rattu, and P.M. Krishna, *Label-free optical biosensors for food and biological sensor applications.* Sensors and Actuators B: Chemical, 2018. **265**: p. 35-49.
25. Kazemi-Darsanaki, R., et al., *Biosensors: Functions and Applications.* Journal of Biology and Today's World, 2013. **2**: p. 20-23.
26. Naresh, V. and N. Lee, *A Review on Biosensors and Recent Development of Nanostructured Materials-Enabled Biosensors.* Sensors, 2021. **21**(4): p. 1109.
27. Juan-Colás, J., S. Johnson, and T.F. Krauss, *Dual-Mode Electro-Optical Techniques for Biosensing Applications: A Review.* Sensors (Basel), 2017. **17**(9).
28. Markets and Markets, *Biosensors Market by Type, Product (Wearable, Non-wearable), Technology, Application (POC, Home Diagnostics, Research Lab, Environmental Monitoring, Food & Beverages, Biodefense) and Region (2021-2026)*. 2021.
29. Akolpoglu, M.B., et al., *Chapter 9 - Biosensing–Drug Delivery Systems for In Vivo Applications*, in *Advanced Biosensors for Health Care Applications*, Inamuddin, et al., Editors. 2019, Elsevier. p. 249-262.
30. Clark Jr., L.C. and C. Lyons, *ELECTRODE SYSTEMS FOR CONTINUOUS MONITORING IN CARDIOVASCULAR SURGERY.* Annals of the New York Academy of Sciences, 1962. **102**(1): p. 29-45.
31. Ypsomed Limited. *mylife Pura X*. 2015 [cited 12-08-2022]; Available from: https://www.mylife-diabetescare.com/en-GB/products/blood-glucose-monitoring-systems/mylife-pura-x.html.
32. Fang, A., H.T. Ng, and S.F.Y. Li, *A high-performance glucose biosensor based on monomolecular layer of glucose oxidase covalently immobilised on indium–tin oxide surface.* Biosensors and Bioelectronics, 2003. **19**(1): p. 43-49.
33. Lim, H.J., et al., *Quartz crystal microbalance-based biosensors as rapid diagnostic devices for infectious diseases.* Biosensors & bioelectronics, 2020. **168**: p. 112513-112513.
34. Nanoscience Instruments. *Quartz Crystal Microbalance (QCM)*. [cited 10-07-2022]; Available from: https://www.nanoscience.com/techniques/quartz-crystal-microbalance/.
35. Adlerberth, J., et al., *Thermometric analysis of blood metabolites in ICU patients.* Journal of Thermal Analysis and Calorimetry, 2020. **140**(2): p. 763-771.
36. Yoo, S.M. and S.Y. Lee, *Optical Biosensors for the Detection of Pathogenic Microorganisms.* Trends in Biotechnology, 2016. **34**(1): p. 7-25.
37. Zygo Corporation. *Interferometry: Measuring with Light*. [cited 09-06-2022]; Available from: https://www.photonics.com/Articles/Interferometry_Measuring_with_Light/a25128.
38. Kussrow, A., C.S. Enders, and D.J. Bornhop, *Interferometric methods for label-free molecular interaction studies.* Analytical chemistry, 2012. **84**(2): p. 779-792.
39. Hradetzky, D., C. Mueller, and H. Reinecke, *Interferometric label-free biomolecular detection system.* Journal of Optics A: Pure and Applied Optics, 2006. **8**(7): p. S360-S364.
40. David D. Nolte, *Optical Interferometry for Biology and Medicine*. Bioanalysis. 2012, New York: Springer.
41. Zhou, C., M.K. Hedayati, and A. Kristensen, *Multifunctional waveguide interferometer sensor: simultaneous detection of refraction and absorption with size-exclusion function.* Optics Express, 2018. **26**(19): p. 24372-24383.

42. Wood, R.W., *On a Remarkable Case of Uneven Distribution of Light in a Diffraction Grating Spectrum.* Proceedings of the Physical Society of London, 1902. **18**(1): p. 269-275.
43. Wood, R.W., *XXVII. Diffraction gratings with controlled groove form and abnormal distribution of intensity.* The London, Edinburgh, and Dublin Philosophical Magazine and Journal of Science, 1912. **23**(134): p. 310-317.
44. Rayleigh, L., *On the Dynamical Theory of Gratings.* Proceedings of the Royal Society of London, 1907. **79**(532): p. 399-416.
45. Kretschmann, E. and H. Raether, *Radiative Decay of Nonradiative Surface Plasmons Excited by Light.* Zeitschrift für Naturforschung A, 1968. **23**: p. 2135-2136.
46. Otto, A., *Excitation of nonradiative surface plasma waves in silver by the method of frustrated total reflection.* Zeitschrift für Physik A Hadrons and nuclei, 1968. **216**(4): p. 398-410.
47. Löfås, S. and B. Johnsson, *A novel hydrogel matrix on gold surfaces in surface plasmon resonance sensors for fast and efficient covalent immobilization of ligands.* Journal of the Chemical Society, Chemical Communications, 1990(21): p. 1526-1528.
48. Drescher, D.G., N.A. Ramakrishnan, and M.J. Drescher, *Surface plasmon resonance (SPR) analysis of binding interactions of proteins in inner-ear sensory epithelia.* Methods in molecular biology (Clifton, N.J.), 2009. **493**: p. 323-343.
49. van der Merwe, P. *Surface plasmon resonance*. [PDF] 2011 [cited 16-04-2019]; Available from: http://www.biophysics.bioc.cam.ac.uk/wp-content/uploads/2011/02/spr1.pdf.
50. Tang, Y., X. Zeng, and J. Liang, *Surface Plasmon Resonance: An Introduction to a Surface Spectroscopy Technique.* Journal of chemical education, 2010. **87**(7): p. 742-746.
51. Reichert Technologies. *What is Surface Plasmon Resonance (SPR)?* 2020 [cited 06-06-2020]; Available from: https://www.reichertspr.com/about/what-is-suface-plasmon-resonance-spr/.
52. Bustos, R.H., et al., *Label-Free Quantification of Anti-TNF-alpha in Patients Treated with Adalimumab Using an Optical Biosensor.* Sensors (Basel), 2018. **18**(3).
53. Hulme, J., et al., *Internally-referenced resonant mirror for chemical and biochemical sensing.* Analyst, 2002. **127**(9): p. 1233-1236.
54. Abbas, A., M.J. Linman, and Q. Cheng, *Sensitivity Comparison of Surface Plasmon Resonance and Plasmon-Waveguide Resonance Biosensors.* Sensors and actuators. B, Chemical, 2011. **156**(1): p. 169-175.
55. Sin, M.L.Y., et al., *Advances and challenges in biosensor-based diagnosis of infectious diseases.* Expert review of molecular diagnostics, 2014. **14**(2): p. 225-244.
56. Tian, X., et al., *Fluorescent small organic probes for biosensing.* Chemical Science, 2021. **12**(10): p. 3406-3426.
57. McCurley, M.F., *An optical biosensor using a fluorescent, swelling sensing element.* Biosensors and Bioelectronics, 1994. **9**(7): p. 527-533.
58. Mukundan, H., et al., *Waveguide-based biosensors for pathogen detection.* Sensors (Basel, Switzerland), 2009. **9**(7): p. 5783-5809.
59. Mukundan, H., et al., *Quantitative multiplex detection of pathogen biomarkers on multichannel waveguides.* Anal Chem, 2010. **82**(1): p. 136-44.
60. Kale, R.R., et al., *Detection of Intact Influenza Viruses using Biotinylated Biantennary S-Sialosides.* Journal of the American Chemical Society, 2008. **130**(26): p. 8169-8171.
61. Mukundan, H., et al., *Understanding the interaction of Lipoarabinomannan with membrane mimetic architectures.* Tuberculosis (Edinb), 2012. **92**(1): p. 38-47.
62. Sakamuri, R.M., et al., *Detection of stealthy small amphiphilic biomarkers.* Journal of microbiological methods, 2014. **103**: p. 112-117.
63. Juan-Colás, J., *Introduction to Label-Free Biosensing*, in *Dual-Mode Electro-photonic Silicon Biosensors*. 2017, Springer International Publishing: Cham. p. 7-35.
64. Toseland, C.P., *Fluorescent labeling and modification of proteins.* Journal of Chemical Biology, 2013. **6**(3): p. 85-95.

65. Peterson, E.M. and J.M. Harris, *Quantitative detection of single molecules in fluorescence microscopy images.* Anal Chem, 2010. **82**(1): p. 189-96.
66. ThermoFisherScientific. *Overview of ELISA*. [cited 17-03-2020]; Available from: https://www.thermofisher.com/uk/en/home/life-science/protein-biology/protein-biology-learning-center/protein-biology-resource-library/pierce-protein-methods/overview-elisa.html.
67. Li, Y. and V.M. Cassone, *A simple, specific high-throughput enzyme-linked immunosorbent assay (ELISA) for quantitative determination of melatonin in cell culture medium.* International immunopharmacology, 2015. **28**(1): p. 230-234.
68. GenWay Biotech. *Sandwich ELISA*. [cited 08-06-2022]; Available from: https://www.genwaybio.com/services/sandwich-elisa#:~:text=Sandwich%20ELISA%20development%20typically%20takes,customers%20or%20developed%20by%20GenWay.
69. Sakamoto, S., et al., *Enzyme-linked immunosorbent assay for the quantitative/qualitative analysis of plant secondary metabolites.* Journal of natural medicines, 2018. **72**(1): p. 32-42.
70. Stanford Health Care. *Western Blot Test*. [cited 08-06-2022]; Available from: https://stanfordhealthcare.org/medical-conditions/sexual-and-reproductive-health/hiv-aids/diagnosis/western-blot-test.html.
71. Sigma Aldrich. *Introduction to SDS-PAGE - Separation of Proteins Based on Size*. 2022 [cited 10-08-2022]; Available from: https://www.sigmaaldrich.com/GB/en/technical-documents/protocol/protein-biology/gel-electrophoresis/sds-page.
72. Nature Education. *Western blot*. [cited 08-06-2022]; Available from: https://www.nature.com/scitable/definition/western-blot-288/#:~:text=A%20western%20blot%20is%20a,particular%20tissue%20or%20cell%20type.
73. Medical & Biological Laboratories Co. LTD. *The principle and method of Western blotting (WB)*. 2017 [cited 11-08-2022]; Available from: https://ruo.mbl.co.jp/bio/e/support/method/westernblotting.html.
74. ThermoFisherScientific. *Overview of Mass Spectrometry for Protein Analysis*. [cited 08-06-2022]; Available from: https://www.thermofisher.com/uk/en/home/life-science/protein-biology/protein-biology-learning-center/protein-biology-resource-library/pierce-protein-methods/overview-mass-spectrometry.html.
75. Henriquez, K.M., et al., *Procalcitonin Levels in Acute Respiratory Infection.* Viral Immunology, 2016. **29**(2): p. 128-131.
76. Gao, L., et al., *Early diagnosis of bacterial infection in patients with septicopyemia by laboratory analysis of PCT, CRP and IL-6.* Experimental and therapeutic medicine, 2017. **13**(6): p. 3479-3483.
77. Gendrel, D., et al., *Comparison of procalcitonin with C-reactive protein, interleukin 6 and interferon-alpha for differentiation of bacterial vs. viral infections.* Pediatr Infect Dis J, 1999. **18**(10): p. 875-81.
78. Siemens Healthineers. *What is Procalcitonin (PCT)?* 2019 14/02/19 [cited 28-05-2019]; Available from: https://www.siemens-healthineers.com/en-uk/clinical-specialities/sepsis/siemens-inflamation-and-infection-assays/what-is-pct.
79. Schuetz, P., Y. Wirz, and B. Mueller, *Procalcitonin Testing to Guide Antibiotic Therapy in Acute Upper and Lower Respiratory Tract Infections.* JAMA, 2018. **319**(9): p. 925-926.
80. Lab Tests Online UK. *C-Reactive Protein*. 2018 [cited 23-07-2020]; Available from: https://labtestsonline.org.uk/tests/c-reactive-protein.
81. DTB, *Point-of-care CRP testing in the diagnosis of pneumonia in adults.* Drug and Therapeutics Bulletin, 2016. **54**(10): p. 117.
82. Nehring, S.M., A. Goyal, and B.C. Patel, *C Reactive Protein*, in *StatPearls*. 2021, StatPearls Publishing LLC.

83. National Health Service. *Tuberculosis (TB)*. 2019 [cited 05-05-2020]; Available from: https://www.nhs.uk/conditions/tuberculosis-tb/diagnosis/.
84. Eurobarometer 338, *Antimicrobial Resistance*. 2010.
85. Florkowski, C., et al., *Point-of-care testing (POCT) and evidence-based laboratory medicine (EBLM) – does it leverage any advantage in clinical decision making?* Critical Reviews in Clinical Laboratory Sciences, 2017. **54**(7-8): p. 471-494.
86. Srinivasan, B. and S. Tung, *Development and Applications of Portable Biosensors.* SLAS Technology, 2015. **20**(4): p. 365-389.
87. Sluss, P.M., *Point-of-Care Pregnancy Testing.* Point of Care, 2016. **15**(4): p. 164-171.
88. Office for National Statistics. *UK Health Accounts: 2016*. 2016 [cited 19-10-2018]; Available from: https://www.ons.gov.uk/peoplepopulationandcommunity/healthandsocialcare/healthcaresystem/bulletins/ukhealthaccounts/2016.
89. Centers for Medicare & Medicaid Services. *National Health Expenditures by type of service and source of funds, CY 1960-2018*. 2018 [cited 08-01-2019]; Available from: https://www.cms.gov/Research-Statistics-Data-and-Systems/Statistics-Trends-and-Reports/NationalHealthExpendData/NationalHealthAccountsHistorical.html.
90. OECD. *Health spending (indicator)*. 2018 [cited 19-11-2018]; Available from: https://data.oecd.org/healthres/health-spending.htm.
91. Centers for Disease Control and Prevention. *Point-of-Care & Rapid Testing*. 2022 [cited 27-05-2022]; Available from: https://www.cdc.gov/coronavirus/2019-ncov/lab/point-of-care-testing.html.
92. King, K., et al., *Point-of-Care Technologies for Precision Cardiovascular Care and Clinical Research: National Heart, Lung, and Blood Institute Working Group.* JACC. Basic to translational science, 2016. **1**(1-2): p. 73-86.
93. Abdulah, R., Antibiotic Abuse in Developing Countries. Pharmaceutical Regulatory Affairs, 2012(1): p. e106.
94. Aidian. *QuikRead go CRP*. 2020 [cited 05-05-2020]; Available from: https://www.aidian.eu/point-of-care/quikread-go/quikread-go-crp#generally.
95. Abbott. *NycoCard CRP*. [cited 12-08-2021]; Available from: https://www.globalpointofcare.abbott/en/product-details/nycocard-crp.html.
96. Biopanda Reagents. *PCT Rapid Tests*. 2013 [cited 10-06-2019]; Available from: https://www.biopanda.co.uk/php/products/rapid/pct.php.
97. Radiometer. *Rapid procalcitonin (PCT) test*. 2017 [cited 10-06-2019]; Available from: https://www.radiometer.co.uk/en-gb/products/immunoassay-testing/aqt90-flex-immunoassay-analyser/rapid-procalcitonin-pct-test.
98. National Health Service. *X-ray*. 2022 [cited 09-05-2022]; Available from: https://www.nhs.uk/conditions/x-ray/.
99. National Health Service. *CT scan*. 2021 [cited 09-05-2022]; Available from: https://www.nhs.uk/conditions/ct-scan/.
100. National Health Service. *MRI scan*. 2018 [cited 09-05-2022]; Available from: https://www.nhs.uk/conditions/mri-scan/.
101. National Health Service. *Ultrasound scan*. 2021 [cited 09-05-2022]; Available from: https://www.nhs.uk/conditions/ultrasound-scan/.
102. National Health Service. *Endoscopy*. 2022 [cited 09-05-2022]; Available from: https://www.nhs.uk/conditions/endoscopy/.
103. National Health Service. *Laparoscopy*. 2018 [cited 09-05-2022]; Available from: https://www.nhs.uk/conditions/laparoscopy/.
104. National Health Service. *Lumbar puncture*. 2021 [cited 09-05-2022]; Available from: https://www.nhs.uk/conditions/lumbar-puncture/.

105. National Health Service. *Blood tests*. 2018 [cited 09-05-2022]; Available from: https://www.nhs.uk/conditions/blood-tests/.
106. Centers for Disease Control and Prevention. *Interferon-Gamma Release Assays (IGRAs) - Blood Tests for TB Infection*. 2011 [cited 05-05-2020]; Available from: https://www.cdc.gov/tb/publications/factsheets/testing/igra.htm.
107. Cepheid. *Xpert MTB/RIF*. 2010 [cited 12-05-2022]; Available from: https://www.cepheid.com/en/tests/Critical-Infectious-Diseases/Xpert-MTB-RIF.
108. Georghiou, S.B., et al., *Equivalence of the GeneXpert System and GeneXpert Omni System for tuberculosis and rifampicin resistance detection.* PloS one, 2021. **16**(12): p. e0261442-e0261442.
109. García-Basteiro, A.L., et al., *Point of care diagnostics for tuberculosis.* Pulmonology, 2018. **24**(2): p. 73-85.
110. National Health Service. *Pneumonia*. 2019 [cited 09-05-2022]; Available from: https://www.nhs.uk/conditions/pneumonia/.
111. Bruning, A.H.L., et al., *Diagnostic performance and clinical feasibility of a point-of-care test for respiratory viral infections in primary health care.* Family Practice, 2017. **34**(5): p. 558-563.
112. mariPOC. *mariPOC tests*. 2020 [cited 12-05-2022]; Available from: https://www.arcdia.com/maripoc/tests/.
113. National Institute for Health and Care Excellence. *Rapid tests for group A streptococcal infections in people with a sore throat*. 2019 [cited 09-05-2022]; Available from: https://www.nice.org.uk/guidance/dg38/chapter/2-The-diagnostic-tests.
114. Yoshida, H., M. Kanamori, and H. Sakemi, *Sore Throat with Normal Oropharyngeal Examination.* The American journal of medicine, 2021. **134**(1): p. e49-e50.
115. Aidian. *QuikRead go Strep A*. 2020 [cited 12-05-2022]; Available from: https://www.aidian.eu/point-of-care/quikread-go/quikread-go-strep-a#generally.
116. Clearview, *Clearview Exact Strep A Cassette*. 2005.
117. BD Veritor. *BD Veritor Plus*. [cited 19-03-2022]; Available from: https://bdveritor.bd.com/en-us/main/rapid-antigen-testing/group-a-strep.
118. National Health Service. *Laryngitis*. 2020 [cited 09-05-2022]; Available from: https://www.nhs.uk/conditions/laryngitis/.
119. Mayo Clinic. *Laryngitis*. 2018 [cited 15-05-2020]; Available from: https://www.mayoclinic.org/diseases-conditions/laryngitis/diagnosis-treatment/drc-20374267.
120. Mayo Clinic. *Needle Biopsy*. 2020 [cited 12-05-2022]; Available from: https://www.mayoclinic.org/tests-procedures/needle-biopsy/about/pac-20394749.
121. Egilmezer, E., et al., *Systematic review of the impact of point-of-care testing for influenza on the outcomes of patients with acute respiratory tract infection.* Reviews in medical virology, 2018. **28**(5): p. e1995-e1995.
122. Mayo Clinic. *C-reactive protein test*. 2021 [cited 12-05-2022]; Available from: https://www.mayoclinic.org/tests-procedures/c-reactive-protein-test/about/pac-20385228.
123. National Institute for Health and Care Excellence. *QuikRead go for C-reactive protein testing in primary care*. 2016 [cited 05-05-2020]; Available from: https://www.nice.org.uk/advice/MIB78.
124. Susanna, E., et al., *Evaluation of a rapid bedside test for the quantitative determination of C-reactive protein.* Clinical Chemistry and Laboratory Medicine (CCLM), 2005. **43**(4): p. 438-440.
125. Dahler-Eriksen, B.S., et al., *Evaluation of a near-patient test for C-reactive protein used in daily routine in primary healthcare by use of difference plots.* Clinical Chemistry, 1997. **43**: p. 2064+.

2 Chapter 2 – Instrumentation and Techniques

2.1 Introduction

In this chapter we will discuss the theoretical principles behind the main instrumentation and techniques used throughout this project. Specifically, **Section 2.2** will explore the theory and background of optical waveguides, with an emphasis on leaky waveguides (LWs). Techniques used for glass slide preparation and film characterisation are also discussed.

2.2 Optical waveguides

Dielectric optical waveguides are structures capable of guiding light, and an ideal choice for monitoring optical biomarkers. Waveguides will respond to changes in refractive index (RI), which is a measure of the speed of light moving through a vacuum versus in a medium [1]. RI is an inherent property of optical materials which does not require the use of any label to visualise, therefore waveguides can be described as a label-free technique.

RI can be explained *via* the following simple equation (**Equation 2.1**):

Equation 2.1. Refractive index.

$$n = \frac{c}{v}$$

Where:

n = refractive index,

c = velocity of light in a vacuum, and

v = velocity of light in a medium.

2.2.1 Conventional optical waveguides

A conventional optical waveguide traps a beam of light within the waveguide and thus restricts the region in which the light can propagate [2]. This leads to total internal reflection (TIR), a specific case of Fresnel reflection, in the longitudinal direction, and is the principle of how basic optical waveguides function.

In general, an optical waveguide is built from a core, which is the waveguide itself, and has a higher RI than the surrounding cladding. The substrate is often a type of glass, crystal, or silicon [3]. This difference in RI means that when the light hits the cladding at, or above, the critical angle (θ_c), TIR occurs, and is visualised in **Figure 2.1**.

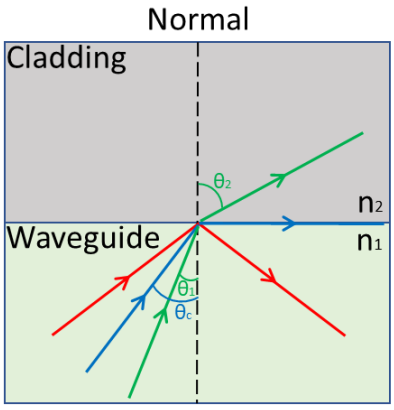

Figure 2.1. A visual representation of light hitting the interface between the waveguide (n_1) and cladding (n_2) at different angles. Above the critical angle (red) and at the critical angle (blue) lead to total internal reflection (TIR), while below the critical angle (green) leads to refraction.

For isotropic media, Snell's Law, **Equation 2.2**, states that the RI in a medium n_1 multiplied by sin of the angle of incidence is equal to the RI in a medium n_2 multiplied by sin of the angle of refraction. This describes the relationship between the refractive indices of each material and the effect this has on the critical angle.

Equation 2.2. Snell's Law.

$$n_1 \times \sin(\theta_1) = n_2 \times \sin(\theta_2)$$

As the entire ray of light undergoes TIR, it hits the cladding at one waveguide/cladding boundary and is reflected back into the waveguide, until it hits the waveguide/cladding boundary at the opposite side where it is once again totally reflected. Under TIR conditions the value of θ_2 is 90°, which leads to a zig-zag pattern of light with no loss of energy with each

successive reflection. It can therefore continue indefinitely, or until the waveguide ends (**Figure 2.2**). As the value of θ_2 is known, Snell's Law can then be used to calculate θ_c.

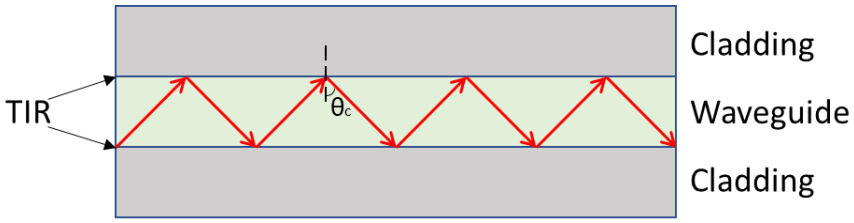

Figure 2.2. Basic principle of total internal reflection (TIR) in a waveguide.

At the critical angle, not only do you get TIR, but also a transverse evanescent wave is released. It is important to note that this evanescent wave does not result in loss of energy from the waveguide; the light is still totally reflected within the waveguide and does not leave. Rather, the evanescent wave is an electromagnetic wave [4], the result of a sinusoidal wave subjected to TIR. This wave extends through the waveguide and cladding, making it useful to help monitor changes within the waveguide or cladding regions. However, the evanescent wave decays exponentially with distance from the waveguide, so it cannot maintain itself at any significant distance away from the waveguide (**Figure 2.3**). This means that any detection based on evanescent waves must occur extremely close to the surface of the waveguide.

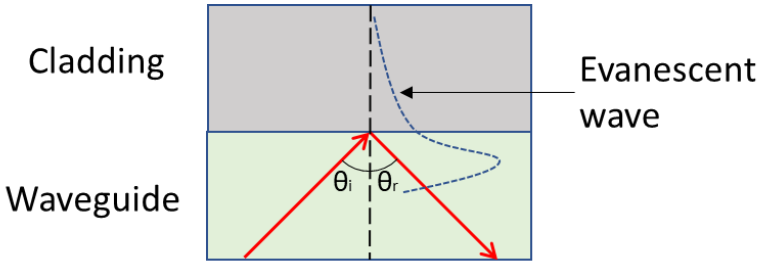

Figure 2.3. The exponentially decaying evanescent wave released at the critical angle.

2.2.2 Leaky optical waveguides

In this project, the focus will be on LWs. The setup of these devices is planar and comprised of three layers: the substrate is a glass slide, the waveguide is a thin hydrogel film, and the sample is an aqueous solution such as a buffer which contains the analyte of interest.

In LWs TIR occurs between the waveguide and the sample, while it is Fresnel reflection which occurs between the waveguide and the substrate, as $n_{substrate} > n_{waveguide} > n_{sample}$. This is therefore referred to as a leaky waveguide, as light can leak in and out of the waveguide layer *via* the substrate [5]. This is achieved by using a set-up similar to **Figure 2.4**.

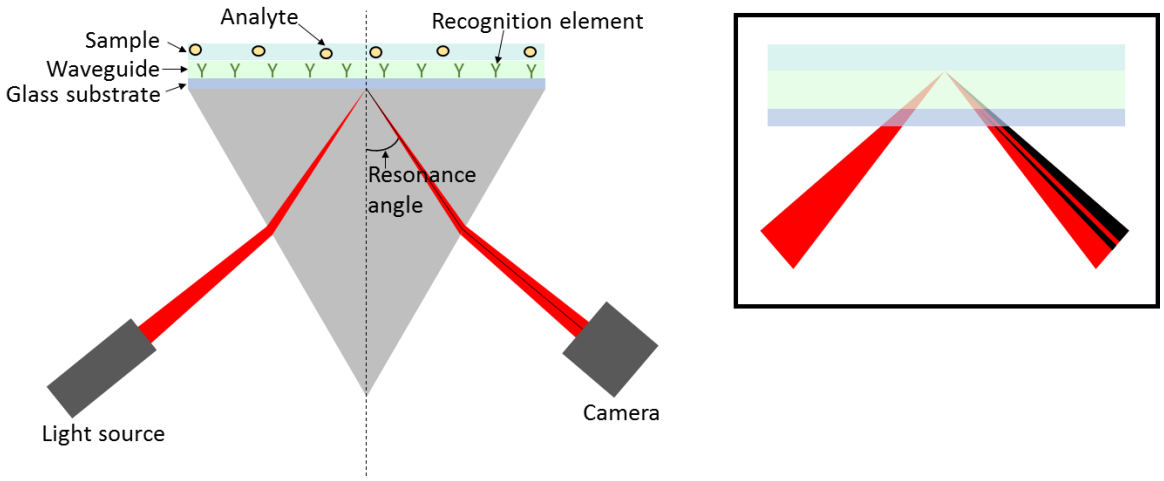

Figure 2.4. Simplified LW optical instrument set-up. Inset shows TIR at the waveguide/sample interface and Fresnel reflection at the substrate/waveguide interface.

The resonance angle, also known as the coupling angle, must be higher than the critical angle of the waveguide/sample and lower than the critical angle of the substrate/waveguide interfaces respectively [6]. When these conditions are satisfied, and the polymer film has a higher RI than the sample, TIR occurs at the waveguide/sample interface. Meanwhile, where the substrate has a higher RI than the polymer film Fresnel reflection is given at the substrate/waveguide interface, shown in **Figure 2.5**.

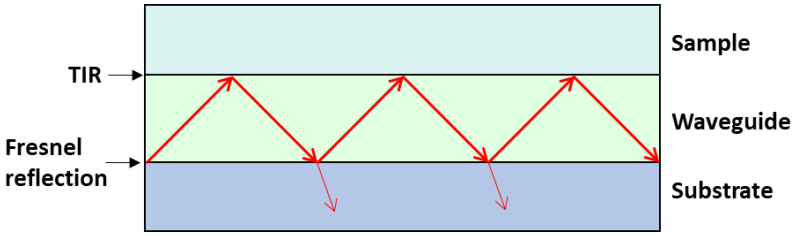

Figure 2.5. A waveguide where $n_{substrate}>n_{waveguide}>n_{sample}$, leading to both TIR and Fresnel reflection. Light is coupled into the waveguide using an equilateral prism.

An equilateral prism is employed to ease the coupling of light into the waveguide by increasing the angle at which light enters the substrate. RI matching oil is placed between the prism and substrate to remove the layer of air between the two surfaces.

Figure 2.6 depicts the path of the light and how this translates into an output image. As TIR occurs at the waveguide/sample interface a dark black line is produced in the output image as the light is unable to penetrate through this boundary and into the sample. A thinner dark line occurs at the substrate/waveguide interface where some light has been lost due to Fresnel reflection. Meanwhile, the light regions of the output image are regions in which the light is reflected.

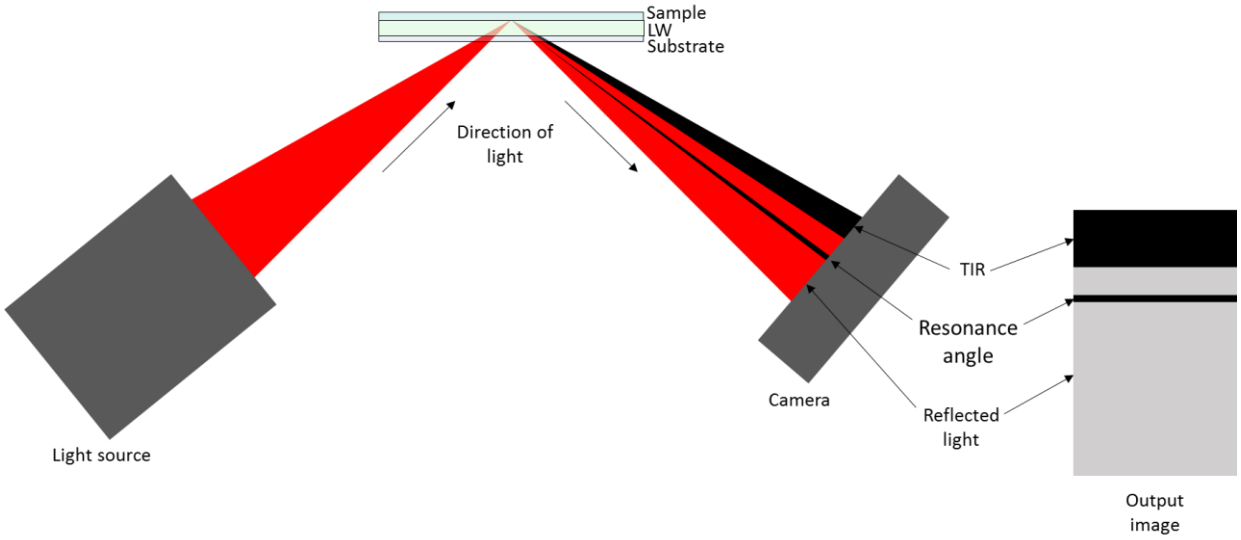

Figure 2.6. Stylised diagram of how the light translates to the output image. Prism not shown for clarity.

LWs have advantages over conventional, TIR-based waveguides for point-of-care (POC) applications, such as:

1. The leaky nature of the film allows light to be easily coupled into the waveguide layer, by using an equilateral prism with a light emitting diode (LED).
2. As conventional waveguides rely on TIR occurring on both sides of the waveguide, the waveguide layer is usually non-porous and therefore will not allow for antibodies to be attached within the layer. Instead, they will be attached to the outside of the waveguide leading to reduced sensitivity of the system as the loading capability will be low, and interaction will only occur with the decaying evanescent field. By attaching the antibodies within the waveguide bulk, a higher sensitivity can be achieved (**Figure 2.7**).
3. Following on from point 2, any imperfections in the surface of the waveguide will lead to drastic differences in results. This effect is minimised in LWs, as receptors can be spread throughout the bulk of the waveguide layer due to the

increased porosity, thus increasing sensitivity and reducing reliance on surface perfection.

4. As the RI of the waveguide only needs to be higher than the sample, not the substrate, there is a much broader range of choices for the waveguide material.
5. The ability to monitor changes within the film itself reduces reliance on the evanescent wave at the surface of the film.

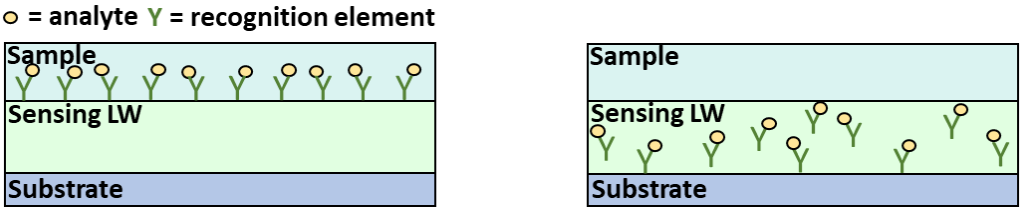

Figure 2.7. A non-porous waveguide with recognition elements attached to the top of the waveguide (left) and a porous LW with recognition elements suspended within the waveguide (right).

The resonance angle can be visualised in the reflectivity curve of the device *via* the losses imposed by the nature of the devices. At the resonance angle, propagation within the waveguide is long and there is a large loss of light which leads to a lower reflectivity at that angle [6]. This dip in reflectivity can be monitored, hence allowing for the tracking of the resonance angle.

2.2.3 Waveguide categories

There are two main categories of optical waveguides: planar and non-planar. Planar waveguides are ordinarily built of a core, surrounded by two layers of cladding parallel to the core in only one transverse direction. These layers of cladding are also sometimes called the cover/sample and the substrate and can either be identical or differ in thickness and material.

Planar waveguides are also known as slab or strip waveguides, owing to their simple geometry. This simple configuration allows for easy manufacture. In this project, planar optical waveguides will be the focus.

As the name suggests, non-planar waveguides are made of a core surrounded by cladding in all transverse directions. This leads to the formation of tubes or cables, such as optical fibre cables for data transfer, in which the light is trapped and guided along a high RI core surrounded by cladding with a lower RI. While these have important uses in data transfer and communications, they are not the focus of this project and hence will not be discussed further.

Waveguide modes are characteristic of a particular waveguide structure and are not affected by the source of light. In short, the waveguide mode is the electromagnetic wave that moves through the optical waveguide. In waveguides, these can be split into transverse electric (TE) and transverse magnetic (TM) modes shown in **Figure 2.8**.

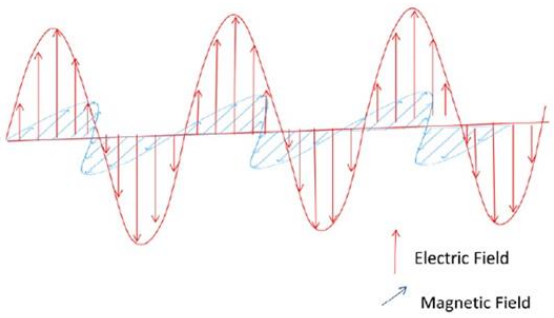

Figure 2.8. Relative positioning of TE (H) and TM (E) waves [7].

TE mode relates to transverse electric waves (H waves). In this situation, the electric field and direction of propagation are transverse, and the magnetic field is parallel to the direction of propagation [8]. TM mode relates to transverse magnetic waves (E waves), in which the magnetic field and direction of propagation are transverse, and the electric field is

parallel to the direction of propagation [8]. Meanwhile, the electric and magnetic fields are always perpendicular to each other and are proven by Maxwell's Laws.

Maxwell's equations are a series of 4 equations made up of Gauss' Law for Electric Fields, Gauss' Law for Magnetic Fields, Faraday's Law, and Ampere's Law [9, 10]. These equations are used to explain the laws of electromagnetics, and thus can be used to prove the existence of the evanescent wave, alongside explaining the physics behind electric and magnetic fields. In very basic terms, they prove that the electric field and magnetic field must always be at 90° to each other.

Waveguides can also be defined in relation to wave mode: single-mode or multimode. The two types are shown in **Figure 2.9**. Single-mode waveguides have a single propagation mode, meaning they can only support one path. For this reason, they have a small core, typically only a few micrometres wide [11]. Alongside this, they have only a small RI difference between the core and the cladding. Most importantly, due to the small core, the signal transferred by a single-mode waveguide can travel further due to decreased attenuation [12].

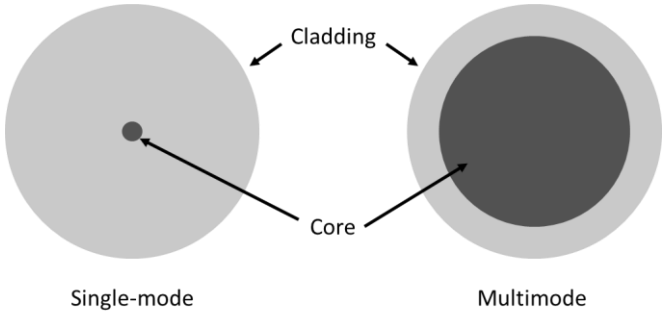

Figure 2.9. Single-mode (left) and multimode (right) waveguide fibres [13].

Multimode waveguides support multiple different propagation modes, thus can support multiple different paths for one particular optical frequency. Therefore they tend to have a much larger core than single-mode waveguides allowing for the increased propagation, but this ultimately leads to higher attenuation [11]. This makes them less suitable than single-mode waveguides for long-distance applications, but they do have much faster data transfer across short distances [12]. While this is a useful property for data transfer, multimode waveguides are less appropriate for uses in optical detection as the increased number of modes will interfere with data interpretation. Hence, single mode waveguides are more desirable for this project.

Multimode waveguides can be further split into two more types: step-index and graded-index. In step-index multimode waveguides the core is made completely of one material compared to the cladding which is a different material. It is a relatively slow mode as the rays of light can travel along different paths and reach the end of the waveguide at different times [12].

Graded-index multimode waveguides have a core made of a mixture of materials which cause a change in RI to occur gradually as you move away from the centre. This helps it to compensate for the different path lengths of the range of propagation modes and allows all the light to reach the end of the waveguide at approximately the same time [12]. Thus, it is faster than the step-index.

Numerical aperture (NA) refers to the maximum light acceptance angle θ_{max} [14], and is related to the number of modes. NA can be derived using **Equation 2.3**.

Equation 2.3. Numerical aperture.

$$NA = \sqrt{n_w^2 - n_c^2}$$

Where:

n_w = waveguide RI, and

n_c = cover RI

A low NA value leads to fewer supported propagation modes, and increased chance of bend losses [15].

Due to the leaky nature of LWs, propagation distance is typically short as light is lost at each point of contact between the waveguide and substrate. While this would be a problem for data transfer applications, it is not an issue in small-scale devices such as those used in this work. The LW assists in easier coupling of light into the structure, and the loss of light leads to easier visualisation of the mode. Hence, it is most advantageous for this application to develop single-moded planar waveguides.

2.2.4 The mode equation

The following set of equations (**Equation 2.4**) can be used to derive the mode equation (**Equation 2.4.5**), which is used to find the resonance angle conditions at which light will be confined within the waveguide [16]. This is of vital importance for understanding the theory behind how waveguides work. In these equations n_w and n_c refer to the waveguide and cover RI respectively, h corresponds to the thickness of the waveguide, and λ is the wavelength of light used.

Equation 2.4. The mode equation.

$$\emptyset_{tot} = 2\emptyset_z + \emptyset_{10} + \emptyset_{12} = 2m\pi \quad \textbf{(2.4.1)}$$

Where:

$\emptyset_{tot}$ = phase shift of one complete circuit reflection between the waveguide and substrate.

$\emptyset_z$= phase shift for the propagation of the wave from one boundary to the other, where β is the real part of $n_{eff} = \beta + iK$, the complex effective mode index.

$$\emptyset_z = \frac{2\pi h}{\lambda}\left(\sqrt{n_w^2 - \beta^2}\right) \quad \textbf{(2.4.2)}$$

$\emptyset_{10}$ = phase shift on reflection at the waveguide/substrate boundary, where θ_i is the angle of incidence and θ_p is the angle of propagation.

$\emptyset_{10} = \pi$ For TE and TM modes where $\theta_i > \theta_p$

$\emptyset_{10} = 0$ for TM modes where $\theta_i < \theta_p$

$\emptyset_{12}$ = phase shift on reflection at the waveguide/cover boundary, in which $p = 0$ for TE modes and 1 for TM modes respectively.

$$\emptyset_{12} = -2tan^{-1}\left[\frac{n_w^{2p}}{n_c^{2p}}\sqrt{\frac{\beta^2 - n_c^2}{n_w^2 - \beta^2}}\right] \quad \textbf{(2.4.3)}$$

Combination of the above equations leads to:

$$2m\pi = \frac{4\pi h}{\lambda}\left(\sqrt{n_w^2 - \beta^2}\right) + \pi - 2tan^{-1}\left[\frac{n_w^{2p}}{n_c^{2p}}\sqrt{\frac{\beta^2 - n_c^2}{n_w^2 - \beta^2}}\right] \quad \textbf{(2.4.4)}$$

Or:

$$(2m-1)\pi = \frac{4\pi h}{\lambda}\left(\sqrt{n_w^2-\beta^2}\right) - 2tan^{-1}\left[\frac{n_w^{2p}}{n_c^{2p}}\sqrt{\frac{\beta^2-n_c^2}{n_w^2-\beta^2}}\right] \qquad \textbf{(2.4.5)}$$

Equation 2.4.5 is the final mode equation, and from this we can therefore derive that $n_w > \beta > n_c$. The value of β can be determined *via* numerical or graphical techniques.

2.3 Ultraviolet-Visible Spectroscopy (UV-Vis)

Ultraviolet-Visible Spectroscopy (UV-Vis) is a technique used extensively to study the absorbance and/or transmission of a sample in comparison to a reference sample known as the blank. To achieve this, a range of different wavelengths of light are directed through the blank in sequence, which is prepared from the same solvent as the sample. This will produce a flat baseline. The sample is then placed in front of the light and the same technique is applied (**Figure 2.10**).

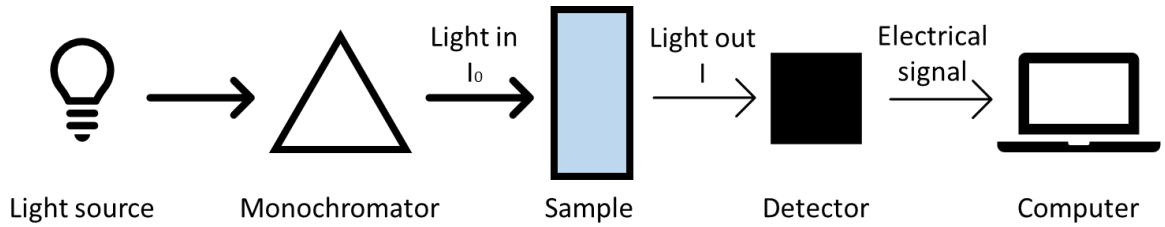

Figure 2.10. Schematic of the process of UV-Vis spectroscopy.

Depending on the sample composition and concentration, certain wavelengths will be absorbed and in different quantities. The light that has passed through the sample will hit the detector and provide an output image in the form of a graph which is usually presented as absorbance/transmission versus wavelength. The Beer-Lambert Law can then be applied [17].

Equation 2.5. The Beer-Lambert Law.

$$A = \varepsilon l c$$

Where A refers to the absorbance, ε is the molar absorption coefficient, l is the path length of the light, and c is the concentration of the sample. This shows that the absorbance of a sample and the concentration of the sample are directly correlated *via* a linear

relationship, and therefore the concentration of unknown samples can be determined using UV-Vis.

When the absorbance is plotted against the sample concentration, a graph such as the example in **Figure 2.11** will be produced.

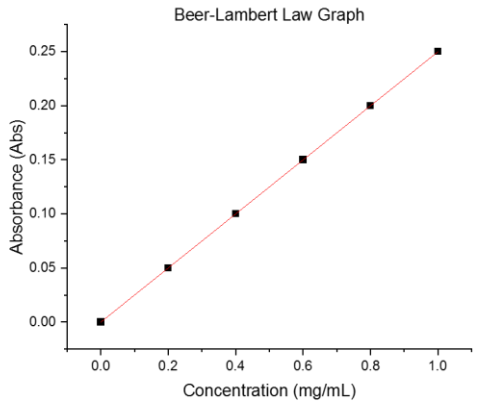

Figure 2.11. An example graph showing the Beer-Lambert Law linear relationship between concentration and absorbance.

This shows the linear relationship between absorbance and concentration. Such concentration curves are extremely useful for interrogating samples of known components but unknown concentrations, as direct comparison of the experimentally observed absorbance to the concentration curve allows for quick determination of the sample concentration.

2.4 Spin coating

The technique of spin coating is widely used to produce thin films with a tailorable thickness ranging from nanometres to microns depending on the settings used. The process involves placing a substrate onto a spin coating chuck, coating with a small volume of solution, and rotating to spread the solution evenly across the surface of the substrate, while any excess solution is thrown from the substrate (**Figure 2.12**). It is a simple and well-known technique, allowing for quick production of thin films with reproducible characteristics.

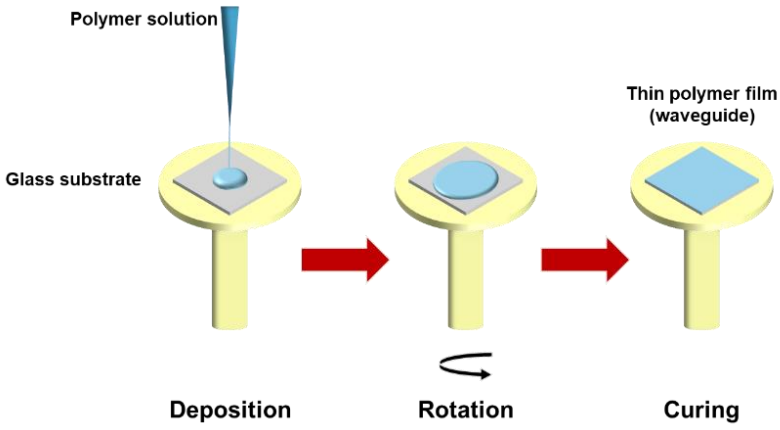

Figure 2.12. The spin coating technique.

There are two main methods of depositing the solution onto the substrate known as static dispensing and dynamic dispensing, both of which have their advantages and disadvantages. It is also possible to automate the process using specialist dispensing instrumentation, however this is not a necessary requirement as equally good results can be achieved by manual dispensing *via* a pipette when the right technique is employed [18]. For large-scale industrial production automation would be desirable, but for small-scale laboratory work it is not needed. Typically, the spin speed, acceleration, and time can all be programmed, allowing for tailorable thickness and substrate coverage. Film quality will also be affected by gelation time and conditions, the mechanism and strength of how the solution

bonds to the substrate, and the viscosity of the solution. If the solution is too viscous it will struggle to spread across the substrate evenly, while a solution that is not viscous is more likely to be flung from the substrate surface entirely. It is therefore important to consider these factors when choosing a solution and the relevant spin conditions.

2.4.1 Static dispensing

The easiest form of spin coating involves placing the solution onto the substrate while it is not moving. The solution can then be carefully spread across the slide using the end of a pipette tip, taking care not to touch the substrate itself. Once the substrate is coated, the spin coater is turned on. This technique can cause issues with film uniformity, as the solution is not always able to be drawn across the substrate adequately before spin coating. This is particularly obvious with solutions which have poor wettability and do not spread easily, and the speed of the spin coater is crucial in getting such solutions to spread optimally without simply flying off the surface entirely. Based on the chosen parameters, it will take a specified amount of time for the spin coater to reach the maximum speed, which in some cases is advantageous as it allows the solution to slowly spread across the substrate before thinning out at higher speeds but may cause issues with film uniformity, particularly if the solution begins to polymerise before maximum speed is achieved.

Static dispensing was employed throughout the project as it provided the most reproducible results for the solutions involved.

2.4.2 Dynamic dispensing

Dynamic dispensing can help avoid some of the issues raised by static dispensing. In this technique, the substrate is placed on the spin coater chuck and allowed to reach the desired speed. At this point, the solution can be quickly pipetted into the centre of the substrate. This tends to give more uniform films for solutions needing a rotation speed of over 1000 rpm but must be performed as close to the centre of the substrate as possible and within one singular motion, hence is prone to human error. This technique was applied during this project to try and improve the uniformity of films, but results were highly variable. It was decided to remain with static dispensing.

2.5 Slide casting

Slide casting is another common technique to form gels with tailorable thickness. This method involves functionalisation of two separate surfaces: a top slide and a bottom slide. The bottom slide is what the gel will bind to, while the top slide should be functionalised with an appropriate agent to discourage the gel from binding to it, providing a smooth surface. Spacer beads of the desired thickness can then be evenly spaced along the edges of the top slide and allowed to dry. The hydrogel solution is placed on the bottom slide, covered by the top slide, and either clamped at each side, or held down using a weight until the gel has fully formed. The slides can then be separated, leaving the gel film attached to the bottom slide. By changing the thickness of the spacer beads and the mass of the weight, these gels can be formed at different thicknesses for the desired application.

Disadvantages of this technique are strongly related to human error. Unless the process is automated, there multiple areas in which this technique can introduce disparities. The spacer beads must be applied evenly around the surface of each slide at the same thickness, and the weights or clamps applied to hold the slides together can cause the slides to shift, potentially damaging the surface of the hydrogel. Upon separation of the top and bottom slides there is also the risk of damage to the hydrogel. On the other hand, the intensive nature of this technique can also allow for more control over the process, as each step can be tailored to suit the requirements of the product and the skills of the practitioner.

This technique is also slow and relatively intensive in comparison to spin coating as each slide must be functionalised first, the spacer beads must be carefully placed by pipette,

and each hydrogel must be carefully prised from the top slide. Overall, the technique can take hours, compared to the much quicker minutes seen with spin coating.

For these reasons spin coating was the method of choice for the majority of hydrogels studied in this project. In certain cases slide casting was used, and this decision will be explained where necessary.

2.6 Glass cleaning

2.6.1 Sonication

Sonication, typically carried out in an ultrasonic water bath, is a well-known method for cleaning surfaces. An ultrasonic wave is sent through the water, which helps to clean a surface *via* cavitation [19].

In this project, glass slides are suspended in a specially designed slide holder within a 1000 mL beaker. The slides are then sufficiently covered in a solution of 5% Decon 90 in deionised (DI) water and sonicated for 30 minutes to allow for cavitation of any contaminants on the surface of the glass. The slides are then rinsed, and the solution is replaced with DI water and sonicated for a further 30 minutes, again removing any remaining contaminants. Following this, the slides are sonicated in ethanol for a final 30 minutes, removing any contaminants soluble in this, before removal from the solution. The slides can then be allowed to air dry and are stored in clean petri dishes.

This is an affordable and safe alternative to other techniques such as vapor rinsing and piranha solution, and the chosen solvents play an important role in the resulting cleanliness. By its nature, sonication is not as thorough a technique as others, and can therefore be combined with ozone or plasma cleaning to achieve a higher level of cleanliness.

Due to the ease of this technique, every glass slide used throughout the project was first cleaned *via* this method. In some cases, ozone cleaning and/or plasma cleaning were also used and will be explicitly stated where relevant.

2.6.2 Ozone cleaning

A UV light source is used to generate highly reactive ozone molecules, which react with contaminants on the surface of the glass to form volatile compounds which evaporate. Ossila describes their ozone cleaner as able to "*produce near-atomically clean surfaces without causing damage to the sample*" [20]. By pre-treatment of the slides first *via* sonication, ozone cleaning has a higher chance of producing exceptionally clean surfaces.

Another useful application of ozone cleaning is to increase the hydrophilicity of a substrate by producing hydroxide groups on the surface of the substrate. This can be beneficial for sample preparation, particularly where the sample has poor wettability. This technique was employed to improve gel adhesion.

2.6.3 Plasma cleaning

Similar to ozone cleaning, plasma cleaning is typically used to remove organic contaminants from the surface of a substrate. Plasma cleaning is advantageous as the generated plasma temperature is near-ambient, reducing temperature-induced damage. This makes it suitable for multiple surfaces, including plastics with a low melting point [21].

Nanoscale organic contaminants, microbial and biomolecules can be removed *via* this technique, and this was used when issues with film-glass separation occurred.

2.7 Summary

This chapter has discussed the theoretical principles behind the LW technique and explored why this has been selected as the method of choice for developing an optical biosensor. While more developed techniques such as surface plasmon resonance (SPR) seem the ideal choice for further research, the benefits obtained from using LWs such as deeper penetration depth and the opportunity for combination with electro-focusing techniques make LWs more appealing for our applications.

Also covered are some of the standard techniques used throughout the project including different fabrication and cleaning techniques.

2.8 References

1. Britannica. *Refractive index*. 2019 [cited 13-05-2022]; Available from: https://www.britannica.com/science/refractive-index.
2. Zangeneh-Nejad, F. and R. Fleury, *Acoustic Analogues of High-Index Optical Waveguide Devices.* Scientific Reports, 2018. **8**(1): p. 10401.
3. RP Photonics Encyclopedia. *Waveguides*. 2021 [cited 08-06-2022]; Available from: https://www.rp-photonics.com/waveguides.html.
4. Ligler, F.S. and C.A. Rowe Taitt, *The Evanescent Wave*, in *Optical Biosensors - Present & Future*. 2002, Elsevier. p. 57-94.
5. Gupta, R., et al., *Method for Determining Average Iron Content of Ferritin by Measuring its Optical Dispersion.* Analytical Chemistry, 2019.
6. Gupta, R. and N.J. Goddard, *Leaky waveguides (LWs) for chemical and biological sensing–A review and future perspective.* Sensors and Actuators B: Chemical, 2020. **322**: p. 128628.
7. CYPRESS. *EZ-BLE™ Module Placement – KBA97095*. 2015 [cited 08-01-2019]; Available from: http://japan.cypress.com/knowledge-base-article/ez-ble-module-placement-kba97095.
8. Herres, D. *Basics of TEM, TE, and TM propagation*. 2015 [cited 30-10-2018]; Available from: https://www.testandmeasurementtips.com/basics-of-tem-te-and-tm-propagation/.
9. Bevelacqua, P. *Maxwell's Equations*. 2012 [cited 29-10-2018]; Available from: http://www.maxwells-equations.com/.
10. Born, M. and E. Wolf, *Principles of Optics: Electromagnetic Theory of Propagation, Interference and Diffraction of Light*. 7 ed. 1999, Cambridge: Cambridge University Press.
11. RP Photonics Encyclopedia. *Multimode Fibers*. 2016 [cited 08-01-2019]; Available from: https://www.rp-photonics.com/multimode_fibers.html.
12. Multicom. *Single Mode vs. Multi-Mode Fiber Optic Cable*. 2014 [cited 08-01-2019]; Available from: https://www.multicominc.com/training/technical-resources/single-mode-vs-multi-mode-fiber-optic-cable/.
13. RP Photonics Encyclopedia. *Multimode Fibers*. [cited 2019 08,01]; Available from: https://www.rp-photonics.com/multimode_fibers.html.
14. Okamoto, K., *Wave Theory of Optical Waveguides*, in *Fundamentals of Optical Waveguides*. 2010, Elsevier. p. 2.
15. Paschotta, R. *Numerical Aperture*. 2018 [cited 28-10-2018]; Available from: https://www.rp-photonics.com/numerical_aperture.html.
16. Gupta, R. and N.J. Goddard, *A proof-of-principle study for performing enzyme bioassays using substrates immobilized in a leaky optical waveguide.* Sensors and Actuators B: Chemical, 2017. **244**: p. 549-558.
17. Edinburgh Instruments. *The Beer-Lambert Law*. 2019 [cited 01-06-2022]; Available from: https://www.edinst.com/blog/the-beer-lambert-law/.
18. Ossila. *Spin Coating: Complete Guide to Theory and Techniques*. 2020 [cited 03-08-2020]; Available from: https://www.ossila.com/pages/spin-coating.
19. Fuchs, F.J., *19 - Ultrasonic cleaning and washing of surfaces*, in *Power Ultrasonics*, J.A. Gallego-Juárez and K.F. Graff, Editors. 2015, Woodhead Publishing: Oxford. p. 577-609.
20. Ossila. *UV Ozone Cleaner*. 2021 [cited 19-07-2021]; Available from: https://www.ossila.com/products/uv-ozone-cleaner?variant=1200242961.
21. Plasma, H., *Harrick Plasma Product Information*. 2021: Online Catalog.

3 Chapter 3 – Single Layer Waveguides

3.1 Introduction

Porous polymers offer exciting opportunities to develop new biocompatible materials for a variety of uses, particularly in drug delivery and diagnostics. These polymers are broadly classed into one of three types: microporous, mesoporous, and macroporous. Microporous polymers have pores <2 nm large, while mesoporous pores are 2-50 nm, and macroporous pores are >50 nm [1]. Porous polymers of all sizes have different uses based on the pore size and inherent qualities; all porous polymers have high surface area due to the pores and, depending on how they are fabricated, other qualities can be combined with this to produce stable and useful materials. For example, while some porous polymers need to be soluble, others need to be permanently microporous. This can be achieved by additional crosslinking within the framework of the polymer, which has the added effect of increased thermal stability [2]. Mesoporous polymers are the most useful for waveguiding functions as the pores will be large enough to allow the analyte to diffuse into the waveguide, but small enough to prevent larger components in the sample matrix such as whole cells from entering the hydrogel and causing interference with the signal.

Different techniques can be employed to achieve the desired pore size. The simplest method involves tailoring the chain length of the polymers and/or crosslinkers, producing a network of pores of designated size. When this is not possible, porogens can be used to allow the formation of the pores around the porogen. Such porogens include SiO_2 [3], Na_2SO_4, and CO_2 [4], but issues can arise with the subsequent removal of the porogen after the hydrogel has formed and with pore-to-pore interconnectivity [5].

Polymers have already been used in waveguides, particularly for applications in data transfer [6, 7]. However, the wide range of polymers available and their specific properties alongside their desired end uses means that polymer waveguide research is an important ongoing process.

The chemical structure of the polymers used to form hydrogels is the first thing to consider, as the structure will affect all future properties. The polymer must contain the correct functional groups to allow for immobilisation of the hydrogel onto a substrate, usually glass or silica, while still retaining enough suitable free functional groups to allow for crosslinking and protein immobilisation. Too few functional groups will reduce the sensitivity of the gel, whereas too many could interfere with the gel structure and increase the extent of non-specific binding. The hydrogel must also be rigid enough to hold its shape but fluid enough to allow for swelling.

There is also the question of whether natural polymers or synthetic polymers are best for the intended use. Natural polymers such as cellulose and proteins can be harvested from natural sources i.e., animals or plants. Synthetic polymers can be synthesised in a lab and are in many commonly used products, such as nylon and poly(vinyl chloride). Both types have their own advantages and disadvantages, and both types are explored during this project.

Natural polymers can be found in nature and are typically easy to biologically degrade and have the added advantage of biocompatibility, making them useful for medicinal products and devices [8]. However, they may need purification before use due to impurities in the structure and variations in conformation. Any inconsistencies in chain length or structure will lead to irregularities in the gel, making it more difficult to achieve the necessary level of quality

control for industrial and medical applications. The ease of biodegradation can also pose problems when choosing storage techniques and reactants, and when considering longevity.

Synthetic polymers can be produced artificially on demand and the conformations and chain lengths are typically easier to control, and such polymers have already been used to form biomedical devices [9]. As these polymers are produced on demand, the cost of specific structures can be high in comparison to some abundant natural polymers which are produced as by-products in other industrial processes and therefore are easily procured. Despite the difference in cost, synthetic polymers typically have fewer impurities than natural polymers while maintaining a higher stability, which reduces the cost of extraction and purification steps. Synthetic polymers are often more difficult to degrade by biological processes, making them useful for long-term biomedical implants. The downside to this is that synthetic polymers can have a lasting negative impact on the planet, which can be seen in plastic wastage [8]. Nevertheless, synthetic polymers have the major advantage of requiring less purification and tailorable functional groups for biomolecule immobilisation. It is therefore important to consider the desired properties of the gel, the length and cost of the procurement process, and the overall suitability for the end use when selecting a polymer for use as a hydrogel.

Synthetic hydrogels based on poly(ethylene glycol) (PEG) have become highly sought after in bioengineering and drug delivery applications [10-12]. The PEG chain is naturally inert, hydrophilic, non-ionic, and resistant to adsorption, making them excellent for biological applications, and modification of the end groups of PEG chains can allow for specific reactivity as per the desired application [11].

Depending on the structure of the polymers, different techniques and chemicals can be employed to crosslink the polymer chains to form a gel. Glutaraldehyde, or pentane-1,5-dial, is a commonly used bifunctional crosslinking agent but is very difficult to control. Glutaraldehyde will readily crosslink with amine groups at acidic pH and then with itself [13]. This can lead to very dense, non-porous hydrogels which are unsuitable for use as waveguides. Therefore, the concentration of glutaraldehyde must be carefully adjusted to suit the polymerisation, and only allowed contact with the polymer solution for a particular length of time before being thoroughly washed out.

Genipin is another crosslinking agent, a natural compound extracted from the plant *Gardenia jasminoides* Ellis. As a naturally occurring agent, genipin has been reported to exhibit lower toxicity and is easier to control than glutaraldehyde [14, 15]. An interesting property of genipin is the distinctive blue colour it forms upon reacting which can be used to monitor the endpoint of the reaction.

Other crosslinking agents exist which are easier to control based on chain length, such as poly(ethylene glycol) diacrylate (PEGDA) and poly(ethylene glycol) diglycidyl ether (PEGDGE), which can be purchased with different PEG chain lengths and stabilised using inhibitors until use. However, there are still issues around self-polymerisation upon removal of the inhibitors. The choice of crosslinker must be determined based on the reactivity of the crosslinker and polymer, the stability of the of the crosslinker prior to reacting and the stability of the product, the porosity, the safety, and the reaction time. It is therefore important to consider the polymer which is being crosslinked and choose the appropriate crosslinker for the application.

In some situations a crosslinking agent is not required. For example, by using a mixture of monomers with complementary functional groups chemical crosslinking can occur between the monomers themselves without the need for an outside crosslinking agent. This has the advantage of higher control over the extent of the crosslinking *via* control of the monomer ratios, along with the exclusion of potentially toxic and expensive crosslinking agents, and simplification of the process.

The first stage to the project was the development of single layer leaky waveguides (LWs). For this, several polymers, both natural and synthetic, were selected and optimised to produce single- or double-moded output images. Within this, different crosslinking methods were investigated such as glutaraldehyde, genipin, bisacrylamide (BAAm), and PEGDA. Also investigated was the use of synthetic 4-arm and 2-arm PEGs with various functional groups which were able to react together and form crosslinks in the structure without the need for an additional crosslinking agent. Additionally, each hydrogel was chosen with the aim of producing LWs which can be easily prepared by solution processing and do not require the deposition of metal films such as those seen in surface plasmon resonance (SPR) [16-18] and metal clad LWs (MCLWs) [19-22].

3.1.1 Characterisation and porosity testing

The characterisation of different LW hydrogels is crucial to allow for comparison of different hydrogels and for the assessment of the properties and reproducibility of each gel. Glycerol solutions prepared in buffer (100 mM 4-(2-hydroxyethyl)piperazine-1-ethanesulfonic acid (HEPES) or phosphate buffered saline (PBS), pH 7.4) at concentrations of 0.125, 0.25, 0.5,

1, 2% (v:v) were used to assess the sensitivity of the films. As glycerol is a small and unreactive molecule it is able to diffuse in and out of the hydrogel without restrictions and without causing permanent changes to the LW itself. As the glycerol solution enters the film it changes the refractive index (RI) of the LW and leads to a shift in resonance angle ($\Delta\theta_R$). The shift in response to each concentration is recorded and used to prepare a calibration curve which provides the refractive index sensitivity (RIS) of the gel. RIS can be defined by the following equation (**Equation 3.1**):

Equation 3.1. Refractive index sensitivity.

$$RIS = \frac{\Delta\theta_R}{RI}$$

As discussed in **Chapter 2** (**2.2.2**), a porous LW is optimal for this form of optical biosensing. However, assessing the porosity of hydrogels is a challenge in itself as most techniques require the sample to be dry, which can significantly change the pore structure and give unrealistic responses. Dehydration of hydrogels will lead to a change in pore shape due to the loss in volume, which in turn may lead to mechanical failure and cause the pores to collapse either permanently or until rehydration [23].

Classic scanning electron microscopy (SEM) and transmission electron microscopy (TEM) are two of the best-known techniques for characterising materials. SEM is ideal for interrogating the surface and composition of a sample, while TEM offers information on the internal structure of samples [24]. Both of these methods are often used in hydrogel characterisation, but such characterisation is carried out on dehydrated samples [23, 25, 26]. Swollen hydrogels can be assessed by drying the gels *via* cryogenic techniques, but may suffer from formation of ice crystals which can further damage the hydrogel structure [27].

Laser scanning confocal microscopy (LSCM) is suited to assessing hydrated hydrogels without the need for drying and/or freezing of a sample. Janoušková *et al.* used SEM and LSCM to evaluate the morphology of N-(2-hydroxypropyl)methacrylamide (HPMA)-based hydrogels and compared the response from each technique [23]. It was clearly visible through comparison of the results that the freeze-drying technique employed for the SEM tests caused major changes in the morphology of the hydrogels, while LSCM avoided this but did require the inclusion of a fluorescent probe in the structure of the hydrogel.

In this work we have employed a much simpler technique to assess the porosity of the hydrogels. Different molecular weights (MWs) of 1% (w:v) PEG prepared in buffer solutions (100 mM HEPES or PBS, pH 7.4) are used. By observing the shift in resonance angle produced upon the exposure of the LW to these solutions we are able to assess the relative porosity of the LWs without the need for dehydrating the films or for additional instrumentation, as this could be carried out on the same instrumentation used throughout the project.

3.1.2 Success criteria

Alongside the characterisation and porosity tests carried out, each film has been assigned a level of uniformity based on qualitative visual assessment:

- High uniformity: ≥90% of the mode is uniform and able to be tracked.
- Medium uniformity: 50-89%
- Low uniformity: ≤49%

While this is not a quantitative measure, it helps to assess and categorise the quality of the films. A film with low uniformity is unlikely to be suitable for use as a LW. These same levels have been assigned to reproducibility.

- High reproducibility: ≥90% of films are successfully formed and maintain a high level of both visual similarity and measured sensitivity.
- Medium uniformity: 50-89%
- Low uniformity: ≤49%

Any film which falls in the low category for uniformity and reproducibility is not considered successful. Medium uniformity and reproducibility are more likely to indicate that further refinement of the films is needed, while high uniformity and reproducibility implies the LWs are nearly, if not fully, optimised. These values give a quick way in which to assess and compare different LWs. However, these values should not be taken as definite and the reasons behind medium or low levels have been explored where possible.

3.2 Polymer leaky waveguides

3.2.1 Poly(ethylene glycol) methyl ether acrylate and Poly(ethylene glycol) diacrylate, PEGMEA/PEGDA

Hydrogels can be formed in different ways; some require initiators while others require crosslinkers. Photoinitiators are able to trigger the polymerisation reaction when exposed to light of a certain wavelength. The aim of using a photoinitiator is to increase the control of the polymerisation reaction. Some spin coaters are equipped with UV treatment capability which means polymerisation of the solution can occur upon the slide directly after spin coating and without moving the slide. The photoinitiator chosen for this reaction was 2,2'-Azobis[2-(2-imidazolin-2-yl)propane] dihydrochloride (AIP), an azo initiator with high water solubility, making it suitable for photopolymerisation of water-soluble monomers such as PEGs.

Poly(ethylene glycol) methyl ether acrylate (PEGMEA) with an average molecular number (Mn) of 480 and poly(ethylene glycol) diacrylate (PEGDA) with an average Mn of 575, 700, or 10,000 were selected as co-polymers and used to prepare a range of gels at different percentages and ratios, using deionised (DI) water as the solvent (**Figure 3.1**). Mn is calculated as the mole fraction of molecules in the sample to produce the statistical average molecular weight, hence gives a good indication of the average chain length in the sample [28].

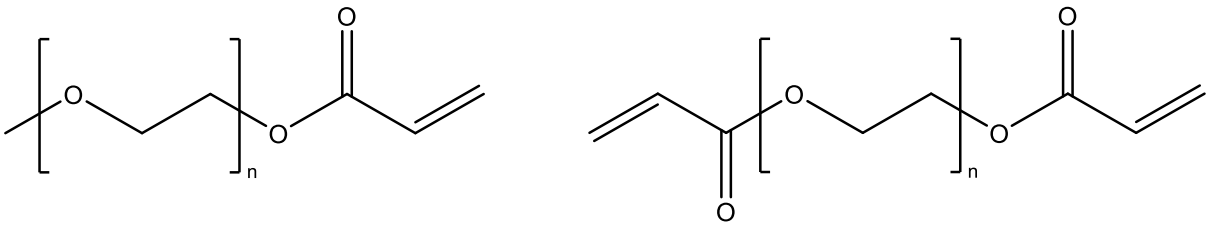

Figure 3.1. The structures of PEGMEA (left) and PEGDA (right).

To achieve this, inhibitor removers were allowed to react with the solutions for 10 minutes, followed by mixing with the AIP solution (AIP final concentration 0.1335% (w:v)). Exposure to 365 nm light for 5 – 60 minutes depending on the gelation time of the mixture was performed (**Table 3.1**).

Table 3.1. Summary of the different PEGMEA/PEGDA gels.

GEL % (V:V)	RATIO OF PEGMEA:PEGDA	PEGDA MW	365 NM UV EXPOSURE TIME FOR GELATION	DESCRIPTION
40	4:1	575	15 min	Very thick Bubbly
20	4:1	575	15 min	Thick Bubbly
15	4:1	575	15 min	Thin Bubbly
10	4:1	575	15 min	Very thin Bubbly
15	8:1	575	20 min	Soft Bubbly
15	16:1	575	30 min	Flimsy Bubbly
15	32:1	575	30 min	Very flimsy Bubbly
15	4:1	700	20 min	Thick Brittle Bubbly
15	8:1	700	20 min	Thick Bubbly Wet
15	16:1	700	30 min	Flimsy Bubbly Wet
15	32:1	700	60 min	Very flimsy Bubbly Wet
15	8:1	10,000	5 min	Very bubbly
15	16:1	10,000	10 min	Larger bubbles than 8:1

The results of these tests show that all the gels prepared are visibly bubbly. This is a phenomenon also described by Cole [29] and Ortyl *et al.* [30], who describe that azo-based photoinitiators decompose upon application of UV light, releasing gaseous products which leads to the formation of bubbles in the structure. This is not ideal for waveguides as the bubbles will interfere with the guiding of light through the structure and cause numerous issues. The number of bubbles was able to be reduced by allowing the gelation mixture to settle for an hour before exposing to UV light, but this was also not ideal as it allows the opportunity for self-polymerisation in the monomer solutions as the inhibitors were previously removed. Even when allowed to settle prior to UV exposure, the resulting gel was still not entirely bubble-free, again due to the evolution of gaseous products upon UV-exposure (**Figure 3.2**).

Figure 3.2. 2 mL gels of 15% PEGMEA-480:PEGDA-10,000 at a ratio of 8:1 (left) and 16:1 (right).

To check the porosity of these films, a solution of 0.1% (w:v) PEG-fluorescein isothiocyanate (PEG-FITC) was prepared and placed on top of three 15% (v:v) gels, at an 8:1 ratio of PEGMEA-480:PEGDA-575/700/10,000 respectively (**Figure 3.3**).

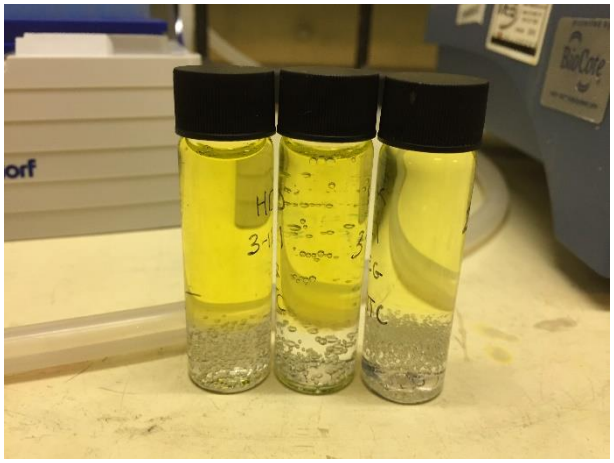

Figure 3.3. 2 mL gels of 15% (v:v) PEGMEA:PEGDA at a ratio of 8:1 treated with 0.1% (w:v) PEG-FITC. PEGDA-575 (left), PEGDA-700 (middle), PEGDA-10,000 (right).

The images in **Figure 3.3** show the different gels soaking in PEG-FITC solution. The gels were soaked for 1 week, after which there had been no visible movement of the PEG-FITC into the gels. While it is possible that some of the PEG-FITC has penetrated the gel, it is not visible to the naked eye and hence implies that the gels are not porous regardless of the chain length of PEGDA used.

As a final attempt to get these gels to work, they were spin coated onto clean glass slides at a range of different conditions followed by UV treatment. Some slides showed an uneven splatter of the solution, while others showed no evidence of a film whatsoever. In all cases, the gels were not suitable for waveguide use and further testing was discontinued due to the various issues with producing smooth, optically clear, and porous gels. At this stage it is assumed that the issues with bubbling were due to the use of AIP as a photoinitiator, and future investigation may remove this issue by using a different initiator.

Poly(ethylene glycol) dimethacrylate (PEGDMA) can be crosslinked using ammonium persulfate (APS) and N,N,N',N'-tetramethylethylenediamine (TEMED) under nitrogen atmosphere as described by Johannsmeier *et al*.; these gels could then be co-polymerised with

methacrylic acid (MAA) and subsequently functionalised to bind biomolecules [31]. Authors noted the gels were uniform and suited for waveguiding, which implies a lack of bubbles. This suggests that perhaps using APS and TEMED for gelation in PEGMEA:PEGDA gels may reduce the bubbling issue. After solving the problem with bubbling the issues surrounding spin coating can then be investigated in more depth.

3.2.2 Chitosan, CS

Chitin, (β-(1–4)-poly-N-acetyl-D-glucosamine) (**Figure 3.4**), is a highly abundant naturally occurring linear aminopolysaccharide found most commonly in the exoskeletons of crustaceans such as shrimp and crabs, but also in insects, plankton, and fungi [32, 33]. An estimated 6 – 8 million tonnes of marine life shell waste are produced each year, with the majority being dumped back into the sea or into landfill [33, 34]. However, these shells can contain between 15 – 40% chitin, which can be extracted and reused [34].

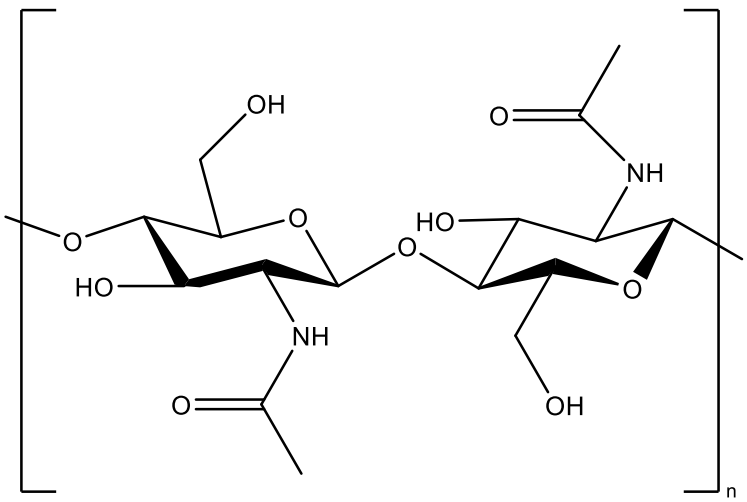

Figure 3.4. The structure of chitin.

Due to the presence of numerous acetamide groups which form hydrogen bonds with the hydroxyl groups, chitin itself is rigid and poorly soluble [35]. Chitosan (CS) (**Figure 3.5**) is the deacetylated form of chitin and was chosen as the first polymer to test as a LW. Already well-known in the bioengineering community, CS is biodegradable, biocompatible, and non-toxic, making it an excellent choice for biological and pharmaceutical applications, and has even been reported to show antimicrobial properties [32, 36, 37]. A high degree of deacetylation produces numerous free primary amine groups, increasing the solubility and reactivity of the polymer [38].

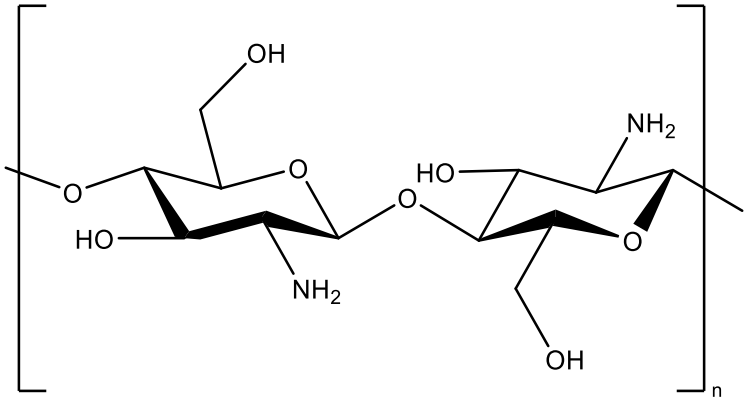

Figure 3.5. The structure of chitosan (CS).

Previous work within the group has shown CS is suited for LW applications, and has been further developed in this work [39]. With a pKa between 6.2 – 7.0, CS is insoluble in water but readily dissolves in dilute acid [40]. Additionally, CS is a cationic and hydrophilic molecule with free primary amine and primary hydroxyl groups which can be exploited for crosslinking and protein immobilisation [41, 42].

3.2.2.1 Fabrication

Commercial CS is readily available in different MWs. 100 – 300K CS was used as purchased to form a 1% (w:v) solution in 0.1 M acetic acid, followed by spin-coating onto clean

glass slides and immersing in the desired crosslinking solution. To visualise the mode, the film was doped using a solution of 0.1 mM Reactive Blue 4 (RB4) (**Figure 3.6**) dye for 5 minutes, making this a dye-doped leaky waveguide (DDLW) [42].

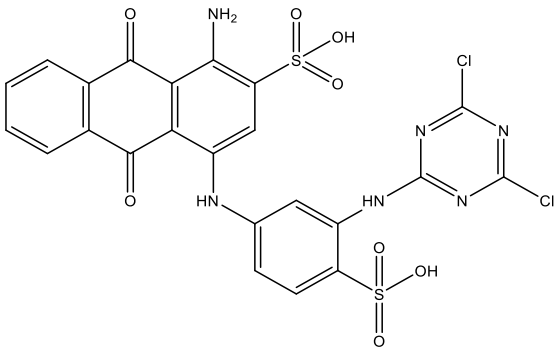

Figure 3.6. The structure of Reactive Blue 4 (RB4).

Different buffers were investigated for formation and storage of CS films. These included 10 mM carbonate-bicarbonate buffer, pH 9.5; 100 mM PBS, pH 9.5; 100 mM PBS, pH 7.4; 100 mM HEPES, pH 7.4. For fabrication, the buffer was used to dissolve the crosslinking agent in prior to immersion of the film. For storage, it was noted that these films cannot be stored dry. Upon drying out, the network making up the film structure will collapse, and rehydration cannot reform the porous structure. This means the films must be stored wet; each buffer, and additionally DI water, was used to store the films in overnight before checking the films. Only 100 mM HEPES, pH 7.4 provided consistent films which worked as waveguides and therefore this buffer was used moving forwards. The other buffers (and DI water for storage) either produced non-uniform films, or films with no waveguide mode, and were disregarded for the remainder of the study.

Different concentrations of CS solution were also investigated: 1%, 1.5%, 2% (w:v). When in solution with 0.1 M acetic acid, CS forms a viscous mixture, particularly at concentrations above 1%. This made handling of the solution difficult and reduced the

accuracy with which higher concentrations could be pipetted. Nevertheless, each concentration was tested to prepare thin films with, and it was apparent that 1% CS provided the most consistent results and was additionally the easiest to handle. For sensing, a single-moded output is desirable as it increases the simplicity of the test; 1.5% and 2% CS solutions tended to produce double- or triple-moded outputs, while 1% CS reliably formed single-moded films. For these reasons, 1% CS was used moving forwards with the study.

In parallel to determining the most suitable concentration of CS, research was also undertaken to discover the best crosslinker and the ideal conditions for crosslinking [36]. This involved variation of incubation time before addition of the crosslinker, followed by variation of exposure time to the crosslinker solution.

Two different crosslinkers were investigated: poly(ethylene glycol) diglycidyl ether (PEGDGE) (10% (w:v)), and glutaraldehyde (0.03125% and 0.0625% (v:v)).

PEGDGE is a non-hazardous water-soluble compound comprised of a PEG backbone with two terminal epoxide rings, shown in **Figure 3.7.** The epoxide rings undergo nucleophilic attack by the primary amine groups in chitosan and produce crosslinked gels. The PEG backbone can be procured with different chain lengths, allowing tailoring of the crosslinking to produce either larger or smaller pores.

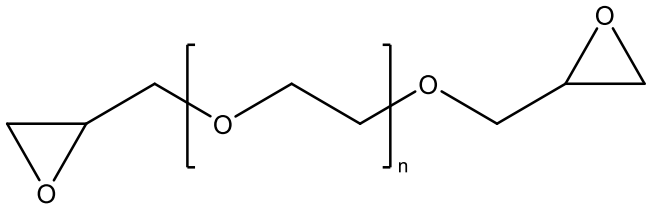

Figure 3.7. The structure of poly(ethylene glycol) diglycidyl ether (PEGDGE).

For the PEGDGE-crosslinked CS, a 10% (w:v) solution of PEGDGE with a Mn of 500 was prepared in pH 9.5 bicarbonate buffer. As the 1% CS solution readily forms a uniform layer when spin coated onto a glass substrate, the decision was taken to firstly spin coat the CS, followed by immersion in the PEGDGE solution. This would allow for the most uniform exposure of the film to the crosslinker, while also ensuring the CS layer itself was as consistent as possible. This had the added advantage of reducing the opportunity for localised crosslinking which would lead to a non-uniform hydrogel.

Films were prepared at various conditions, from 1% - 2% (w:v) CS and spin conditions ranging from 800 rpm to 2000 rpm, at 100 rpm/s and 30 s. Additionally, each film was allowed to air dry for between 3 and 6 minutes before immersion in the PEGDGE solution overnight.

To check for the formation of a thin film, the slides were stained with 0.1 M RB4 solution, pH 7.4, for a maximum of 30 minutes. Seen in **Figure 3.6**, RB4 is a dichlorotriazine dye which is able to bind to the free primary amines in CS.

Upon removal from the staining solution, no film was visible. This is likely due to the PEGDGE not forming the desired crosslinking in the film, which may be due to the use of the pH of the bicarbonate buffer. Further investigations were not carried out using this crosslinker.

As discussed briefly in the introduction to this chapter, glutaraldehyde is a highly reactive compound which readily reacts with primary amines at acidic pH (**Figure 3.8**). Glutaraldehyde has been well-reported in literature as a crosslinker of CS [32, 36, 42, 44-47].

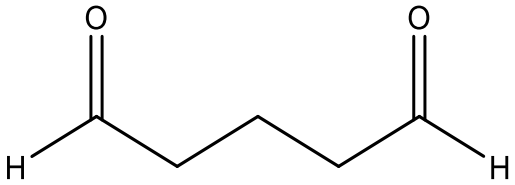

Figure 3.8. The structure of glutaraldehyde.

At basic and neutral conditions, glutaraldehyde will readily react with primary amines in CS and form a network of strongly crosslinked CS molecules. At acidic conditions, glutaraldehyde is also able to react with the CS, forming an acetal between the aldehyde in glutaraldehyde and the alcohol in CS. As we are ultimately working with proteins, it is ideal to keep the pH of the gel as neutral as possible. We therefore used pH 7.4 and hence encouraged the formation of crosslinks between the primary amine groups on CS rather than the hydroxyl groups.

Of the two crosslinkers investigated, glutaraldehyde produced superior results. Similar to the PEGDGE, these films were prepared at various conditions in each buffer, from 1% - 2% (w:v) CS and spin conditions ranging from 800 rpm to 2000 rpm, at 100 rpm/s and 30 s. Additionally, films were tested at different incubation times of 0 – 10 minutes, along with glutaraldehyde exposure times of 1-20 minutes and glutaraldehyde concentrations of 0.03125% and 0.0625% (v:v). Ultimately, the best conditions were determined to be 1% CS solution prepared in 0.1 M acetic acid, 900 rpm, 100 rpms/s, 30 s, an incubation time of 3 minutes and exposure to 0.03125% (v:v) glutaraldehyde for 10 minutes. These conditions are used throughout the project, with the CS films prepared and stored in 100 mM HEPES, pH 7.4.

3.2.2.2 Purification

As CS is a naturally occurring polymer it is subjected to impurities and irregularities in structure. The deacetylation of chitin to prepare CS can produce different levels of

deacetylation, typically between 70% and 95%, and the methods employed can introduce additional impurities [48]. This makes it difficult to produce consistent and reliable results with commercial CS as batch-to-batch differences can significantly impact the results. The MW, purity, degree of deacetylation, appearance, and solubility can vary between batches and make standardisation difficult to achieve [48].

In this project, batch-to-batch differences in the commercial CS, and even inconsistencies throughout one batch, led to non-reproducible results and interference with the visualisation of the mode. Some batches would form films while others would not, and a range of different techniques were employed to attempt to improve this. This included:

- Increasing the concentration of glutaraldehyde from 0.03125% to 0.0625%.
- Ozone cleaning the slides prior to film fabrication.
- Modifying spin conditions.
- Modifying gelation time and crosslinker exposure.
- Switching from a humidifier to an incubator.
- Increasing/decreasing how long the CS was mixed for before forming films.
- Changing to different batches of glass slides.
- Changing buffer solution.

These techniques had limited success, therefore we turned to the issues presented by CS itself to try and solve the issues. As a natural polymer, CS is susceptible to inconsistent structure and numerous impurities such as ash, proteins, and metals [45]. Therefore, the commercial CS was purified in large batches to maintain consistency and improve the stability

and reliability of the subsequent hydrogels. Three different batches of commercial CS were procured, and the top row in **Figure 3.9** shows the visual differences between the batches.

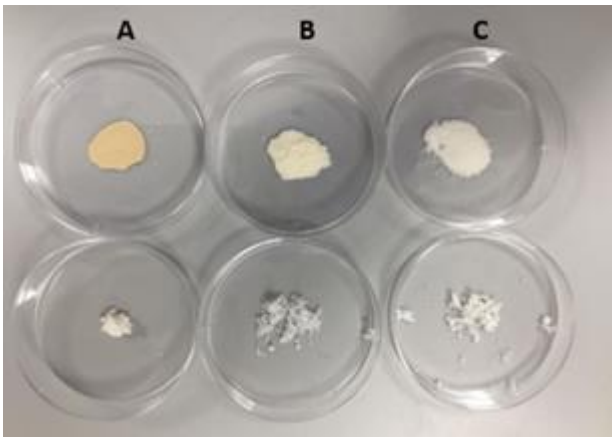

Figure 3.9. A visual comparison of three separate batches of CS before (top row) and after (bottom row) purification.

A purification procedure was adapted from Filho and Signini [49]. This involved dissolution of the impure CS in 0.1 M acetic acid, followed by filtration and consequent precipitation via addition of excess 1 M sodium hydroxide. The precipitate was extensively washed and collected *via* centrifugation before dialysis against DI water for 5 days, further washing, and collection of the final product by rotary evaporation and freeze drying. **Figure 3.9** shows the differences in the impure and purified batches of CS. The purified CS presents as white fluffy flakes, while the impure CS varies in colour and is a powder. The gels produced from each purified batch were comparable, while gels produced by the commercial CS batches gave considerably different results.

Not only did CS which had undergone this purification procedure yield much more reproducible results when used to prepare LWs, it also facilitated removal of dye-doping to visualise the mode. This is an important achievement, as the dye causes severe broadening of the dip in the DDLW versus the non-doped LW, seen in **Figure 3.10**.

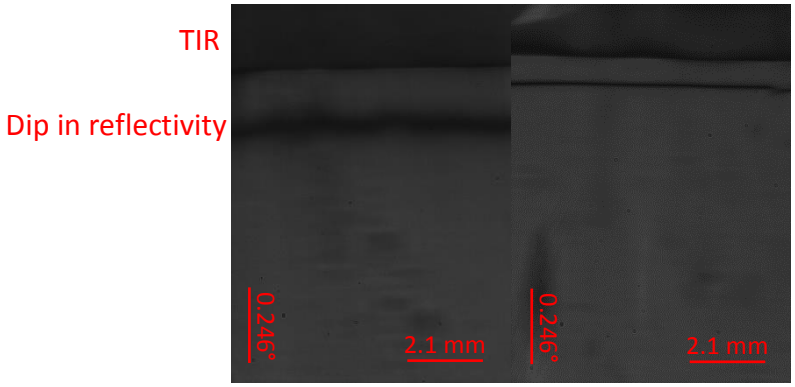

Figure 3.10. Output images of a 1% CS DDLW (left) and a non-doped 1% CS LW (right).

The broadening of the dip reduces the accuracy of the measurement as a broader dip is subjected to more noise due to the software tracking a wider region. Additionally, binding of RB4 to the film reduces the availability of primary amine groups for further binding with proteins, hence reducing the sensitivity of the film. In these images, the dark region at the top corresponds to the total internal reflection (TIR) produced at the sample/waveguide interface, while the dark line below this corresponds to the dip in reflectivity caused by the leakage of light at the waveguide/substrate interface. Therefore, this will henceforth be referred to as either the "dip" or the "mode" and will be tracked throughout the project. This is discussed in more detail in **Chapter 2 (2.2.2)**.

3.2.2.3 Results

Using 100 mM HEPES, pH 7.4, solutions of glycerol were prepared *via* serial dilutions at the following concentrations: 2%, 1%, 0.5%, 0.25%, 0.125% (v:v). Additionally, 1% (w:v) solutions of PEGs of various MWs were prepared by dissolving the PEGs in 100 mM HEPES, pH 7.4 with stirring. The refractive indices of the solutions were measured in triplicate using a refractometer with the units of refractive index units (RIU), and typical values are reported below in **Table 3.2**.

Table 3.2. Typical RI values for glycerol and PEG solutions prepared in 100 mM HEPES, pH 7.4, measured in triplicate on a refractometer as described in **Section 8.7.4**. Errors reported as 1σ.

SOLUTION	REFRACTIVE INDEX (RIU)
0.125% GLYCEROL	1.33697 ± 0.00001
0.25% GLYCEROL	1.33715 ± 0.00001
0.5% GLYCEROL	1.33746 ± 0.00001
1% GLYCEROL	1.33805 ± 0.00001
2% GLYCEROL	1.33930 ± 0.00001
10 kDa PEG (1%)	1.33810 ± 0.00001
100 kDa PEG (1%)	1.33813 ± 0.00001
300 kDa PEG (1%)	1.33814 ± 0.00001
100 mM HEPES, pH 7.4	1.33686 ± 0.00001

The instrumentation theory is described in **Chapter 2** (**2.2.2**), with the components used listed in **Chapter 8** (**8.7**) and the experimental method for glycerol and PEG characterisation described in **Chapter 8** (**8.4**). The output images were separated into between 5 and 10 evenly spaced boxes across the width of the dip in reflectivity. The dip was tracked in real-time as solutions were introduced *via* the flow cell. The response of each LW to the glycerol solutions was used to prepare calibration graphs and determine the sensitivity of the LWs as glycerol is a small and unreactive molecule which can enter and exit the pores of the film without restriction.

The PEGs were used to investigate the porosity of the films as they are easily procured in various different sizes and are unreactive. Shorter PEGs which are able to diffuse into the bulk of the LW will provide a much higher response than larger PEGS which cannot. Porous films are desirable as they will allow analytes to diffuse into the bulk of the hydrogel and hence the analytes will be within the range of the guided optical mode. Non-porous hydrogels will be restricted to sensing in the evanescent field as discussed in **Chapter 2** (**2.2.2**), still producing a response but at a reduced value. It should be noted that the molecular weight distribution

of the PEG solutions may also partially contribute to the increase in resonance angle, with the small volume of shorter PEG chains able to diffuse into the film. This is not anticipated to have a significant impact on the results as only a small quantity of shorter PEG chains are expected to be present in the larger MW PEGs.

Figure 3.11 shows a glycerol and PEG porosity test on the DDLW films, and **Figure 3.12** shows the same tests on undoped LW films. In the glycerol sensorgrams, glycerol of increasing concentrations was introduced sequentially and allowed to plateau before adding the next. The resonance angle increases with increasing glycerol concentration due to an increase in the RI of the glycerol which diffuses into the hydrogel and changes the RI of the film. In the output image, this results in the dip shifting down the image. At the end of the run the glycerol is replaced with buffer and returns to the original resonance angle, indicating that no permanent change in RI of the film has been caused by the glycerol.

The PEG sensorgram follows a similar pattern, with each PEG preceded and succeeded by a buffer wash to ensure all of the PEG has left the hydrogel before addition of the next. This was necessary as the larger size of the PEG molecules in comparison to the small glycerol molecules mean it is more likely that the PEG will become trapped in the hydrogel pores.

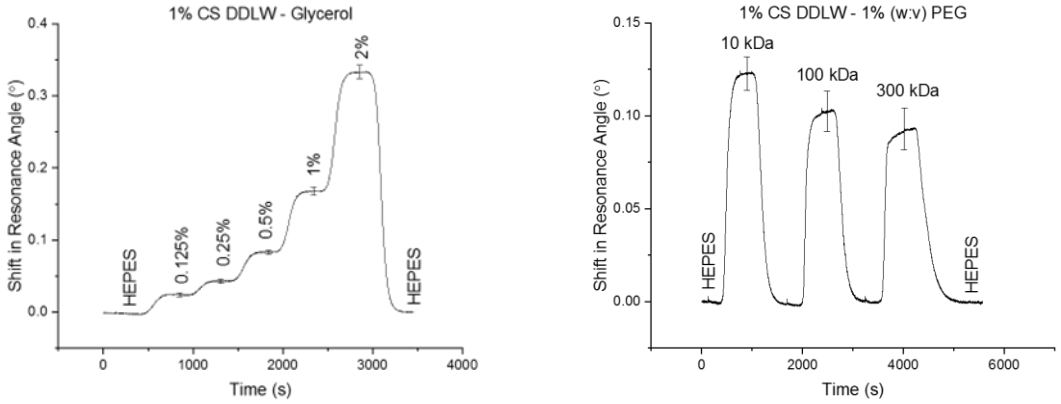

Figure 3.11. Glycerol (left) and PEG (right) runs on 1% CS DDLW films. Error bars were calculated as 1σ across three different DDLWs.

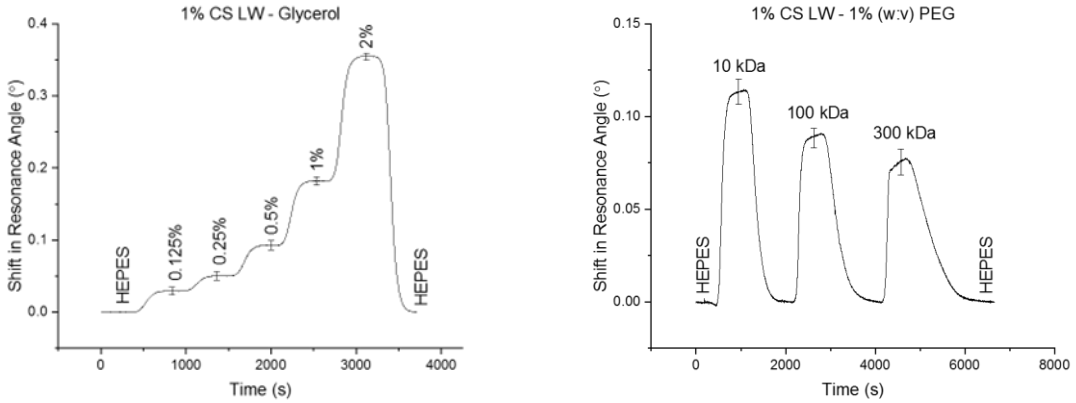

Figure 3.12. Glycerol (left) and PEG (right) runs on 1% CS LW films. Error bars were calculated as 1σ across three different LWs.

While the response for both the DDLW and LW are similar, the error bars for the DDLW are larger due to increased noise from the broader dips. The method used to calculate the error bars is described in **Chapter 8** (**8.4.3**). It was also noted that parts of the DDLW film were susceptible to flaking off the glass substrate and could be seen floating in the buffer solution, calling into question the stability of these DDLWs. The inclusion of the dye may be negatively affecting the structural integrity of the CS film, causing it to detach from the glass and breaking the crosslinks. This phenomenon was seen in DDLWs prepared from both the commercial and purified CS.

The theoretical response of the films to PEG solutions can be calculated using the following equation (**Equation 3.2**):

Equation 3.2. Theoretical response.

$$\Delta\theta_{R\ (theoretical)} = (RIS \times RI) + c$$

Where RIS is the refractive index sensitivity calculated in relation to the glycerol solutions, RI is the refractive index of each PEG solution, and c is the y-intercept of the glycerol calibration graph. The theoretical response is therefore the shift expected if all of the PEG solution is able to enter the film.

If we compare the data presented in **Table 3.3**, we can see that the porosity of both the DDLW and LW are very similar, with the LW having a very slight increase versus the DDLW. The porosity percentage decreases as the PEG MW increases which is expected as the larger molecules will find it more difficult to diffuse into the structure of the film. Porosity (%) refers to the difference in response between the actual and theoretical values expressed as a percentage, and has been calculated using:

Equation 3.3. Porosity (%) calculation.

$$Porosity\ (\%) = \frac{Actual\ response}{Theoretical\ response} \times 100$$

Therefore from **Table 3.3** we can see that the LW is 66.84% porous to the 10 kDa PEG in comparison to the theoretical porosity.

Table 3.3. PEG response and percentage porosity of 1% CS DDLWs and LWs.

1% PEG	RI (RIU)	THEORETICAL RESPONSE (°)		ACTUAL RESPONSE (°)		POROSITY (%)	
		DDLW	LW	DDLW	LW	DDLW	LW
10 kDa	1.33810	0.169383	0.174163	0.110360	0.116419	65.15	66.84
100 kDa	1.33813	0.173510	0.178490	0.087345	0.091583	50.32	51.31
300 kDa	1.33814	0.175000	0.179932	0.076586	0.080598	43.76	44.79

Figure 3.13 shows calibration curves for the DDLW and LW films, where the RIS is calculated as the gradient of the line of RI versus shift in resonance angle.

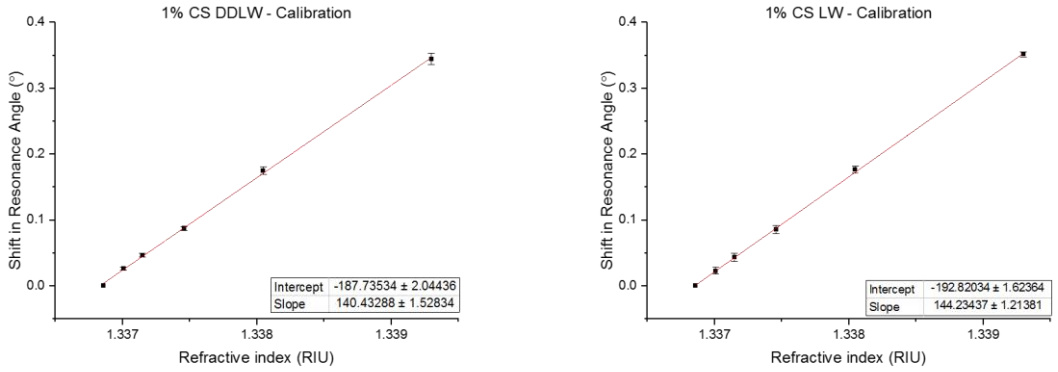

Figure 3.13. Calibration curves for the 1% CS DDLW (left) and LW (right). Error bars were calculated as 1σ across three different DDLWs/LWs.

The DDLW has an overall lower RIS than the LW, with values of 140.43 ± 1.53 °/RIU and 144.23 ± 1.21 °/RIU respectively. This implies that the LW is more suited to detection of lower concentrations as it is able to detect smaller shifts in RI compared to the DDLW. However, the difference between RIS is not significant and the DDLW is still highly sensitive. Additionally, all points on both graphs are in strong agreement with the line of best fit, suggesting a low degree of deviation from this line in both measurements and strong concordance between the DDLW and LW pattern in response to the glycerol solutions.

The major issues envisaged with the DDLWs versus the non-doped LWs is not related to the sensitivity, but instead in relation to the reduction in available primary amine groups and long-term stability of such LWs. Considering the similar porosity and lower stability combined with the decreased availability of primary amine groups in the DDLW, further experiments were conducted on the non-doped LWs produced using the purified CS.

An important aspect of these devices is the ability to be stored for long periods of time; the CS films have a shelf-life of ≥6 months when stored correctly. This involves keeping them hydrated in 100 mM HEPES, pH 7.4, protected from light, and at room temperature. The downside to CS films is the requirement for wet storage, as this could pose issues with transport and long-term storage. However, the excellent shelf-life is remarkable, and CS should not be disregarded based on storage conditions.

CS has been reported in literature to have poor longevity, particularly in solid form due to the hygroscopic nature of the compound and the ability to readily form hydrogen bonds with moisture [44]. This was also observed when in 0.1 M acidic solution, where the solution was only stable for 5 days before it stopped forming reproducible gels. Once in gel form, the stability significantly increases, and no degradation was observed in the LWs.

Overall, these results show that CS is an excellent choice for a LW, with high porosity, ease of preparation, long storability, reproducible response, and reliable formation. Additionally, the purification step has removed the requirement for dye-doping the film to make the dip visible, further increasing the stability and response of these films. In regard to the success criteria defined in **Section 3.1.2**, both the DDLW and LW formed from CS are

ranked as high for reproducibility and uniformity. The 1% CS LW has therefore been used as the standard with which all other films are compared throughout this project.

3.2.2.4 High molecular weight chitosan, HMW CS

In addition to the 100 – 300K CS used above, a higher MW CS was also investigated. This CS had a MW of 600 – 800K and is therefore referred to as high MW CS (HMW CS). This was first purified in the same manner as for the original, low MW CS (LMW CS), before spin coating into thin films.

The aim of using the HMW CS was to increase the structural integrity of the films, reducing the opportunity for this film to merge with a reference layer as discussed later in **Chapter 4**. As seen in **Figure 3.14**, the HMW CS gave a reduced response to glycerol solutions compared to the LMW CS, indicating that the film was less sensitive than the LMW CS variant.

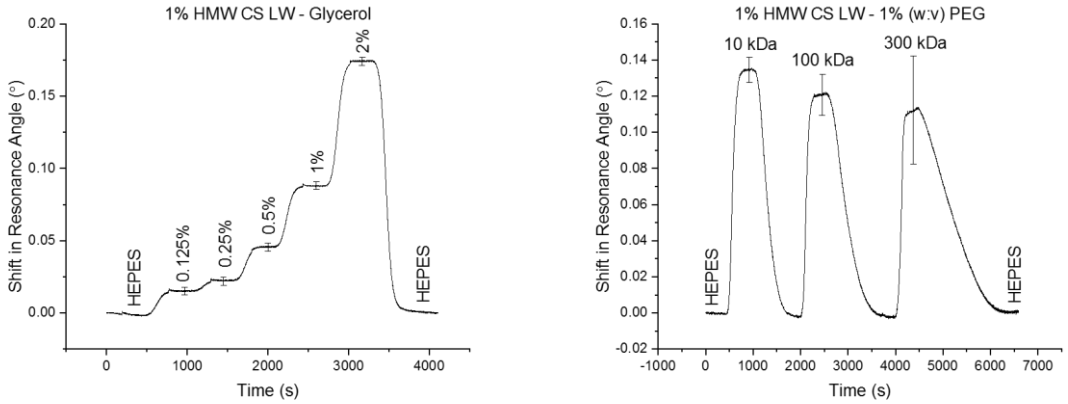

Figure 3.14. Glycerol (left) and PEG (right) runs on 1% HMW CS LW films. Error bars were calculated as 1σ across three different LWs.

Additionally, the PEG run results showed a fairly even response for each PEG which suggests that the films are porous to all MWs of PEG tested and therefore would be suited to sensing of larger molecules, but the error bars clearly show the large variation between different films. While the porosity of these films appears to be higher than that of the LMW

CS, the lower sensitivity and the film variation makes them unsuitable for mass production. The large error bar on 300 kDa PEG further solidifies the fact that these films are not producing consistent results.

Table 3.4 shows the percentage porosity of the films is closer to the theoretical value than that of the LMW CS, with an excellent response for all PEGs. This further proves that these films have very high porosity, making them suited to testing of large biomolecules. A downside to such a high porosity is that there is no size discrimination occurring in the device; larger interferents will be able to enter the film alongside the smaller analytes and cause interference.

Table 3.4. PEG response and percentage porosity of 1% HMW CS LWs.

1% PEG	RI (RIU)	THEORETICAL RESPONSE (°)	ACTUAL RESPONSE (°)	POROSITY (%)	ACTUAL VERSUS 1% CS RESPONSE (%)
10 kDa	1.33818	0.151750	0.143582	94.62	123.33
100 kDa	1.33826	0.161133	0.134803	83.66	115.79
300 kDa	1.33834	0.170515	0.142225	83.41	122.17

Some studies have been done into the differences in structure and porosity of CS of different MWs such as the 2021 study by Wei *et al.*, who determined that hydrogels formed from LMW CS have a faster water absorption rate, lower porosity, and lower maximum stress level than HMW CS hydrogels [50]. This is expected as the LMW will contain fewer network imperfections such as crossing of polymer chains and hence is less likely to have blocked access to hydrophilic groups, enhancing the water absorption rate. On the other hand, LMW CS will produce smaller pores as the shorter chains allow for crosslinking of the functional

groups in close proximity. Meanwhile the HMW CS is more porous as the gaps between crosslinking regions are larger.

It is important to note that this study was completed using citric acid as a crosslinker, and in this case the authors referred to LMW CS at 50-190K and HMW CS at 310-375K. Regardless of the difference in crosslinker and chosen MWs, this study is important in highlighting the differences between CS hydrogels of different MWs.

Finally, a calibration curve was made for the HMW CS, showing an RIS of 117.28 ± 8.12 °/RIU (**Figure 3.15**). When compared to the RIS of both the DDLW and the lower MW CS this value clearly indicates a reduced sensitivity, making them unsuitable for further testing.

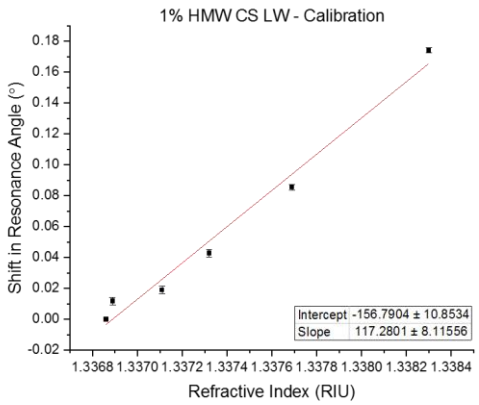

Figure 3.15. Calibration curve for 1% HMW CS LWs. Error bars were calculated as 1σ across three different LWs.

The output of the films tended to show a single dip very close to the TIR, making tracking difficult (**Figure 3.16**).

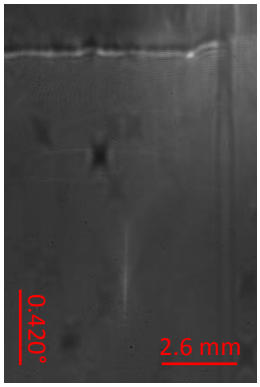

Figure 3.16. Output image of a 1% HMW CS LW.

The dip produced regions of uniformity and irregularities which is in contrast to the CS films which are typically uniform across the width of the entire LW. When considering both the reduced sensitivity, low reproducibility, and medium uniformity from film-to-film, particularly in comparison to the 1% CS LWs, the HMW CS films were not tested any further. Any further work reported on CS films was performed on the original, LMW CS of 100 – 300K.

3.2.3 Poly(acrylamide-*co*-acrylic acid), PAAm-Ac

Poly(acrylamide-*co*-acrylic acid) (PAAm-Ac), a non-toxic synthetic polymer built from polyacrylamide (PAAm) and acrylic acid moieties, was investigated next (**Figure 3.17**). PAAm is a well-known and widely utilised inert and hydrophilic gel, and the addition of the carboxylic acid functional groups *via* the acrylic acid comonomer would allow for protein immobilisation *via* exploitation of this functional group.

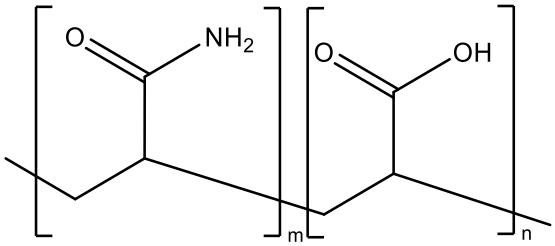

Figure 3.17. The structure of poly(acrylamide-*co*-acrylic acid) (PAAm-Ac) repeating subunits.

Advantageously, PAAm-Ac was already provided in polymeric form, which both reduced the potential dangers from using the carcinogenic acrylamide (AAm) monomer, and also allowed for easy spin coating. Different concentrations were tested, from 2% - 5% (w:v) with 3% (w:v) solution dissolved in 1 M HCl with 5% (v:v) glycerol providing optimal results. The final gel percentage was 2.88% (w:v) PAAm-Ac, containing 0.025% (v:v) glutaraldehyde as a crosslinker and 4.8% glycerol as a humectant. When glycerol was not used, the films still formed but did not give any modes on the output image, which suggests that the glycerol contributes towards the dip in reflectivity. Additionally, glutaraldehyde concentrations were tested from 0.025% - 0.1% (v:v) to ensure that 0.025% (v:v) was most suited.

As seen in **Figure 3.18**, these gels gave a smooth, consistent, and thin mode, making them highly suited to tracking cleanly and with minimal noise.

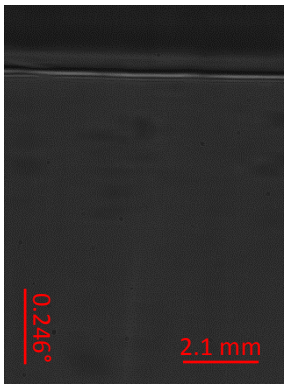

Figure 3.18. Output image of a 2.88% PAAm-Ac LW.

3.2.3.1 Glass functionalisation

Unlike with the CS films, the PAAm-Ac films did not bind covalently to the glass surface and were observed to either:

- Not form a film at all, with the solution being flung from the surface of the glass during spin coating or,
- Form a patchy film which detached from the glass when soaked in water or buffer.

To ensure strong binding of the film to the glass substrate, the glass slides were first ozone cleaned for 2 minutes. Next, (2-aminopropyl)triethoxysilane (APTES) was employed as a functionalisation agent (**Figure 3.19**).

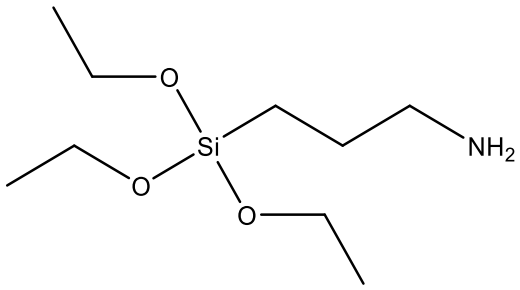

Figure 3.19. The structure of (2-aminopropyl)triethoxysilane (APTES).

The silane groups were able to bind with the hydroxyl groups on the clean glass slides, while the free primary amine group could bind to the carboxylic acid on the acrylic acid moiety and produce an amide, effectively anchoring the hydrogel to the glass substrate (**Figure 3.20**).

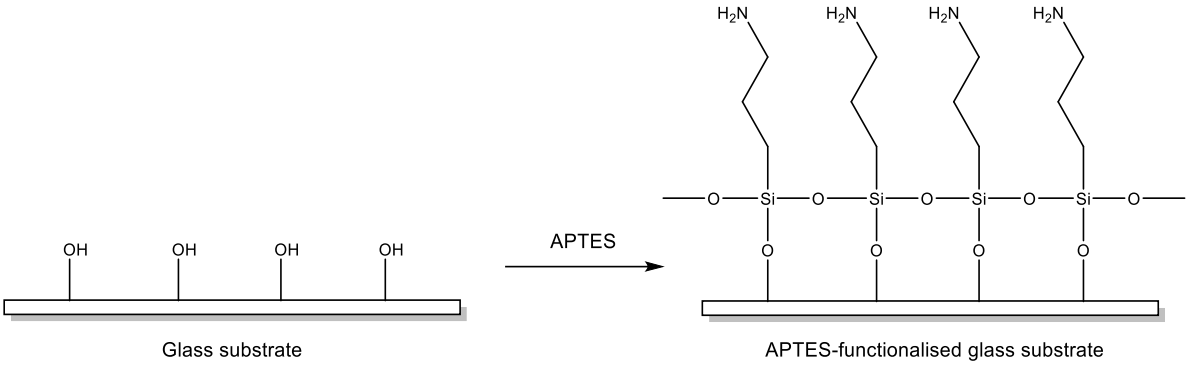

Figure 3.20. Schematic of glass functionalisation with APTES [51].

Figure 3.20 shows the functionalisation of a glass substrate with APTES. This is an ideal functionalisation, where all the APTES molecules line up in sequence. In reality, the APTES can bind in different orientations, leading to patchy and unreliable binding [52]. Additionally, multilayers can form due to the three silane groups on the APTES. Some of the different possible configurations are shown in **Figure 3.21**.

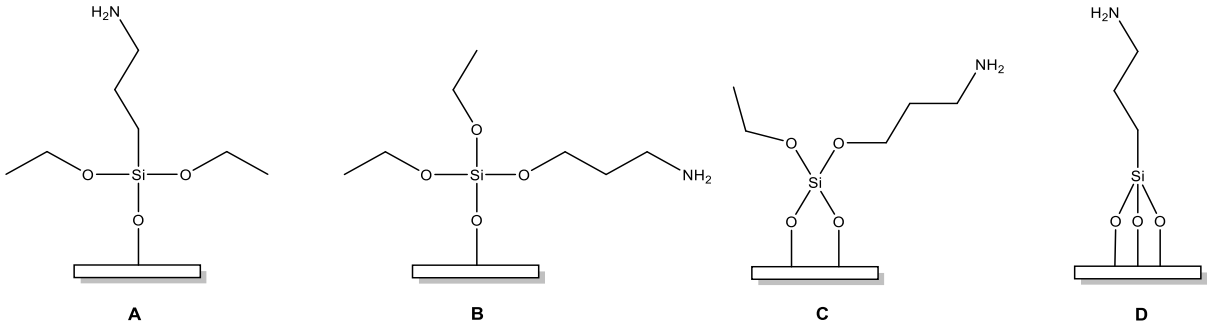

Figure 3.21. Some of the possible orientations of APTES on a glass surface [52].

For ideal functionalisation, orientation D is most desirable as it ensures the strongest anchoring to the glass substrate. Orientation A will allow for binding between APTES molecules to form a layer as in **Figure 3.20** but does risk the formation of multilayers. Orientations B and C increase steric hinderance and risk multilayer formation. Unfortunately, it is not possible to control the orientation of the molecules during the silanisation process, and a mixture of the orientations is highly likely.

To achieve the most reproducible APTES functionalisation different methods were investigated, using toluene, ethanol and anhydrous toluene as the solvent, and concentrations of APTES from 1 – 2% (v:v).

The most reliable method we could achieve involved using freshly cleaned and dried glass slides, functionalising in 1% APTES for 30 minutes, rinsing in toluene, and drying in an oven at 60 °C for 45 minutes. The drying step was particularly important for producing strongly bonded silane, and allowed any remaining APTES and solvent to fully dry before spin coating the solution [53]. While we cannot confirm the orientation of the APTES molecules formed via this technique, this method provided the most reproducible results and therefore was used going forwards.

3.2.3.2 Results

In comparison to the CS LWs the PAAm-Ac LWs are less porous; this is apparent from the smaller response to the 1% (w:v) PEG solutions (**Figure 3.22**). The response to 10 kDa PEG is 68.93% of that of CS, while 100 kDa and 300 kDa PEG responses are 42.18% and 37.58% respectively.

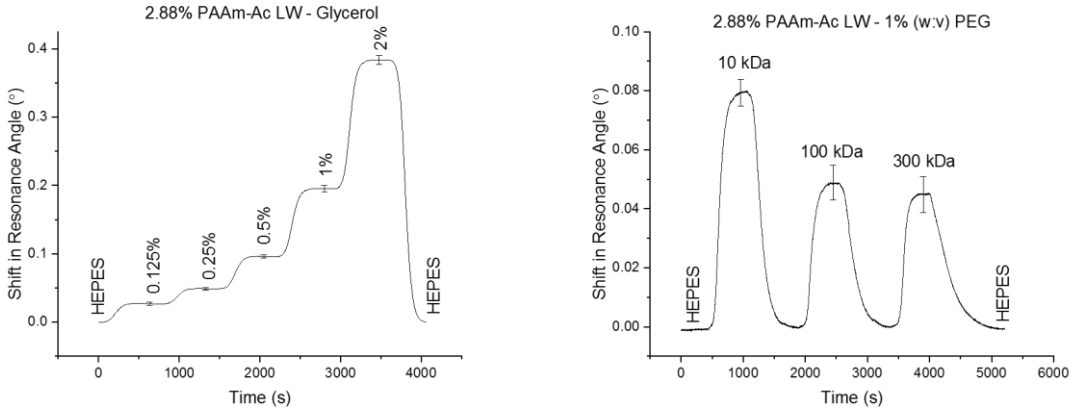

Figure 3.22. Glycerol (left) and PEG (right) runs on 2.88% PAAm-Ac LW films. Error bars were calculated as 1σ across three different LWs.

The response of the PAAm-Ac films to both 100 kDa and 300 kDa PEGs is also very similar, suggesting that the solutions are unable to fully penetrate into the pores of the hydrogel and the shift is caused partially by the RI change of the solutions at the surface of the gel. This lower porosity could pose an issue in protein detection, where large proteins may be unable to enter the gel network and bind with the reactive groups.

Despite having a lower overall porosity than the CS films, the PAAm-Ac films have an excellent percentage porosity for 10 kDa PEG, indicating that the majority of the 10 kDa PEG solution is able to diffuse into the film (**Table 3.5**). This drops significantly for 300 kDa PEG, with far less of the solution able to enter the LW.

Table 3.5. PEG response and percentage porosity of 2.88% PAAm-Ac LWs.

1% PEG	RI (RIU)	THEORETICAL RESPONSE (°)	ACTUAL RESPONSE (°)	POROSITY (%)	ACTUAL VERSUS 1% CS RESPONSE (%)
10 kDa	1.33763	0.087712	0.080252	91.49	68.93
100 kDa	1.33770	0.096038	0.049107	51.13	42.18
300 kDa	1.33801	0.132909	0.043748	32.92	37.58

Calibration of the PAAm-Ac films was carried out to determine the sensitivity of these films (**Figure 3.23**).

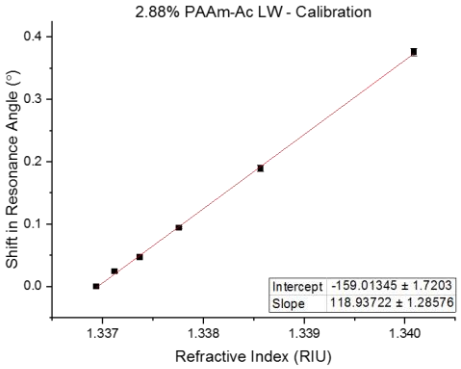

Figure 3.23. Calibration curve for 2.88% PAAm-Ac LWs. Error bars were calculated as 1σ across three different LWs.

Again, when compared to the CS LWs these PAAm-Ac LWs have a lower RIS of 118.94 ± 1.29 °/RIU. This makes them less sensitive than the CS LWs, with a comparative sensitivity of 82.47%. When considering reproducibility and uniformity, these have been ranked as "medium" and "high" respectively, as the films typically showed clear and uniform modes, but the sensitivity of the films was not as consistent.

In terms of storage, these films showed stability for up to 3 months; longer time periods were not tested. Additionally, these films were able to be stored dry with rehydration occurring directly before testing. This is a major advantage for long-term storage and transport and therefore ideal for point-of-care (POC) usage.

Literature shows studies on PAAm-Ac hydrogels typically formed *via* free radical polymerisation from AAm, acrylic acid, and BAAm co-monomers [54, 55]. By preparing the hydrogels in this manner, greater control is exerted over the final properties of the hydrogel such as viscosity, strength, and functional group availability. This method was not investigated in this project as the PAAm-Ac co-monomer could be purchased and easily crosslinked with glutaraldehyde to produce spin coated films. While investigation into the monomeric versions would be useful to compare the properties of the gels, the increased safety and ease of

fabrication achieved using the PAAm-Ac co-monomer mixture was much more suited to spin-coating and mass production. Future research into these films produced from the monomers could offer better results for LW sensing, but time limitations prevented this during this project.

3.2.4 N-(3-aminopropyl)methacrylamide, APMA

N-(3-aminopropyl)methacrylamide (APMA) was used to prepare LWs with free primary amine groups similar to the CS. For this to work, the APMA required a co-monomer of AAm, and a crosslinker (**Figure 3.24**). BAAm and PEGDA were both tested for this, with PEGDA producing the more porous gels due to a longer chain length and therefore being used moving forwards. The gels formed by free radical polymerisation induced by APS and TEMED.

APMA can be polymerised with different co-monomers. Hoskins *et al.* developed thermally active APMA-based hydrogels for drug delivery by co-polymerising APMA with HPMA, producing hydrogels capable of encapsulating drugs, followed by further modification with PEG to enhance drug release [56]. Dubey *et al.* similarly co-polymerised APMA with MAA, using different monomer ratios and pH values to assess the effect of conditions on the final polymer [57]. In our case, we selected AAm as the co-monomer as it is highly water soluble, easily polymerised and well-researched as a co-polymer in multiple fields including medicine [58]. The similarities in structure between APMA and AAm were expected to enhance the uniformity of the hydrogel and reduce the introduction of multiple different functional groups.

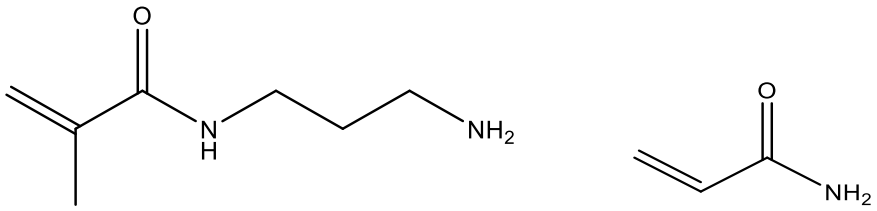

Figure 3.24. The structures of N-(3-aminopropyl)methacrylamide (APMA) (left) and acrylamide (AAm) (right).

Instead of spin coating, these films were cast. This was for the following reasons:

- The hazardous nature of the chemicals used. AAm is a carcinogen and spin coating is by nature a messy technique, with some of the solution being flung from the surface of the film before gelation occurs. Therefore, spin coating such a substance will require careful clean-up.
- The increased gelation time required for these films. Depending on the concentrations used, these gels could take anywhere from 1 – 10 minutes to form a firm gel, providing ample time for the solution to be flung from the substrate during spin coating, and requiring longer for the gel to fully form on the glass surface before removing from the spin coating chuck.
- The viscosity of the gelation solution. The viscosity of these solutions is visibly lower than that of CS, making it easier to pipette but also less likely to remain on the surface of the glass particularly when high speeds are applied.

The free primary amine content could be tailored by modifying the ratio of APMA to AAm, while the volume of BAAm or PEGDA could be modified to affect the porosity and stability of the gel. Overall, it was found that a 4.5% total monomer gel was most suited to this type of film, with a molar ratio of 1:0.04 AAm:APMA. This was in line with previously published work by Gupta *et al.* who noted that 4.5% APMA LWs produced the most porous films [59].

3.2.4.1 Glass functionalisation

For the casting of the APMA films, two functionalisation steps were required. Firstly, the slide that would bind with the gel was functionalised using chloro(dimethyl)vinylsilane (CDMVS) (**Figure 3.25**). Secondly, a top slide was functionalised using trimethoxy-(3,3,3-trifluoropropyl)silane (TMTFS). Eight 1 µL drops of 1.1 µm latex beads were placed evenly around the edges of the TMTFS-functionalised slide and allowed to dry to act as spacers. The gel solution was placed onto the CDMVS-functionalised slide and covered with the TMTFS-functionalised slide, before holding in place with a 500 g weight. To separate the slides, they were soaked for 10 minutes in DI water before gently separating the slides with the edge of a spatula. The TMTFS prevented the gel from binding to the top slide, while the CDMVS ensured the gel did not detach from the bottom slide.

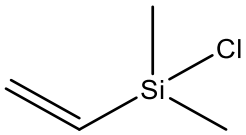

Figure 3.25. The structure of chloro(dimethyl)vinylsilane (CDMVS).

Unlike APTES, CDMVS only has one hydrolysable group and therefore cannot bind in different orientations. This allows for a more uniform monolayer of CDMVS-functionalisation across the surface of the glass (**Figure 3.26**).

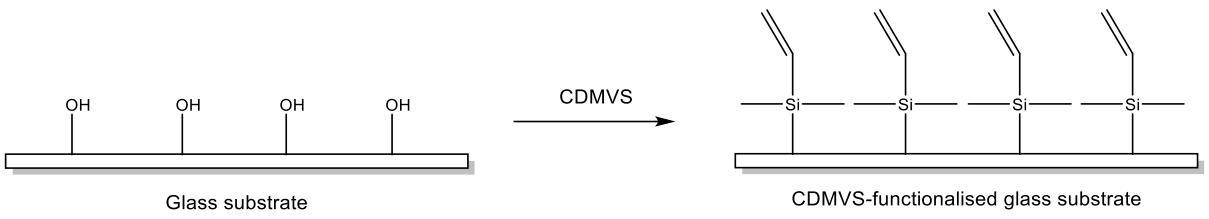

Figure 3.26. Schematic of glass functionalisation with CDMVS.

The adoption of CDMVS allowed these films to bind strongly to the glass substrate while the TMTFS provided a smooth surface at the top of the gel to reduce surface imperfections.

3.2.4.2 Results

Due to the nature of this technique, cast films are thicker than their spin coated counterparts. This is as a result of the size of latex beads used to separate the top and bottom slides, and the weight applied during gelation. Thicker films will have a higher percentage of available functional groups for protein immobilisation but are also more likely to produce multiple modes due to the additional thickness supporting more guided modes.

Characterisation was carried out via glycerol and PEG tests (**Figure 3.27**).

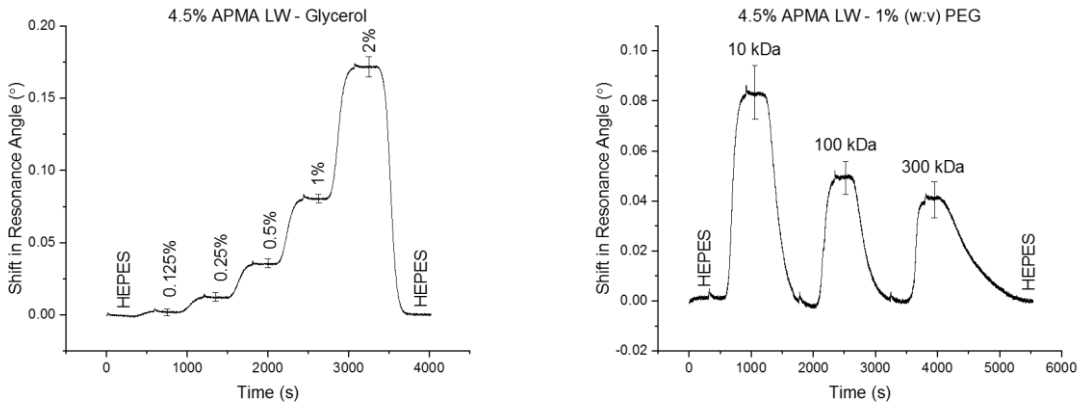

Figure 3.27. Glycerol (left) and PEG (right) runs on 4.5% APMA LW films. Error bars were calculated as 1σ across three different LWs.

The glycerol and PEG data shows a reduced response in comparison to the CS data, with PEG responses between 40 – 60% of the corresponding CS data along with significant error bars caused by device-to-device variability.

In comparison to the theoretical response, the actual responses are severely reduced, while the percentage porosity responses are also much lower than ideal. This is particularly

noticeable at MWs above 10 kDa PEG (**Table 3.6**). This suggests that these films are not porous and may contain too much crosslinking, but reducing the concentration of the polymers used leads to much more flimsy hydrogels, or no gel is formed at all.

Table 3.6. PEG response and percentage porosity of 4.5% APMA LWs.

1% PEG	RI (RIU)	THEORETICAL RESPONSE (°)	ACTUAL RESPONSE (°)	POROSITY (%)	ACTUAL VERSUS 1% CS RESPONSE (%)
10 kDa	1.33790	0.126994	0.070383	55.42	60.46
100 kDa	1.33803	0.142186	0.041621	29.27	35.75
300 kDa	1.33816	0.157378	0.032506	20.65	27.92

With these films, inconsistencies were high due to the hand-casting method of fabrication. Slide casting is explained in more detail in **Chapter 2** (**2.5**), but briefly the method is prone to human error and inconsistencies leading to irreproducible results and a low success rate. This is apparent from the images of some of the APMA films shown below in **Figure 3.28**.

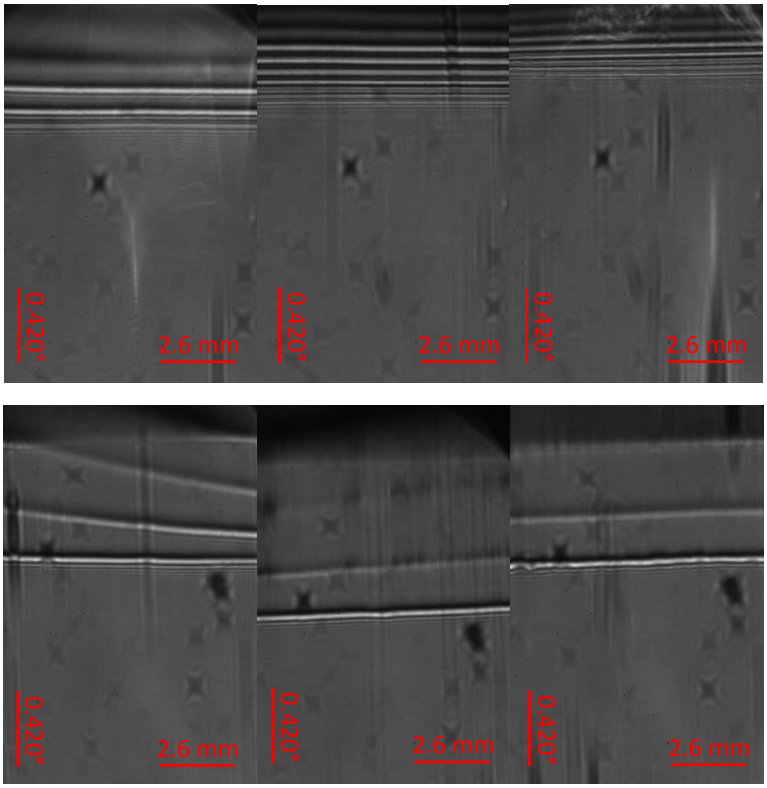

Figure 3.28. A range of different 4.5% APMA LWs, stored wet (top) and dry (bottom). Consistent artifacts visible are due to dust particles on the camera lens.

Slide casting of these films had a success rate of approximately 40%. **Figure 3.28** shows the difference between films that have been stored wet and films stored dry. The wet films typically show multiple dips very close together and are difficult to test. The dry films show much better separation of the dips which aids accurate tracking, while also being advantageous for storage and transportation techniques. This is likely due to the dry films shrinking in structure, allowing for more defined guided modes and a reduction in porosity. Upon rehydration, the structure of the film does not expand to the same degree as a film which is kept permanently wet, leading to dips appearing further down the image which indicates lower porosity.

Despite the dry films providing at least one clear mode each, the position of the mode shifts from device to device and indicates low device-to-device reproducibility. Similar to the

PAAm-Ac films, the APMA films have a lower RIS of 116.86 ± 8.70 °/RIU (**Figure 3.29**). While this suggests they are not as sensitive as the CS films, they do have a significant advantage in that they can be stored dry, and the ratio of available primary amine groups can be tailored.

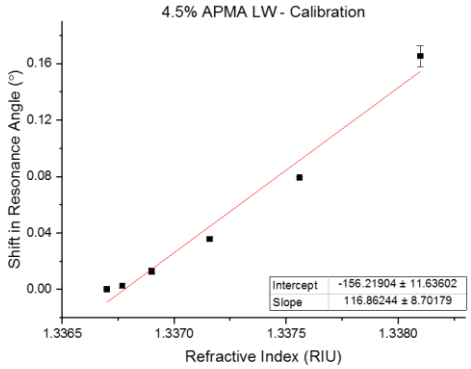

Figure 3.29. Calibration curve for 4.5% APMA LWs. Error bars were calculated as 1σ across three different LWs.

On the other hand, the APMA films have very poor longevity; such films tend to last an average of 5 days regardless of storage options. This makes them less suited than CS for use as a biosensor as they will need replacing so often and cannot be stored in bulk, regardless of the improved dry storage ability. This, combined with the low reproducibility, medium uniformity, and large error bars makes the APMA films less ideal than CS for LW sensing.

3.2.5 4-arm-PEG-NH_2, PEG-NH_2

A 4-arm PEG containing free primary amine groups was crosslinked using genipin. Genipin is a naturally occurring iridoid glycoside crosslinker, commonly extracted as geniposide from the plant *Gardenia jasminoides* Ellis [60]. Reaction of geniposide with β-glucosidase produces genipin. Similar to CS, this has the benefits of being readily available and non-toxic, and has been reported to be significantly less cytotoxic than glutaraldehyde; in

particular, the cytotoxicity is reported to be up to 10,000 times lower than glutaraldehyde in relation to controlled release systems [15, 46, 61]. Additionally, by using genipin as the crosslinker and a synthetic polymer as the backbone it was thought that gels with an even spread of pores and functional groups could be produced rather than using the less reliable glutaraldehyde with chitosan, where the concentration of free amines is not readily known.

The mechanism for how genipin forms crosslinks is not yet fully understood but is expected to occur as in **Figure 3.30**.

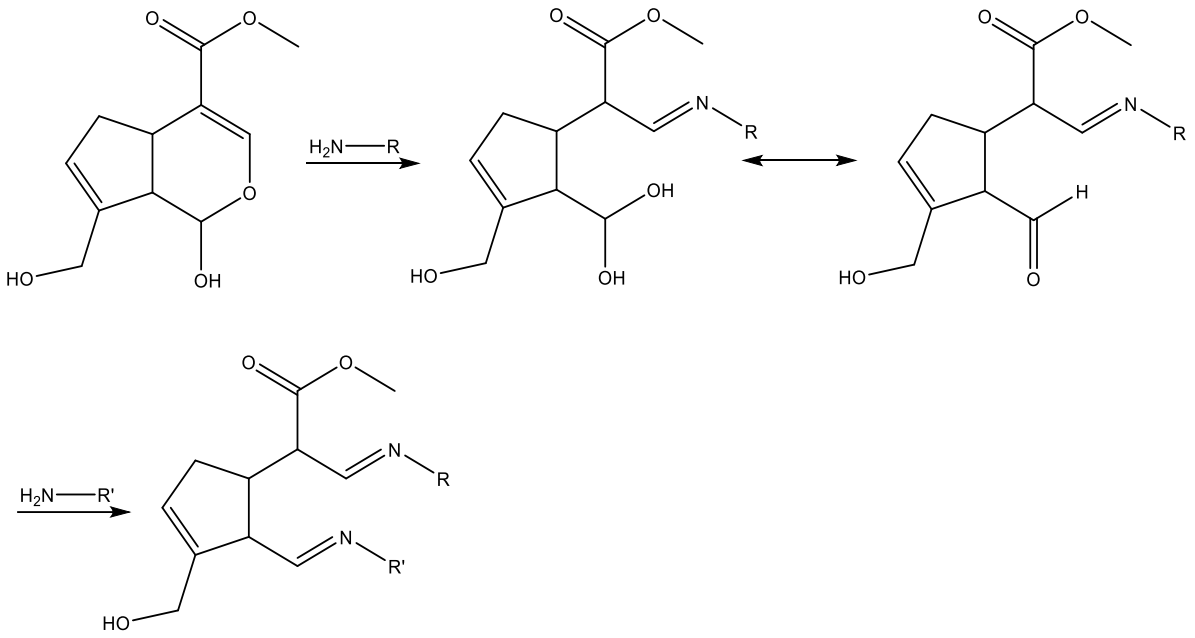

Figure 3.30. Schematic of the proposed method of genipin crosslinking [62].

An amine-initiated nucleophilic ring opening reaction occurs on the olefinic carbon, and the amine is then able to covalently bond to the genipin. A tautomeric aldehyde is formed as an unstable intermediate, which can be attacked by a further primary amine and repeat the covalent bonding to form the crosslink between two monomers [62].

Using 100 mM PBS, pH 7.4, a range of different concentrations of genipin were reacted with 4-arm-PEG-NH_2 (**Figure 3.31**), producing different concentration solutions with 10K-PEG and 20K-PEG.

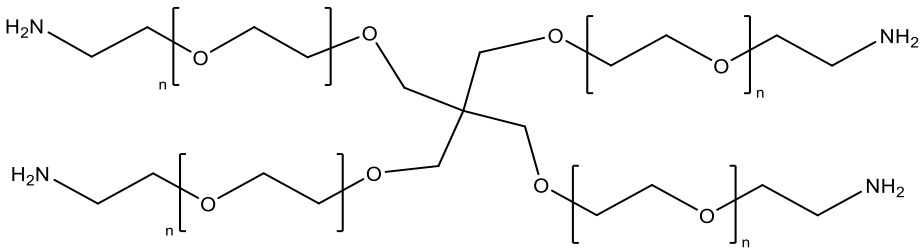

Figure 3.31. The structure of 4-arm-PEG-NH_2.

The solutions slowly turned from clear to dark blue over 20 hours (**Figure 3.32**). This was first performed in microtubes, but most solutions failed to gel. It was next performed in small droplets in petri dishes to allow us to assess the fluidity and rehydration potential of each concentration to narrow down the range suitable for hydrogel films.

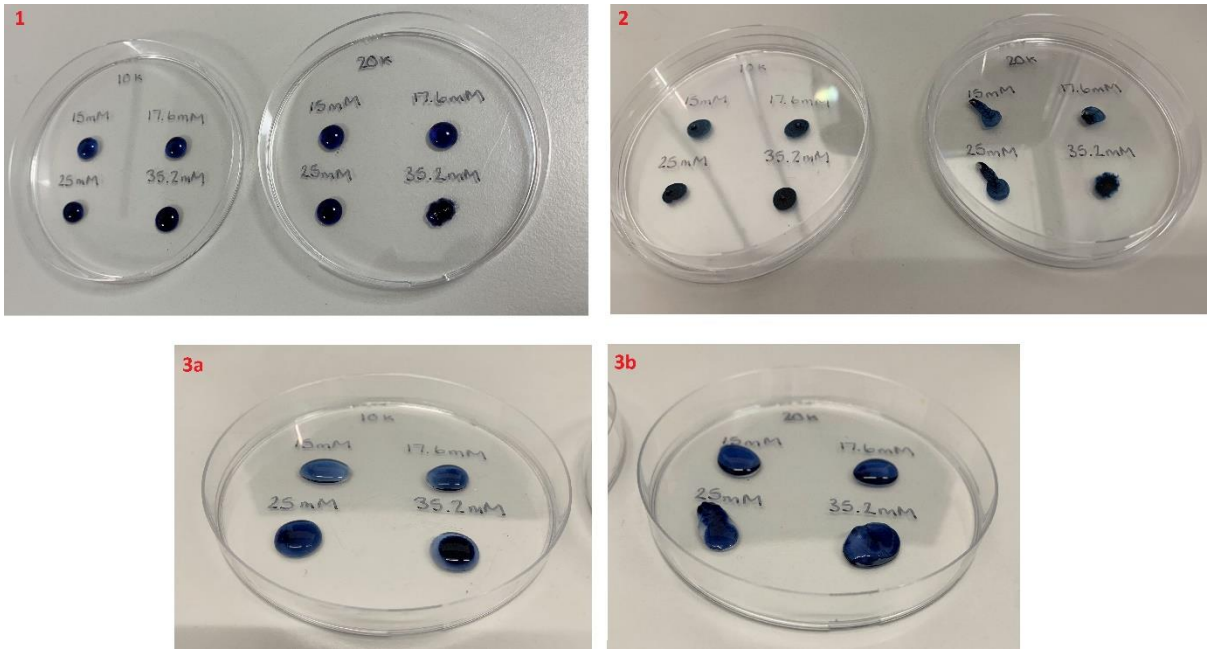

Figure 3.32. PEG-genipin solutions at 15 mM, 17.6 mM, 25 mM and 35.2 mM of genipin. Solutions before drying (1), after drying (2), after rehydrating (3a and 3b).

As we can see in **Figure 3.32**, the 20K-PEG at 35.2 mM of genipin was the only solution which formed a gel prior to dehydration. Upon dehydration all specimens formed dried, flaky films. Upon rehydration, the majority of the films turned back into solution; again, only the 20K-PEG 35.2 mM swelled back up as a gel rather than a solution (**Table 3.7**). Therefore, the 6% 20K-PEG at 35.2 mM genipin was chosen for further studies.

Table 3.7. Concentrations and gelation of 4-arm-PEG-NH_2/Genipin gels.

CONCENTRATION OF 4-ARM-PEG_N-NH_2 (% W:V) N = 10K OR 20K	**CONCENTRATION OF GENIPIN**	**GELLED?**	**REHYDRATED?**
8.3%	15 mM	No	No
8.0%	17.6 mM	No	No
7.2%	25 mM	No	No
6.0%	35.2 mM	Yes (N = 20K)	Yes (N = 20K)

Literature suggests pH 4.5 – 6.0 is optimum for genipin crosslinking, along with a temperature of 60-85 °C [63]. For this reason, 100 mM PBS, pH 5.0 was used to prepare the 6.0% gel reported above. However, the solubility of genipin is subject to conflicting reports, with some sources quoting varied solubility in water, buffer, dimethylsulfoxide (DMSO), and ethanol [64-66]. At pH 5.0 the genipin would not dissolve despite stirring overnight, in contrast to at pH 7.4. The suspension was heated to 50 °C with continuous stirring and the genipin slowly dissolved.

The genipin solution was mixed with the PEG solution to produce the gelation solution; this was then heated at 50 °C with continuous stirring for between 50 minutes – 24 hours. The hot solution was spin coated at 800-1500 rpm, 100 rpm/s, 30-60 s, and the films were left to dry overnight. All solutions produced patchy films, and due to the difficulties in producing

consistent and uniform films these gels were not investigated any further but may hold potential for future research (**Figure 3.33**).

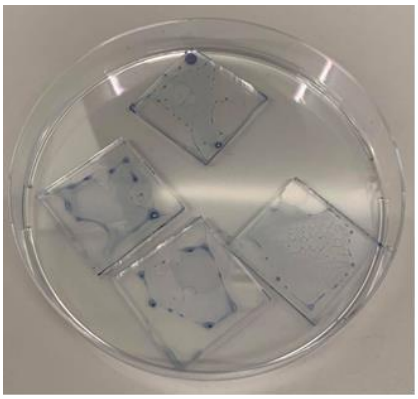

Figure 3.33. Spin coated PEG-NH_2/Genipin gels showing the distinctive blue colour of genipin and the patchy film formation.

It is thought that functionalising the glass, along with optimising the gelation times, would improve film uniformity. Certainly, the lengthy gelation times are not ideal when compared to the much quicker gelation that can be achieved using crosslinkers such as glutaraldehyde, and hence the chitosan and glutaraldehyde combination produces superior results to the genipin.

3.2.6 PEG-thiol and PEG-maleimide, SH:MAL 4- or 2-arm

The Michael-addition reaction between maleimides and thiols produces a stable, uncleavable thioether bond [67]. The reaction is often referred to as a click-chemistry reaction, owing to the extremely simple reaction conditions. These reactions can be carried out in a polar solvent such as water, buffer or DMSO with no initiators or catalysts required. The structure of the maleimide is well-suited to the reaction, with the two electron-withdrawing carbonyl groups present in the cis-conformation in the ring, along with the strain introduced by the double bond also within the ring. Both of these factors contribute towards

the high reactivity to the thiolate ion, which is readily produced when present with the maleimide and a polar solvent [68].

This is ideal for waveguide gels, as it suggests the gel structure formed will be strong and irreversible regardless of the conditions applied later. The reaction is well-known to proceed quickly between pH 6.5-7.5 [69], and gelation speed can be slowed down by reducing the pH to allow for easier processing.

A selection of long chain PEG-maleimide and PEG-thiols were procured. These were: 4-arm-$PEG_{40,000}$-maleimide (4-MAL), 2-arm-$PEG_{20,000}$-maleimide (2-MAL), 4-arm-$PEG_{20,000}$-thiol (4-SH), 2-arm-$PEG_{20,000}$-thiol (2-SH). High MWs were selected to enhance porosity and reduce steric hinderance during polymerisation (**Figure 3.34**). These compounds were tested in various conformations, either 4-arm:4-arm or 4-arm:2-arm, and at ratios including 1:1, 1.25:1, 1.5:1, 2:1.

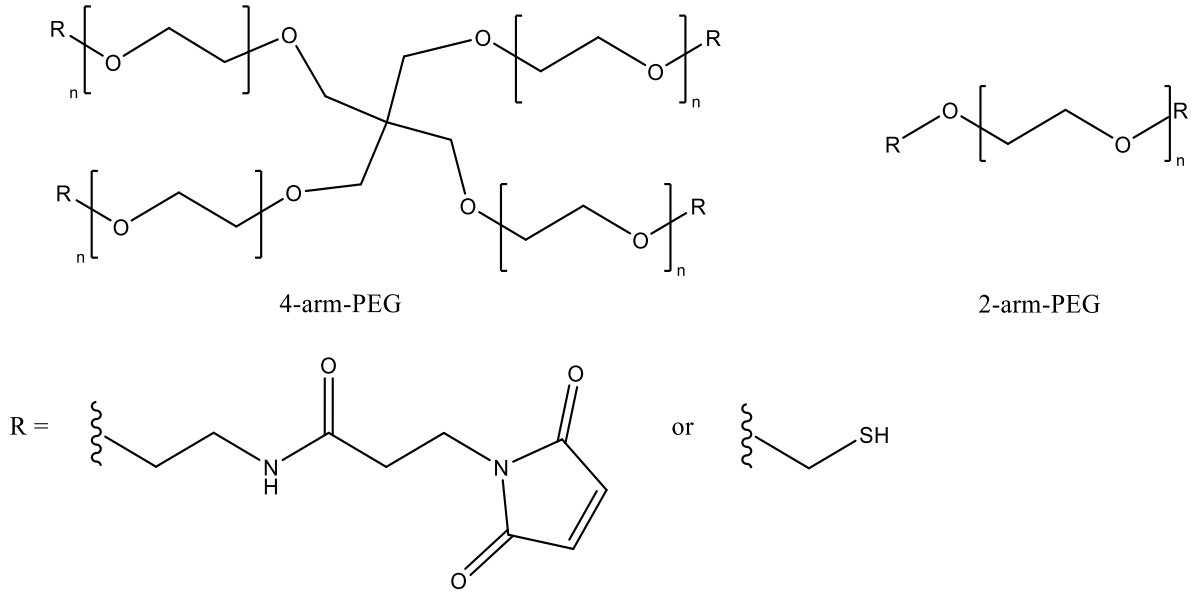

Figure 3.34. The structures of the 4- and 2-arm PEGs with maleimide or thiol R groups.

To ensure gelation would occur, the monomers were initially reacted as pot gels at a 1:1 molar ratio, forming optically clear gels in a matter of seconds in 100 mM PBS, pH 7.4. To reduce the rate of reaction, the polymerisation was carried out in microtubes at pH 4.5 and pH 5.0 PBS. At pH 4.5, the reaction took approximately 30 minutes, while the pH 5.0 reaction began visible gelation at 9 minutes. For this reason, pH 5.0 was selected as it gave enough time to spin coat the gel without excessive and unnecessary waiting times.

3.2.6.1 Glass functionalisation

Firstly, glass slides were cleaned *via* plasma cleaning to ensure the surface was clean. To ensure strong adhesion of the film to the glass slide, (3-mercaptopropyl)trimethoxysilane (MPTMS) was chosen as a glass functionalisation agent (**Figure 3.35**).

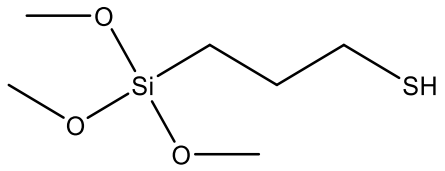

Figure 3.35. The structure of (3-mercaptopropyl)trimethoxysilane (MPTMS).

As a trimethoxysilane, MPTMS is subject to the same problems as APTES discussed in **Section 3.2.3.1**, thus it was important to optimise the functionalisation method. There is no single agreed method for MPTMS-functionalisation in the literature, therefore different reported methods were attempted and modified into a final method based on the results [70, 71]. Working with thiols themselves is a challenge as they are able to self-react and produce disulfide bonds; tris(2-carboxyethyl)phosphine (TCEP) was employed to ensure any disulfide bonds were reduced back to thiols and free for reaction with the PEGs.

By plasma cleaning the slides first we ensured the environment was as clean as we could achieve. As MPTMS is moisture reactive, the functionalisation was carried out within a nitrogen-filled glove box, further increasing the cleanliness of the procedure.

3.2.6.2 Results

Films were fabricated at 1.5:1, 1.25:1 and 1:1 molar ratios depending on the free functional groups desired and which PEG was used. Of these, only 4-SH:4-MAL at a 1:1.5 ratio is reported and tested as the other combinations did not form uniform gels when spin coated (**Figure 3.36**). This ratio produced a hydrogel network with free maleimide groups.

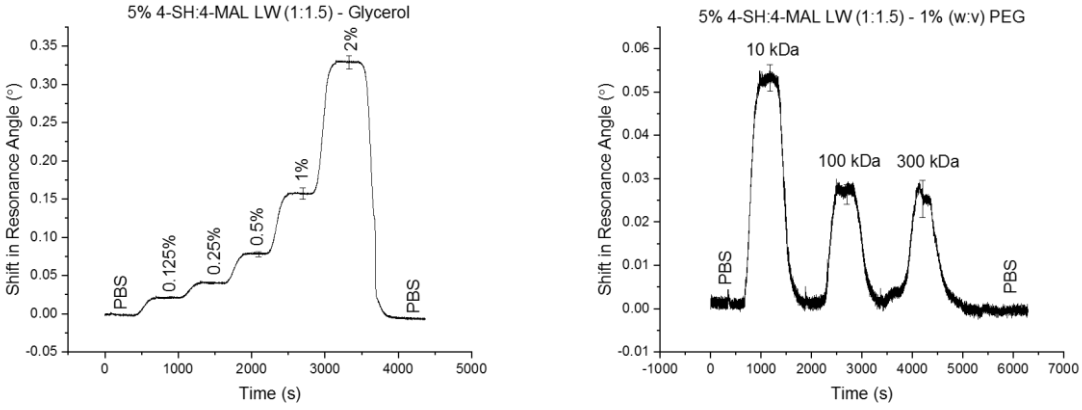

Figure 3.36. Glycerol (left) and PEG (right) runs on a 5% 4-SH:4-MAL LW film (1:1.5). Error bars were calculated as 1σ across the width of one LW.

As can be seen, these films were not porous as their response to 10 kDa PEG is approximately half that of CS. This is disappointing as the porosity was expected to be higher due to the long PEG chains. It is possible that the long chains have instead hindered the porosity by folding into orientations in which the pores are in fact not open.

This is further proven by the very low percentage porosity determined using the glycerol RIS (**Table 3.8**). The porosity to 10 kDa PEG is less than half of the theoretical, with 100 kDa and 300 kDa giving an extremely poor response. In comparison to the theoretical

values for CS, these films would be expected to have upwards of 75% the porosity of CS, but this is clearly not the case.

Table 3.8. PEG response and percentage porosity of 5% 4-SH:4-MAL (1:1.5) LWs.

1% PEG	RI (RIU)	THEORETICAL RESPONSE (°)	ACTUAL RESPONSE (°)	POROSITY (%)	ACTUAL VERSUS 1% CS RESPONSE (%)
10 kDa	1.33655	0.131055	0.053014	40.45	45.54
100 kDa	1.33668	0.146185	0.027155	18.57	23.33
300 kDa	1.33678	0.157824	0.025147	15.93	21.60

The RIS is also lower at 116.39 ± 3.80 °/RIU (**Figure 3.37**). This suggests that these films are not as responsive to small changes in RI as CS which is expected due to the low porosity. This drop in sensitivity and porosity compared to the CS films indicates that these 4-SH:4-MAL (1:1.5) films are not going to be useful for use as LWs as the analytes will not be able to diffuse in and out of the pores and the films will not react to small changes in RI.

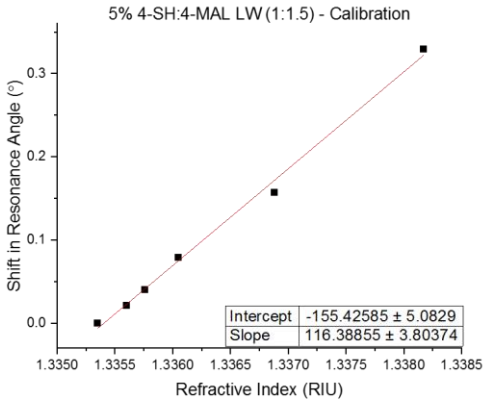

Figure 3.37. Calibration curve for a 5% 4-SH:4-MAL LW (1:1.5).

The uniformity of these films is also poor, with **Figure 3.38** showing a typical output. Between one and two modes were seen, neither of which were uniform, which shows that the spin coating method has not been as successful as hoped. This may be due to the speed

of the polymerisation, or uneven glass functionalisation. Compared to the 1% CS LWs, reproducibility and uniformity of these films are classes as “low”.

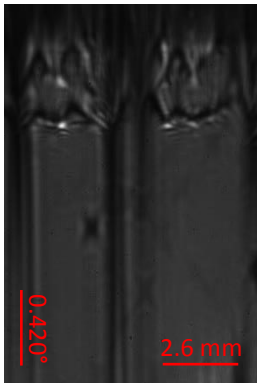

Figure 3.38. Output image of a 5% 4-SH:4-MAL LW (1:1.5) under a 2-channel flow cell.

3.2.6.3 Thiol availability

In parallel, thick 4-SH:2-MAL (1:1) films were cast and tested for thiol availability. To do this, a concentration curve was prepared of fluoresceinamine absorbance *via* ultraviolet-visible (UV-Vis) spectroscopy (**Figure 3.39**).

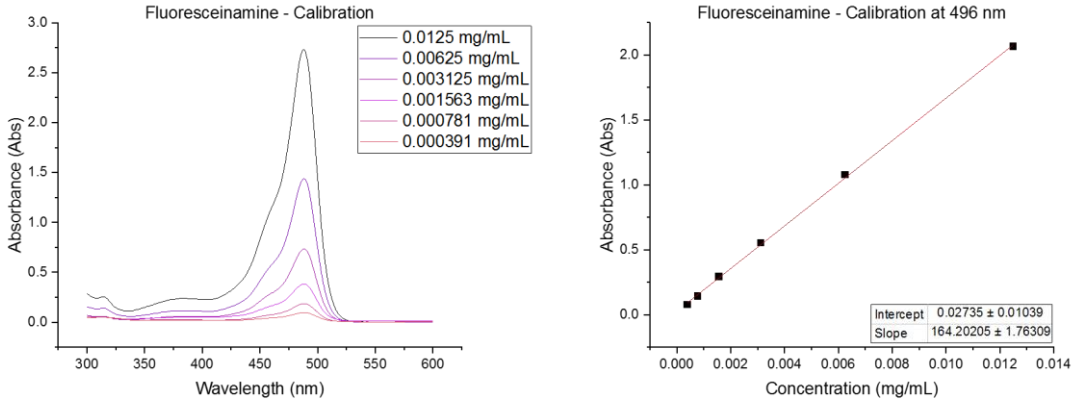

Figure 3.39. UV-Vis calibration curves for fluoresceinamine solutions prepared in 100 mM PBS, pH 7.4.

The films were prepared via a modified form of slide casting. A plastic holder was prepared which sandwiched an MPTMS-functionalised glass slide between two poly(methyl methacrylate (PMMA) sheets, with a thin spacer placed on top of the slide to produce a 100

μm gap. The polymer solution is then injected into the cavity and allowed to gel, before dismantling the holder. The films are then allowed to hydrate in 100 mM PBS, pH 7.4 for 18 h. The swollen circular regions visible in **Figure 3.40** are due to the inlet and outlet holes for the gel solution, which led to additional gelling in these regions.

These films were then reacted with NHS-PEG$_3$-maleimide for 20 minutes, which was expected to react with the free thiols and produce free NHS groups for further functionalisation. This produced no visible change in the films. 0.1 mg/mL fluoresceinamine was used to stain the films for 3 h, producing bright yellow films. Films were then soaked in PBS for 1 hour, after which it is apparent that much of the fluoresceinamine has leeched from the gel and was not chemically bound. After a total of 18 h in PBS the films had returned to their optically clear state (**Figure 3.40**).

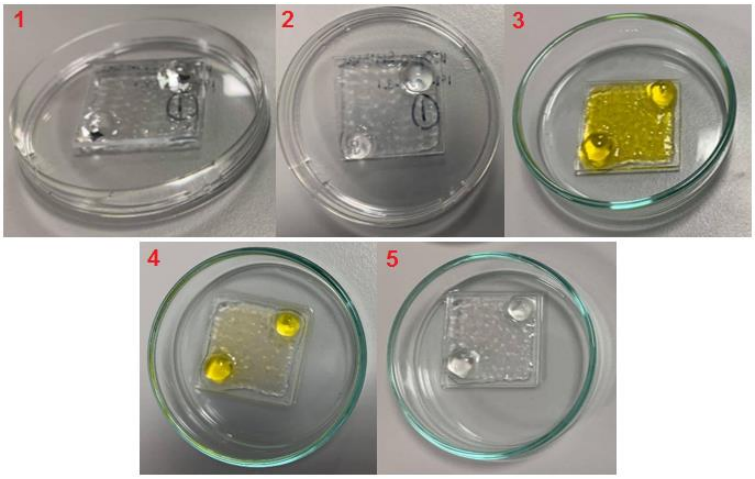

Figure 3.40. A cast 5% 4-SH:2-MAL LW (1:1). 1) After fabrication. 2) After reacting with NHS-PEG$_3$-maleimide. 3) Immediately after staining with fluoresceinamine (0.1 mg/mL). 4) After washing in 100 mM PBS, pH 7.4 for 1 h. 5) After washing in PBS for 18 h.

This suggested that the fluoresceinamine was not able to bind to the film, which in turn implies that the NHS-PEG$_3$-maleimide did not bind. This may be due to a lack of free thiols in the film; while the gels were expected to contain free thiols due to the ratio of

maleimide:thiol used, it is possible the structure of the film is blocking the free thiols, or that the thiols have reacted together and by the time of staining there were no longer any free thiols remaining.

UV-Vis was performed on the gels at each stage; by 25 h the response of the film was very similar to that of the unreacted film (**Figure 3.41**). While there may still be a small amount of fluoresceinamine within the gel matrix it is unlikely that it is bound to the film, and therefore it does not appear as though the fluoresceinamine staining was successful.

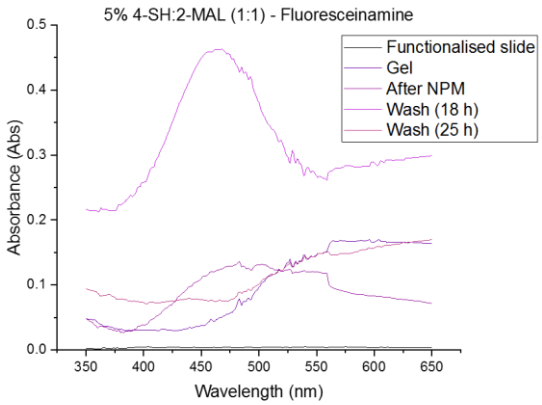

Figure 3.41. UV-Vis of the 5% 4-SH:2-MAL LW (1:1) treated with fluoresceinamine at various stages of washing.

As it was not clear whether the functionalisation had failed at the NHS-PEG_3-maleimide or the fluoresceinamine stage, fresh films were prepared and subsequently stained with 1 mM N-(5-Fluoresceinyl)maleimide (F5M) for 2 h and left in DI water, changing two times per day. This should be able to react directly with the thiols in the film, and is again suitable to track *via* UV-Vis. A concentration curve was prepared for F5M at 494 nm (**Figure 3.42**).

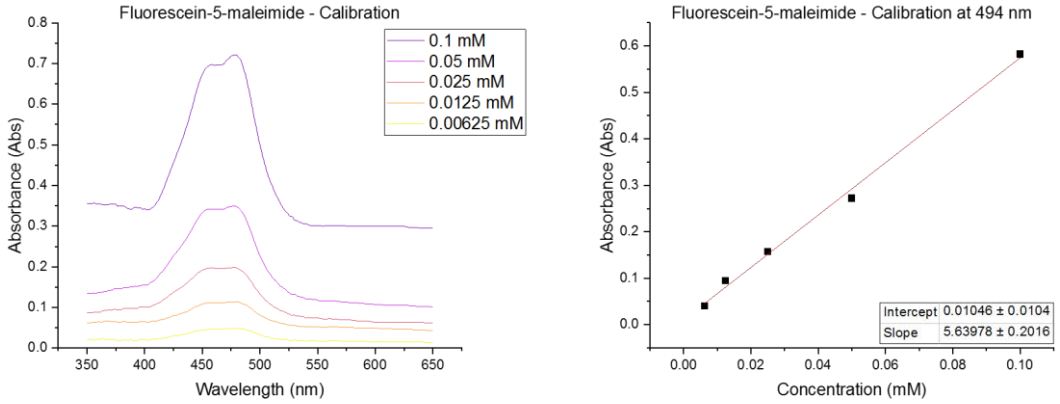

Figure 3.42. UV-Vis calibration curves for fluorescein-5-maleimide solutions prepared in DI water.

This calibration curve was subsequently used to help interrogate F5M-stained gels (**Figure 3.43**). Upon staining films immediately after fabrication, a consistent absorbance was recorded around 0.5 even after multiple days of washing. This indicates that the F5M has bound at a concentration of approximately 0.9 mM, indicating that there are free thiols available in this hydrogel.

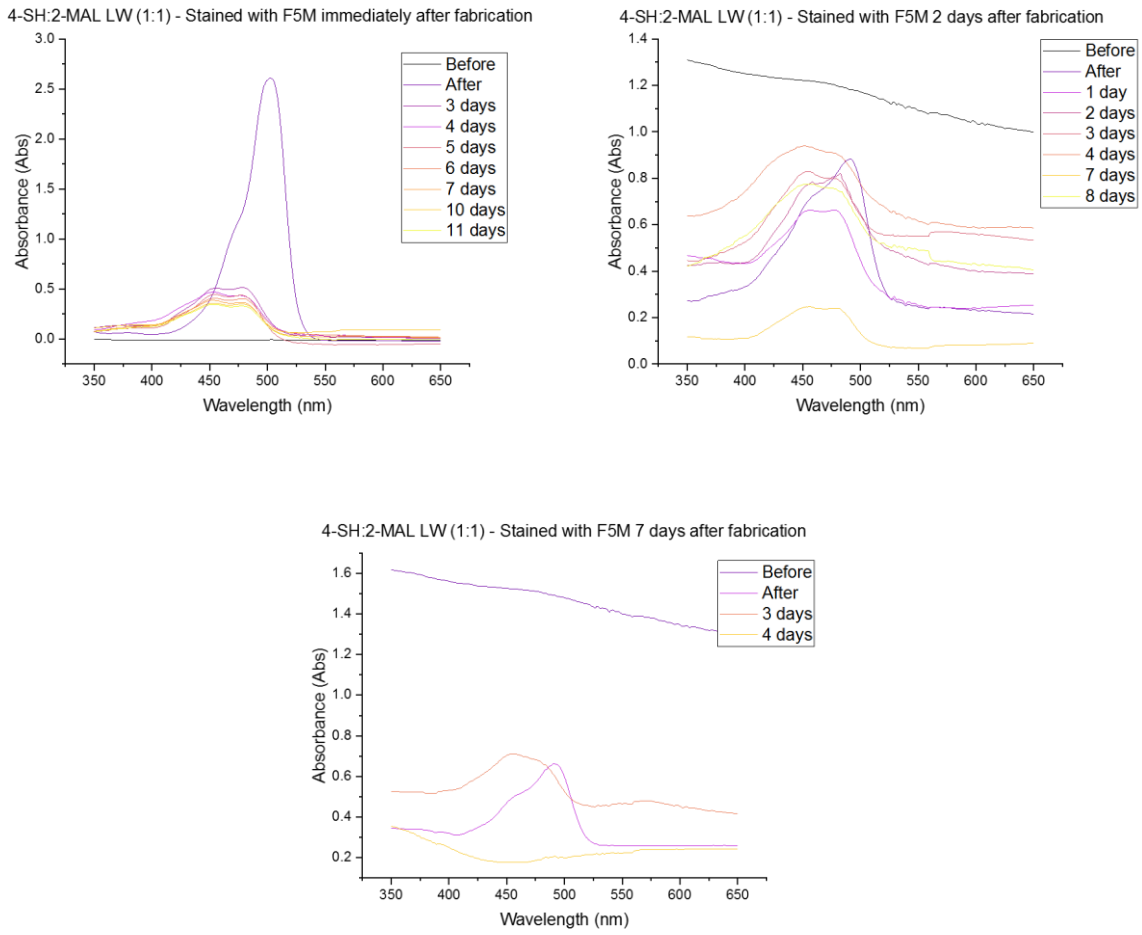

Figure 3.43. UV-Vis of 5% 4-SH:2-MAL LWs (1:1) treated with F5M at different lengths of time since fabrication and at various stages of washing.

There is a definite decrease in F5M binding when films are left longer between fabrication and staining. This implies that the availability of the free thiol groups decreases with time, either due to thiol-thiol bonding or another form of film degradation. Therefore, it is important to use these films as soon as possible after fabrication, making them unsuitable for long-term storage.

It should also be noted that the "before" line in the top left graph in **Figure 3.43** has been recorded on a wet film due to this hydrogel having just been fabricated. Meanwhile, the films were not rehydrated at 2 and 7 days immediately before staining with F5M, leading to

the “before” response of these films being recorded on dried films. This led to optical scattering of the light and produced the high responses.

Also attempted was treating the films with TCEP solution, which should reduce any thiol-thiol bonds and reform the free thiol groups. Unfortunately, this led to visible damage of the films and was therefore not explored further.

3.2.6.4 Porosity

To try and improve the porosity of these gels, two methods were employed. Firstly, gels were made using 5% glycerol as a porogen. In this case, films were prepared with excess thiols. As shown in **Figure 3.44**, the addition of glycerol had the opposite effect than expected.

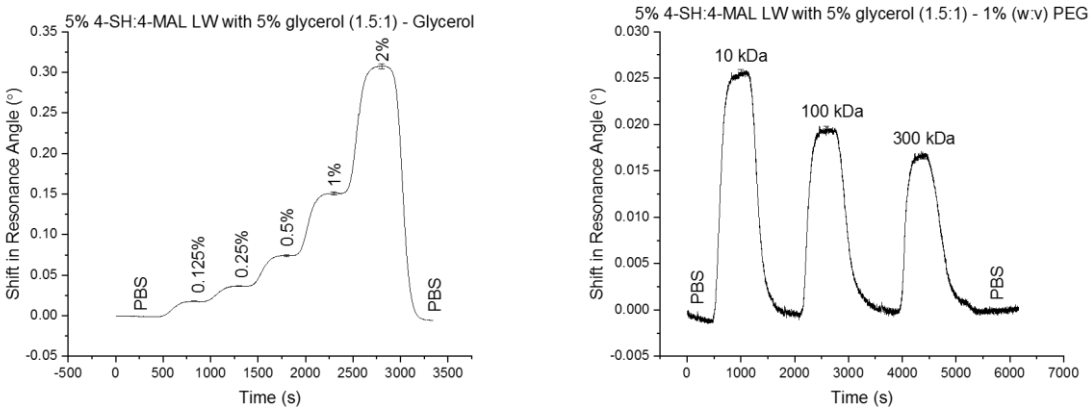

Figure 3.44. Glycerol (left) and PEG (right) runs on a 5% 4-SH:4-MAL LW film with 5% glycerol (1.5:1). Error bars were calculated as 1σ across the width of one LW.

While the addition of glycerol was expected to improve the porosity, these films have a significantly lower response to the PEGs compared to the non-glycerol containing films. The glycerol molecules may be trapped within the hydrogel structure leading to a reduced response to the PEG molecules which are then blocked from entering. The response of this film to 10 kDa PEG is only ~50% of the response seen in the non-glycerol containing film.

In line with the reduced experimental porosity, the percentage porosity is even lower than that seen for the 5% 4-SH:4-MAL (1:1.5) LWs (**Table 3.9**). Overall, this very low porosity signifies that these films are not porous enough to allow larger analytes in for detection and will therefore have limited use as a sensor.

Table 3.9. PEG response and percentage porosity of 5% 4-SH:4-MAL LWs with 5% glycerol (1.5:1).

1% PEG	RI (RIU)	THEORETICAL RESPONSE (°)	ACTUAL RESPONSE (°)	POROSITY (%)	ACTUAL VERSUS 1% CS RESPONSE (%)
10 kDa	1.33655	0.114819	0.025367	22.09	21.79
100 kDa	1.33668	0.129024	0.019289	14.95	16.57
300 kDa	1.33678	0.139951	0.016614	11.87	14.27

The RIS is also slightly lower than the LW without glycerol, at 109.27 ± 2.99 °/RIU (**Figure 3.45**). This along with the poor porosity suggests that the glycerol is hindering the formation of pores in the structure.

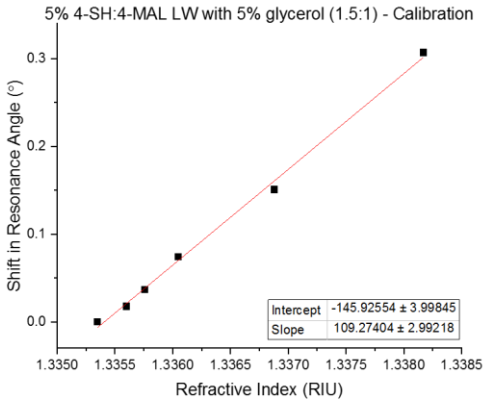

Figure 3.45. Calibration curve for a 5% 4-SH:4-MAL LW film with 5% glycerol (1.5:1).

However, the glycerol did encourage more uniform film formation, with a range of these films shown in **Figure 3.46**.

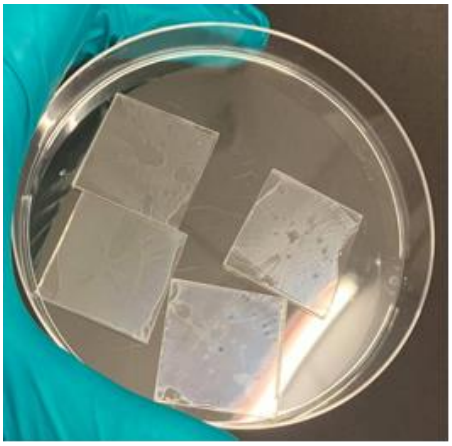

Figure 3.46. Spin coated 5% 4-SH:4-MAL LW films with 5% glycerol (1.5:1).

The films are notably covering a good proportion of the glass slide but are visibly patchy and not ideal for a uniform and reproducible response. The films are also slightly cloudy, which is only visible when the gels are dry. Yet, when placed on the instrument there are clearly defined and uniform modes which are significantly improved in comparison to the LW without glycerol (**Figure 3.47**).

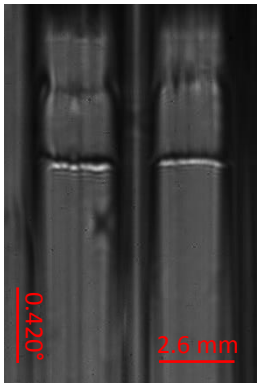

Figure 3.47. Output image of a 5% 4-SH:4-MAL LW with 5% glycerol (1.5:1) under a 2-channel flow cell.

The next attempt used 5% bovine serum albumin (BSA); BSA is a large biomolecule with a MW of ~66.5 kDa. The idea behind this was to form the gel around the large BSA molecules and use trypsin, a digestive enzyme, to digest the BSA and leave larger cavities.

Figure 3.48 shows the output of the films with BSA. The modes are more defined than in the plain 4-SH:4-MAL films but not quite as uniform as the glycerol films. Again, these films are visibly cloudy when dry.

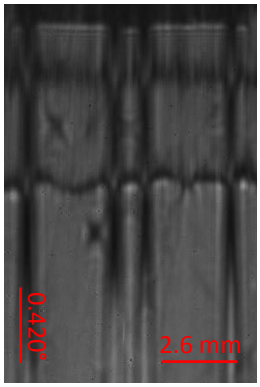

Figure 3.48. Output image of a 5% 4-SH:4-MAL LW with 5% BSA (1.5:1) under a 2-channel flow cell.

These films showed two modes rather than one, with the top mode providing the highest response to PEG (**Figure 3.49**). This PEG response was lower than the CS LWs, but higher than the LW without BSA or glycerol. The response to 10 kDa PEG was 117.39% that of the non-BSA/glycerol containing films, and 53.46% of the CS LWs. In terms of uniformity these films are categorised as “medium”.

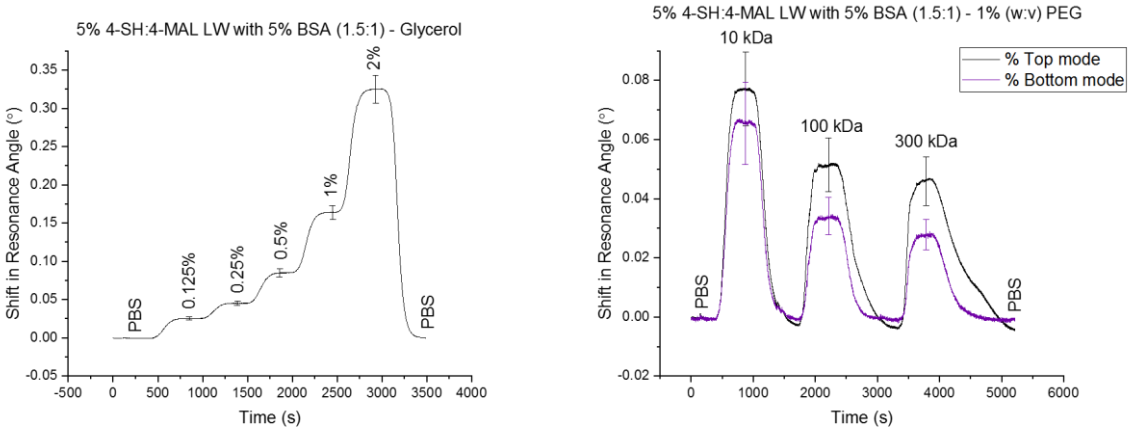

Figure 3.49. Glycerol (left) and PEG (right) runs on 5% 4-SH:4-MAL LW films with 5% BSA (1.5:1). Error bars were calculated as 1σ across three different LWs.

Again, the actual response compared to the theoretical response is extremely low, giving a percentage porosity of undesirable values (**Table 3.10**).

Table 3.10. PEG response and percentage porosity of 5% 4-SH:4-MAL LWs with 5% BSA (1.5:1).

1% PEG	RI (RIU)	THEORETICAL RESPONSE (°)	ACTUAL RESPONSE (°)	POROSITY (%)	ACTUAL VERSUS 1% CS RESPONSE (%)
10 kDa	1.33655	0.258696	0.062234	24.06	53.46
100 kDa	1.33668	0.288415	0.043387	15.04	37.27
300 kDa	1.33678	0.311276	0.042550	13.67	36.55

The calibration data showed an impressive RIS at 228.61 ± 10.20 °/RIU, an improvement over the RIS values obtained for the other iterations of 4-SH:4-MAL films (**Figure 3.50**).

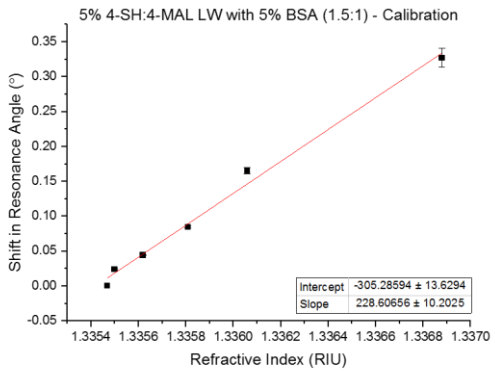

Figure 3.50. Calibration curve for 5% 4-SH:4-MAL LW films with 5% BSA (1.5:1). Error bars were calculated as 1σ across three different LWs

To test whether the BSA was removable, a solution of 0.25% (v:v) trypsin-ethylenediaminetetraacetic acid (trypsin-EDTA) was reacted with the LW for 1 h at 37 °C (**Figure 3.51**). To achieve this temperature a water bath was used, and the solutions were constantly heated on a hot plate throughout.

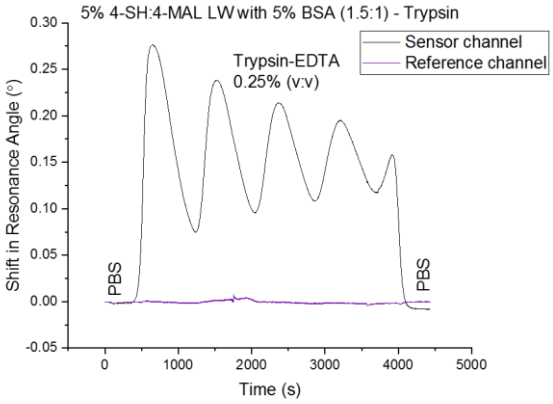

Figure 3.51. A 5% 4-SH:4-MAL LW with 5% BSA (1.5:1) treated with 0.25% (v:v) trypsin solution at 37 °C.

There was an overall negative shift in resonance angle in the sensor channel after 1 h. This was promising, but it was not yet clear whether the increased temperature had affected the film. To see whether the films were reactive after this a solution of 0.4 mg/mL biotin-PEG_6-maleimide (BPM) was applied (**Figure 3.52**). The maleimide should be able to react with the free thiols in the film and leave free biotin groups, which will be able to react with streptavidin.

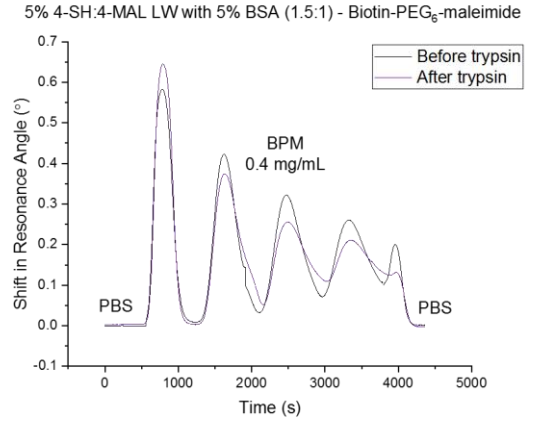

Figure 3.52. A 5% 4-SH:4-MAL LW with 5% BSA (1.5:1) treated with 0.4 mg/mL Biotin-PEG_6-maleimide before and after treatment with trypsin.

For this, BPM was applied to the film before and after treating with trypsin. As seen in **Figure 3.52** there is no overall difference in resonance angle between the two, nor is there a difference from start to end of each run. This implies that the BPM is not binding to the film,

which suggests that there are either no free thiol groups available for binding, either due to internal thiol-thiol binding or blocking of the thiol groups by the BSA and/or a crosslinked hydrogel network preventing the BPM from reaching them.

To check if this was the case, a LW containing 5% BSA was tested with BPM and streptavidin before treating with trypsin. In the other channel, the film was treated with trypsin before BPM and streptavidin (**Figure 3.53**).

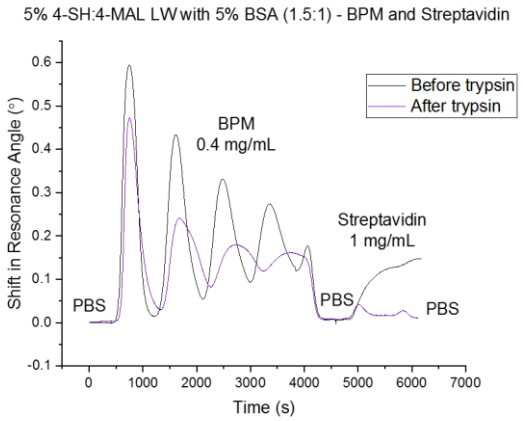

Figure 3.53. A 5% 4-SH:4-MAL LW with 5% BSA (1.5:1) treated with 0.4 mg/mL Biotin-PEG_6-maleimide and 1 mg/mL streptavidin before and after treatment with trypsin.

Interestingly the channel that was reacted with BPM before trypsin showed a good amount of binding with streptavidin, indicating that the film does have free thiol groups despite there being no visible binding with BPM. It is also possible that the streptavidin is not binding to the BPM, but instead adsorbing to the BSA.

Conversely the channel treated with trypsin followed by BPM and streptavidin showed almost no binding for streptavidin. We can therefore assume that the trypsin treatment damages the film and prevents streptavidin binding and is therefore not an ideal solution.

Finally, the glycerol and BSA steps were combined. 2.5% (v:v) glycerol was chosen to encourage uniform film formation, while 5% (w:v) BSA was selected to form the cavities. This resulted in a three-moded film with very poor uniformity and only the lowest mode could be tracked (**Figure 3.54**). This poor uniformity and jagged mode output shows that the hydrogel structure struggles to guide a mode evenly. This is attributed to uneven polymerisation, potentially impacted by the presence of glycerol and BSA which could block the reactive groups in some regions, while the multi-mode output is due to the film being too thick and guiding multiple modes. Another potential cause is uneven mixing of the polymerisation solution before spin coating leading to polymerisation in localised regions. When compared to the success criteria, both reproducibility and uniformity are low.

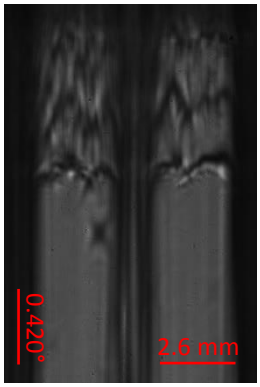

Figure 3.54. Output image of a 5% 4-SH:4-MAL LW with 5% BSA and 2.5% glycerol (1.5:1) under a 2-channel flow cell.

The PEG data showed that these films had slightly higher porosity than the 5% glycerol film (118.45% response to 10 kDa PEG), but much lower than the 5% BSA film (48.28% response to 10 kDa PEG) (**Figure 3.55**).

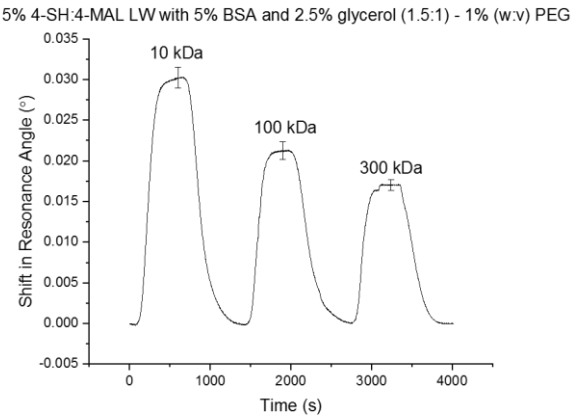

Figure 3.55. PEG run on a 5% 4-SH:4-MAL LW film with 5% BSA and 2.5% glycerol (1.5:1). Error bars were calculated as 1σ across the width of one LW.

When developing these PEG-based hydrogels it is important to consider the polymerisation mechanism. Such films are formed *via* step-growth polymerisation, in which the PEG chains containing two or more functional groups react together to form the network and no initiator is required. In an ideal scenario this would lead to films with evenly spaced pores and predictable free groups. However, network defects are common and cannot be controlled, such as permanent entanglements and loops produced within the crosslinking structures [72]. Such defects can disrupt the matrix and lead to the lack of reactivity seen in these films.

Literature shows that polymers produced *via* step-growth polymerisation are typically more homogeneous than those formed *via* chain-growth polymerisation, which produce much more random and uncontrolled structures [73]. Variation of monomer chain length and concentration will affect the final structure of the hydrogel. PEGs of higher MW and lower concentrations should produce the most porous hydrogels in comparison to those of lower MW and high concentration. This is due to the crosslinking network formed between the monomers, with longer chain lengths allowing for greater spacing between the crosslinks and

a lower concentration contributing to less crosslinking. However, longer chains increase the risk of looping and entanglement, both of which can drastically reduce the porosity of the films and block any remaining functional groups.

In regard to using a passive porogen such as glycerol or BSA, there are further problems introduced. The pores created by such porogens are often isolated with a lack of pore-to-pore interconnectivity within the hydrogel network [5]. A passive porogen allows the hydrogel to form directly around the porogen molecule but does not initiate the formation of linked pores. In this case there is no link between the pores and larger molecules will struggle to reach the pores.

Overall, due to the lack of reproducibility, poor uniformity and poor porosity, these films were not investigated as sensors any further. It is suggested that further work could be carried out using the same functional groups on different MW PEGs to assess the impact of this on the results.

3.2.7 4-arm-$PEG_{20,000}$-aldehyde and 4-arm-PEG_{2000}-hydrazide, 4-CHO:4-HZ

Similarly to the thiol:maleimide, aldehyde and hydrazide reactions are simple and quick, forming a hydrazone bond. Using a 4-arm-PEG_{2000}-hydrazide (4-HZ) and a 4-arm-$PEG_{20,000}$-aldehyde (4-CHO), strongly crosslinked gels were formed (**Figure 3.56**). This reaction is known to work best at pH 5-7 [74], therefore reducing the pH allowed the reaction to occur more slowly and provide time for sample preparation. Using a 100 mM sodium acetate buffer, pH 4.0, allowed for gel formation in approximately 2 minutes, an ideal length of time to allow for sample mixing and spin coating.

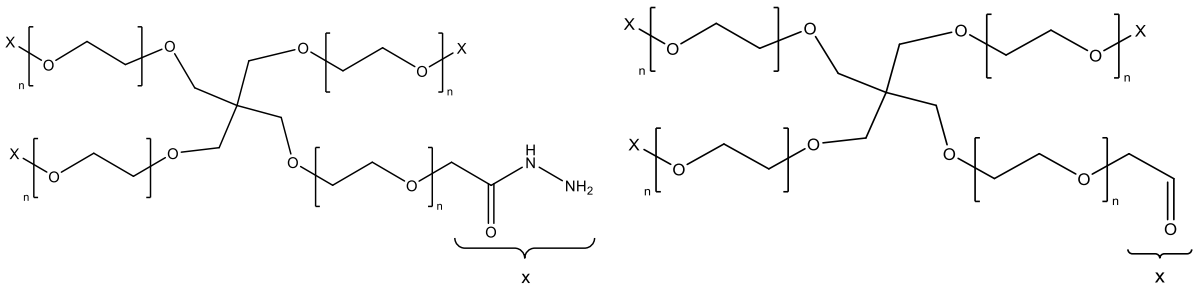

Figure 3.56. The structures of 4-arm-PEG-HZ (left) and 4-arm-PEG-CHO (right).

Films were fabricated at 1.5:1 and 1.25:1 molar ratios and could be tailored to provide either free aldehyde or free hydrazide groups depending on the free functional groups desired. These films were suitable to be stored dry and could be rehydrated in an appropriate buffer solution before testing.

3.2.7.1 Glass functionalisation

Gels were initially formed on untreated clean glass slides but were observed to detach from the glass when treated with buffer, hence different functionalisation agents were used to improve gel adhesion. As seen in **Figure 3.57**, the 5% 4-CHO:4-HZ (1:1) films are cloudy and have produced an uneven pattern on the glass slide. After applying a two-channel flow cell and treating with buffer for 10 minutes, the film has detached from the slide in this region and been washed away by the pump.

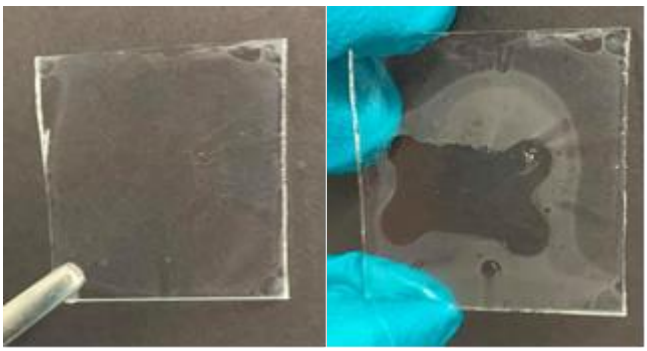

Figure 3.57. Spin coated 4-CHO:4:HZ LW films before (left) and after (right) application of a flow cell and 100 mM PBS, pH 7.4.

To improve the adhesion, CDMVS and APTES were both tested. APTES produced superior results, leading to a much stronger bonding of the film to the glass slide, and was used moving forwards.

3.2.7.2 Results

Reported below are two different films; 4-CHO:4-HZ films at a 1:1.5 ratio, affording free hydrazide groups, and 4-CHO:4-HZ films at a 2:1 ratio, affording free aldehyde groups. Both aldehyde and hydrazide groups could be used for further functionalisation, therefore at this stage both were tested to see which produced the best results.

Before these films could be tested, they had to be rehydrated for a minimum of five days. This allowed the films to fully rehydrate and produce clear and easily trackable dips in reflectivity (**Figure 3.58**). This was also useful as it proved that while these films cannot be used dry, they can be stored dry and rehydrated in the future.

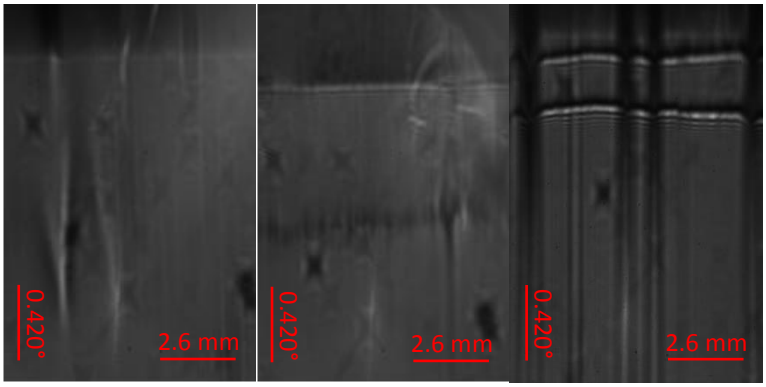

Figure 3.58. Output images of a 5% 4-CHO:4-HZ (1:1.5) film immediately after fabrication (left), 24 hours after rehydration (middle), and 5 days after rehydration (right).

The 4-CHO:4-HZ at 1:1.5 produced a double-moded film, with the lower mode giving a fairly non-porous response, and the top mode providing a reasonable porosity when compared to CS (**Figure 3.59**).

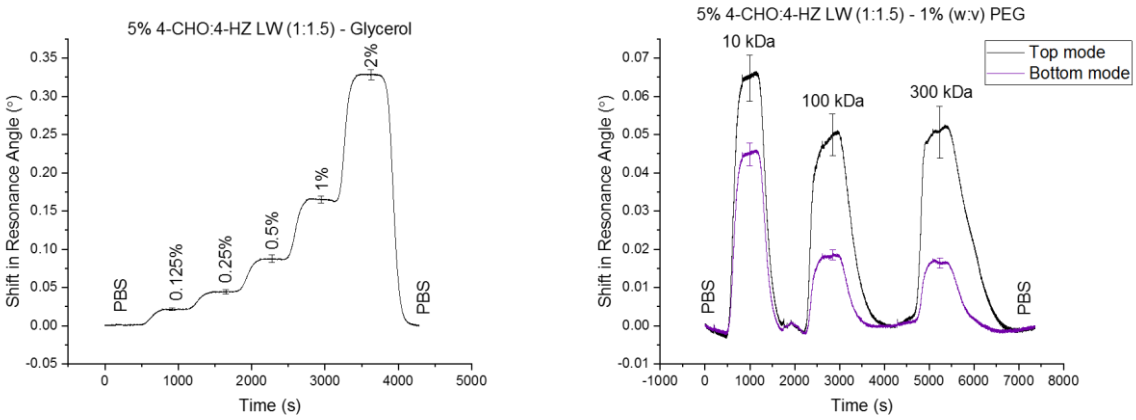

Figure 3.59. Glycerol (left) and PEG (right) runs on 5% 4-CHO:4-HZ LW films (1:1.5). Error bars were calculated as 1σ across two different LW devices.

The porosity percentage for these films was once again quite low, but higher than seen for the SH:MAL combinations reported above (**Table 3.11**). This may be due to the difference in PEG chain lengths used to form the polymer; as the aldehyde and hydrazide are both shorter than the maleimide and thiol compounds chosen there is less opportunity for network defects to occur in the structure.

Table 3.11. PEG response and percentage porosity of 5% 4-CHO:4-HZ (1:1.5) LWs.

1% PEG	RI (RIU)	THEORETICAL RESPONSE (°)	ACTUAL RESPONSE (°)	POROSITY (%)	ACTUAL VERSUS 1% CS RESPONSE (%)
10 kDa	1.33655	0.129414	0.069920	54.03	60.06
100 kDa	1.33668	0.144478	0.053559	37.07	46.01
300 kDa	1.33678	0.156066	0.056702	36.33	48.71

The calibration curve affords an RIS of 115.88 ± 3.06 °/RIU, a value lower than CS (**Figure 3.60**).

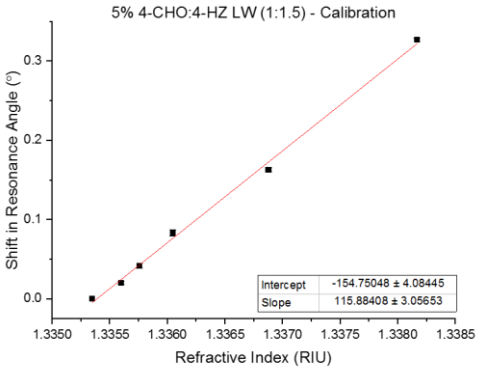

Figure 3.60. Calibration curve on 5% 4-CHO:4-HZ LW films (1:1.5). Error bars were calculated as 1σ across two different LW devices.

While individual films are highly uniform, there is a high degree of device-to-device variability which is shown *via* the large error bars. Due to issues with fabricating these films, only two runs were able to be collected. This is unfortunate as the individual films showed excellent dip separation and uniformity (**Figure 3.61**).

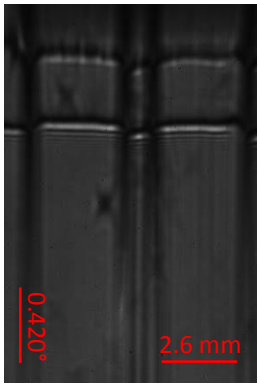

Figure 3.61. Output image of a 5% 4-CHO:4-HZ LW (1:1.5) film under a 2-channel flow cell.

To test for free hydrazide groups in the 4-CHO:4-HZ (1:1.5) films, a solution of glutaraldehyde was reacted with the films to bind with the free hydrazide groups (**Figure 3.62**).

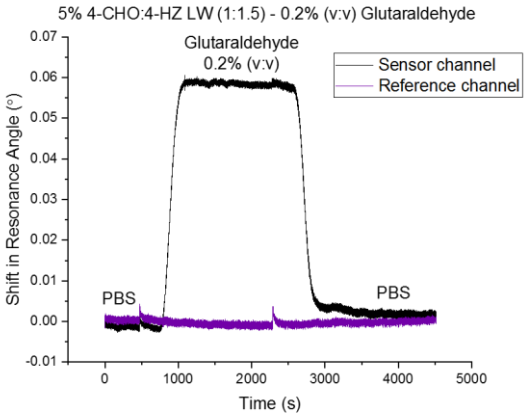

Figure 3.62. 5% 4-CHO:4-HZ LW (1:1.5) treated with 0.2% (v:v) glutaraldehyde.

There is very minimal binding from the glutaraldehyde, suggesting that there is either no free hydrazide groups or any free hydrazide groups are blocked by the matrix formed by the hydrogel structure. This slight increase in resonance angle may be attributed to very minor hydrazide-aldehyde bonding, or more likely to non-specific adsorption (NSA) or glutaraldehyde becoming trapped within the pores of the hydrogel.

Next, 5% 4-CHO:4-HZ (2:1) films were prepared and tested in the same manner. These produced either one or two moded films with varying success. **Figure 3.63** shows that the top mode of these films has a higher porosity than the 1:1.5 variant for 10 kDa and 100 kDa PEGs, while the response for 300 kDa is slightly lower. The higher porosity is expected as these films will have larger pores due to the higher ratio between the aldehyde and hydrazide PEGs, but the lower response to 300 kDa PEG is not ideal.

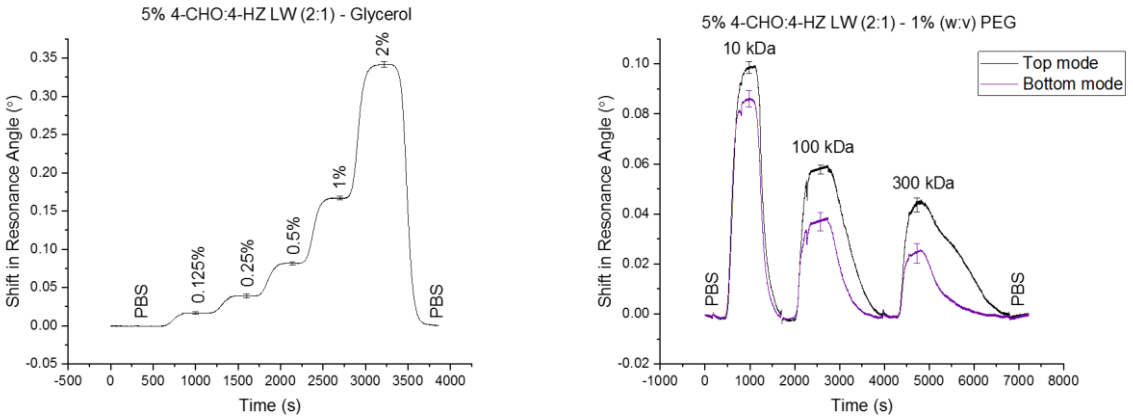

Figure 3.63. Glycerol (left) and PEG (right) runs on a 5% 4-CHO:4-HZ LW film (2:1). Error bars were calculated as 1σ across the width of one LW.

We can see in **Table 3.12** that the percentage porosity for 10 kDa PEG is very high, while for 300 kDa it is only a quarter of the potential. This is a good indication that these films are porous to analytes of around 10 kDa MW, while larger analytes will be hindered by the porosity of the films.

Table 3.12. PEG response and percentage porosity of 5% 4-CHO:4-HZ (2:1) LWs.

1% PEG	RI (RIU)	THEORETICAL RESPONSE (°)	ACTUAL RESPONSE (°)	POROSITY (%)	ACTUAL VERSUS 1% CS RESPONSE (%)
10 kDa	1.33655	0.135638	0.097992	72.25	84.17
100 kDa	1.33668	0.151493	0.056758	37.47	48.75
300 kDa	1.33678	0.163689	0.041922	25.61	36.01

Figure 3.64 show the 5% 4-CHO:4-HZ (2:1) films have a slightly higher RIS of 121.96 ± 3.59 °/RIU compared to 115.88 ± 3.06 °/RIU for the 1:1.5 variant.

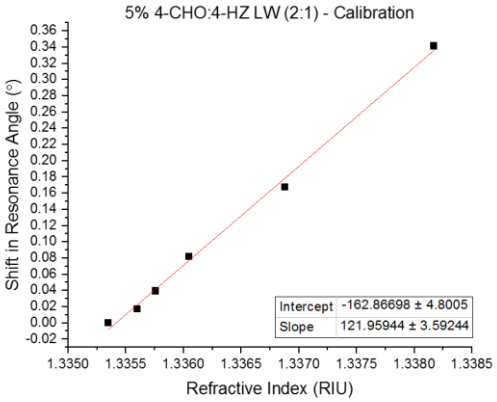

Figure 3.64. Calibration curve on a 5% 4-CHO:4-HZ LW film (2:1).

These films have the closest response to the PEG solutions as the CS LWs. For 10 kDa PEG, the response is 84.17% of that seen in the CS LWs, with 100 kDa PEG at 48.75% and 300 kDa PEG at 36.01% respectively. This shows that while these films are relatively porous to high MW species, they are still not on par with the CS films investigated initially.

The 2:1 ratio also forms less uniform films than the 1:1.5 ratio; this is seen in **Figure 3.65**, where the modes are slanted and uneven. Additionally, there was a large difference in appearance from film-to-film, suggesting that these films are not forming evenly or reproducibly. They are therefore classed as ”medium” and “low” against the success criteria for uniformity and reproducibility respectively.

Figure 3.65. Output image of a 5% 4-CHO:4-HZ LW (2:1) under a 2-channel flow cell.

Finally, 4-CHO:4-HZ (2:1) films were reacted with hydrazide-biotin to test for the presence of free aldehyde groups (**Figure 3.66**).

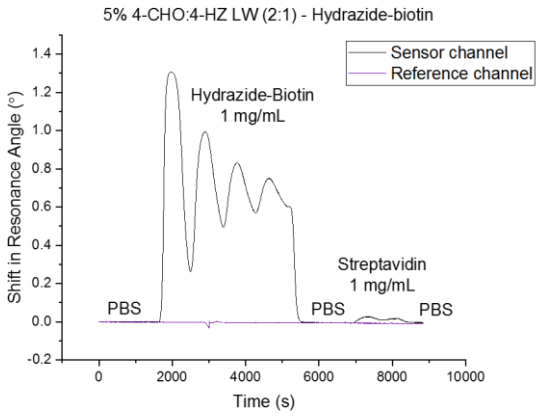

Figure 3.66. 5% 4-CHO:4-HZ LW (2:1) treated with 1 mg/mL hydrazide-biotin.

Again, these films did not show any binding with the hydrazide-containing reactant. To ensure this was the case, streptavidin was then reacted with the film which should now contain free biotin groups. This was unsuccessful.

Similar to the thiol:maleimide films, these structures are likely subjected to network defects and hence have severely reduced reactivity from what was expected. As neither the excess hydrazide nor the excess aldehyde films appeared to have any of the expected reactivity, these films were not researched further as sensing LWs.

3.3 Flow cell shapes

To apply solutions directly to the LWs a flow cell is required. This is placed on top of the LW and held with a clamp. This prevents the flow cell and LW from shifting during measurements and facilitates streamlined fluid flow without leakage. A flow cell requires a minimum of one inlet and one outlet to allow the solution to enter and exit the cell, along with a peristaltic pump to push the fluid.

The design and shape of a microfluidic flow cell is integral to the success of protein immobilisation. The flow cell used must allow for simple application of a liquid sample to the LW without leakage or damage to the LW. The channel must be fully visible in the output image, free from obstructions and of high quality to facilitate smooth fluid flow. It must be compatible with a peristaltic pump or syringe system and suited to the ideal volume and flow rate to prevent LW damage or the accumulation of reagent gradients within the flow channel [75].

The motion of a solution moving through a flow cell is dependent on both advection and diffusion of the analyte, which in turn indicates the importance of flow rate and volume, channel shape and width, and analyte concentration [76]. Therefore, as part of the optimisation process multiple flow cells were used to assess the flow of the sample across the film. Each flow cell was fabricated *via* computer numerical control (CNC) machining of 3 mm thick PMMA sheets to form a 0.2 mm deep cavity of the desired shape, surrounded by a 1 mm wide and 0.75 mm deep groove to allow mounting of an O-ring.

3.3.1 Circular

The circular flow cell is the simplest configuration, comprised of a single circular recess and one inlet and one outlet (**Figure 3.67**). This produces a single, broad flow channel.

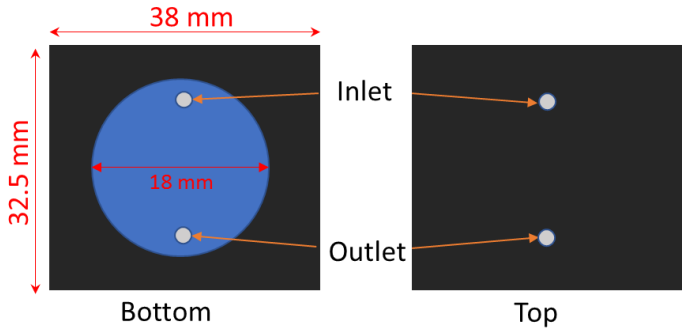

Figure 3.67. A circular flow cell.

This flow cell encountered two major issues. Firstly, the flow cell is prone to dead zones/air bubbles becoming trapped within the sensing region. This is a consequence of the broad nature of the channel which is difficult to fill along with the overall shape of the flow cell which does not encourage streamlined fluid flow. Instead, the solution can spread throughout the channel, which provides a larger sensing area but also produces more areas for air bubbles to become stuck. Secondly, the broadness of the channel does not provide consistent and reproducible fluid flow; as the liquid is able to spread out across the entire width of the channel different regions of the channel are likely to come into contact with the analyte solution at different times, leading to irregular interactions and a non-uniform response. As the width of the channel increases the risk of reverse fluid flow also increases which can lead to the formation of eddies [76]. It is also likely that certain regions will be subjected to analyte build-up. For these reasons, the circular flow cell was phased out early in the experimental investigations, replaced with one of the following flow cells depending on the requirements.

3.3.2 Two-channel

The two-channel flow cell is comprised of two spatially separated channels, with a gap of 2 mm between, effectively separated by rubber O-rings to prevent mixing of the channels (**Figure 3.68**). This allows for the simultaneous recording of two separate solutions on the same sensor chip. For example, one channel could be used as the sample channel, while the other acts as a reference, or both channels can be used simultaneously to interrogate samples of different concentrations. The narrow design of the flow cell channels encourages uniform solution flow, unlike with the circular flow cell.

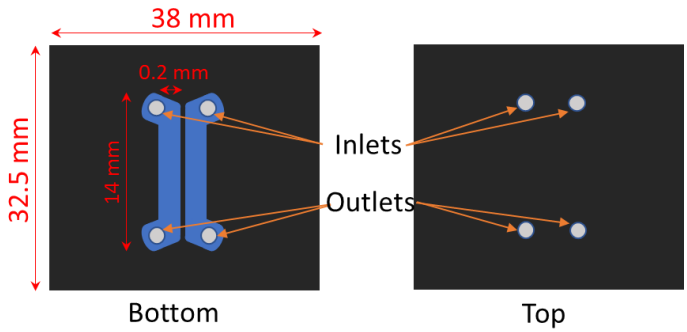

Figure 3.68. A two-channel flow cell.

The shape of these channels reduces the occurrence of air bubbles while providing more uniform results. This makes this flow cell useful for internal referencing as both channels are visible on the output image simultaneously, but the narrow width of the channels does reduce the area of sensing region exposed to the sample and hence makes it more difficult to interrogate the uniformity of the film itself.

3.3.3 Y-shaped

The Y-shaped flow cell is an upgraded version of the circular flow cell (**Figure 3.69**). With two inlet pipes, the solution is forced to fill the entire channel much more evenly and quickly. There is also less opportunity for the introduction of dead zones.

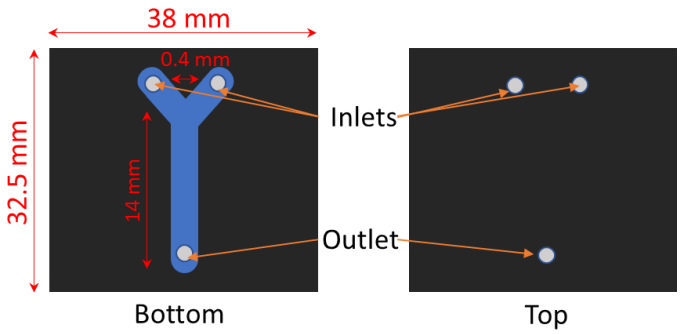

Figure 3.69. A Y-shaped flow cell.

The channel itself is narrower than the circular flow cell, making solution flow much more even and consistent, directing the fluid in a uniform manner to the outlet pipe with minimal spreading. This flow cell does not allow for internal referencing *via* the flow cell but has a wider channel to allow more of the LW to be interrogated.

3.4 Summary

Different natural and synthetic polymers were used to produce hydrogel waveguides, which were then tested with glycerol and PEG solutions to determine sensitivity and porosity. Ultimately, the natural polymer CS provided the most reliable and reproducible results, while providing free functional groups for future functionalisation of the films. CS has been used as a LW in previous work [39, 77, 78], and during the course of this project was purified and optimised to provide consistent results with excellent storage life and sensitivity. The structure of CS makes it suited for further functionalisation and subsequent protein immobilisation and will be explored in **Chapter 5**.

Synthetic polymers such as PAAm-based hydrogels and multi-arm PEGs were also investigated with varying results, but no multi-arm PEG was comparable to the results gained from CS which will be used going forwards in this project. The PEG films also did not behave as expected, with minimal or no reactivity to analytes. This was thought to be due to network defects in the polymer structure, severely impacting the porosity and reactivity of the hydrogels. These films were expected to produce more reliable results than natural polymers but were not successful, leading to these hydrogels being disregarded as sensing LWs at this point in time.

Multiple different flow cell designs were also tested, including a two-channel flow cell which provided additional information in the form of referencing.

3.5 References

1. Gokmen, M.T. and F.E. Du Prez, *Porous polymer particles—A comprehensive guide to synthesis, characterization, functionalization and applications.* Progress in Polymer Science, 2012. **37**(3): p. 365-405.
2. Qiu, S. and T. Ben, *Chapter 1: Introduction*, in *Porous Polymers: Design, Synthesis and Applications*. 2015, The Royal Society of Chemistry. p. 1-7.
3. Liu, F., et al., *Design and synthesis of micro–meso–macroporous polymers with versatile active sites and excellent activities in the production of biofuels and fine chemicals.* Green Chemistry, 2016. **18**(24): p. 6536-6544.
4. Mansour, F.R., et al., *Porogens and porogen selection in the preparation of porous polymer monoliths.* Journal of Separation Science, 2020. **43**(1): p. 56-69.
5. Chen, G. and N. Kawazoe, *5 - Preparation of polymer-based porous scaffolds for tissue engineering*, in *Characterisation and Design of Tissue Scaffolds*, P. Tomlins, Editor. 2016, Woodhead Publishing. p. 105-125.
6. Dangel, R., et al., *Polymer waveguides for electro-optical integration in data centers and high-performance computers.* Optics Express, 2015. **23**(4): p. 4736-4750.
7. Sumitomo Bakelite Co. LTD. *About Polymer Waveguide*. 2015 [cited 12-11-2018]; Available from: https://www.sumibe.co.jp/english/product/coin/how-to-opto/index.html.
8. PEDIAA. *Differences Between Natural and Synthetic Polymers*. 2017 [cited 10-06-2019]; Available from: https://pediaa.com/difference-between-natural-and-synthetic-polymers/.
9. Bhatia, S., *Natural Polymers vs Synthetic Polymer*, in *Natural Polymer Drug Delivery Systems: Nanoparticles, Plants, and Algae*. 2016, Springer International Publishing: Cham. p. 95-118.
10. Weber, L.M., et al., *PEG-based hydrogels as an in vitro encapsulation platform for testing controlled β-cell microenvironments.* Acta Biomaterialia, 2006. **2**(1): p. 1-8.
11. Lin, C.-C. and K.S. Anseth, *PEG Hydrogels for the Controlled Release of Biomolecules in Regenerative Medicine.* Pharmaceutical Research, 2009. **26**(3): p. 631-643.
12. Beamish, J.A., et al., *The effects of monoacrylated poly(ethylene glycol) on the properties of poly(ethylene glycol) diacrylate hydrogels used for tissue engineering.* J Biomed Mater Res A, 2010. **92**(2): p. 441-50.
13. Dmitriev, I., et al., *Swelling behavior and network characterization of hydrogels from linear polyacrylamide crosslinked with glutaraldehyde.* Materials Today Communications, 2015. **4**: p. 93-100.
14. Yoo, J.S., et al., *Study on genipin: a new alternative natural crosslinking agent for fixing heterograft tissue.* The Korean journal of thoracic and cardiovascular surgery, 2011. **44**(3): p. 197-207.
15. Ninh, C., et al., *Diffusion–reaction models of genipin incorporation into fibrin networks.* Journal of Materials Chemistry B, 2015. **3**(22): p. 4607-4615.
16. Su, H., S. Li, and K. Kerman, *Novel thiolated-PEG linker molecule for biosensor development on gold surfaces.* Biosens Bioelectron, 2019. **141**: p. 111477.
17. Reichert Technologies. *What is Surface Plasmon Resonance (SPR)?* 2020 [cited 06-06-2020]; Available from: https://www.reichertspr.com/about/what-is-suface-plasmon-resonance-spr/.
18. Shrivastav, A.M., U. Cvelbar, and I. Abdulhalim, *A comprehensive review on plasmonic-based biosensors used in viral diagnostics.* Communications Biology, 2021. **4**(1): p. 70.
19. Zourob, M., et al., *An Integrated Metal Clad Leaky Waveguide Sensor for Detection of Bacteria.* Analytical Chemistry, 2005. **77**(1): p. 232-242.
20. Zourob, M. and N.J. Goddard, *Metal clad leaky waveguides for chemical and biosensing applications.* Biosensors & bioelectronics, 2005. **20**(9): p. 1718-1727.

21. Im, W.J., et al., *Immunosensing using a metal clad leaky waveguide biosensor for clinical diagnosis.* Sensors and Actuators B: Chemical, 2012. **173**: p. 288-294.
22. Gupta, R., et al., *Absorption spectroscopy in microfluidic flow cells using a metal clad leaky waveguide device with a porous gel waveguide layer.* Analyst, 2013. **138**(1): p. 307-314.
23. Podhorská, B., et al., *Revealing the True Morphological Structure of Macroporous Soft Hydrogels for Tissue Engineering.* Applied Sciences, 2020. **10**(19): p. 6672.
24. ThermoFisherScientific. *Transmission Electron Microscopy vs Scanning Electron Microscopy*. [cited 15-07-2022]; Available from: https://www.thermofisher.com/uk/en/home/materials-science/learning-center/applications/sem-tem-difference.html#:~:text=The%20main%20difference%20between%20SEM,sample)%20to%20create%20an%20image.
25. Leal-Egaña, A., et al., *Determination of pore size distribution at the cell-hydrogel interface.* J Nanobiotechnology, 2011. **9**: p. 24.
26. Ito, E., H. Takase, and K. Yamamoto, *TEM observation of inorganic substances distributed in gel materials for medical devices using ultra-thin cryosectioning.* Microscopy, 2020. **69**(6): p. 408-410.
27. Kaberova, Z., et al., *Microscopic Structure of Swollen Hydrogels by Scanning Electron and Light Microscopies: Artifacts and Reality.* Polymers (Basel), 2020. **12**(3).
28. Agilent Technologies. Polymer Molecular Weight Distribution and Definitions of MW Averages [cited 18-05-2023]; Available from: https://www.agilent.com/cs/library/technicaloverviews/Public/5990-7890EN.pdf
29. Cole, M.B., *An "azo" substitute for benzoyl peroxide in polymerizing glycol methacrylate (GMA).* Micron (1969), 1979. **10**(2): p. 135-137.
30. Petko, F., A. Świeży, and J. Ortyl, *Photoinitiating systems and kinetics of frontal photopolymerization processes – the prospects for efficient preparation of composites and thick 3D structures.* Polymer Chemistry, 2021. **12**(32): p. 4593-4612.
31. Johannsmeier, S., et al., *PEGDMA Hydrogels for Cell Adhesion and Optical Waveguiding.* ACS Applied Bio Materials, 2020. **3**(10): p. 7011-7020.
32. Elieh-Ali-Komi, D. and M.R. Hamblin, *Chitin and Chitosan: Production and Application of Versatile Biomedical Nanomaterials.* International journal of advanced research, 2016. **4**(3): p. 411-427.
33. Chen, X., H. Yang, and N. Yan, *Shell Biorefinery: Dream or Reality?* Chemistry – A European Journal, 2016. **22**(38): p. 13402-13421.
34. Yan, N. and X. Chen, *Sustainability: Don't waste seafood waste.* Nature, 2015. **524**(7564): p. 155-157.
35. Ahmadi, F., et al., *Chitosan based hydrogels: characteristics and pharmaceutical applications.* Res Pharm Sci, 2015. **10**(1): p. 1-16.
36. Dimida, S., et al., *Effects of Genipin Concentration on Cross-Linked Chitosan Scaffolds for Bone Tissue Engineering: Structural Characterization and Evidence of Biocompatibility Features.* International Journal of Polymer Science, 2017. **2017**: p. 8410750.
37. Jayakumar, R., et al., *Biomaterials based on chitin and chitosan in wound dressing applications.* Biotechnology Advances, 2011. **29**(3): p. 322-337.
38. Vicente, F.A., et al., *Chitin Deacetylation Using Deep Eutectic Solvents: Ab Initio-Supported Process Optimization.* ACS Sustainable Chemistry & Engineering, 2021. **9**(10): p. 3874-3886.
39. Goddard, N.J., et al., *3D Printed Instrumentation for Point-of-Use Leaky Waveguide (LW) Biochemical Sensor.* IEEE Transactions on Instrumentation and Measurement, 2020: p. 1-1.
40. Wu, Q.X., D.Q. Lin, and S.J. Yao, *Design of chitosan and its water soluble derivatives-based drug carriers with polyelectrolyte complexes.* Mar Drugs, 2014. **12**(12): p. 6236-53.

41. Vo, N.T.N., et al., *Genipin-crosslinked chitosan hydrogels: Preliminary evaluation of the in vitro biocompatibility and biodegradation.* Journal of Applied Polymer Science, 2021. **138**(34): p. 50848.
42. Galan, J., et al., *Optimization of Chitosan Glutaraldehyde-Crosslinked Beads for Reactive Blue 4 Anionic Dye Removal Using a Surface Response Methodology.* Life, 2021. **11**(2): p. 85.
43. Gupta, R. and N.J. Goddard, *A proof-of-principle study for performing enzyme bioassays using substrates immobilized in a leaky optical waveguide.* Sensors and Actuators B: Chemical, 2017. **244**: p. 549-558.
44. Urrutia, P., et al., *Influence of chitosan derivatization on its physicochemical characteristics and its use as enzyme support.* Journal of Applied Polymer Science, 2014. **131**(8).
45. Szymańska, E. and K. Winnicka, *Stability of chitosan-a challenge for pharmaceutical and biomedical applications.* Mar Drugs, 2015. **13**(4): p. 1819-46.
46. Klein, M.P., et al., *Chitosan crosslinked with genipin as support matrix for application in food process: Support characterization and β-D-galactosidase immobilization.* Carbohydr Polym, 2016. **137**: p. 184-190.
47. Verma, M.L., et al., *Chitin and chitosan-based support materials for enzyme immobilization and biotechnological applications.* Environmental Chemistry Letters, 2020. **18**(2): p. 315-323.
48. Franzén, H.M., et al., *Characterization and Properties of Hydrogels Made from Neutral Soluble Chitosans.* Polymers, 2015. **7**(3): p. 373-389.
49. Signini, R. and S.P. Campana Filho, *On the preparation and characterization of chitosan hydrochloride.* Polymer Bulletin, 1999. **42**(2): p. 159-166.
50. Wei, B., et al., *One-step preparation of hydrogel based on different molecular weights of chitosan with citric acid.* Journal of the Science of Food and Agriculture, 2022. **102**(9): p. 3826-3834.
51. Gunda, N.S.K., et al., *Optimization and characterization of biomolecule immobilization on silicon substrates using (3-aminopropyl)triethoxysilane (APTES) and glutaraldehyde linker.* Applied Surface Science, 2014. **305**: p. 522-530.
52. Kyaw, H.H., et al., *Self-organization of gold nanoparticles on silanated surfaces.* Beilstein journal of nanotechnology, 2015. **6**: p. 2345-2353.
53. Neuhoff, V., *Improved procedure for silanization of glass plates as supports for polyacrylamide gels.* ELECTROPHORESIS, 1984. **5**(4): p. 251-251.
54. Prouvé, E., et al., *Evaluating Poly(Acrylamide-co-Acrylic Acid) Hydrogels Stress Relaxation to Direct the Osteogenic Differentiation of Mesenchymal Stem Cells.* Macromolecular Bioscience, 2021. **21**(6): p. 2100069.
55. Nesrinne, S. and A. Djamel, *Synthesis, characterization and rheological behavior of pH sensitive poly(acrylamide-co-acrylic acid) hydrogels.* Arabian Journal of Chemistry, 2017. **10**(4): p. 539-547.
56. Alsuraifi, A., et al., *Thermally reactive N-(2-hydroxypropyl)methacrylamide (HPMA) amphiphiles for drug solubilisation.* International Journal of Pharmaceutics, 2021. **601**: p. 120570.
57. Dubey, A., N.A.D. Burke, and H.D.H. Stöver, *Preparation and characterization of narrow compositional distribution polyampholytes as potential biomaterials: Copolymers of N-(3-aminopropyl)methacrylamide hydrochloride (APM) and methacrylic acid (MAA).* Journal of Polymer Science Part A: Polymer Chemistry, 2015. **53**(2): p. 353-365.
58. Smith, E.A. and F.W. Oehme, *Acrylamide and polyacrylamide: a review of production, use, environmental fate and neurotoxicity.* Rev Environ Health, 1991. **9**(4): p. 215-28.
59. Gupta, R., A.K. Pal, and N.J. Goddard, *Biosensing by Direct Observation of Leaky Waveguide Modes.* Journal of Physics: Conference Series, 2021. **1919**(1): p. 012002.

60. Tsm, T.H., et al., *Identification and Determination of Geniposide, Genipin, Gardenoside, and Geniposidic Acid from Herbs by HPLC/Photodiode-Array Detection.* Journal of Liquid Chromatography, 1994. **17**(10): p. 2199-2205.
61. Xi-xun, Y., et al., *In vitro study in the endothelial cell compatibility and endothelialization of genipin-crosslinked biological tissues for tissue-engineered vascular scaffolds.* Journal of Materials Science: Materials in Medicine, 2010. **21**(2): p. 777-785.
62. Pal, K., A.T. Paulson, and D. Rousseau, *CHAPTER 16 - Biopolymers in Controlled-Release Delivery Systems*, in *Modern Biopolymer Science*, S. Kasapis, I.T. Norton, and J.B. Ubbink, Editors. 2009, Academic Press: San Diego. p. 519-557.
63. *Handbook on Natural Pigments in Food and Beverages: Industrial Applications for Improving Food Color*, ed. R. Carle and R.M. Schweiggert. 2016: Woodhead Publishing.
64. Manickam, B., R. Sreedharan, and M. Elumalai, *'Genipin' - the natural water soluble cross-linking agent and its importance in the modified drug delivery systems: an overview.* Curr Drug Deliv, 2014. **11**(1): p. 139-45.
65. Hanson, M. and A. Wypych, *3 - Curatives and Crosslinkers*, in *Databook of Curatives and Crosslinkers*, M. Hanson and A. Wypych, Editors. 2019, ChemTec Publishing. p. 15-537.
66. Sigma Aldrich. *Genipin*. 2022 [cited 07-06-2022]; Available from: https://www.sigmaaldrich.com/GB/en/product/sigma/g4796.
67. Northrop, B.H., S.H. Frayne, and U. Choudhary, *Thiol–maleimide "click" chemistry: evaluating the influence of solvent, initiator, and thiol on the reaction mechanism, kinetics, and selectivity.* Polymer Chemistry, 2015. **6**(18): p. 3415-3430.
68. Abel, B.A. and C.L. McCormick, *"One-Pot" Aminolysis/Thiol–Maleimide End-Group Functionalization of RAFT Polymers: Identifying and Preventing Michael Addition Side Reactions.* Macromolecules, 2016. **49**(17): p. 6193-6202.
69. ThermoFisherScientific. *Sulfhydryl-reactive Crosslinker Chemistry*. [cited 26-04-2022]; Available from: https://www.thermofisher.com/uk/en/home/life-science/protein-biology/protein-biology-learning-center/protein-biology-resource-library/pierce-protein-methods/sulfhydryl-reactive-crosslinker-chemistry.html#2.
70. Chen, W.-H., et al., *Silanization of solid surfaces via mercaptopropylsilatrane: a new approach of constructing gold colloid monolayers.* RSC Advances, 2014. **4**(87): p. 46527-46535.
71. Vistas, C.R., A.C.P. Águas, and G.N.M. Ferreira, *Silanization of glass chips—A factorial approach for optimization.* Applied Surface Science, 2013. **286**: p. 314-318.
72. Kasko, A.M. and Sigma Aldrich. *Degradable Poly(ethylene glycol) Hydrogels for 2D and 3D Cell Culture*. [cited 04-07-2022]; Available from: https://www.sigmaaldrich.com/GB/en/technical-documents/technical-article/materials-science-and-engineering/tissue-engineering/degradable-polyethylene-glycol-hydrogels.
73. Lee, S., X. Tong, and F. Yang, *Effects of the poly(ethylene glycol) hydrogel crosslinking mechanism on protein release.* Biomater Sci, 2016. **4**(3): p. 405-11.
74. ThermoFisherScientific. *Carbonyl-reactive Crosslinker Chemistry*. [cited 07-01-2022]; Available from: https://www.thermofisher.com/uk/en/home/life-science/protein-biology/protein-biology-learning-center/protein-biology-resource-library/pierce-protein-methods/carbonyl-reactive-crosslinker-chemistry.html.
75. Madariaga-Marcos, J., et al., *Characterizing microfluidic approaches for a fast and efficient reagent exchange in single-molecule studies.* Scientific Reports, 2020. **10**(1): p. 18069.
76. Pike, D.J., et al., *Flow cell design for effective biosensing.* Sensors (Basel), 2012. **13**(1): p. 58-70.
77. Pal, A.K., et al., *A Self-Referenced Diffraction-Based Optical Leaky Waveguide Biosensor Using Photofunctionalised Hydrogels.* Biosensors, 2020. **10**(10): p. 134.
78. Gupta, R. and N.J. Goddard, *A study of diffraction-based chitosan leaky waveguide (LW) biosensors.* Analyst, 2021. **146**(15): p. 4964-4971.

4 Chapter 4 – Stacked Waveguides

4.1 Introduction

Referenced biosensors present the opportunity for quick and accurate detection of analytes within a single system, removing the need for lengthy data correction after data collection. Such referencing technology is desired in many settings including healthcare environments and industrial testing, and the target analytes can be a range of different biological molecules such as enzymes, antibodies, proteins, DNA and more.

External referencing is typically easier to incorporate into pre-existing instrumentation, such as the addition of a separate channel parallel to the sensing channel. This has the advantage of being cheaper than developing an entirely new piece of equipment but can present another opportunity to introduce further errors into measurements. An external reference is not subjected to the exact same conditions as the sample region, therefore any small changes occurring between the two regions will lead to errors. Such errors could be introduced by a difference as simple as a very small temperature gradient between the two channels, the introduction of air bubbles into a single channel, or slight mechanical fluctuations. While these may be accounted for in post-processing it is not ideal for the collection of the most highly accurate results.

Internal referencing places the sample and reference regions as physically close together as possible with the intention of reducing such errors. Both regions are recorded simultaneously, and a differential response can then be taken, leading to visualisation of the response of the sample channel only. Thus, internal referencing is required for biosensing applications to ensure readings are as accurate as possible.

A notable internal reference is seen in gas chromatography systems in which the unknown sample is added to a species of known concentration and retention time [1]. This allows the known species to act as a reference under the same conditions as the sample. Internal referencing can negate issues which arise during data collection, such as fluctuations in temperature and changes in bulk composition [2]. Ideally, the referencing area will be affected by any bulk changes but not affected by the analyte, allowing for any bulk changes to be subtracted from the analyte sample. However, internally referenced systems tend to be bulky and expensive, making them unsuitable for point-of-care (POC) use.

As discussed in **Chapter 1** (**1.2.4**), label-based biosensors are undesirable as they can change the properties of the analyte and cause false-positives or false-negatives [3, 4], along with the practical issues raised with the labelling process itself, which can be lengthy and low-yielding [1]. Label-free biosensors are more ideal and the addition of an internal reference to these systems will further increase the accuracy and reliability of these techniques [5].

Internal referencing can be achieved in various ways, including but not limited to spatially separated regions such as those in **Figure 4.1**, tailoring penetration depth, use of multiple different polarisations of light, gratings, and stacked structures.

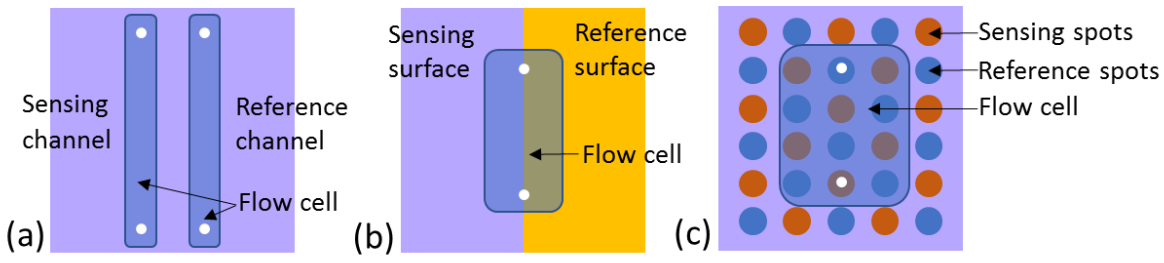

Figure 4.1. Spatially separated sample and reference regions via: (a) parallel sensing and referencing channels using a two-channel flow cell, (b) adjoined sensing and referencing surfaces using one channel, and (c) surface patterned sensing and referencing spots.

Surface plasmon resonance (SPR) techniques are the most dominant type of label-free optical sensors and can be designed to incorporate internal referencing systems. A detection element is bound to a thin metal film, usually gold, and the corresponding analyte is exposed to the film where it binds with the detection element. This leads to a change in refractive index (RI) which can be measured.

However, SPR instruments are extremely costly to purchase and repair, and the gold film layers are not particularly durable [6, 7]. Internal referencing can be achieved by addition of a separate reference channel which has decreased attraction to the analyte, but this secondary channel often requires a completely separate optical system which further increases the cost [8-11]. Other methods used in SPR include the development of multiple surfaces using one flow cell [12-14], multiple polarisations of light [15, 16], tailored penetration depth of the evanescent field [17-19], and gratings [8].

Solutions to some of the issues raised by SPR sensors have been developed such as the combination of an SPR sensor with a diffraction grating, producing surface plasmon diffraction (SPD). The advantages of this technique include the fact that the self-referencing system is incorporated directly into the grating, removing the requirement for a separate referencing channel. This also produces a high baseline stability, making data processing quicker and reducing errors [8]. A similar technique uses protein contact printing to modify the surface of half of the sensor and therefore gives an internal referencing system which again can be used with a single light beam and one sample volume [12]. Problems encountered with this included lengthy slide preparation and difficulty in surface functionalisation due to the two separate layers.

A more recent SPR-based sensor known as a plasmon waveguide resonance sensor (PWR) with the ability to guide both transverse electric (TE) and transverse magnetic (TM) polarisation modes gave impressive sensitivity, with the TM mode able to detect 55 ng/mL and the TE mode up to 9 ng/mL. This is in contrast to conventional SPR methods which use only TM polarisation. Each mode is subjected to the same environment but produce different signals due to the ability of the TM mode to penetrate deeper into the sample, hence can be used as a reference [16].

SPR has also been combined with the Mach-Zehnder interferometric (MZI) set-up by including a Wollaston prism within the interferometer [15]. This allows for the simultaneous monitoring of both s and p polarisation. As SPR only impacts p polarised light, the s polarised light can therefore be used as a reference signal. This setup achieves a sensitivity of 5.5×10^{-8} refractive index units (RIU)/0.01°, with estimated detection limit of 7.4 ng/mL.

Each method has its own advantages and disadvantages, and consideration must be given to the fabrication techniques, cost, sensitivity, and durability of each technique when weighing the best options.

Optical waveguides are also capable of incorporating an internal reference. Waveguides work *via* the change in RI caused when an analyte attaches to the waveguide, which displaces water and produces a different optical signal due to the change in RI. However, waveguides are particularly prone to fluctuations in temperature and bulk RI changes, and an internal reference is highly desirable [2].

One type of optical waveguide is the resonant mirror (RM) waveguide which has been incorporated with internal referencing. This technique relies on detection of the evanescent

field and has been described by Goddard *et al*. as a "*sensor which combines the enhanced sensitivity of waveguiding devices with the simple construction and use of SPR sensors*" [20]. Internal referencing can be achieved by adding a buried layer beneath the sensing layer of the waveguide, forming internally referenced resonant mirror (IRRM) waveguides. This additional waveguide layer improves upon traditional optical waveguides by negating the effects of temperature and light sensor fluctuations, but is still prone to modal drift as the reference layer was not entirely inert [20]. It does however offer insight into the applications of a reference layer within the waveguide and proposes that an inert reference layer is possible.

Gupta *et al.* went on to develop a metal clad leaky waveguide (MCLW) with internal referencing achieved again by stacking of the films [21]. In this case, agarose was used as the both the sensor and reference layers, with activation of the sensor layer to allow for covalent antibody immobilisation (**Figure 4.2**). This was reported to achieve a reduction in temperature sensitivity by 18.0 and bulk RI change by 30.5 in direct comparison to a single layer waveguide.

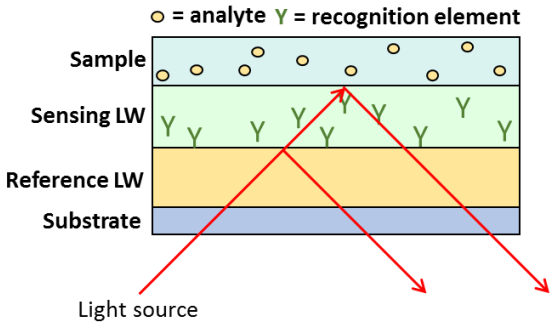

Figure 4.2. Depiction of a stacked leaky waveguide (LW), in which the reference layer is beneath the sensing layer.

From the literature it is plausible that an internally referenced waveguide is feasible, and by using cheap, easily available polymers it should be possible to significantly reduce the cost of the system and make the instrumentation more accessible.

There are two main goals within this chapter. Firstly, to develop an internally referenced waveguide, and secondly to incorporate an internal filtration system into the waveguide. This can be achieved by stacking two different polymers, where one has functional groups suitable for protein immobilisation and the other is an inert reference material.

As shown in **Figure 4.3**, the stacked leaky waveguide (LW) can be tested on the same instrumentation used for the single layer LWs. There is no need for additional light sources or detectors and the only difference is in the fabrication of the LW which requires two steps rather than one.

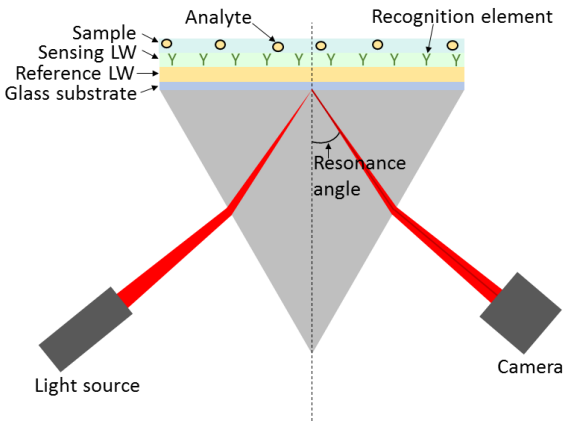

Figure 4.3. Depiction of the LW instrumentation with a stacked LW.

4.1.1 Reference layer porosity

In **Chapter 2** (**2.2.2**) we discussed the importance of using porous hydrogels for the sensor layer. This is to allow for easy film functionalisation and protein immobilisation, with the analytes able to diffuse in and out of the whole film structure.

For the reference layer, it would be ideal to also have good porosity. If we consider the stacked structure in which the reference layer is on top of the sensing layer, if the reference

layer had slightly reduced porosity in comparison to the sensor layer it would be able to filter out larger molecules and prevent them from reaching the sensor layer where they may become trapped. This would be very useful in whole samples where large cells and proteins may interfere with the sensor layer. It would however mean the porosity of this layer must be high enough to readily allow through the analytes of interest, therefore the porosity must be carefully controlled.

In comparison, if the sensor layer is placed on top of the reference layer we lose this filtration ability, but the porosity of the reference layer is no longer as important. As long as the reference layer is still able to respond to changes in RI on a level equal to that of the sensor layer, the overall sensitivity of the reference layer should be high enough to detect changes at the surface of the reference layer and within the sensor layer itself.

Ultimately, a level of porosity just below that of the sensor layer is desirable for the reference layer, but not essential if using the sensor/reference/substrate configuration. In cases where the reference/sensor/substrate configuration is used, the porosity of the reference must be close to that of the sensor.

4.2 Reference leaky waveguides

To produce an accurate reference, the referencing material must remain inert to the analyte while responding to bulk effects in the same manner as the sensor layer. This means that using a reference layer that is structurally and chemically similar to the sensor layer should be most accurate, provided it contains no reactive groups. This is not always possible, therefore finding a gel which is inert with similar sensitivity to the sensor layer is the next best scenario. For the reference LW multiple hydrogels were investigated and reported below, before moving on to stacked LWs in **Section 4.3**. The success criteria defined in **Chapter 3** (**3.1.2**) has also been applied to the LWs described in this chapter.

4.2.1 Poly(acrylamide), PAAm

Polyacrylamide (PAAm) is a well-known water-soluble polymer which can be cross-linked using glutaraldehyde. PAAm has found applications in various industries, including biomedical, agricultural, and waste treatment [22]. A widely used polymer, PAAm is inert and resists non-specific interactions, and is commonly used in polyacrylamide gel electrophoresis (PAGE) techniques for protein separation in the range of 5 – 250 kDa [23, 24].

While PAAm can be formed *via* free radical polymerisation of acrylamide (AAm) and bisacrylamide (BAAm) monomers, which is explored in **Section 4.2.2**, PAAm can alternatively be purchased as a linear polymer (**Figure 4.4**).

Linear PAAm was investigated as an inert polymer layer; crosslinking was achieved using glutaraldehyde at acidic pH, forming imine bonds between the amide groups of PAAm and the aldehyde groups of glutaraldehyde [25]. By controlling the concentration of

glutaraldehyde and PAAm, films with optimal porosity were achieved using a 0.96% PAAm solution containing 0.025% (v:v) glutaraldehyde and 4.8% (v:v) glycerol. Glycerol was included as a humectant and to increase the viscosity of the solution to aid spin coating.

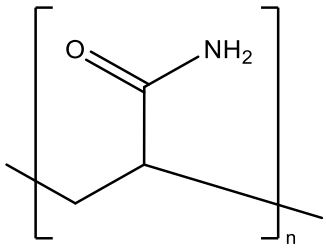

Figure 4.4. The structure of a poly(acrylamide) (PAAm) repeating subunit.

Various concentrations of PAAm were investigated, from 0.96% to 1.96% (w:v), along with two different molecular weights: low molecular weight (LMW), average molecular weight (MW) = 150K, and high molecular weight (HMW), MW = 5,000-6,000K.

Figure 4.5 shows the difference between the LMW and HMW PAAm LWs. The dip of the LMW is within the total internal reflection (TIR) boundary, preventing the software from tracking it. Meanwhile, the HMW dip is adequately spaced from the TIR. For this reason, the HMW PAAm was used going forward. Additionally, HMW PAAm LWs at higher concentrations than 0.96% typically produced multi-moded films which again interfered with tracking, so 0.96% was chosen at this stage.

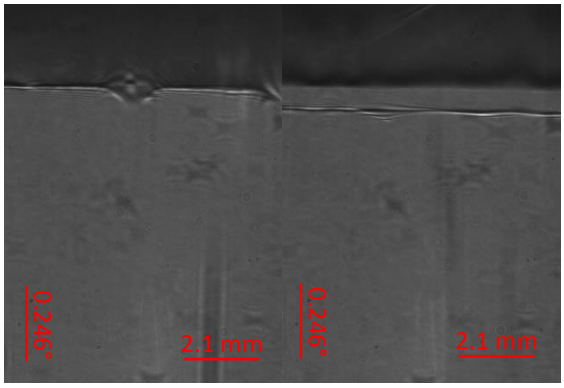

Figure 4.5. Output image of a 0.96% LMW PAAm LW (left) and a 0.96% HMW PAAm LW (right).

As seen in **Figure 4.6**, the large error bars on the poly(ethylene glycol) (PEG) graph indicate high variability between different devices. This is not ideal as accuracy and reproducibility will vary from device to device and make optimisation difficult.

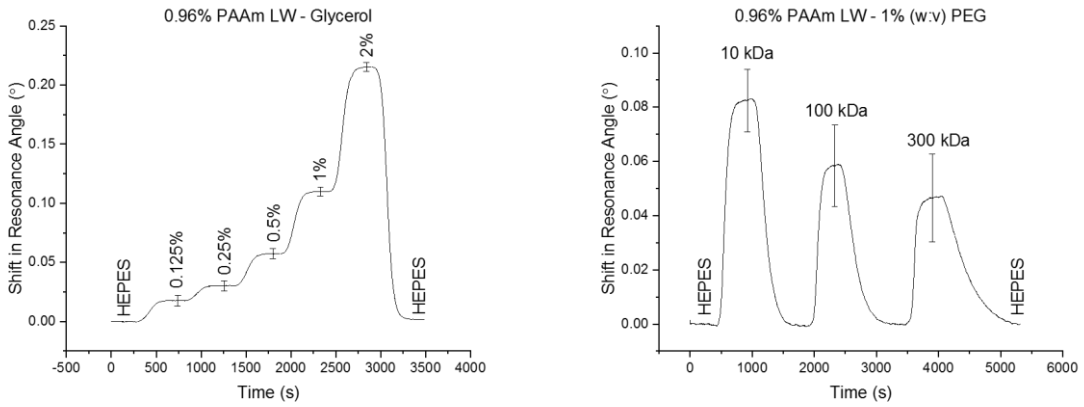

Figure 4.6. Glycerol (left) and PEG (right) runs on 0.96% PAAm LWs. Error bars were calculated as 1σ across three different LWs.

The porosity of these films is also fairly low even at the theoretical values presented in **Table 4.1**. At 300 kDa PEG the 0.96% PAAm LW gives a response half of that seen for 1% chitosan (CS).

Table 4.1. PEG response and percentage porosity of 0.96% PAAm LWs.

1% PEG	RI (RIU)	THEORETICAL RESPONSE (°)	ACTUAL RESPONSE (°)	POROSITY (%)	ACTUAL VERSUS 1% CS RESPONSE (%)
10 kDa	1.33836	0.118338	0.088122	74.47	75.69
100 kDa	1.33843	0.123514	0.068089	55.13	58.49
300 kDa	1.33844	0.124254	0.057916	46.61	49.75

This difference in porosity between the PAAm and CS LWs implies that PAAm would work well as a filtration layer on top of a sensor layer by preventing large molecules from reaching the sensing layer. However, this does risk blocking some of the analyte depending on the size of the analyte and concentration of interferents in the sample.

The refractive index sensitivity (RIS) of these devices is very poor at 73.94 ± 2.77 °/RIU which is just 51.27% of the RIS for CS reported in **Chapter 3** (**3.2.2**) as 144.23 ± 1.21 °/RIU (**Figure 4.7**).

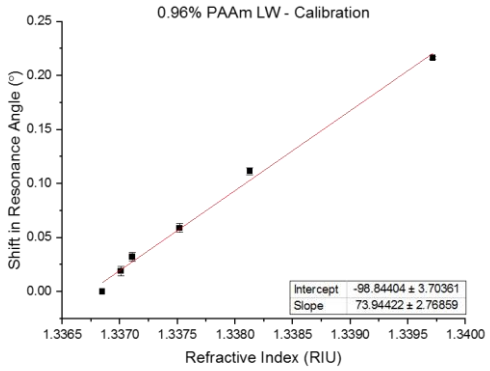

Figure 4.7. Calibration curve for 0.96% PAAm LWs. Error bars were calculated as 1σ across three different LWs.

This suggests that any stacked film built from PAAm and CS would have different sensitivities per layer, which is not desirable for accurate referencing. The sensor and reference layers need to have a similar sensitivity so they can accurately reflect each other.

Against the success criteria the 0.96% HWM PAAm LWs produced films with high uniformity and medium reproducibility. Ideally the reproducibility would be higher to make these films more suited for mass production, but further development may achieve this.

4.2.2 Acrylamide, AAm

While PAAm could be used to prepare non-toxic hydrogels *via* spin coating, a solution of AAm monomer was used along with BAAm monomer to form a polymer *via* slide casting (**Figure 4.8**). Slide casting was used as opposed to spin coating due to both practical and safety issues. AAm is a known carcinogen and hence not ideal for use in a spin coating instrument,

and polymerisation can take a few minutes to complete at which point most of the solution will likely have been flung from the substrate. These reasons are discussed in more detail in **Chapter 3** (**3.2.4**). Polymerisation occurs *via* free radical polymerisation and hence can only be controlled *via* the concentrations of AAm and BAAm used.

The advantage of preparing AAm films from the monomer constituents as opposed to the pre-formed linear polymer includes tailorable gel properties. By modifying the monomer and crosslinker concentrations the resulting hydrogel can be tailored to produce smaller or larger pores, differences in elasticity and swelling properties, and modifications in durability [26]. Calvet *et al.* also investigated the importance of temperature during polymerisation on the final properties of the gel [27]. Such a wide range of conditions allows for higher control over the final hydrogel, but also increases the opportunity for errors and inconsistencies to be introduced. It is therefore important to consider the benefits and drawbacks of such methods when developing a hydrogel intended for mass production.

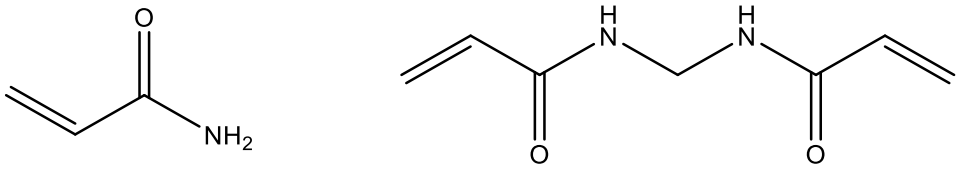

Figure 4.8. The structures of acrylamide (AAm) (left) and bisacrylamide (BAAm) (right) monomers.

These hydrogels were tested at concentrations from 3% - 5% total monomer. Casting these films often led to multi-moded films as the cast films typically end up thicker than the spin coated films (**Figure 4.9**). Additionally, hand-casting films introduces more human error than spin coating as it is highly reliant on the practitioner, discussed in **Chapter 2** (**2.5**). It was noted that the 3% total monomer gels produced the fewest number of modes and were therefore most suited to behaving as LWs.

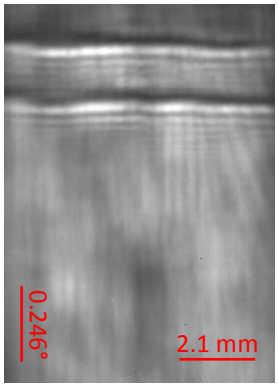

Figure 4.9. Output image of a 3% AAm LW.

These LWs could be stored wet or dry but had a success rate of 50%. While these AAm films did give good responses, the inconsistencies in thickness and uniformity due to errors introduced during fabrication made further investigations unideal. Uniformity has been ranked as medium as some films were highly uniform, but others were not. This links with reproducibility, which is ranked as low.

Despite AAm hydrogels having extensive uses in the biomedical community, for a technique requiring a uniform surface and structure this fabrication technique is not ideal and does not show AAm to its full potential. With a different fabrication technique AAm hydrogels may prove to be more suitable for LW usage.

4.2.3 Agarose

Agarose is a natural, non-toxic linear polysaccharide derived from agar, which is extracted from some red seaweeds [28]. The structure of agarose is built from repeating agarobiose units; agarobiose itself is built from alternating units of β-D-galactose and 3,6-anhydro-L-galactose (**Figure 4.10**), and is commonly used in agarose gel electrophoresis techniques [29]. As agarose is known to form reliable gels it was a natural choice to test as a

waveguide. Gupta *et al.* have reported a dye-doped LW (DDLW) formed from agarose doped with Reactive Blue 4 (RB4) dye [30, 31]; based on the work on CS in **Chapter 3** (**3.2.2**), it was thought that these films could be produced without the need for the RB4. Gupta *et al.* have also reported agarose-based MCLWs, which rely on the metal layer between the substrate and waveguide to produce a reflectivity peak at the resonance angle [32, 33]. This in turn allows for direct visualisation of the leaky mode. While this technique does produce excellent response and allow for the detection of 2.3 μM of methylene blue, the introduction of the metal layer is undesirable in terms of fabrication and cost. Hence, we have definitive proof that agarose can behave as a LW in both DDLW and MCLW configurations and aim to remove the requirement for dye doping and/or metal layers.

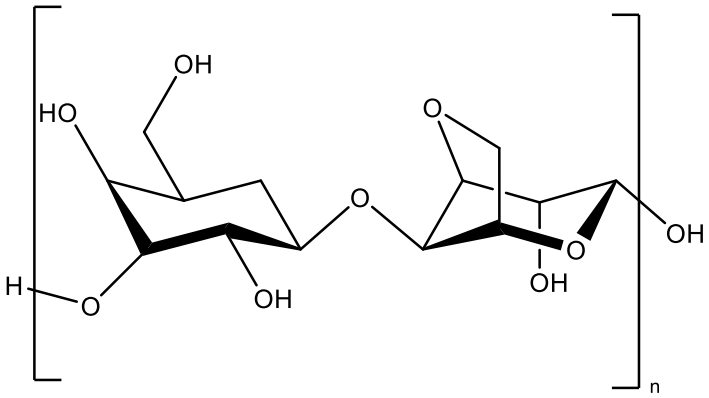

Figure 4.10. The structure of agarobiose.

Agarose is poorly soluble in water, but when adequate heat is applied it will dissolve and form a thick solution depending on the concentration of agarose used. When allowed to cool down, the solution will rapidly thicken and form a gel. This is a desirable quality as no crosslinker is required to form this gel, making the gel entirely non-toxic, physically and chemically inert, and hydrophilic [34].

As an inert natural polymer with easy gelation, agarose is ideal for LW preparation and was used to form LW films at 2% and 2.5% (w:v). To prevent premature gelation of the agarose solution, all equipment was heated to 70 °C and only removed from heat directly prior to spin coating. This included pipette tips and glass slides, reducing the opportunity for the agarose to start gelling before spin coating was carried out.

The 2% agarose LWs produced two- or three-moded films with clear definition, without the need for RB4 doping or a metal layer (**Figure 4.11**). This may be due to differences in batches of agarose in comparison to the data reported by Gupta *et al*. [30, 31], similar to the differences seen between batches of CS in **Chapter 3** (**3.2.2**). It is therefore suggested that batch-to-batch purification is carried out if agarose is to be used long-term, allowing for more consistent results.

Figure 4.11. Output image of a 2% agarose LW

The definition of these modes makes these films excellent for tracking, but the multi-moded nature is less ideal and may interfere with the sensor mode when used as a reference layer.

Moderate porosity was seen for the 2% agarose films, with the response for 10 kDa PEG very similar to that of 0.5% glycerol, and 85% of the response of 1% CS (**Figure 4.12**).

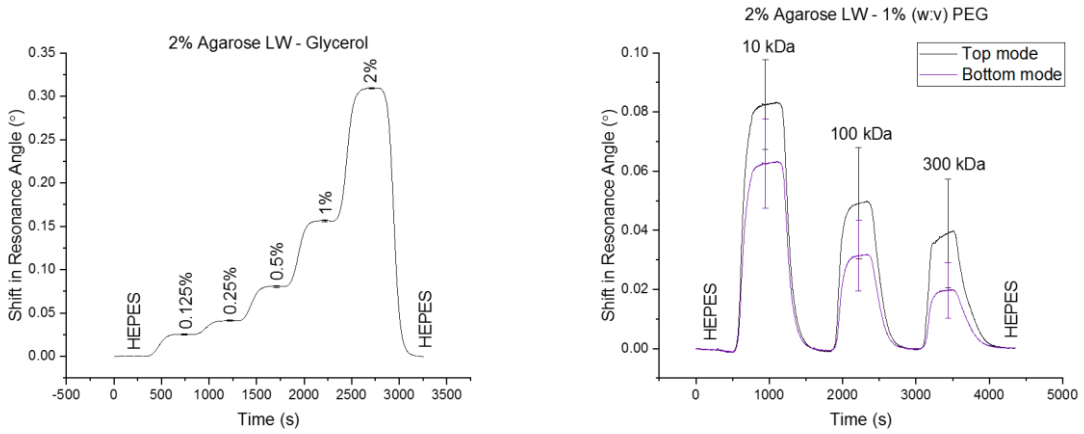

Figure 4.12. Glycerol (left) and PEG (right) runs on 2% agarose LWs. Error bars were calculated as 1σ across three different LWs.

There is also high variation in film-to-film response, suggesting these films do not form in a reproducible manner and indicates a low ranking of reproducibility. This was unfortunately expected, partly due to the necessity to keep the solution hot. Commercial spin coaters are not equipped with a heating function and the glass slide will rapidly cool down once removed from the hotplate. This leads to uneven gelation of the agarose on the glass. The time taken to prepare the slide and start spin coating is also an issue, as any discrepancies between slides will make themselves known in the uniformity of the final gel.

Similarly to the 0.96% PAAm LW, the response to 300 kDa PEG is half that of 1% CS to the same solution, with theoretical responses also comparable (**Table 4.2**).

Table 4.2. PEG response and percentage porosity of 2% agarose LWs.

1% PEG	RI (RIU)	THEORETICAL RESPONSE (°)	ACTUAL RESPONSE (°)	POROSITY (%)	ACTUAL VERSUS 1% CS RESPONSE (%)
10 kDa	1.33773	0.115247	0.099158	86.03	85.17
100 kDa	1.33774	0.116502	0.071017	60.95	51.00
300 kDa	1.33777	0.120268	0.057894	48.13	49.73

A respectable RIS of 125.53 ± 1.45 °/RIU was achieved, which is lower than that of CS but still suggests a reasonable level of sensitivity that could be considered compatible with CS (**Figure 4.13**). It is also higher than the 0.96% PAAm RIS.

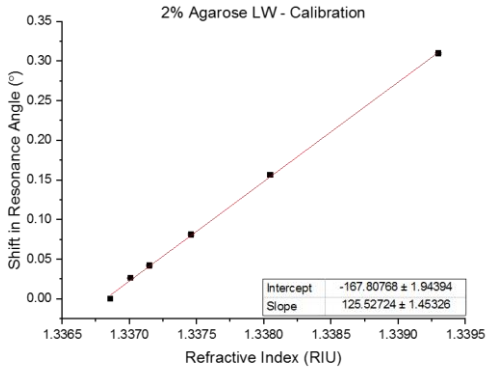

Figure 4.13. Calibration curve for 2% agarose LWs. Error bars were calculated as 1σ across three different LWs.

Next we tested the 2.5% agarose LWs, which were prepared in the same manner as the 2% (**Figure 4.14**).

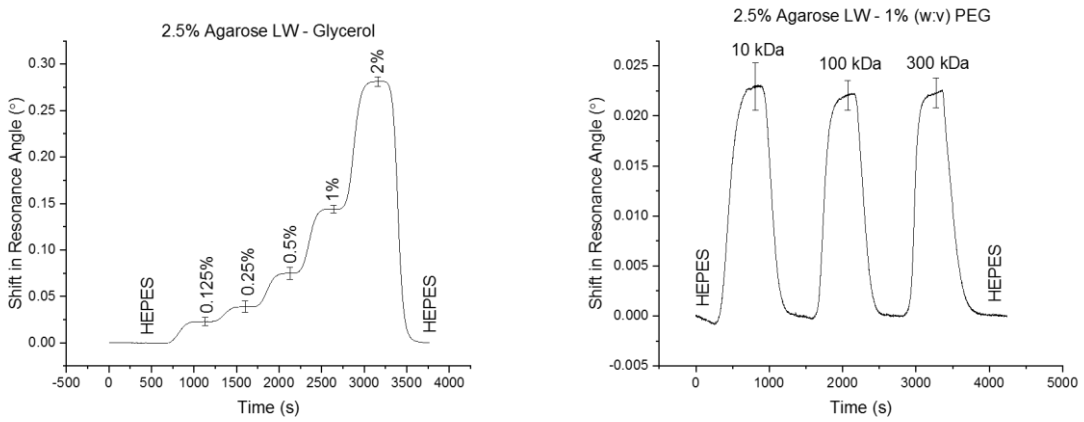

Figure 4.14. Glycerol (left) and PEG (right) runs on 2.5% agarose LWs. Error bars were calculated as 1σ across three different LWs.

The porosity of the 2.5% agarose LWs is extremely low. The films responded equally to all the different PEG MWs, suggesting that the response corresponds only to the change in RI at the surface of the film and none of the PEGs are actually able to enter the film.

When compared to both the theoretical response and versus the 1% CS response it is clear that the porosity is very poor (**Table 4.3**). The difference in porosity between the 2% and 2.5% agarose LWs shows the impact of a small change in concentration and highlights the need to determine the best concentration to achieve optimal results.

Table 4.3. PEG response and percentage porosity of 2.5% agarose LWs.

1% PEG	RI (RIU)	THEORETICAL RESPONSE (°)	ACTUAL RESPONSE (°)	POROSITY (%)	ACTUAL VERSUS 1% CS RESPONSE (%)
10 kDa	1.33773	0.097076	0.023572	24.28	20.25
100 kDa	1.33774	0.098237	0.022234	22.63	19.10
300 kDa	1.33777	0.101719	0.021688	21.32	18.63

2% Agarose gave a better RIS of 125.53 ± 1.45 °/RIU compared to 116.09 ± 1.52 °/RIU for 2.5% agarose; however, the film-to-film variability and uniformity was much improved for the 2.5% agarose (**Figure 4.15**). This may be due to the solution being thicker and spreading more evenly across the surface of the slide. Against the success criteria 2.5% agarose is ranked as “high” for both uniformity and reproducibility.

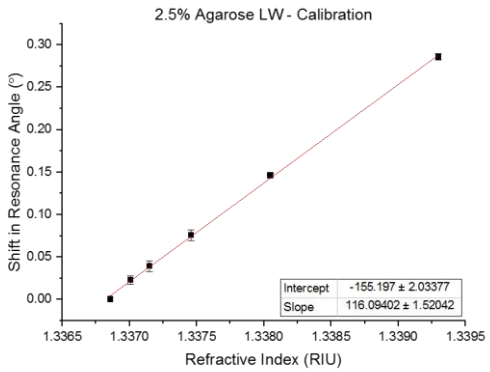

Figure 4.15. Calibration curve for 2.5% agarose LWs. Error bars were calculated as 1σ across three different LWs.

There is also a significant shift in position of the mode between the 2% and 2.5% LWs (**Figure 4.16**). The 2% LW modes are much closer to the TIR boundary, which may impact stacked film formation as the sensor layer mode may overlap with the reference layer mode.

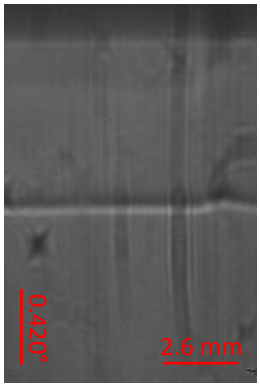

Figure 4.16. Output image of a 2.5% agarose LW.

The 2.5% LW mode is much further down, separating it from the sensor layers. This makes the 2.5% agarose most suited to combination with CS, but the severe reduction in porosity and sensitivity could pose issues.

4.2.4 4-arm-PEG$_{20,000}$-thiol and 4-arm-PEG$_{40,000}$-maleimide, 4-SH:4-MAL

As discussed in **Chapter 3** (**3.2.6**), the 4-arm-PEG$_{20,000}$-thiol:4-arm-PEG$_{40,000}$-maleimide (4-SH:4-MAL) LW films are not ideal for sensors due to low porosity and inactivity. These properties do not exclude them from behaving as reference layers; by reacting 4-SH:4-MAL in a 1:1 ratio there will be no free functional groups and the resulting gel should be inert.

These films were prepared with 5% glycerol included to improve the uniformity and spreading of the spin coated film by increasing viscosity. **Figure 4.17** shows a spin coated film with a clearly defined lower mode, and a less defined and skewed top mode. The lower mode is ideal for a reference as it should not overlap with a sensor mode, which is likely to be closer

to the TIR as it is more porous. The skewed upper mode is less useful, owing both to the positioning and the lopsided orientation.

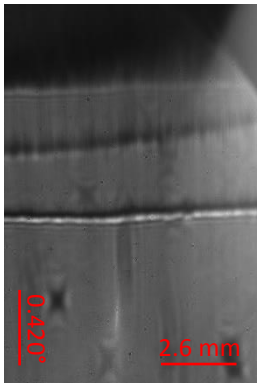

Figure 4.17. Output image of a 5% 4-SH:4-MAL LW with 5% glycerol (1:1).

As expected, these films have very low porosity due to the high crosslinking nature of the films (**Figure 4.18**). While this is not ideal, it does not rule these films out as reference layers as they will still be able to respond to changes within the sensing film above. It does however make them unsuitable for use as a reference layer on top of a sensing layer, as this will prevent the solution and analytes from reaching the sensing layer.

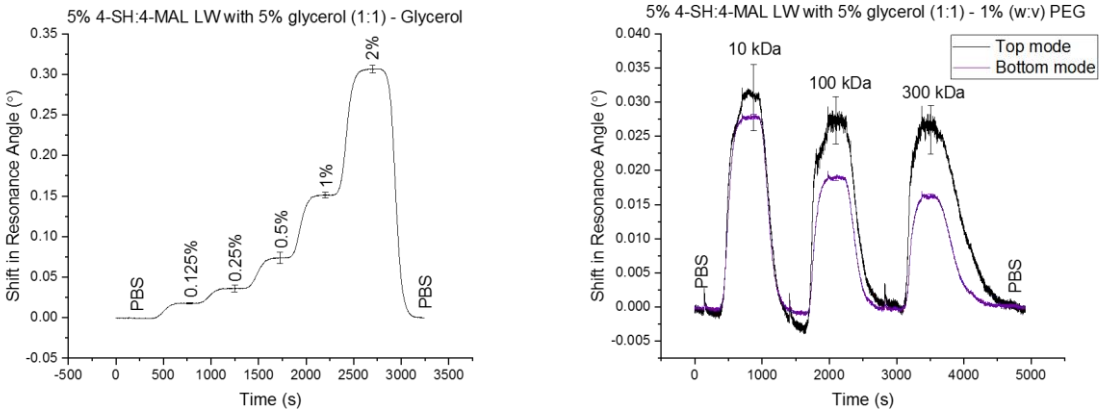

Figure 4.18. Glycerol (left) and PEG (right) runs on a 5% 4-SH:4-MAL LW with 5% glycerol (1:1). Error bars were calculated as 1σ across the width of one LW.

The low porosity is reminiscent of the 2.5% agarose films, with a slightly improved response, while the recorded response is significantly lower than the theoretical (**Table 4.4**).

Table 4.4. PEG response and percentage porosity of 5% 4-SH:4-MAL (1:1) LWs with 5% glycerol.

1% PEG	RI (RIU)	THEORETICAL RESPONSE (°)	ACTUAL RESPONSE (°)	POROSITY (%)	ACTUAL VERSUS 1% CS RESPONSE (%)
10 kDa	1.33639	0.132641	0.030732	23.17	26.40
100 kDa	1.33668	0.179697	0.027186	15.13	23.35
300 kDa	1.33682	0.202413	0.026483	13.08	22.75

The high RIS of 162.26 ± 6.78 °/RIU suggests these films will be sensitive to RI changes and are likely ideal for use when combined with a sensitive sensing layer (**Figure 4.19**).

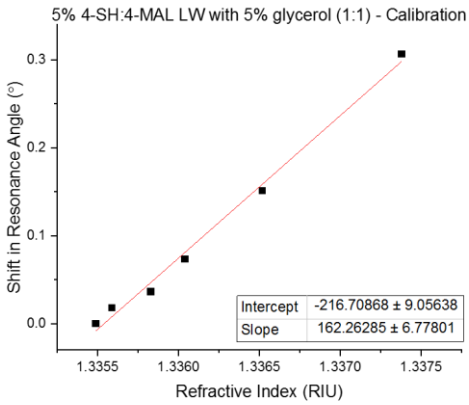

Figure 4.19. Calibration curve for a 5% 4-SH:4-MAL LW with 5% glycerol (1:1).

Unfortunately, the film-to-film uniformity was less ideal, making reproducibility an issue with these LWs. The double-moded output is also likely to cause further issues when combined with a sensing layer.

4.2.5 4-arm-PEG$_{20,000}$-aldehyde and 4-arm-PEG$_{2000}$-hydrazide, 4-CHO:4-HZ

Similar to the 4-SH:4-MAL films, the 4-arm-PEG$_{20,000}$-aldehyde:4-arm-PEG$_{2000}$-hydrazide (4-CHO:4-HZ) films were deemed unsuitable as sensing layers in **Chapter 3** (**3.2.7**). They were instead tested as reference layers in a 1:1 ratio.

Figure 4.20 shows the high uniformity of these films, with one highly defined mode and one fainter mode above. These films have high reproducibility from film to film, and both modes are uniform and narrow. Against the success criteria, these films are most similar to the 1% CS LWs.

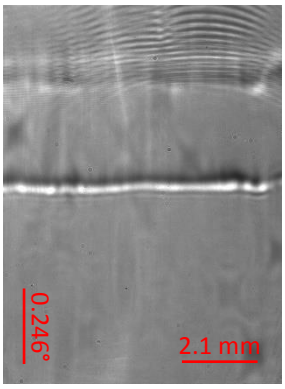

Figure 4.20. Output image of a 5% 4-CHO:4-HZ LW (1:1).

These films are even less porous than the 5% 4-SH:4-MAL and 2.5% agarose films and therefore have the same caveats; they may be useful as a reference layer below a sensing layer but cannot be used on top of the sensing layer (**Figure 4.21**).

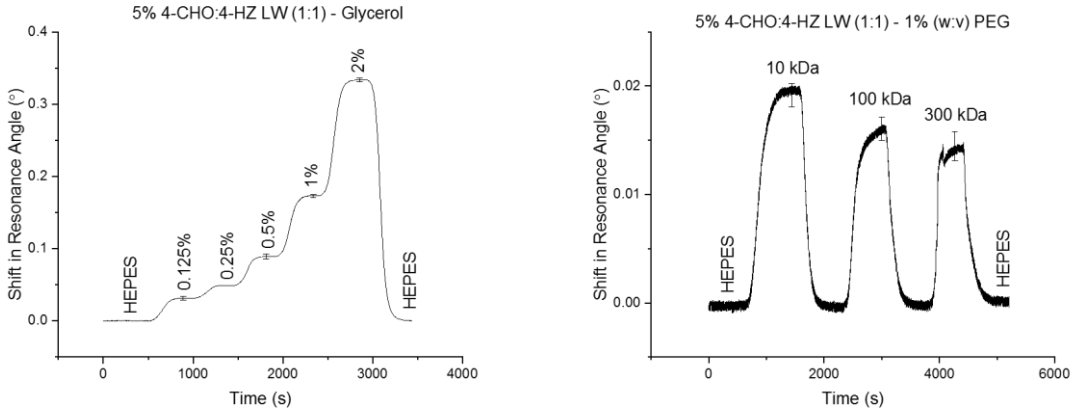

Figure 4.21. Glycerol (left) and PEG (right) runs on 5% 4-CHO:4-HZ LWs (1:1). Error bars were calculated as 1σ across three different LWs.

The porosity is exceedingly low compared to both the theoretical and 1% CS values (**Table 4.5**). This further implies that these films are poorly porous and not comparable to CS.

Table 4.5. PEG response and percentage porosity of 5% 4-CHO:4-HZ (1:1) LWs.

1% PEG	RI (RIU)	THEORETICAL RESPONSE (°)	ACTUAL RESPONSE (°)	POROSITY (%)	ACTUAL VERSUS 1% CS RESPONSE (%)
10 kDa	1.33773	0.129461	0.019838	15.32	17.04
100 kDa	1.33774	0.130802	0.016129	12.33	13.85
300 kDa	1.33777	0.134824	0.014097	10.46	12.11

On the other hand the RIS of these films is very close to that of the CS LWs at 134.07 ± 3.35 °/RIU compared to 144.23 ± 1.21 °/RIU, suggesting a sensitivity nearly on par with the CS LWs (92.96% of the CS response) (**Figure 4.22**). This implies they will be a good match for a stacked system including CS as they will be able to respond to RI changes in a very similar manner.

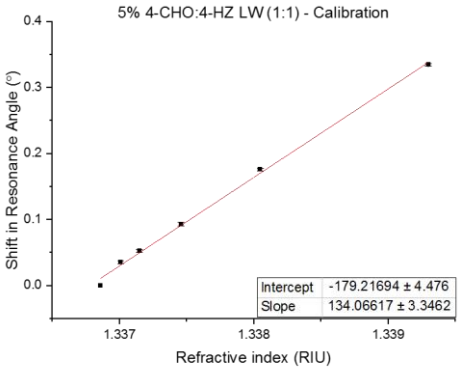

Figure 4.22. Calibration curve for 5% 4-CHO:4-HZ LWs. Error bars were calculated as 1σ across three different LWs.

Based on the response of each reference layer, the 4-CHO:4-HZ appears to be the most suitable for use as a reference layer with a CS sensing layer due to the similarities in RIS and consistent film formation. While the severely low porosity is an issue and would certainly render these LWs unsuitable if used as a reference layer on top of the sensor layer, the high RIS and ease of film formation suggest a high reproducibility and sensitivity regardless of the low porosity. By stacking the sensor layer on top of the reference layer the issues presented by the low porosity are minimised.

4.3 Stacked leaky waveguides

4.3.1 Poly(acrylamide-*co*-acrylic acid)/Poly(acrylamide), PAAm-Ac/PAAm

Poly(acrylamide-*co*-acrylic acid) (PAAm-Ac) and PAAm both contain the repeating poly(acrylamide) subunit; the clear similarities between the structures of these individual layers imply that they will respond similarly to fluctuations in environmental conditions. The additional acrylic acid moiety on the PAAm-Ac film will allow for protein immobilisation *via* the carboxylic acid, while the PAAm layer should remain unaffected.

2.88% (w:v) PAAm-Ac was deposited as the bottom layer, with 0.96% or 1.44% PAAm applied on top. This was to create an internal filtration system, with the PAAm preventing larger molecules from reaching the PAAm-Ac layer and becoming trapped. The output image of one such stacked film shows a clear lower dip but an uneven and faint upper dip when using the higher PAAm concentration (**Figure 4.23**). When the PAAm concentration is reduced the lower mode shifts up the output image and the upper mode becomes clearer although not uniform. This suggests that the lower PAAm concentration is better for this application as it leads to a clearer definition of both modes, but further work must be done to improve the uniformity of the stacked LWs.

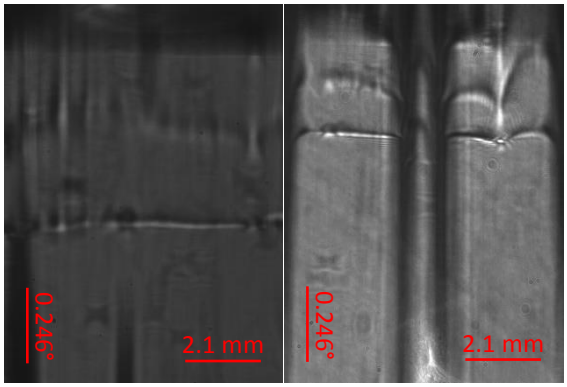

Figure 4.23. Output image of 2.88% PAAm-Ac/1.44% PAAm (left) and 2.88% PAAm-Ac/0.96% PAAm (right) stacked LWs.

The response of these films clearly shows variation between the two layers (**Figure 4.24**). The sensor layer built from PAAm-Ac has a lower response than the reference layer, PAAm. This is expected as the PAAm will be responding to any change in RI both within the bulk of the PAAm and at the surface of the PAAm. Conversely, the PAAm-Ac will be responding to changes in the RI within the bulk of the PAAm-Ac and the PAAm, but not at the surface of the PAAm. The PAAm will be blocking any larger PEG molecules from reaching the PAAm-Ac, therefore the response for PAAm-Ac will be lower.

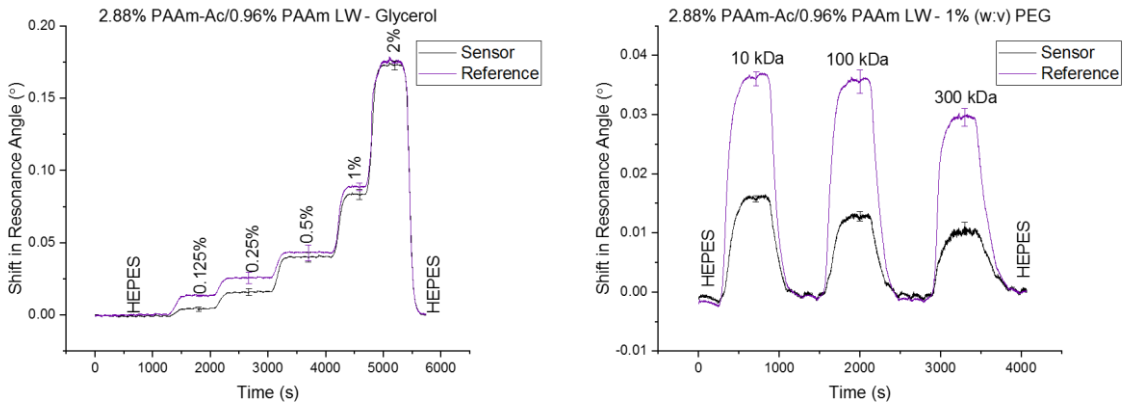

Figure 4.24. Glycerol (left) and PEG (right) runs on a 2.88% PAAm-Ac/0.96% PAAm stacked LW. Error bars were calculated as 1σ across the width of one LW.

However, the response of the PAAm-Ac layer in the stacked formation to the PEG solutions is significantly reduced from the response of a PAAm-Ac layer on its own, with the

response to 10 kDa PEG dropping to just 32% of the response seen for a single layer PAAm-Ac LW (**Table 4.6**). Additionally, the response of the PAAm layer also decreases to 53% of the single layer PAAm LW response.

Table 4.6. PEG response and percentage porosity of 2.88% PAAm-Ac/0.96% PAAm stacked LWs.

1% PEG	RI (RIU)	THEORETICAL RESPONSE (°)		ACTUAL RESPONSE (°)		POROSITY (%)	
		PAAm-Ac	PAAm	PAAm-Ac	PAAm	PAAm-Ac	PAAm
10 kDa	1.33836	0.053128	0.060668	0.025778	0.046337	48.52	76.38
100 kDa	1.33843	0.055956	0.063601	0.023217	0.037341	41.49	58.71
300 kDa	1.33844	0.056360	0.064020	0.018728	0.030061	33.23	46.96

The difference in response of the PAAm-Ac layer could be due to the PAAm on top in the stacked formation, blocking some of the solution from reaching the PAAm-Ac. It could also be due to the fabrication method; both layers use glutaraldehyde as the crosslinker, and it is possible that the use of this for the second layer also triggered additional crosslinking in the lower PAAm-Ac layer and reduced the porosity. Yet, this does not explain why the PAAm layer has also had such a drastic decrease in response. Nevertheless, there is a good definition between the sensor and reference layers.

When we look at the RIS values for these films there is some clear reductions when compared with the corresponding single layer LWs, with the RIS of the stacked film at 40.41 ± 0.79 °/RIU for PAAm-Ac and 41.91 ± 2.03 °/RIU for PAAm respectively (**Figure 4.25**).

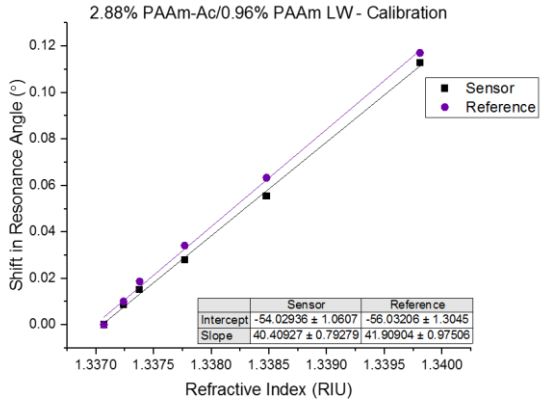

Figure 4.25. Calibration curve for a 2.88% PAAm-Ac/0.96% PAAm stacked LW.

The single layer LWs both have significantly higher RIS values than the stacked LWs, suggesting that the stacked formation has negatively impacted the sensitivity (**Table 4.7**). The stacked PAAm-Ac layer has a response 66.02% lower than that of the single layer LW, while the PAAm suffers a decrease of 43.32%.

Table 4.7. Comparison of the RIS values for single and stacked 2.88% PAAm-Ac and 0.96% PAAm LWs and the percentage difference between the two.

	SINGLE (°/RIU)	**STACKED (°/RIU)**	**DIFFERENCE (%)**
2.88% PAAm-Ac	118.94 ± 1.29	40.41 ± 0.79	66.02
0.96% PAAm	73.94 ± 2.77	41.91 ± 2.03	43.32

Regardless of this decrease, it is promising that the RIS values of both layers in the stacked LW are so similar. This implies that both layers will be equally sensitive to changes in RI, an ideal property for these films. Unfortunately, the low RIS does suggest that these films will not have the sensitivity required to detect small concentrations of biomolecules.

Against the success criteria these stacked LWs are ranked as “medium” for both reproducibility and uniformity, showing there is some potential for these films, but more development is required.

4.3.2 Poly(acrylamide)/Chitosan DDLW, PAAm/CS (doped)

While in **Chapter 3** (**3.2.2**) we discussed the benefits of non-doped CS LWs using purified CS, the work in this section was carried out before this was known. Therefore, 0.96% PAAm films were prepared and allowed to dry out before spin coating 1% CS on top and doping with RB4 for 5 minutes. This produced films such as the one seen in **Figure 4.26**. There are two modes in this configuration, but the formation is not uniform across the entire width of the film.

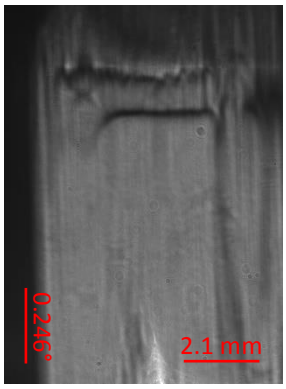

Figure 4.26. Output image of a 0.96% PAAm/1% CS stacked DDLW.

The glycerol run shows a slight difference in response between the modes, while the PEG run shows a clear difference (**Figure 4.27**). However, there has been a decrease in the porosity of the CS layer, with the response decreasing from 0.11° for 10 kDa PEG in single layer DDLWs to 0.09° in the stacked configuration. In fact, the response of the stacked CS DDLW layer remains relatively consistent for all PEG solutions. This implies that the porosity of these stacked films has been decreased when compared to the single layer DDLWs. Similarly, the PAAm layer has also seen a decrease in response.

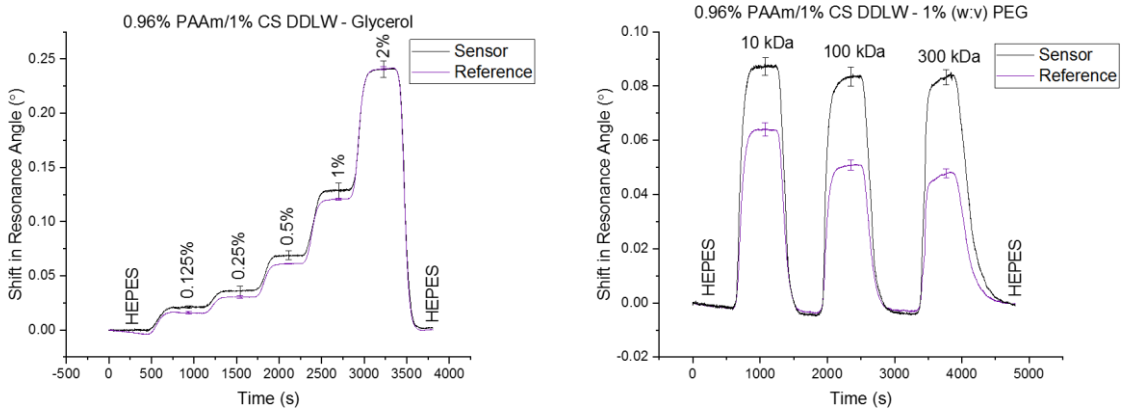

Figure 4.27. Glycerol (left) and PEG (right) run on a 0.96% PAAm/1% CS stacked DDLW. Error bars were calculated as 1σ across the width of one LW.

The PAAm films have a larger reduction in response compared to their theoretical value than the CS, which can be attributed to the blocking effect of the CS layer above (**Table 4.8**).

Table 4.8. PEG response and percentage porosity of 0.96% PAAm/1% CS stacked LWs.

1% PEG	RI (RIU)	THEORETICAL RESPONSE (°)		ACTUAL RESPONSE (°)		POROSITY (%)	
		CS (RB4)	PAAm	CS (RB4)	PAAm	CS (RB4)	PAAm
10 kDa	1.33836	0.113399	0.118074	0.087199	0.063889	76.90	54.11
100 kDa	1.33843	0.119435	0.124175	0.083325	0.050719	69.77	40.84
300 kDa	1.33844	0.120297	0.125046	0.082658	0.047130	68.71	37.69

The RIS values for both layers were determined to be 86.22 ± 1.64 °/RIU and 87.15 ± 0.95 °/RIU for the CS DDLW and PAAm LW layers respectively (**Figure 4.28**).

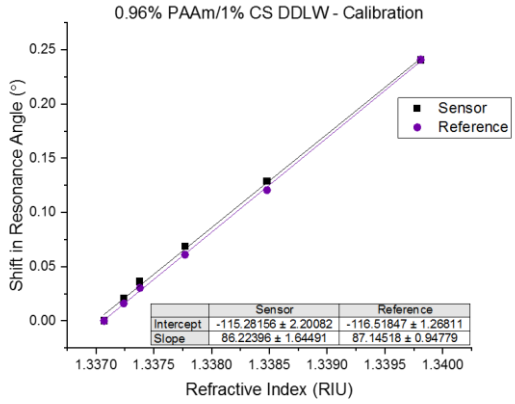

Figure 4.28. Calibration curve for a 0.96% PAAm/1% CS stacked DDLW.

Uniformity and reproducibility have been classed as "medium", and comparing the RIS values it is seen that the single layer CS DDLW has a significantly higher RIS than the same film in the stacked conformation (**Table 4.9**). The stacked film sees a reduction in response of 38.60% compared to the single layer CS DDLW, indicating a significant loss in sensitivity. The PAAm RIS has increased slightly, and both the CS and PAAm in the stacked DDLWs have similar RIS values. This is a good sign for consistent sensitivity across both films and therefore accurate referencing, but the sharp reduction in RIS for the CS DDLW is not ideal.

Table 4.9. Comparison of the RIS values for single and stacked 1% CS (doped) and 0.96% PAAm LWs and the percentage difference between the two.

	SINGLE (°/RIU)	**STACKED (°/RIU)**	**DIFFERENCE (%)**
1% CS (DOPED)	140.43 ± 1.53	86.22 ± 1.64	38.60
0.96% PAAm	73.94 ± 2.77	87.15 ± 0.95	-17.87

4.3.3 Poly(acrylamide/Chitosan LW, PAAm/CS

Due to the inherent properties of CS, this configuration required the referencing layer of PAAm to be placed below the CS. This is because the CS films must not be allowed to dry out, as this causes the pores to collapse and cannot be rehydrated to the original state. The

PAAm layer therefore cannot be spin coated on top of the CS, as the liquid in the CS film would prevent the PAAm from forming a smooth and uniform layer. Thus, for the PAAm/CS films, PAAm was deposited first and allowed to dry out overnight. CS was added the following day, after which the films could be stored in buffer solution. The main disadvantage of this technique is the lack of internal filtration system, as the sample and any interferents will come into direct contact with the CS film rather than first passing through the PAAm for size-exclusion.

An advantage of this technique is the ability to form the reference layer first and therefore ensure it is uniform and suitable to be used before adding the sensing layer. As the CS single layer LWs have high reproducibility and uniformity in comparison to the PAAm layer, the PAAm layer can be perfected before adding the CS.

Unfortunately, these films have very low uniformity and reproducibility. **Figure 4.29** shows one of these films with varied modes; on the left there is a top mode merged with the TIR and a partial lower mode, while on the right there is a single mode a reasonable distance from the TIR. This lack of uniformity will certainly impact the results obtained with these films.

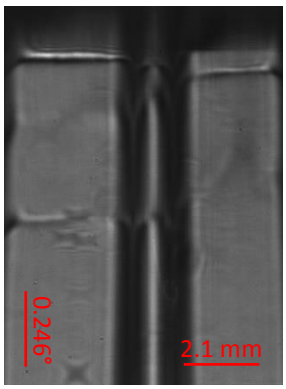

Figure 4.29. Output image of a 0.96% PAAm/1% CS stacked LW under a two-channel flow cell.

Figure 4.30 shows a PEG run on a single PAAm/CS stacked LW. There is a very clear visible difference in porosity between the two layers, with the CS layer being significantly more porous.

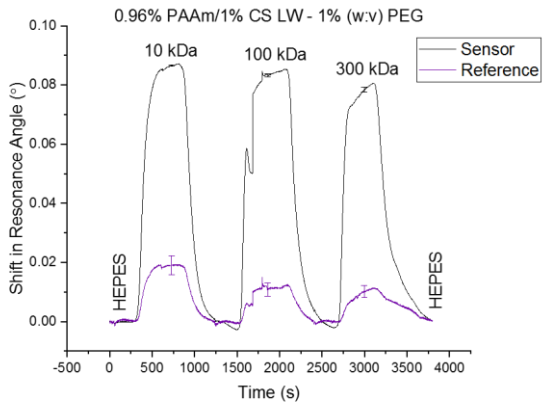

Figure 4.30. PEG run on a 0.96% PAAm/1% CS stacked LW. Error bars were calculated as 1σ across the width of one LW.

It is however worth noting that the porosity of the CS layers in this stacked conformation is slightly lower than in single CS LWs, dropping from 0.12° to 0.9° for 10 kDa PEG. This could be due to the influence of the PAAm layer. The PAAm layer also has reduced porosity compared to single layer LWs but this is expected for two reasons:

1. The CS layer above will slow down the flow of the PEG into the PAAm.
2. The PAAm layer has been re-exposed to glutaraldehyde during the CS crosslinking process. This may have caused additional crosslinking within the PAAm layer itself, further reducing porosity.

To test the effect of additional glutaraldehyde exposure on a single layer PAAm film, 0.05% glutaraldehyde was used to treat the film and the response measured (**Figure 4.31**).

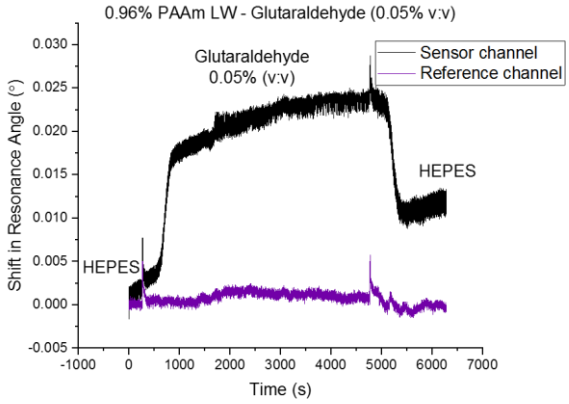

Figure 4.31. 0.96% PAAm LW treated with glutaraldehyde.

It is clearly visible that exposure to more glutaraldehyde causes a permanent change within the films and implies that the porosity will therefore be reduced.

Overall, the lack of uniformity and reproducibility along with the potential for additional PAAm crosslinking due to glutaraldehyde use during CS formation suggest that these stacked films are not ideal for further investigation in their current form. Further work could be done to improve PAAm uniformity and to assess the effects of additional glutaraldehyde exposure to the PAAm film, but this has not been investigated at this time.

4.3.4 Agarose/Chitosan, Agarose/CS

2.5% Agarose films were prepared and allowed to dry out overnight. 1% CS was spin coated on top, and the films were left to rehydrate for a further 24 h. This produced stacked films such as in **Figure 4.32**.

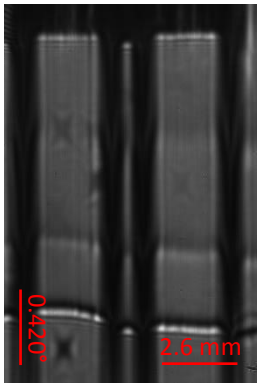

Figure 4.32. Output image of a 2.5% agarose/1% CS stacked LW under a two-channel flow cell.

When these films are compared with the 2.5% agarose single layer LWs there is a clear addition of a second mode, along with a very faint third mode closest to the TIR. The CS mode was expected to be much closer to the TIR as seen in the CS single layer LWs, but this was not the case.

The stacked films were characterised with glycerol and PEG (**Figure 4.33**). The glycerol run shows a slight difference between the two trackable modes, while the PEG run is more unusual. It appears that:

- The film is more porous to higher MWs.
- The reference layer is slightly more porous than the CS layer to 10 kDa PEG.
- There is no real difference between the modes.

These properties can be explained by considering that the films are not rehydrated to their full porosity when treated with the 10 kDa PEG; the 10 kDa PEG molecules may be slowly entering the film and opening the pores, allowing for the larger PEG molecules to fit in more easily afterwards. Additionally, the lack of difference in response for each mode suggests that there may be some level of merging of the two layers. This would prevent the agarose from behaving as a fully inert film, while the CS porosity would be reduced by the agarose.

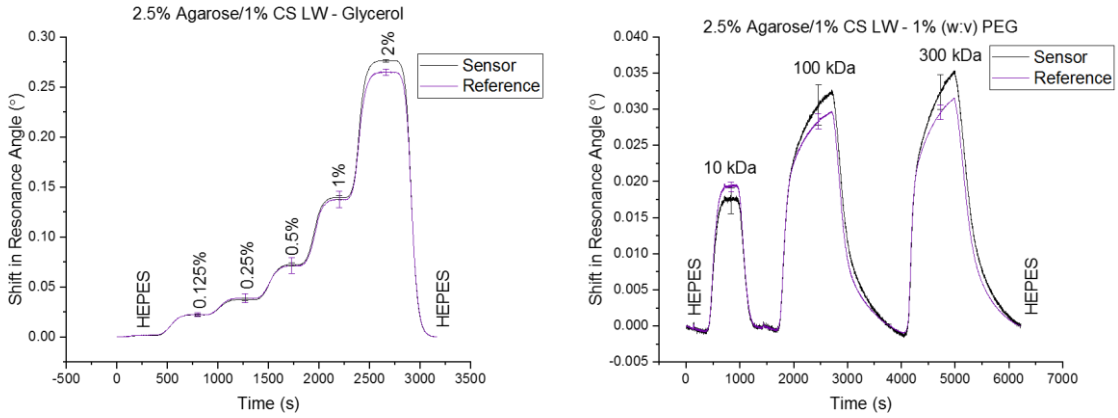

Figure 4.33. Glycerol (left) and PEG (right) run on a 2.5% agarose/1% CS stacked LW. Error bars were calculated as 1σ across the width of one LW.

The similarities in response are clearly shown in **Table 4.10** alongside the poor porosity compared to the theoretical values.

Table 4.10. PEG response and percentage porosity of 2.5% agarose/1% CS stacked LWs.

1% PEG	RI (RIU)	THEORETICAL RESPONSE (°)		ACTUAL RESPONSE (°)		POROSITY (%)	
		CS	Agarose	CS	Agarose	CS	Agarose
10 kDa	1.33822	0.155645	0.151749	0.017552	0.019368	11.28	12.76
100 kDa	1.33827	0.161228	0.157088	0.031176	0.028798	19.34	15.33
300 kDa	1.33831	0.165695	0.161359	0.033782	0.030527	20.39	18.92

The calibration curve for these stacked films produces an RIS of 111.66 ± 2.99 °/RIU for the CS layer and 106.77 ± 3.12 °/RIU for the agarose (**Figure 4.34**).

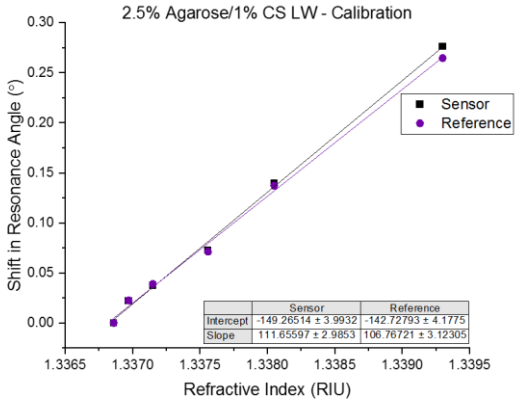

Figure 4.34. Calibration curve for a 2.5% agarose/1% CS stacked LW.

When considering the RIS values, there is a clear reduction in sensitivity versus the single layer LWs, particularly for the CS (**Table 4.11**). The similarity in RIS between the two modes in the stacked configuration may further indicate merging of the layers.

Table 4.11. Comparison of the RIS values for single and stacked 1% CS and 2.5% agarose LWs and the percentage difference between the two.

	SINGLE (°/RIU)	STACKED (°/RIU)	DIFFERENCE (%)
1% CS	144.23 ± 1.21	111.66 ± 2.99	22.58
2.5% AGAROSE	116.09 ± 1.52	106.77 ± 3.12	8.03

While the RIS decrease is not as severe as seen in other films, these LWs do not seem very promising for stacked LWs due to the multiple issues surrounding porosity, sensitivity, and medium reproducibility, therefore further work was discontinued on these LWs.

4.3.5 4-arm-PEG$_{20,000}$-thiol:4-arm-PEG$_{40,000}$-maleimide/Chitosan, 4-SH:4-MAL/CS

The 4-SH:4-MAL films were prepared with 5% glycerol to maintain even gel formation before drying out overnight. 1% CS was then spin coated on top, and the films were left to rehydrate for 24 h.

Figure 4.35 shows one of these stacked films, with the brighter lowest mode corresponding to the reference layer and the two upper modes corresponding to the CS sensing layer. The formation of these modes is not entirely uniform but is more consistent than in some of the other stacked films, leading to a ranking of “medium” uniformity but “low” reproducibility from film-to-film.

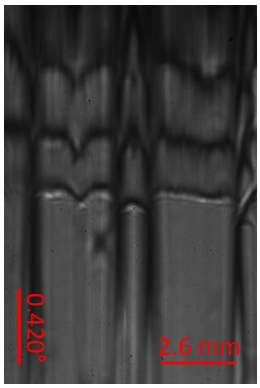

Figure 4.35. Output image of a 5% 4-SH:4-MAL with 5% glycerol (1:1)/1% CS stacked LW under a two-channel flow cell.

The PEG run for these films shows a good separation between the two main modes, with the CS layer producing the highest response (**Figure 4.36**). However, the porosity of this layer is much lower than that of a single layer CS LW, which is around 0.11° compared to the significantly reduced value of 0.03° seen here for 10 kDa PEG. This is extremely discouraging for protein sensing as it suggests that larger biomolecules will not be able to attach within the bulk of the sensing layer and instead will be restricted to the surface.

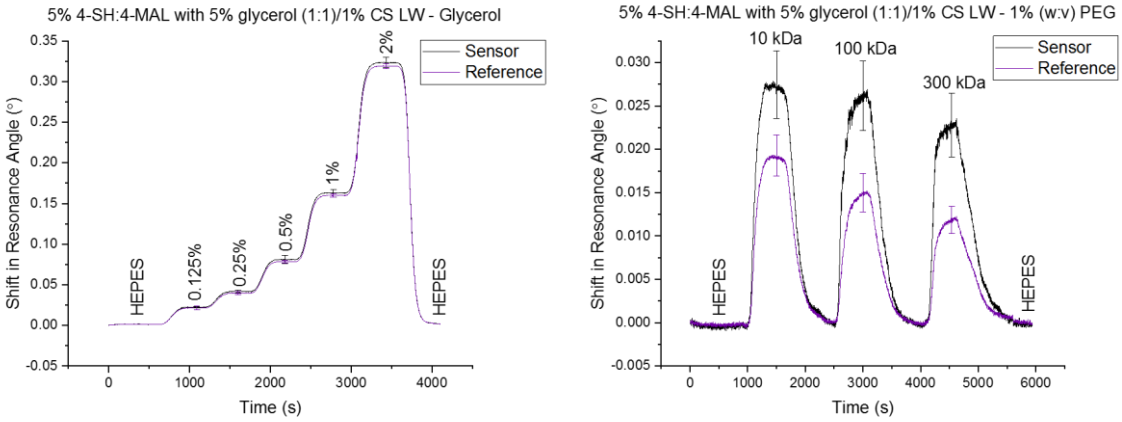

Figure 4.36. Glycerol (left) and PEG (right) run on a 5% 4-SH:4-MAL with 5% glycerol (1:1)/1% CS stacked LW. Error bars were calculated as 1σ across the width of one LW.

Table 4.12 shows the low actual percentage porosity compared to the theoretical response. While the theoretical data shows us that both layers should have similar and significant responses to each PEG if they are porous, the low real values show this is not the case and the porosity is severely impacted in this stacked formation.

Table 4.12. PEG response and percentage porosity of 5% 4-SH:4-MAL with 5% glycerol (1:1)/1% CS stacked LWs.

1% PEG	RI (RIU)	THEORETICAL RESPONSE (°)		ACTUAL RESPONSE (°)		POROSITY (%)	
		CS	4-SH: 4-MAL	CS	4-SH: 4-MAL	CS	4-SH: 4-MAL
10 kDa	1.33810	0.129662	0.12718	0.027064	0.018888	20.87	14.85
100 kDa	1.33813	0.132933	0.130414	0.025195	0.013998	18.95	10.73
300 kDa	1.33814	0.134023	0.131492	0.022771	0.011636	16.99	8.85

The calibration data for these films shows an RIS of 109.02 ± 1.87 °/RIU for the CS layer and 107.80 ± 1.58 °/RIU for the 4-SH:4-MAL with 5% glycerol (1:1) (**Figure 4.37**).

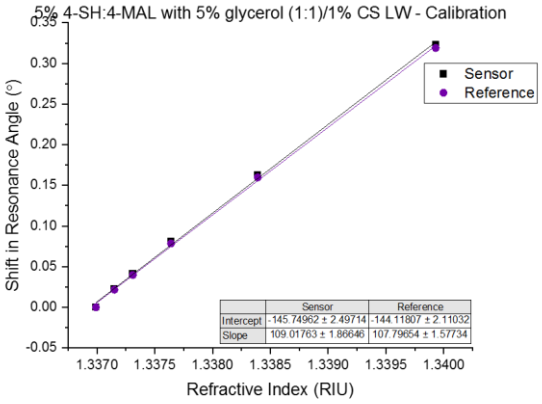

Figure 4.37. Calibration curve for a 5% 4-SH:4-MAL with 5% glycerol (1:1)/1% CS stacked LW.

Finally, the RIS values are compared for the single and stacked films; both layers have seen a reduction in sensitivity, and this is unsurprising when considering the extremely poor porosity (**Table 4.13**). As less of the analyte is able to diffuse into the LWs the sensitivity is confined to the interface between the sensor LW/sample for the sensor layer, and the reference LW/sensor LW interface for the reference LW.

Table 4.13. Comparison of the RIS values for single and stacked 1% CS and 5% 4-SH:4-MAL with 5% glycerol (1:1) LWs and the percentage difference between the two.

	SINGLE (°/RIU)	**STACKED (°/RIU)**	**DIFFERENCE (%)**
1% CS	144.23 ± 1.21	109.02 ± 1.87	24.41
5% 4-SH:4-MAL (1:1)	162.26 ± 6.78	107.80 ± 1.58	33.56

4.3.6 4-arm-PEG$_{20,000}$-aldehyde:4-arm-PEG$_{2000}$-hydrazide/Chitosan, 4-CHO:4-HZ/CS

The final configuration tested was expected to be the most suitable; the 4-CHO:4-HZ single layer LWs previously gave an RIS similar to that of single layer CS while also giving excellent reproducibility and uniformity.

Figure 4.38 shows the output of one such film. Both dips are uniform and very clear with excellent definition between the dips. This is very hopeful for the stacked layer configuration.

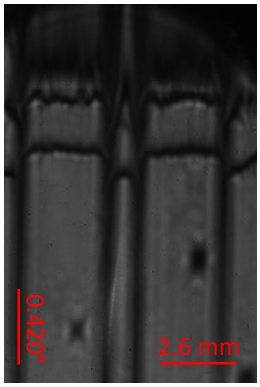

Figure 4.38. Output image of a 5% 4-CHO:4-HZ (1:1)/1% CS stacked LW under a two-channel flow cell.

The porosity of the CS appears to have dropped slightly, from 0.11° to 0.10° for 10 kDa PEG (**Figure 4.39**). However, the porosity of the 4-CHO:4-HZ layer has actually increased, from 0.02° to 0.035°. These minimal porosity changes are a good sign that the sensitivity and porosity will be consistent.

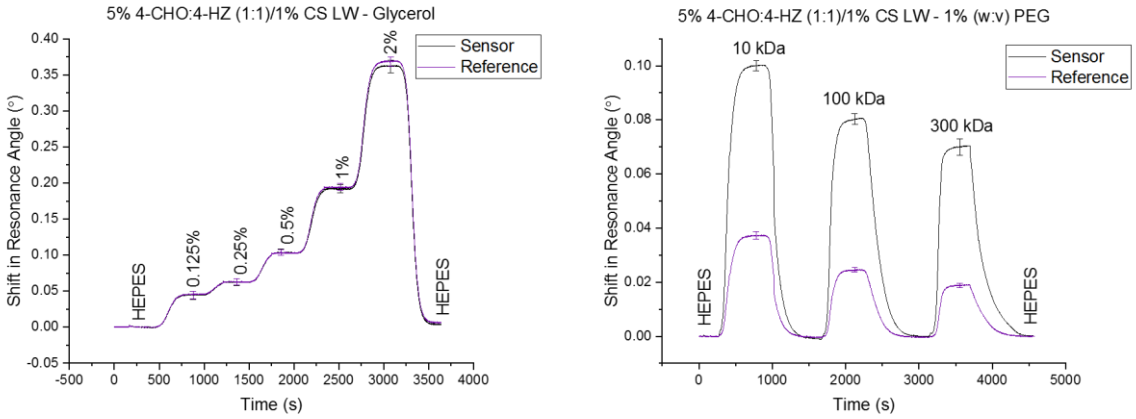

Figure 4.39. Glycerol (left) and PEG (right) runs on 5% 4-CHO:4-HZ (1:1)/1% CS stacked LWs. Error bars were calculated as 1σ across three different LWs.

In this configuration the CS has maintained a higher percentage porosity when compared to the other stacked configurations (**Table 4.14**). The 4-CHO:4-HZ films have a much

lower percentage porosity, but this was also the case for the single layer 4-CHO:4-HZ films and hence does not imply a significant difference between the single and stacked formations.

Table 4.14. PEG response and percentage porosity of 5% 4-CHO:4-HZ (1:1)/1% CS stacked LWs.

1% PEG	RI (RIU)	THEORETICAL RESPONSE (°)		ACTUAL RESPONSE (°)		POROSITY (%)	
		CS	4-CHO: 4-HZ	CS	4-CHO: 4-HZ	CS	4-CHO: 4-HZ
10 kDa	1.33773	0.133884	0.140583	0.097639	0.035514	72.93	25.26
100 kDa	1.33774	0.135341	0.142070	0.077673	0.023679	57.39	16.67
300 kDa	1.33777	0.139711	0.146532	0.066507	0.018120	47.60	12.37

The RIS values of the stacked films were 145.69 ± 3.39 °/RIU for the CS and 148.73 ± 3.25 °/RIU for the 4-CHO:4-HZ (1:1) (**Figure 4.40**).

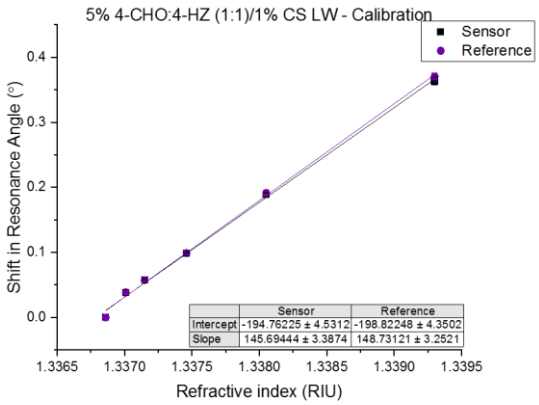

Figure 4.40. Calibration curve for 5% 4-CHO:4-HZ (1:1)/1% CS stacked LWs. Error bars were calculated as 1σ across three different LWs.

As expected, the RIS values between the single and stacked CS layers were consistent, while the 4-CHO:4-HZ layers increased (**Table 4.15**). This puts the sensitivity of both layers in the stacked conformation at a very similar value, indicating that both layers will respond to RI changes to the same degree.

Table 4.15. Comparison of the RIS values for single and stacked 1% CS and 5% 4-CHO:4-HZ (1:1) LWs and the percentage difference between the two.

	SINGLE (°/RIU)	STACKED (°/RIU)	DIFFERENCE (%)
1% CS	144.23 ± 1.21	145.69 ± 3.39	-1.01
5% 4-CHO:4-HZ (1:1)	134.07 ± 3.35	148.73 ± 3.25	-10.93

Overall, these 5% 4-CHO:4-HZ (1:1)/1% CS are the most uniform and consistent out of all the combinations attempted.

4.4 Reproducibility issues

Throughout the development and optimisation of these films there have been numerous issues with reproducibility and uniformity of certain hydrogel films. In some cases, these issues have been solved by purification of the polymers or changing the gelation components i.e., adding glycerol, while in other cases modifying the gelation conditions has improved the outcome.

The main source of reproducibility issues was caused during fabrication. There were some problems with achieving uniform films as single layer LWs, but these problems were exacerbated when translating to the stacked conformation as the bottom layer hydrogel changed the surface on which the top layer hydrogel was spin coated. This meant spin conditions had to be modified and could not always be optimised. In some cases, merging of the two layers was seen, while in other cases the top hydrogel wouldn't spread across the surface of the bottom hydrogel evenly leading to patchy film formation and uneven guided modes. Furthermore, any stacked devices which used the same crosslinker for both hydrogel layers, such as the PAAm and CS films, were at risk of causing additional crosslinking in the bottom layer when re-exposed to the crosslinker. This consequently reduced porosity and sensitivity of the bottom layer.

One major issue that presented at the end of the project was regarding the 4-CHO:4-HZ films. These are specialist polymers which were developed and purchased from an outside company rather than preparing them in-house. Throughout the course of the project two different batches of the polymers were purchased, with most of the work carried out using the first batch. Upon receipt of the second batch there was a clear difference in the behaviour

of the new aldehyde compared to the aldehyde of the previous batch. While the previous aldehyde dissolved with stirring in pH 4.0 acetate buffer, the new batch formed a very thick gel-like solution. If heated and stirred vigorously it would slowly dissolve but the resulting solution was still significantly more viscous than the previous batch and had a corresponding negative effect on gelation with the hydrazide.

The difference in behaviour of the two aldehydes highlights issues with different batches in all polymers; while one batch may produce the desired results, if there are any structural differences or impurities present in the next batch the results may not be concordant. The nuclear magnetic resonance (NMR) data for these compounds was supplied by Biopharma PEG Scientific Inc. and is presented in **Chapter 8** (**8.4.8**) with their permission. The NMR for the original batch is seen in **Figure 8.1**, while the second batch is presented in **Figure 8.2**.

As can be seen in the spectra, there is an additional peak around 2.0 ppm in the second batch of 4-CHO, along with some peak intensity differences. The 2.0 ppm peak could be left over from the synthesis method, but as this was not performed in house the procedure that was used is not known.

This difference in batches is clearly shown using the 4-arm-$PEG_{20,000}$-aldehyde batches but is likely to be a potential issue for the other polymers used too. For the other polymers only a single batch was needed throughout the project therefore this issue was not experienced but could be a problem in the future. Unless the purity and conformation of each polymer is exceedingly similar between batches, further optimisation may be required between batches which will not be ideal for mass production.

4.5 Summary

Throughout this chapter different combinations of inert and functionalised hydrogels have been investigated. The aim of this was to develop a stacked LW with an internal referencing layer incorporated into the structure of the device. This was expected to have the following advantages over single layer waveguides and multi-component internal referenced devices:

- Current instrumentation can be used without modification as no additional light source, prism, camera, flow cell etc. are required.
- Highly accurate internal referencing as both hydrogel layers would be subjected to the same conditions.
- Incorporation of an internal filtration system, in which large sample components are prevented from reaching the sensing layer and hence the opportunity for such components to adsorption to the sensor is minimised.

Results have been varied, with the response of the stacked LWs typically being lower than that of their individual counterparts. The use of CS as a sensing layer has prevented the development of an internal filtration system via the reference layer, but this can be achieved using the PAAm-Ac sensing layer instead.

The optimal configuration researched so far appears to be the 5% 4-CHO:4-HZ (1:1)/1% CS stacked LWs. This showed the lowest decrease in porosity from single to stacked conformations, with a consistently high RIS and low degree of film-to-film variability. However, the reproducibility issues caused by batch-to-batch differences must be addressed

sooner rather than later and will involve further optimisation and probable purification to remove any unreacted starting materials and/or side-products.

Overall, the stacked LWs have shown potential but are not yet on par with the results shown by the single layer LWs. This is likely due to fabrication issues, with films not forming uniform layers or merging into each other.

4.6 References

1. Syahir, A., et al., *Label and Label-Free Detection Techniques for Protein Microarrays.* Microarrays (Basel, Switzerland), 2015. **4**(2): p. 228-244.
2. Gupta, R. and N.J. Goddard. *A novel optical biosensor with internal referencing*. in *17th International Conference on Miniaturized Systems for Chemistry and Life Sciences*. 2013. Freiburg, Germany.
3. Daniels, J.S. and N. Pourmand, *Label-Free Impedance Biosensors: Opportunities and Challenges.* Electroanalysis, 2007. **19**(12): p. 1239-1257.
4. Chen, X., et al., *Label-free techniques for laboratory medicine applications.* Frontiers in Laboratory Medicine, 2017. **1**(2): p. 82-85.
5. Jensen, E.C., *Use of fluorescent probes: their effect on cell biology and limitations.* Anat Rec (Hoboken), 2012. **295**(12): p. 2031-6.
6. Bustos, R.H., et al., *Label-Free Quantification of Anti-TNF-α in Patients Treated with Adalimumab Using an Optical Biosensor.* 2018. **18**(3): p. 691.
7. Hulme, J., et al., *Internally-referenced resonant mirror for chemical and biochemical sensing.* Analyst, 2002. **127**(9): p. 1233-1236.
8. Yu, F. and W. Knoll, *Immunosensor with Self-Referencing Based on Surface Plasmon Diffraction.* Analytical Chemistry, 2004. **76**(7): p. 1971-1975.
9. Nenninger, G.G., et al., *Reference-compensated biosensing using a dual-channel surface plasmon resonance sensor system based on a planar lightpipe configuration.* Sensors and Actuators B: Chemical, 1998. **51**(1): p. 38-45.
10. Homola, J., H.B. Lu, and S.S. Yee, *Dual-channel surface plasmon resonance sensor with spectral discrimination of sensing channels using dielectric overlayer.* Electronics Letters, 1999. **35**(13): p. 1105-1106.
11. O'Brien II, M.J., et al., *SPR biosensors: simultaneously removing thermal and bulk-composition effects.* Biosensors and Bioelectronics, 1999. **14**(2): p. 145-154.
12. Lu, H.B., et al., *Protein contact printing for a surface plasmon resonance biosensor with on-chip referencing.* Sensors and Actuators B: Chemical, 2001. **74**(1): p. 91-99.
13. Akimoto, T., K. Ikebukuro, and I. Karube, *A surface plasmon resonance probe with a novel integrated reference sensor surface.* Biosens Bioelectron, 2003. **18**(12): p. 1447-53.
14. Zhang, H.Q., S. Boussaad, and N.J. Tao, *High-performance differential surface plasmon resonance sensor using quadrant cell photodetector.* Review of Scientific Instruments, 2003. **74**(1): p. 150-153.
15. Wu, S.Y., et al., *Highly sensitive differential phase-sensitive surface plasmon resonance biosensor based on the Mach–Zehnder configuration.* Optics Letters, 2004. **29**(20): p. 2378-2380.
16. Bahrami, F., et al., *Self-referenced spectroscopy using plasmon waveguide resonance biosensor.* Biomedical Optics Express, 2014. **5**(8): p. 2481-2487.
17. Donipudi, R., S. Pochiraju, and J.T. Hastings. *Self-referenced SPR sensing via simultaneous excitation of long- and short-range surface plasmons*. in *2006 Conference on Lasers and Electro-Optics and 2006 Quantum Electronics and Laser Science Conference*. 2006.
18. Hastings, J.T., et al., *Optimal self-referenced sensing using long- and short- range surface plasmons.* Optics Express, 2007. **15**(26): p. 17661-17672.
19. Nizamov, S. and V.M. Mirsky, *Self-referencing SPR-biosensors based on penetration difference of evanescent waves.* Biosensors and Bioelectronics, 2011. **28**(1): p. 263-269.
20. Cush, R., et al., *The resonant mirror: a novel optical biosensor for direct sensing of biomolecular interactions Part I: Principle of operation and associated instrumentation.* Biosensors and Bioelectronics, 1993. **8**(7): p. 347-354.

21. Gupta, R. and N.J. Goddard, *A Novel Optical Biosensor with Internal Referencing*, in *17th International Conference on Miniaturized Systems for Chemistry and Life Sciences*. 2013: Freiburg, Germany. p. 1490-1492.
22. Caulfield, M.J., G.G. Qiao, and D.H. Solomon, *Some Aspects of the Properties and Degradation of Polyacrylamides.* Chemical Reviews, 2002. **102**(9): p. 3067-3084.
23. EL Sharif, H.F., F. Giosia, and S.M. Reddy, *Investigation of polyacrylamide hydrogel-based molecularly imprinted polymers using protein gel electrophoresis.* Journal of Molecular Recognition, 2022. **35**(1): p. e2942.
24. Bio-Rad Laboratories Inc. *A Guide to Polyacrylamide Gel Electrophoresis and Detection*.
25. Dmitriev, I., et al., *Swelling behavior and network characterization of hydrogels from linear polyacrylamide crosslinked with glutaraldehyde.* Materials Today Communications, 2015. **4**: p. 93-100.
26. Subramani, R., et al., *The Influence of Swelling on Elastic Properties of Polyacrylamide Hydrogels.* Frontiers in Materials, 2020. **7**.
27. Calvet, D., J.Y. Wong, and S. Giasson, *Rheological Monitoring of Polyacrylamide Gelation: Importance of Cross-Link Density and Temperature.* Macromolecules, 2004. **37**(20): p. 7762-7771.
28. Marcus, J.B., *Chapter 2 - Food Science Basics: Healthy Cooking and Baking Demystified: The Science behind Healthy Foods, Cooking and Baking*, in *Culinary Nutrition*, J.B. Marcus, Editor. 2013, Academic Press: San Diego. p. 51-97.
29. Sigma Aldrich. *Agarose*. [cited 17-05-2022]; Available from: https://www.sigmaaldrich.com/GB/en/products/chemistry-and-biochemicals/biochemicals/agarose.
30. Gupta, R. and N.J. Goddard, *Optical waveguide for common path simultaneous refractive index and broadband absorption measurements in small volumes.* Sensors and Actuators B: Chemical, 2016. **237**: p. 1066-1075.
31. Gupta, R. and N.J. Goddard, *A proof-of-principle study for performing enzyme bioassays using substrates immobilized in a leaky optical waveguide.* Sensors and Actuators B: Chemical, 2017. **244**: p. 549-558.
32. Gupta, R., et al., *Absorption spectroscopy in microfluidic flow cells using a metal clad leaky waveguide device with a porous gel waveguide layer.* Analyst, 2013. **138**(1): p. 307-314.
33. Gupta, R. and N.J. Goddard, *Broadband absorption spectroscopy for rapid pH measurement in small volumes using an integrated porous waveguide.* Analyst, 2017. **142**(1): p. 169-176.
34. Zucca, P., R. Fernandez-Lafuente, and E. Sanjust, *Agarose and Its Derivatives as Supports for Enzyme Immobilization.* Molecules, 2016. **21**(11): p. 1577.

5 Chapter 5 – Protein Detection

5.1 Introduction

For practical applications of this biosensor, the films need to be able to accurately detect clinically relevant levels of certain biomolecules. To achieve this the films must be developed to contain a functional group appropriate for further modification and hence lead to protein immobilisation for detection. Primarily we have focused on producing films with free primary amine groups to allow for easy linking of immobilisation agents. Immobilisation strategies in literature use one of five broad methods [1, 2]:

- Physical adsorption/physisorption.
- Encapsulation/entrapment.
- Covalent bonding.
- Crosslinking (extreme form of covalent bonding).
- Bioaffinity bonding.

Each of these methods has advantages and disadvantages and the decision of which method to use must be carefully chosen based on these.

Physical adsorption is the most straightforward and cheapest of the five methods, carried out by immersing the support in a solution of the protein (**Figure 5.1**). This is a very simple method and typically will not reduce enzyme/antibody activity which makes it useful for protein assays. On the other hand, this method produces weak bonding *via* interactions such as electrostatic, van der Waals, hydrophobic, and hydrogen bonding. This makes the technique reversible which can be useful in some situations as it allows for regeneration of

the support but may have a negative impact on the sensitivity of the sensor. This also makes it very sensitive to environmental changes such as pH, ionic strength, and temperature fluctuations [1, 3]. Another aspect to consider is the orientation of protein adsorption, as this cannot be controlled and can cause a reduction in activity [3].

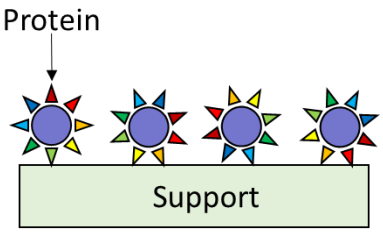

Figure 5.1. Physical adsorption [4, 5].

On the other hand, encapsulation and entrapment are irreversible techniques, making them perfect for permanent immobilisation but removing the opportunity for reuse of the support and therefore increasing the cost. In encapsulation the proteins are surrounded by a semi-permeable membrane, while in the entrapment technique the enzymes or antibodies are trapped within the structure of the support material (**Figure 5.2**). This prevents the antibody from leaving the matrix, but the analyte is able to move in and out of the structure and bind where possible. This involves tailoring of the support material to provide a pore size suitable for entrapping the antibody but allowing the free movement of the analyte which can prove challenging. If the pore size is incorrect it can lead to antibody leakage, deactivation, low loading capability, and slow response due to difficulty of the analyte moving through the matrix. The thickness of the support is also a factor to consider [1, 3]. Hydrogels and sol-gels are particularly suited for this technique as the pore size can be easily tailored [3].

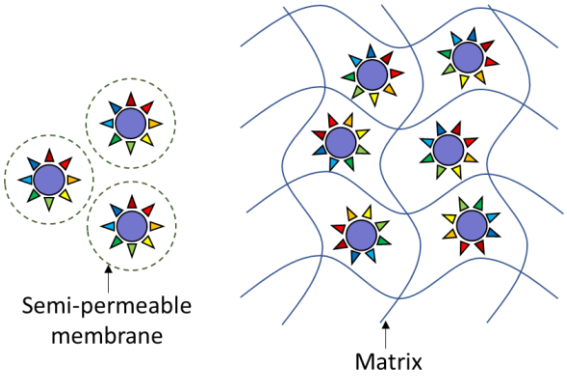

Figure 5.2. Encapsulation (left) and entrapment (right) [4, 5].

Covalent binding and crosslinking also form irreversible bonds (**Figure 5.3**). As the reliance is not on pore size, but instead a strong covalent bond between the support and the antibody, leaching is reduced and bonding is high. However, as these techniques involve the use of functional groups on the protein it can lead to a loss in activity and reactivity of the protein itself, particularly if a single protein is able to bind in multiple regions to the support. This could have negative implications if those regions of the protein are needed for further binding during the immobilisation strategy. It is also difficult to control uniform immobilisation and therefore reproducibility can be an issue with this technique. Nevertheless, the strong bonds formed are highly suited to preventing leaching and improving robustness [1].

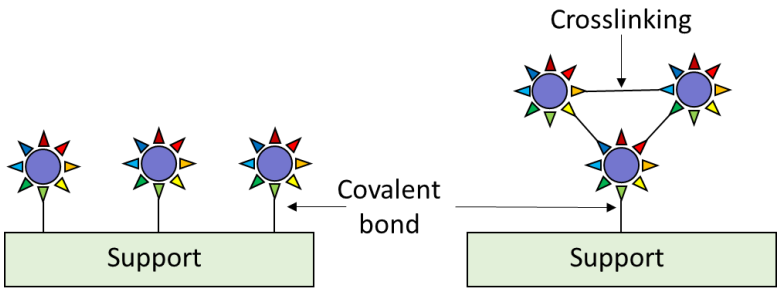

Figure 5.3. Covalent binding (left) and crosslinking with covalent binding (right) [4, 5].

Finally, bioaffinity immobilisation relies on the natural affinity of one protein to a complementary biomolecule. This is a reversible technique and is often used in conjunction with covalent binding. An affinity ligand/antibody is attached to the support, followed by addition of the complementary protein *via* bioaffinity binding (**Figure 5.4**). This is an advantageous method as it can achieve high specificity and selectivity along with predictable orientation. Some complementary biomolecules are very well reported such as the (strept)avidin-biotin interaction with a 1.3 x 10^{-15} M dissociation constant, making it one of the strongest noncovalent affinities recorded thus far [2]. Protein A-Immunoglobulin G (IgG) is another well-reported complementary pair, with various types available for different animal species [2]. Unfortunately, the affinity ligands tend to be expensive, increasing the cost of this technique significantly. The covalent binding used to attach the affinity ligand must also be carefully selected to prevent damage to the binding region. Both the streptavidin-biotin and Protein A-IgG interactions are used within this chapter.

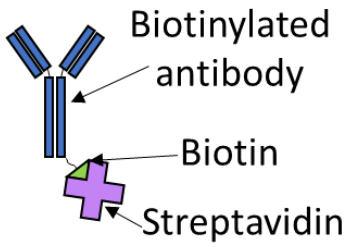

Figure 5.4. Bioaffinity binding of streptavidin to biotin [6].

It is not only the immobilisation strategy that must be considered. Biosensors use antibodies or antigens as receptors to bind the desired analyte, but an unfortunate issue with such techniques is that both desired antibodies and undesired interferents in the sample matrix often adsorb to a surface or molecule non-specifically. This is called non-specific

adsorption (NSA), or biofouling, and causes issues with both qualitative and quantitative measurements. NSA can be classified into two different types [7, 8]:

- Immunological NSA. This is caused by antibody/antigen affinity and likely requires changing the antibody/antigen pair to solve.
- Methodological NSA.
    - Protein-protein adsorption *via* electrostatic or hydrophilic/ hydrophobic interactions.
    - Mis-orientation of analyte and/or receptor.
    - Denaturation of analyte and/or receptor.
    - Substrate reactivity due to available reactive groups.
    - Substrate charge due to pH.
    - Free substrate space allowing for aggregation.

As immunological NSA is not commonly a problem found in laboratory samples, this chapter will focus on protein immobilisation with interference *via* methodological NSA [7]. In turn, NSA can be split into four broad methods [7]:

- Adsorption of desired analyte onto non-immunological sites, reducing the concentration of analyte available to bind to the recognition element.
- Adsorption of foreign molecules onto the recognition elements, which can block the sensing site and also provide a false-positive/negative signal.
- Adsorption of the analyte and/or foreign molecules to the surface of the sensor, leading to aggregation and possible false-positives/negatives depending on the sensing method.

- Adsorption of foreign molecules to the analyte, causing increased signals and masking of the intended signal.

As biosensors are often required to detect very small concentrations of an analyte in an unclean sample matrix, it is important to reduce the extent of NSA as far as possible to allow for an accurate and quantitative response. This is particularly important for a sensor such as the leaky waveguide (LW), which is designed to maximise the surface area available for binding and therefore carries a high risk of NSA.

For this reason, two types of blocking method have been investigated in this chapter. First is physical blocking, which uses blocking agents such as the proteins bovine serum albumin (BSA) [9-12] and casein [10, 13]. These are cheap and readily available, but can cause further issues by non-specifically binding to analytes themselves, and also by blocking receptor sites [14].

The second type explored in this chapter is chemical blocking, which involves reacting a blocking agent directly with the surface of the hydrogel and forming a stable covalent bond with no free reactive groups.

For this chapter protein immobilisation was first carried out on single layer LW films to assess the sensitivity and practicality of the films and immobilisation techniques. Once reproducible results were obtained, the best techniques were applied to stacked films, achieving internally referenced protein immobilisation while also allowing for the comparison in sensitivity between the single and stacked films. Finally, the effect of different sample matrices were investigated using synthetic urine and human serum.

For the duration of this chapter, 1% chitosan (CS) LWs were used as the single layer sensing waveguides, while the reference layer of the stacked waveguides varies and will be clearly stated.

5.2 Immunoglobulin G, IgG

The first protein detected was immunoglobulin G, abbreviated as IgG (**Figure 5.5**). IgG is an abundant antibody found in blood serum and is relatively cheap to purchase. This allowed for the investigation of multiple protein immobilisation strategies to optimise the process, using IgG as the exemplar analyte.

Classic methods of IgG detection lean towards enzyme-linked immunosorbent assays (ELISA), discussed in more detail in **Chapter 1** (**1.3**). For example, a sheep IgG ELISA kit from abcam boasts a sensitivity of 4.28 ng/mL [15], while a human IgG ELISA kit from the same manufacturer has a sensitivity of 0.02 ng/mL[16]. Typical levels of IgG in human serum range from 8 – 17 mg/mL [17], making it an excellent target to assess the response of a protein immobilisation strategy before reducing the detectable concentration. Commercially available ELISA tests can detect IgG well below the average levels in a quantitative manner, making them suitable for detecting the presence of IgG in samples. Yet, as we already discussed, ELISA has problems including but not limited to expensive and lengthy protocols and the use of labels.

For our IgG tests, concentrations between 0.1 – 1 mg/mL were typically employed so that clear and visible binding could be seen instantaneously without overloading the sensor.

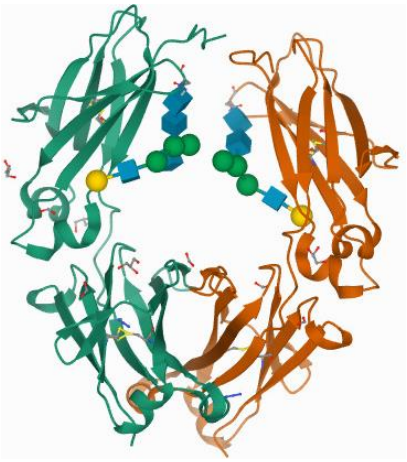

Figure 5.5. Crystal structure of rabbit IgG Fc Fragment [18].

Initially sensing was performed by binding biotin anti-IgG (biotin A-IgG) to the film and used to detect sheep IgG. However, further studies proved that protein A biotin (PAB) was able to bind more strongly to the linking agent, therefore PAB replaced biotin A-IgG. Consequently the sheep IgG was then replaced with rabbit IgG which has a much stronger binding affinity with protein A than sheep IgG [19]. Therefore, the strategies discussed below which use PAB also use rabbit IgG.

5.2.1 Non-specific binding

Throughout the development of protein immobilisation strategies 1% CS LWs were used and non-reproducible results were consistently causing issues in protein detection. CS is already reported as a naturally adsorbent material and is useful for adsorbing textile dyes, organic pollutants and heavy metals [20]. This is a direct consequence of the free amine and hydroxyl groups throughout the structure of CS which are required for the protein immobilisation. The reactivity of CS as an immobilisation support therefore becomes a double-

edged sword as the reactivity is necessary for the immobilisation of proteins but also encourages NSA.

The inconsistencies in response were determined to be the effect of non-specific binding of analytes to the CS film, thus tests were carried out on 1% CS LWs to find which stages were causing the issues and causing different results each time. For each of these tests a two-channel flow cell was used to allow for a direct reference channel containing 100 mM 4-(2-hydroxyethyl)piperazine-1-ethanesulfonic acid (HEPES), pH 7.4 to run alongside the experiment for ease of comparison.

Streptavidin, a protein often used to bind biotin, was tested on a 1% CS LW. As seen below, streptavidin is used in protein immobilisation strategies and therefore it is very important to know whether it will bind directly to the film. **Figure 5.6** shows a significant amount of binding from a 1 mg/mL streptavidin solution which is permanent, therefore any strategy using streptavidin will be at risk of this non-specific binding and will require a blocking agent.

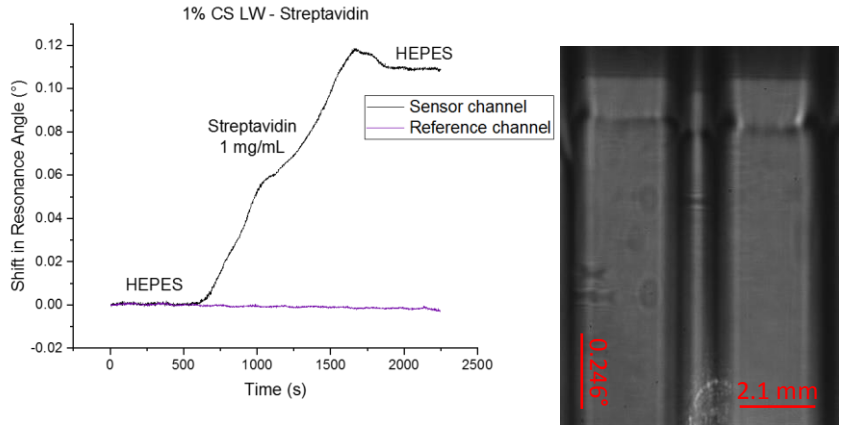

Figure 5.6. A 1% CS LW treated with 100 mM HEPES, pH 7.4, followed by streptavidin (1 mg/mL) and HEPES (left). Output image of the streptavidin-treated 1% CS LW (right). Left channel = reference, right channel = sensor.

IgG was also tested directly onto a 1% CS LW. As shown in **Figure 5.7**, the IgG does produce a small but noticeable permanent shift in baseline compared to the reference channel, which was only treated with HEPES throughout. This indicates that IgG can non-specifically adsorb to the CS film, and therefore once again a blocking agent is required.

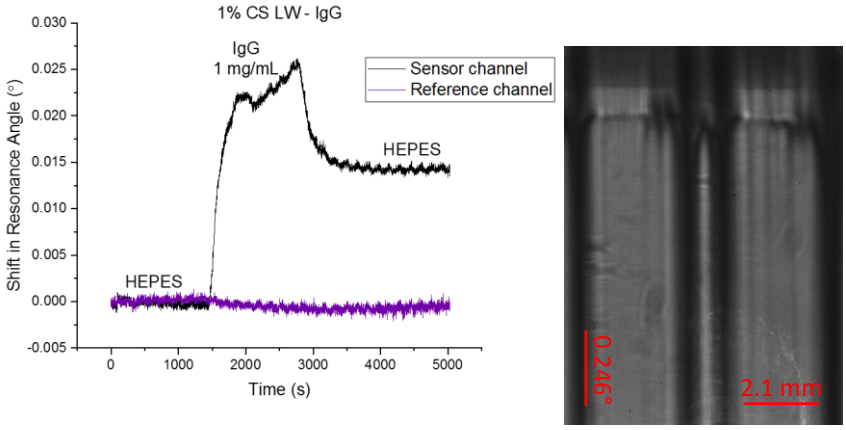

Figure 5.7. A 1% CS LW treated with 100 mM HEPES, pH 7.4, followed by IgG (1 mg/mL) and HEPES. Output image of the IgG-treated 1% CS LW (right). Left channel = reference, right channel = sensor.

5.2.1.1 Bovine serum albumin, BSA

To combat the issues of non-specific binding different techniques were investigated. BSA (**Figure 5.8**) was initially used as a blocking agent as it is easily accessible and known to bind well to a vast range of molecules and is often used as a blocking agent in ELISA [21-23].

Figure 5.8. Crystal structure of Bovine Serum Albumin (BSA) [24].

Serum albumin is found in the range of 34-54 mg/mL in healthy human blood samples, making it a significant interferent in whole blood samples [25]. Tested from 0.1 mg/mL to 50 mg/mL, it is seen in **Figure 5.9** that BSA will physically bind irreversibly to 1% CS LWs by a significant amount. This is useful as it will be able to block any free binding sites from suffering NSA from other constituents of the sample matrix. However, such a high level of NSA may lead to any signal from the desired analyte being completely hidden beneath the BSA signal. BSA is also a large protein at 66.5 kDa [26], and could risk physically blocking any binding sites due to the bulk of the protein.

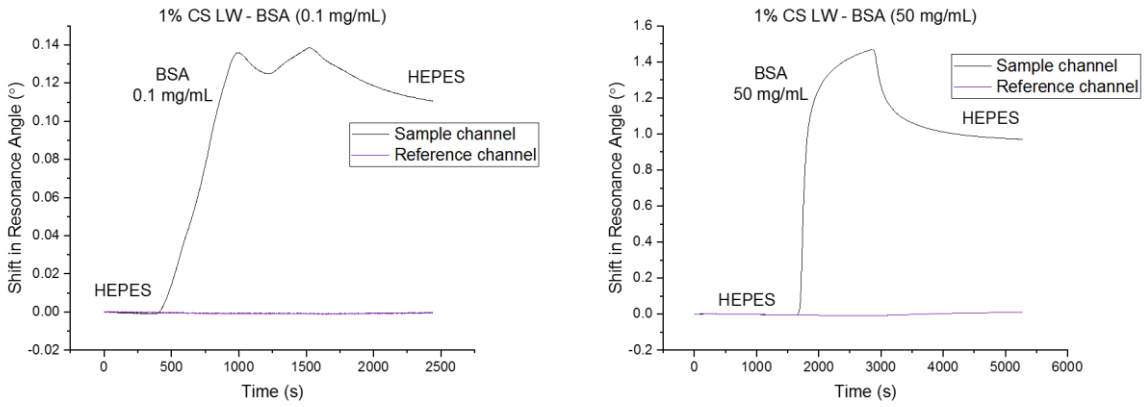

Figure 5.9. 1% CS LW films treated with 100 mM HEPES, pH 7.4, followed by BSA (left: 0.1 mg/mL, right: 50 mg/mL) and HEPES.

Figure 5.10 shows a 1% CS LW treated with 50 mg/mL BSA. It is clear that the channel exposed to BSA has undergone permanent and significant adsorption due to the shift of the dip.

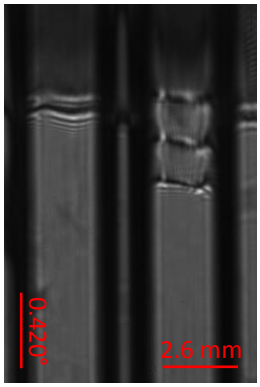

Figure 5.10. Output image of the 50 mg/mL BSA-treated 1% CS LW. Left channel = reference, right channel = sensor.

Unfortunately, this propensity to bind non-specifically also hindered the binding of desired molecules as necessary binding sites were filled with BSA. As discussed above, BSA will easily adsorb to the film and prevent further NSA, but at the cost of blocking some of the desired free functional groups in the film [27]. Without additional modification steps, it is not possible to control the BSA adsorption to prevent it from blocking the desired functional groups and therefore exposure to BSA at any concentration or exposure time risks a reduction in film sensitivity.

To investigate the blocking ability of BSA, a 1% CS LW was treated with 5 mg/mL BSA. Then 1 mg/mL IgG was introduced, followed by a buffer wash. No IgG adsorbed to the film, shown in **Figure 5.11**, compared with **Figure 5.7** where we saw NSA of IgG. It is therefore likely that the BSA was able to prevent NSA. This shows us that BSA works as a blocking agent but does not indicate the effect this has on sensitivity of the film to specific binding.

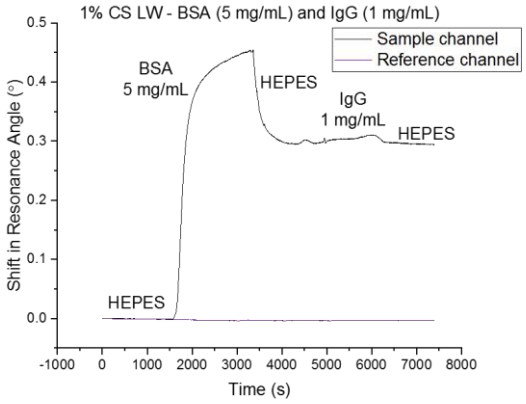

Figure 5.11. 1% CS LW treated with 100 mM HEPES, pH 7.4, followed by BSA (5 mg/mL) and IgG (1 mg/mL), with each step preceded and succeeded by HEPES.

It is apparent in **Figure 5.12** that the BSA has bound to the film, owing to the modes on the right-side channel moving down the image. This irreversible shift in resonance angle indicates a permanent change in the refractive index (RI) of the film caused by the binding of BSA to the CS.

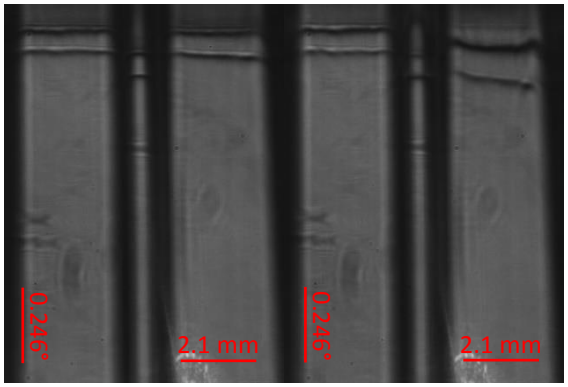

Figure 5.12. Output images of a 1% CS LW before (left) and after (right) 5 mg/mL BSA and 1 mg/mL IgG binding. Left channel = reference, right channel = sensor.

This permanent change can be attributed to adsorption of the BSA to the CS, potentially *via* electrostatic attraction between the positively charged CS and the negatively charged BSA at pH 7.4 [27]. BSA is also known to form multilayers, which is further backed up by the lack of plateau in the sensorgram in **Figure 5.11**. It is likely that a plateau would be

reached after an extended period of time, however this was not investigated as it was not seen to be directly relevant to this project.

5.2.1.2 Sulfo NHS acetate, SNA

Sulfo NHS acetate (SNA) is a small molecule comprised of an inert acetate moiety bound to a sulfo-NHS group which is water soluble and readily reacts with primary amines to produce irreversible acetamides (**Figure 5.13**) [28, 29]. For these reasons it was chosen as a chemical blocking agent for any unreacted primary amines in the CS LW after reaction with a linker. The small size of the molecule reduces steric hinderance while the acetate group prevents further reaction.

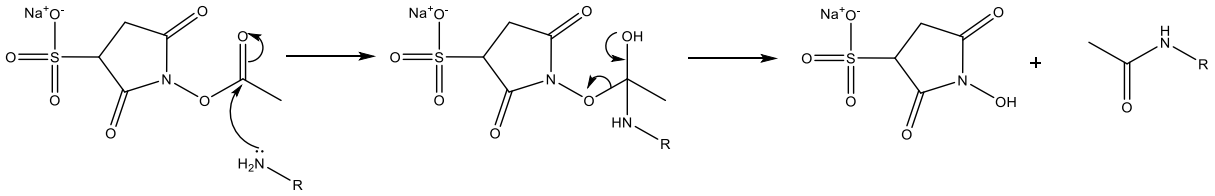

Figure 5.13. Reaction between sulfo NHS acetate and a primary amine.

SNA is seen in literature as a blocking agent by Wu *et al.* [30] and Bax *et al.* [31], where lysine side chains in tropoelastin were blocked. SNA is highly susceptible to hydrolysis and must be used immediately after preparation; in this case there will still be some competing reaction occurring between the hydrolysis reaction and the acylation, hence SNA must be used in high excess to the amine groups [29].

To test the suitability of SNA, 1 mg/mL SNA was used to treat a 1% CS LW, followed by 1 mg/mL IgG (**Figure 5.14**). As with the BSA, the SNA caused a permanent shift in resonance angle which was expected as it will react with the free primary amines in the film. The addition

of the IgG did not cause a permanent shift, indicating that the SNA was successful in reducing NSA of IgG to CS films by effectively blocking the primary amine groups in CS.

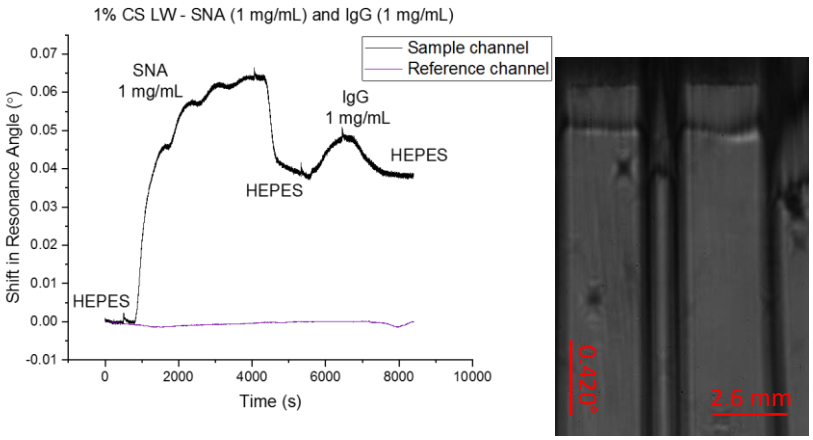

Figure 5.14. 1% CS LW treated with 100 mM HEPES, pH 7.4, followed by SNA (1 mg/mL) and IgG (1 mg/mL), with each step preceded and succeeded by HEPES (left). Output image of the SNA and IgG-treated 1% CS LW (right). Left channel = reference, right channel = sensor.

This method was determined to be superior to the physical blocking achieved by BSA as it reduced steric hinderance and did not risk introducing further functional groups except the acetate.

5.2.2 Glutaraldehyde

The first immobilisation strategy employed used glutaraldehyde to functionalise the free primary amine groups in the CS and provide available aldehyde groups for further reaction. This method is referred to as GA-v2 (**Figure 5.15**).

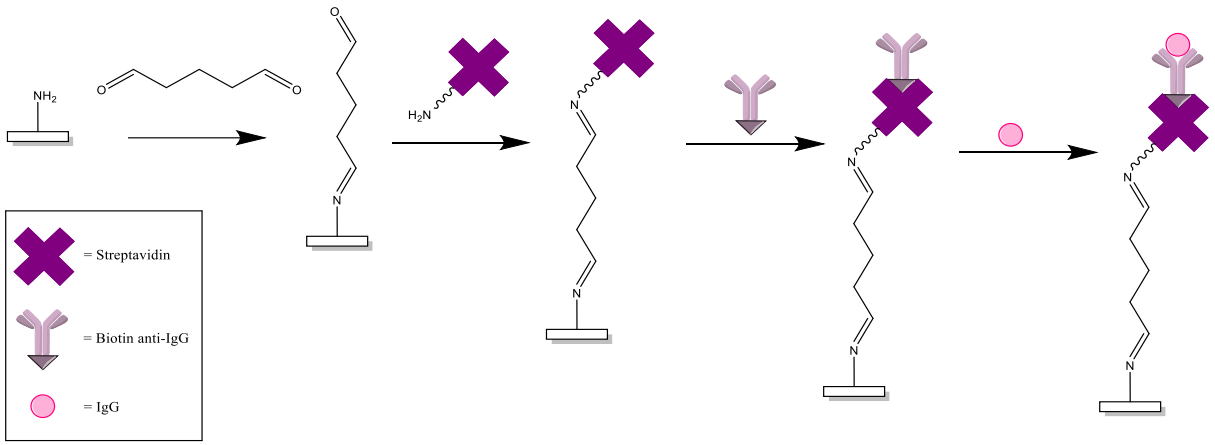

Figure 5.15. Schematic of the GA-v2 glutaraldehyde protein immobilisation strategy.

Streptavidin is a tetrameric protein with high affinity for biotin ($K_d = 10^{-14}\ to\ 10^{-15}\ M$) [32]. Along with the four biotin binding sites, streptavidin also contains free primary amines which can bind with the free aldehyde from glutaraldehyde, anchoring the streptavidin to the CS film and then providing up to four regions per streptavidin molecule for a biotin-containing moiety to bind. For this, PAB was selected as it has high affinity for rabbit IgG. Once the PAB has bound to the streptavidin, rabbit IgG is introduced and allowed to bind.

As shown in **Figure 5.16**, this method gave an excellent response for 1 mg/mL IgG, with an overall shift of 0.7253°. The mode has almost disappeared in the sensor channel, suggesting that something has damaged the film to the point where it can no longer support the waveguide mode properly.

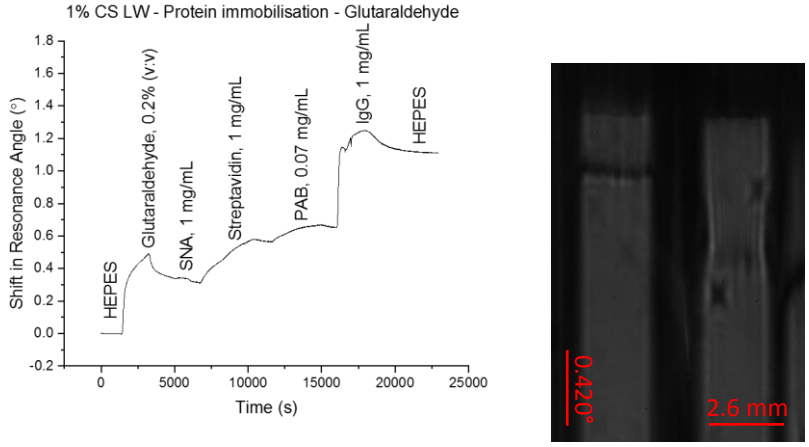

Figure 5.16. 1% CS LW treated with the GA-v2 glutaraldehyde protein immobilisation strategy (left). Output image of the treated 1% CS LW (right). Left channel = reference, right channel = sensor.

As the SNA step gave no real response, the experiment was repeated without this blocking step, along with shorter exposure times to streptavidin and PAB to allow for a quicker response. This modification of the method is referred to as GA-v3 (**Figure 5.17**).

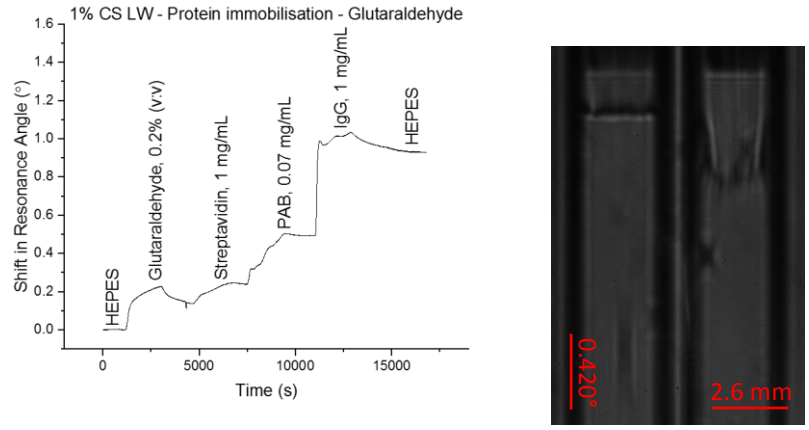

Figure 5.17. 1% CS LW treated with the GA-v3 glutaraldehyde protein immobilisation strategy (left). Output image of the treated 1% CS LW (right). Left channel = reference, right channel = sensor.

This led to a shift of 0.67705°. On repeating, 0.6254° and 0.6088° were achieved for the IgG binding. This indicates that the method is not reproducible at this stage, with an average response of 0.6371° ± 0.0291°. This is likely due to the use of glutaraldehyde; as discussed in **Chapter 3** (**3.1**), glutaraldehyde is a highly reactive molecule and can react with itself. As it cannot be controlled further than limiting the concentration and exposure time,

glutaraldehyde is not an ideal linker for reactions requiring a high level of reproducibility. Even between **Figure 5.16** and **Figure 5.17** there is an obvious difference in the glutaraldehyde response despite using the same concentration for both. For this reason, this form of glutaraldehyde-based protein immobilisation was not investigated further.

5.2.3 NHS-PEG_{12}-biotin, NPB

The next method used NHS-PEG_{12}-biotin (NPB), which can react with the free CS amines *via* the NHS group, adding a PEG_{12} chain to reduce steric hinderance, and has a biotin group which can bind to one of four biotin-accepting groups on each streptavidin moiety. The streptavidin will then react with PAB, followed by rabbit IgG (**Figure 5.18**).

This method was particularly susceptible to non-specific binding issues, leading to the introduction of SNA as a blocking agent. This was combined with the NPB step, allowing for a competing reaction between the two molecules.

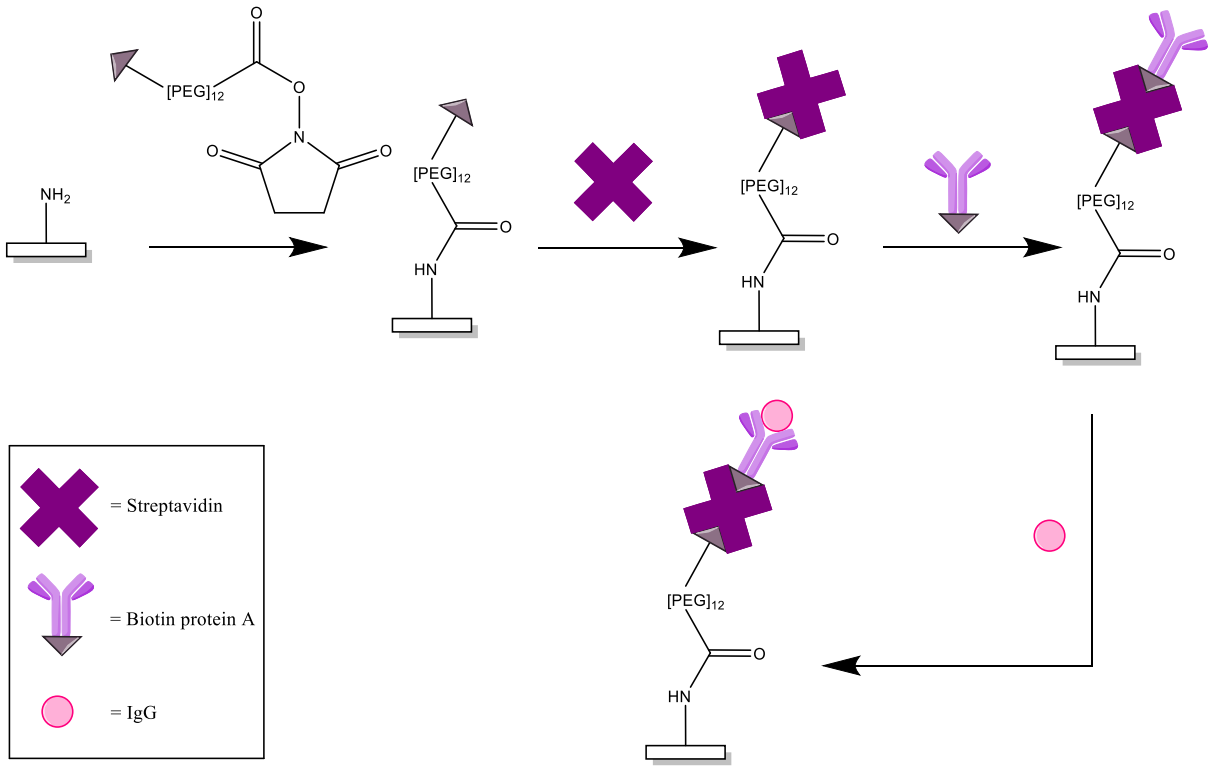

Figure 5.18. Schematic of the NHS-PEG$_{12}$-biotin (NPB) protein immobilisation strategy.

Figure 5.19 depicts a typical NPB protein immobilisation strategy. For this, 1 mg/mL IgG was selected to ensure the binding was clearly visible and the immobilisation strategy could be assessed. Between each step 100 mM HEPES, pH 7.4 is used which allows for any unreacted reagent to be washed out of the film and therefore any remaining shift in resonance angle is assumed to be due to chemical binding of the reagent to the film. Each step shows clear binding which suggests that this strategy is working. However, upon repeating this strategy the results were not as concordant as expected, with an average IgG response of 0.050° ± 0.019° for 1 mg/mL IgG.

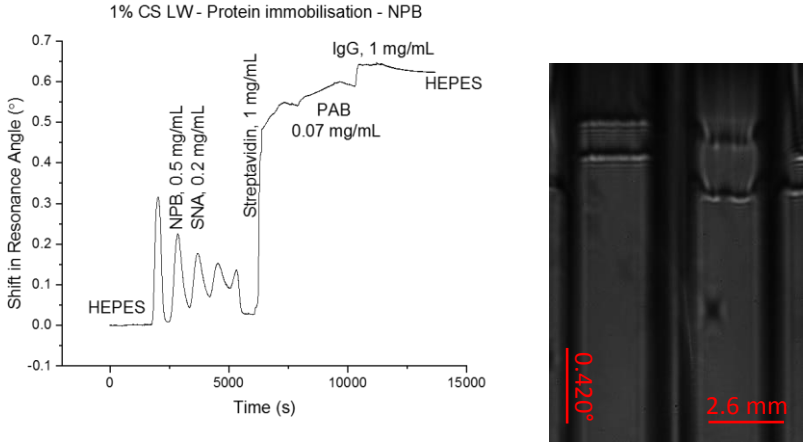

Figure 5.19. 1% CS LW treated with the NPB protein immobilisation strategy (left). Output image of the treated 1% CS LW (right). Left channel = reference, right channel = sensor.

An attempt was made to increase the reproducibility by separating the NPB and SNA steps. Previously we combined these steps to encourage a competing reaction; by separating them, the NPB should be able to bind without hinderance and the SNA can be used afterwards to block any remaining free primary amine groups. **Figure 5.20** shows this technique, which gave an excellent response for IgG but also caused additional damage to the film. This technique also did not give reproducible results, with an average IgG response of 0.114 ° ± 0.061°.

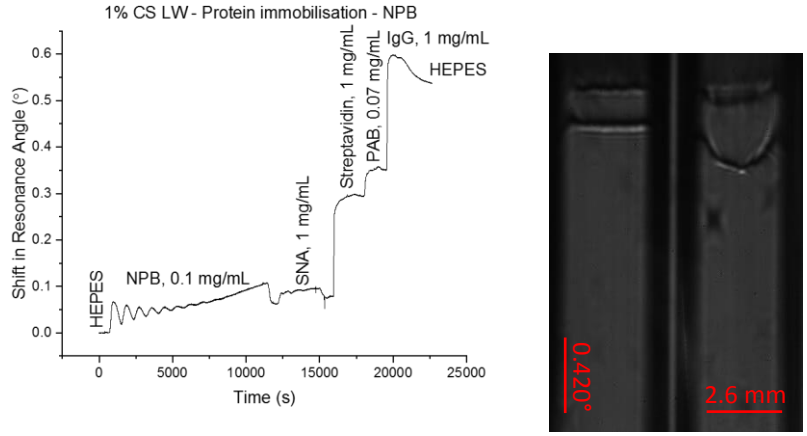

Figure 5.20. 1% CS LW treated with the modified NPB protein immobilisation strategy (left). Output image of the treated 1% CS LW (right). Left channel = reference, right channel = sensor.

To check for concordance with stacked LWs, 0.96% poly(acrylamide)/1% CS (0.96% PAAm/1% CS) stacked LWs were tested with NPB and SNA followed by streptavidin (**Figure 5.21**).

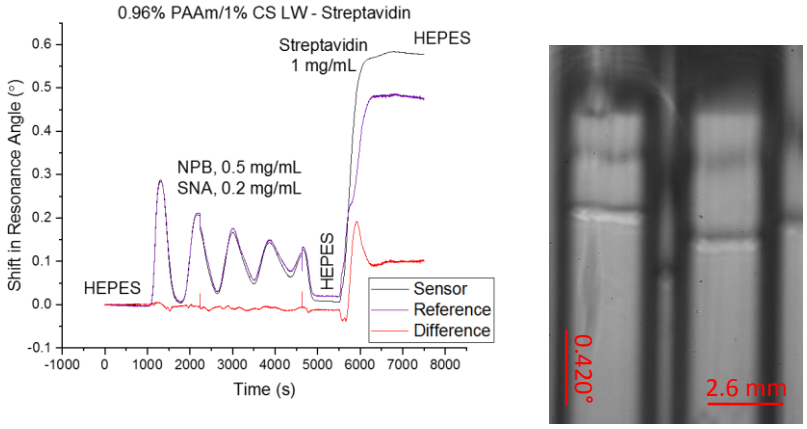

Figure 5.21. 0.96% PAAm/1% CS stacked LW treated with streptavidin (NPB strategy) (left). Output image of the treated 0 .96% PAAm/1% CS stacked LW (right). Left channel = reference, right channel = sensor..

The response of the CS layer to streptavidin is similar to what was shown in **Figure 5.19**, indicating that the CS layer is intact and behaving as expected. The results show that the response of both modes to streptavidin are within 0.1° of each other, which suggests the PAAm film may have reacted with either the NPB or the streptavidin. This leads to the differential response being significantly lower than that of the sensor layer alone, which is unexpected and suggests that further work is needed on these stacked films to decide whether the PAAm is suitable. The experiment was then repeated on 5% 4-arm-$PEG_{20,000}$-aldehyde:4-arm-PEG_{2000}-hydrazide/1% CS (4-CHO:4-HZ/1% CS) LWs (**Figure 5.22**).

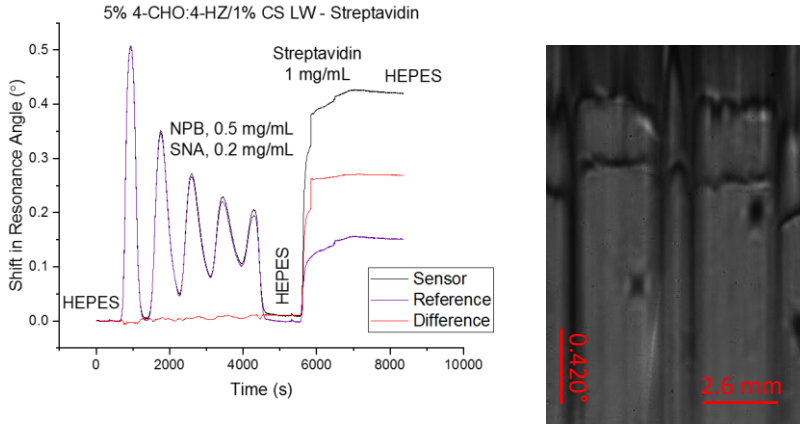

Figure 5.22. 5% 4-CHO:4-HZ/1% CS stacked LW treated with streptavidin (NPB strategy) (left). Output image of the treated 5% 4-CHO:4-HZ/1% CS stacked LW (right). Left channel = reference, right channel = sensor.

The results for both modes appear promising, with a large difference between the sensor and reference channel. However, upon repeating the experiment it became apparent that the response for streptavidin varies significantly. Across three different LWs, the average response for streptavidin is 0.287° ± 0.109°. This is due in part to device-to-device variation; we can see in **Figure 5.22** that the output image shows the top mode extremely close to the total internal reflection (TIR) boundary, along with moderate uniformity.

The inclusion of NSA blocking agents improved the reproducibility of the techniques studied so far. Yet, truly reproducible immobilisation is exceedingly difficult to achieve when using streptavidin within the strategy. By its very nature streptavidin has four biotin binding sites which means that each streptavidin moiety can bind with four biotin groups. In an ideal situation where streptavidin is bound to the film *via* one of these sites it should leave three available to bind with biotin-containing moieties; it is not however possible to prevent the streptavidin from binding multiple times to the film and therefore leave fewer binding regions available for the biotin-containing moieties required for the next immobilisation step. As this cannot be controlled, some variance in results from device-to-device is expected. Similar

issues with a lack of accuracy and specificity are seen in streptavidin-biotin based immunoassays [33]; a great reliance is placed upon the high binding affinity of the streptavidin-biotin interaction and in most cases a 4:1 ratio of biotin:streptavidin is assumed. This ratio cannot be effectively maintained when using two separate biotin-containing linkers such as in this work, and the additional issues presented by steric hinderance also play a part in the lack of reproducibility of this technique. Due to this unreliability, the next strategies do not use streptavidin as a linker.

5.2.4 Strain-promoted alkyne-azide cycloaddition, SPAAC

The reaction between alkynes and azides *via* a simple copper-free click chemistry reaction is well-reported and was used for the next protein immobilisation strategy. A dibenzocyclooctyne (DBCO)-containing reagent is able to react with an azide-containing reagent through strain-promoted alkyne-azide cycloaddition (SPAAC) [34]. This is typically done by functionalising one biomolecule with DBCO and another biomolecule with the azide, then reacting these together to produce two conjugated biomolecules linked *via* a triazole bond. This reaction mainly has uses in bioconjugation as the lack of toxic copper catalyst makes this reaction biocompatible, while the reaction itself typically occurs at mild conditions at room temperature in aqueous media. The reaction is also high yielding, stable, and perhaps most importantly it is specific and does not lead to unwanted by-products through reactions with other functional groups found in proteins [34]. This excellent track record makes the SPAAC DBCO-azide reaction an interesting choice for protein immobilisation onto CS films.

Trilling *et al*. studied the effect of random and uniform SPAAC-based antibody immobilisation on the sensitivity of a surface plasmon resonance (SPR) biosensor [35]. By modifying llama antibody fragments with between one and five azide groups and attaching these to an SPR chip containing available cyclooctyne groups the authors were able to determine that the uniformly oriented antibody fragments with a single azide group could increase the sensitivity of the detector chip by up to 800-fold compared to the antibody fragments containing multiple azide groups. The control of orientation subsequently leads to the binding sites in the antibody being exposed to the analyte solution, while a random orientation can leave these binding sites blocked.

To achieve SPAAC, IgG was first reacted with sodium periodate, breaking the vicinal diols and leaving free aldehyde groups. The free aldehydes are then able to react with the hydrazide bond in azido-PEG_4-hydrazide, producing an antibody with free azide groups (**Figure 5.23**).

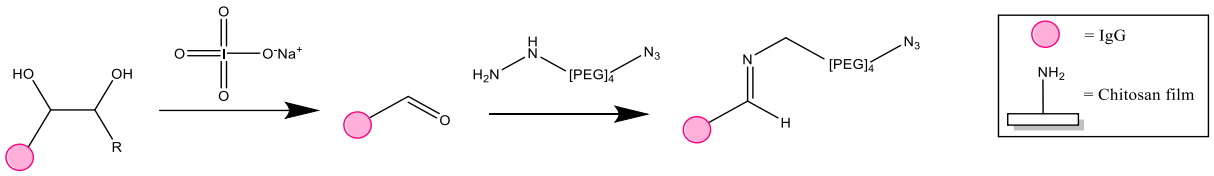

Figure 5.23. Step 1: Oxidation of the antibody followed by azide functionalisation.

In parallel, DBCO-PEG_4-NHS ester was reacted with the CS film. The NHS ester will react with the free primary amines in the CS film, providing a CS film with free DBCO groups (**Figure 5.24**).

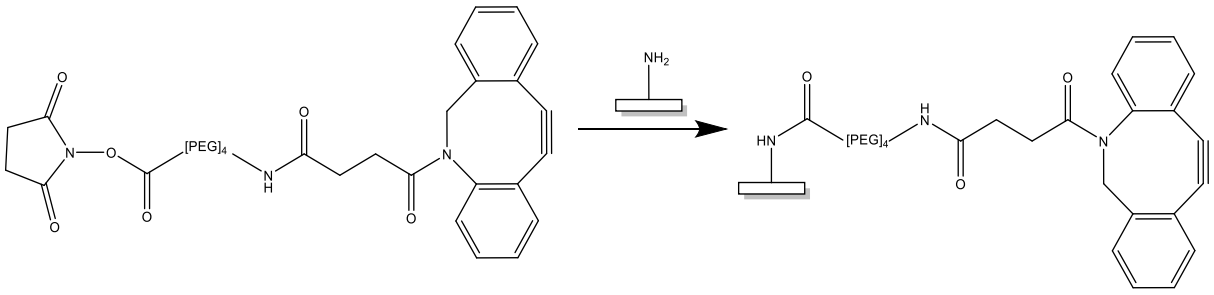

Figure 5.24. Step 2: 1% CS LW functionalisation with a DBCO-containing reagent.

The final stage combines the two products, reacting the azide group on the antibody with the DBCO group on the CS film. This will leave the antibody bound to the CS film *via* the triazole (**Figure 5.25**).

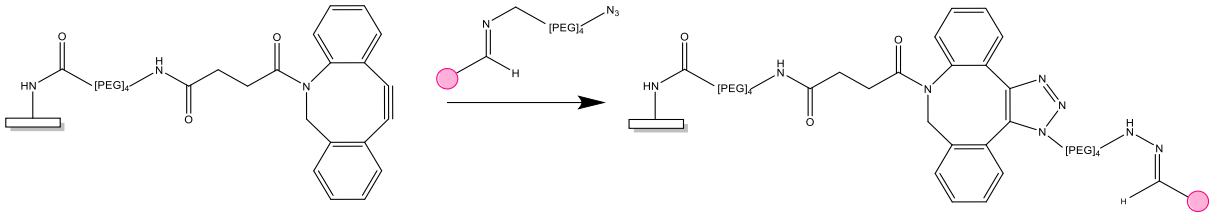

Figure 5.25. Step 3: Reaction of the products from steps 1 and 2 to form the final product.

The CS film was set up using a two-channel flow cell, and the DBCO solution was run through only one of the channels. The final step, combining the DBCO-functionalised film with the 0.5 mg/mL azide-functionalised IgG, was performed by running the functionalised IgG through both channels. This was expected to produce a permanent change in RI only in the sample channel due to the reaction of the DBCO and azide groups. However, as can be seen in **Figure 5.26**, it actually bound significantly in both channels.

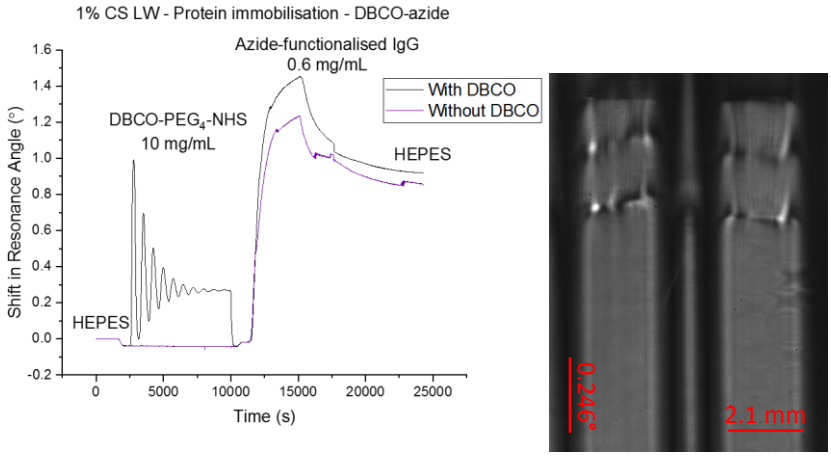

Figure 5.26. 1% CS LW treated with the DBCO-azide protein immobilisation strategy (left). Output image of the treated 1% CS LW (right). Left channel = reference, right channel = sensor.

This shows that the functionalised IgG had bound to the CS film without the need for the presence of the DBCO; this is suggested to be due to partial imine hydrolysis in buffer solution, turning some of the azide-functionalised IgG back into the aldehyde which can react with the CS amine, while the reformed hydrazide-PEG_4-azide can react with the DBCO. The response for the DBCO-free channel is lower than that of the DBCO-containing channel which suggests that less binding was able to occur, but the response is still significantly higher than would be expected.

Additional issues could be due to unwanted by-products, such as those reported by Zhang and Dai *et al.* [36], where it is shown that proteins containing free thiol groups such as cysteine are able to react with the alkyne in the DBCO-moiety, rather than *via* the azide. While the DBCO-azide reaction itself is specific and has no side-products, this cannot be relied upon in the presence of cysteine residues. IgG itself contains a number of disulfide bonds and free thiol moieties *via* cysteine residues [37].

Repeating this experiment produced the same response, and the method was not studied further due to time limitations.

5.2.5 Oxidised IgG

Based on the results from **Section 5.2.4**, attempts were made to bind oxidised IgG directly to the CS film *via* the reaction between the aldehyde group on the oxidised IgG and the primary amine group on the CS to form an imine (**Figure 5.27**). Due to the sensitive nature of proteins, a neutral pH of 7.4 along with a longer reaction time was chosen over an acid-catalysed reaction in an attempt to preserve the nature of the IgG.

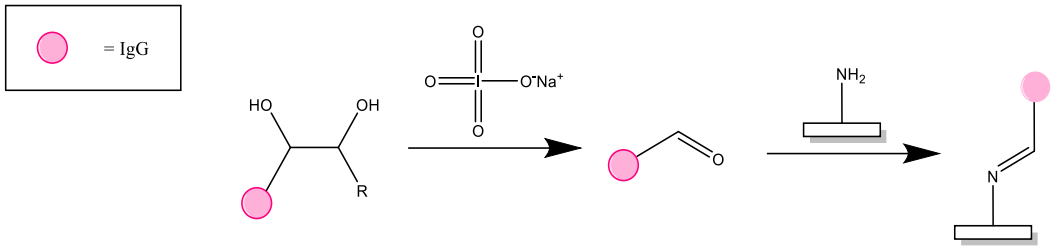

Figure 5.27. Schematic of the oxidised IgG protein immobilisation strategy.

The results of this method were significantly better than for the other protein immobilisation strategies, giving a response of 0.89° ± 0.02° for 2 mg/mL oxidised sheep IgG (**Figure 5.28**).

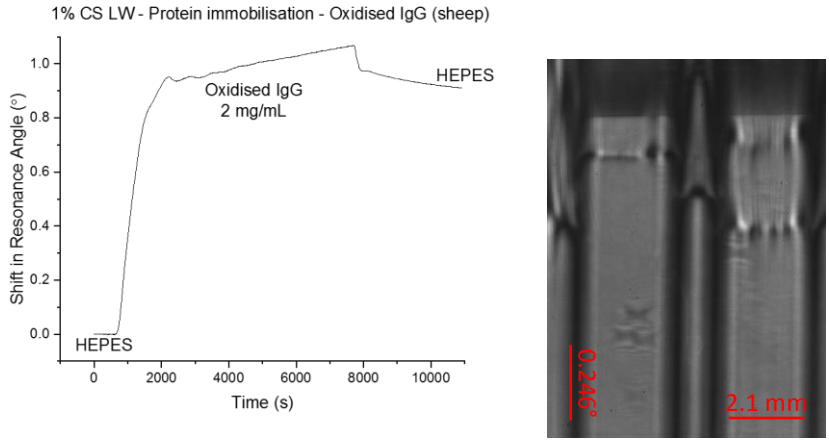

Figure 5.28. 1% CS LW treated with the oxidised IgG (sheep) protein immobilisation strategy (left). Output image of the treated 1% CS LW (right). Left channel = reference, right channel = sensor.

As this was successful with sheep IgG, we wanted to test the effect of a different IgG and therefore prepared some oxidised rabbit IgG *via* the same method and applied it to 1% CS LWs at a concentration of 1 mg/mL (**Figure 5.29**).

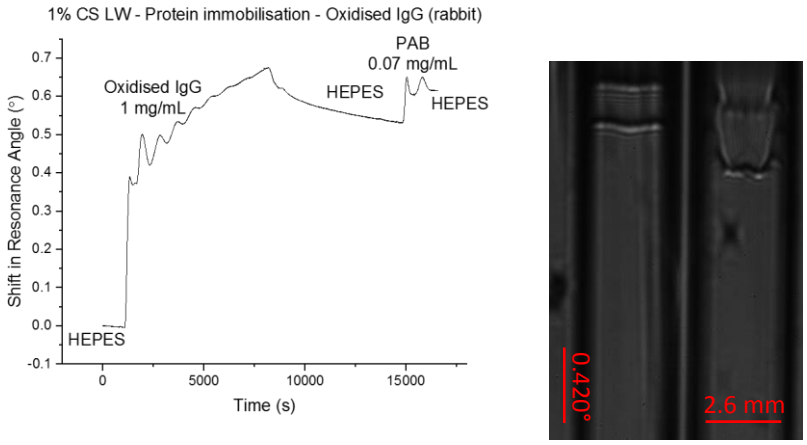

Figure 5.29. 1% CS LW treated with the oxidised IgG (rabbit) protein immobilisation strategy (left). Output image of the treated 1% CS LW (right). Left channel = reference, right channel = sensor.

After the IgG treatment and a subsequent buffer wash, PAB was introduced to the film to check if the oxidised IgG was:

1. Sufficiently bound to the film and not just adsorbed and,
2. Still able to bind with protein A and therefore not denatured.

This was successful, giving a response of approximately 0.1° for 0.07 mg/mL PAB. This is a good indication that this method can bind oxidised IgG without damaging the binding sites of the IgG.

Next, 0.1 mg/mL of oxidised IgG (rabbit) was tested in the same manner (**Figure 5.30**). The response for this was 10 times smaller than that of the 1 mg/mL IgG as expected, implying that the IgG is binding in a quantitative manner to the CS LW. The response is also noisier, which is due to the much lower concentration and shift in resonance angle.

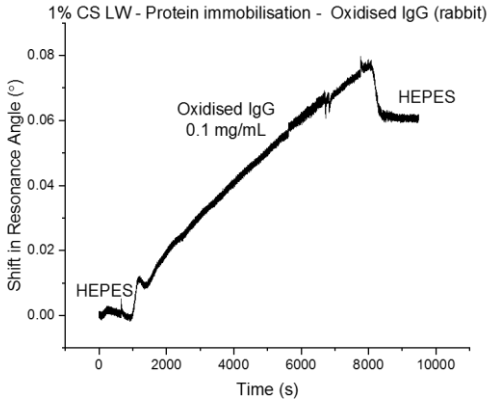

Figure 5.30. 1% CS LW treated with the oxidised IgG (rabbit) protein immobilisation strategy.

Due to the success of the single layer LWs, 1.2% PAAm/1% CS stacked LWs were treated in the same manner (**Figure 5.31**).

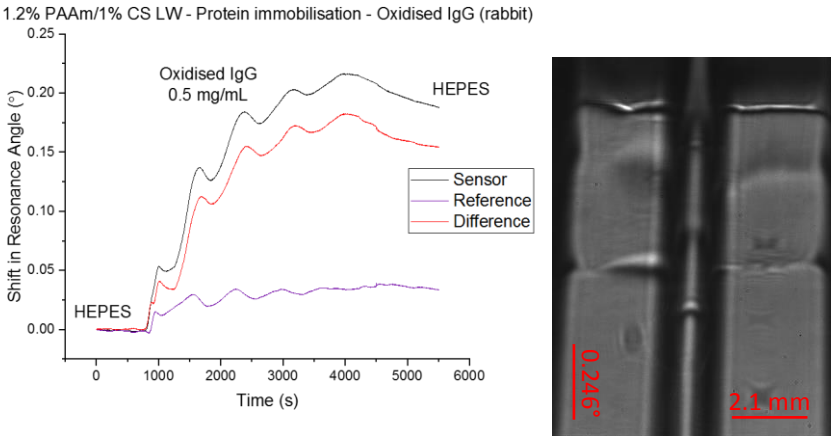

Figure 5.31. 1.2% PAAm/1% CS LW treated with the oxidised IgG (rabbit) protein immobilisation strategy (left). Output image of the treated 1.2% PAAm/1% CS stacked LW (right). Left channel = reference, right channel = sensor.

Figure 5.31 shows a very definite difference between the response of the sensor and reference layers, with the difference between the two providing a final response of ~0.15° for 0.5 mg/mL oxidised IgG. The uncorrected response is slightly lower than would be expected for a 1% CS LW, however the addition of the 1.2% PAAm may have reduced the sensitivity slightly and would account for this difference.

This method does have certain issues. Firstly, any method designed for point-of-care (POC) use must be quick (<20 minutes). Currently these experiments are taking 2 hours. That being said, it may be possible to reduce the time taken for this experiment by correlating the slope of the binding over a shorter period of time to a concentration curve.

Secondly, the oxidation method of IgG is equally lengthy, requiring approximately 3 hours. When this is factored in with sample clean-up, the method as a whole does not seem ideal for POC.

Thirdly, whole blood samples will need to be thoroughly cleaned before oxidation. Without this, multiple components of the sample may be oxidised and able to bind directly to the CS LW. This would lead to a very high response which is not indicative solely of the desired protein.

On this basis, the oxidised IgG experiment has been considered successful but does not warrant further investigation due to practical issues for the end goal of POC.

5.2.6 Glycine

A method which again uses glutaraldehyde was designed. Instead of binding a receptor to the film and then binding the analyte, the film was functionalised with glutaraldehyde and the analyte was bound directly to this. To then prove that the analyte had bound, any remaining unreacted glutaraldehyde was reacted with 1% glycine (w:v) for 1 h, followed by PAB to bind to the IgG and prove the presence (**Figure 5.32**).

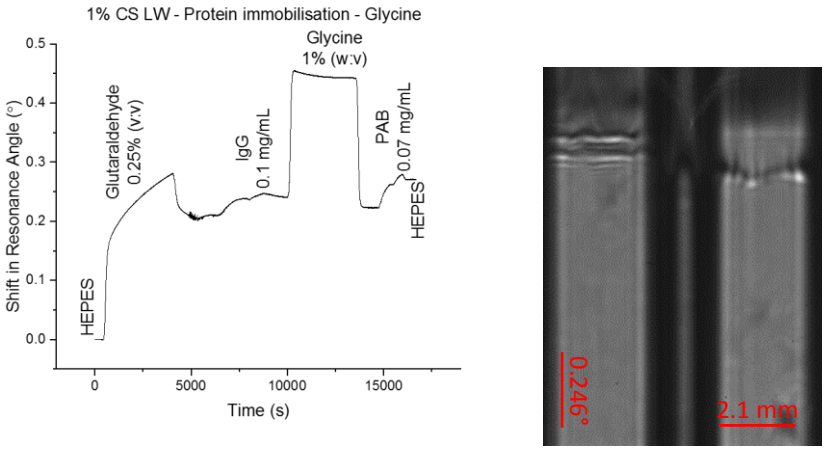

Figure 5.32. 1% CS LW treated with the glycine protein immobilisation strategy (left). Output image of the treated 1% CS LW (right). Left channel = reference, right channel = sensor.

This gave very promising results, with strong binding from 0.1 mg/mL IgG and 0.07 mg/mL PAB. The PAB did not plateau, so the experiment was repeated with the PAB step for 2 hours rather than the original 20 minutes. Again, the PAB did not plateau which suggests it is continuing to bind to something in the film. Unsure as to whether the PAB was binding to the IgG or to any unreacted glutaraldehyde, further investigations were carried out.

5.2.6.1 Glycine optimisation

To find out what the PAB was binding to, the experiment was repeated but the IgG step removed **(Figure 5.33**).

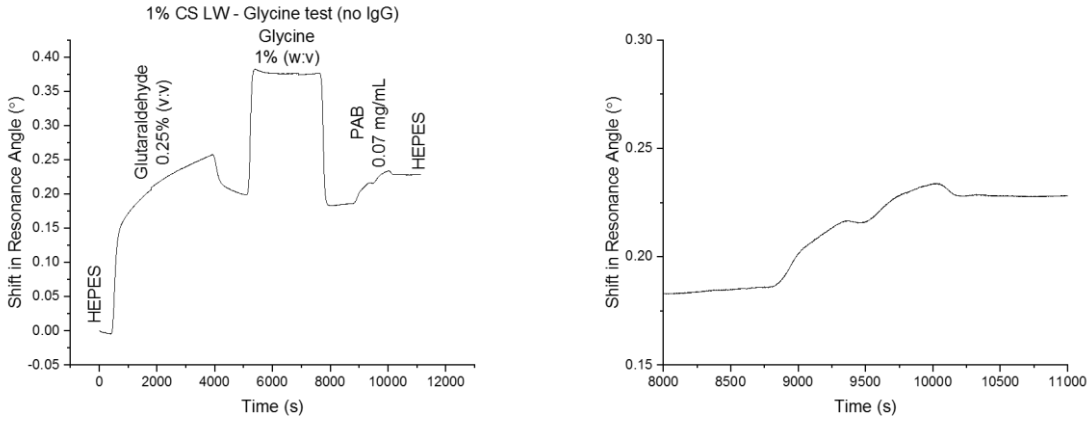

Figure 5.33. 1% CS LW treated with the glycine protein immobilisation strategy without IgG.

It is clear that PAB is still able to bind significantly despite the lack of IgG. This indicates that the PAB is binding non-specifically with the glutaraldehyde and the glycine step needs modification to prevent this. Three methods were considered:

1. Increase the temperature. This would bring the method in line with literature which suggests a temperature of 37 °C for optimum conditions [38], but this would be difficult to achieve consistently and could lead to damage of the CS film. For these reasons, this method was not investigated.
2. Increase the concentration of glycine.
3. Increase the exposure time.

The concentration of glycine was increased from 1% (w:v) to 5% (w:v). As seen in **Figure 5.34** this has significantly reduced the amount of PAB that is binding with the film, but not entirely, hence further measures are required. As 5% glycine already gives such a substantial response, it was decided to maintain this concentration rather than further increasing it to ensure the film remains undamaged and can be tracked by the software.

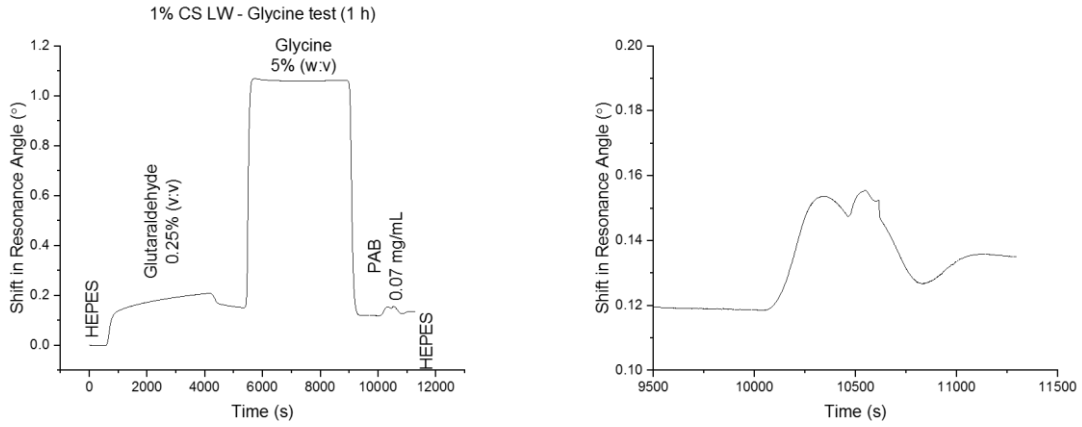

Figure 5.34. 1% CS LW treated with the modified glycine protein immobilisation strategy without IgG.

Keeping the 5% glycine, we then investigated different exposure times. Previously we had been working using 1 h exposure, therefore this was first increased to 3 h (**Figure 5.35**). Again, this reduced PAB binding but did not eliminate it.

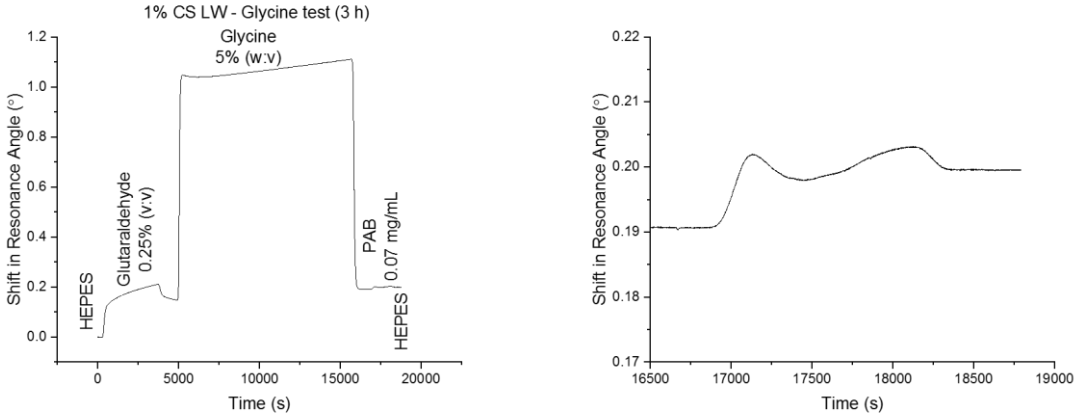

Figure 5.35. 1% CS LW treated with the modified 3 h-glycine protein immobilisation strategy without IgG.

While maintaining the concentration of 5% glycine, exposure time was increased further to 5 h (**Figure 5.36**). This almost eliminated all NSA of PAB. It was decided to continue with the 5 h exposure time, as the additional binding of IgG before the glycine should sufficiently react with any remaining aldehyde groups in the glutaraldehyde.

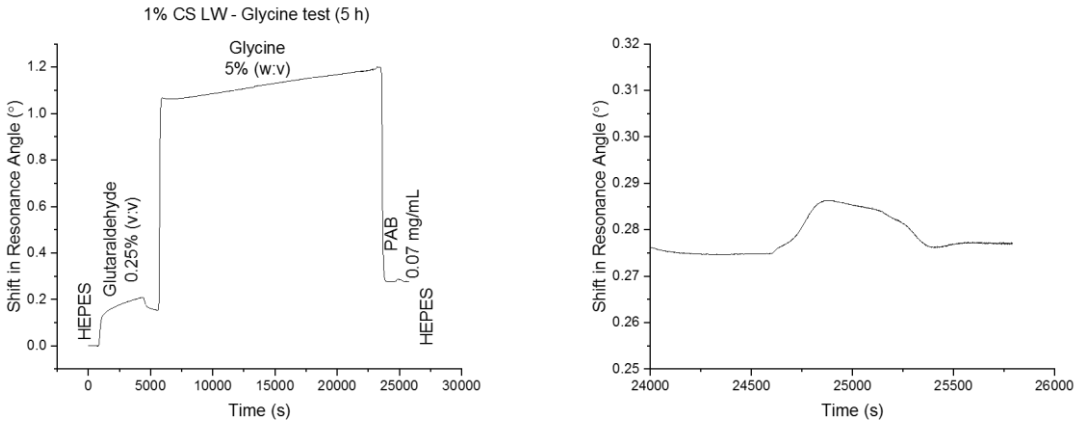

Figure 5.36. 1% CS LW treated with the modified 5 h-glycine protein immobilisation strategy without IgG.

Briefly, this method was tested on a 5% 4-CHO:4-HZ (1:1)/1% CS stacked LW, without testing the blocking ability of the glycine afterwards (**Figure 5.37**). Both layers gave the expected response with a large gap between the two, suggesting that the reference layer was responding to the change in RI of the sensor layer and not binding with the glutaraldehyde or IgG itself. The differential response of the two layers showed a good level of binding, making this a promising technique.

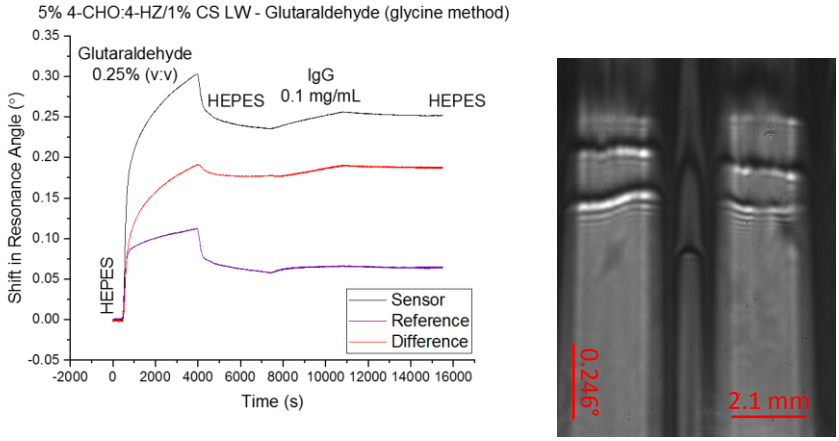

Figure 5.37. 5% 4-CHO:4-HZ/1% CS stacked LW treated with the modified glycine protein immobilisation strategy up to the IgG step (left). Output image of the treated 5% 4-CHO:4-HZ/1% CS stacked LW (right). Left channel = reference, right channel = sensor.

Current issues with translating this method to POC use are as follows:

- While the IgG sensing step is quick (20 minutes), it requires a 1 h functionalisation with glutaraldehyde directly prior to the IgG. This is due to the high reactivity of glutaraldehyde; it is not possible to store glutaraldehyde-functionalised films without reducing the porosity and sensitivity of the films.
- Samples would need to be clean before film application to prevent binding of other sample components to the film as the method is not specific to IgG.

Overall, this method does provide promising results; the IgG sensing stage is quick and appears to be reproducible at this stage. Further investigation would be needed to see whether the length of the procedure can be reduced while maintaining sensitivity and functionality.

5.3 Anti-biotin antibody, ABA

An anti-biotin antibody (ABA) was used for the next immobilisation method. This work was based on the report by Gupta *et al.* [27], therefore conditions were maintained as presented in this paper. The method begins with a 5 h conditioning of the film, to replace the 100 mM HEPES, pH 7.4 with 10 mM phosphate buffered saline (PBS), pH 7.4. PBS is a more biologically-relevant buffer than HEPES, often used in biological research [39]. Initial testing proved that the CS films will not form directly in PBS buffer, discussed in **Chapter 3** (**3.2.2**). Equally, storage of the films overnight in 10 mM PBS results in irreversible damage. However, a 5 h conditioning with the 10 mM PBS, pH 7.4 appears to cause minimal damage to the film and is long enough to recondition the film into PBS. This gives a permanent change in RI of -0.0109° (**Figure 5.38**).

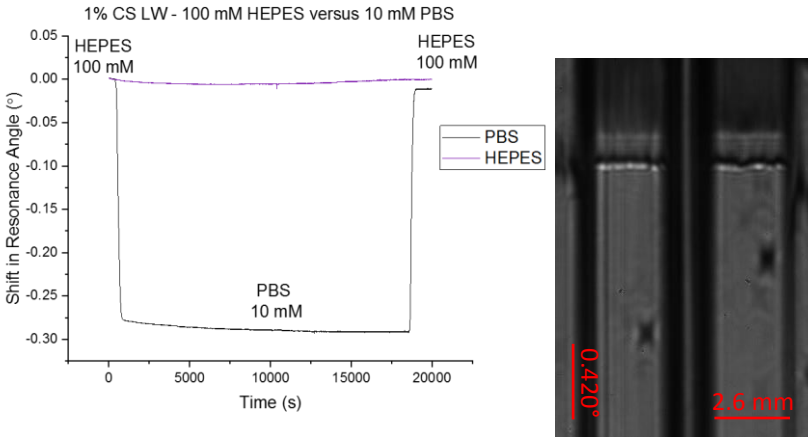

Figure 5.38. 1% CS LW treated with 10 mM PBS, pH 7.4 (left). Output image of the treated 1% CS LW (right). Left channel = reference, right channel = sensor.

Using a two-channel flow cell to allow for removal of common-mode effects, the films were then treated in the sensor channel with 50 µg/mL of NPB in PBS, and in the reference channel with 10 mM PBS, pH 7.4 throughout. After 30 minutes the NPB was replaced with PBS and allowed to plateau before adding the ABA solution. **Figure 5.39** shows the ABA method

subsequent to the PBS conditioning. There is a clear response to 25 nM ABA which is permanent.

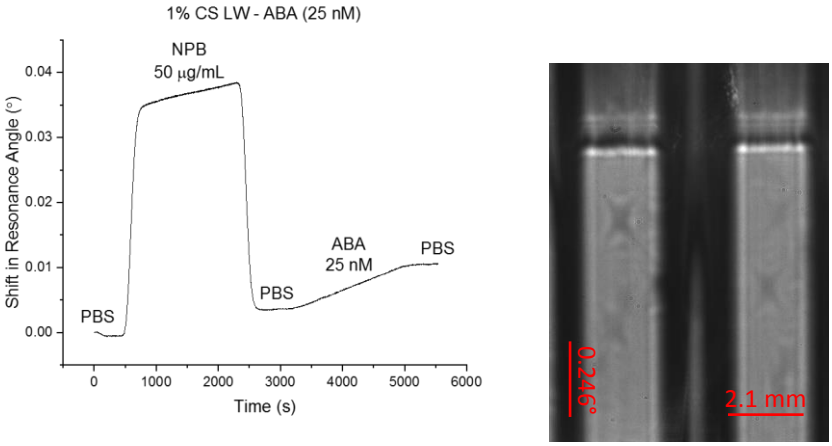

Figure 5.39. 1% CS LW treated with the ABA protein immobilisation strategy (left). Output image of the treated 1% CS LW (right). Left channel = reference, right channel = sensor.

This was repeated three times, and the response for ABA is reported in **Figure 5.40**. The overall average response across the three LWs was 0.007266° ± 0.000643°. This suggests this method is reproducible and therefore successful.

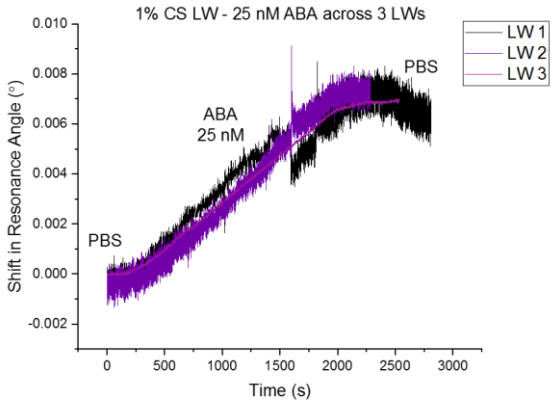

Figure 5.40. The response of ABA on three different 1% CS LW devices.

This method was then tested on 5% 4-CHO:4-HZ/1% CS stacked LWs (**Figure 5.41**). The response of the reference layer to the ABA was minimal, therefore when subtracted from the response of the sensor layer the final differential response was still exceedingly good. This was

taken as a good sign that the reference layer is inert and did not bind with either the NPB or ABA as hoped. As the samples were clean, any shift in resonance angle for the reference layer should correspond only to unwanted fluctuations that may have occurred throughout the experiment such as temperature and mechanical drifts. There will also be a very slight response to the change in RI of the sensor layer on top, but this is minimal and can be disregarded.

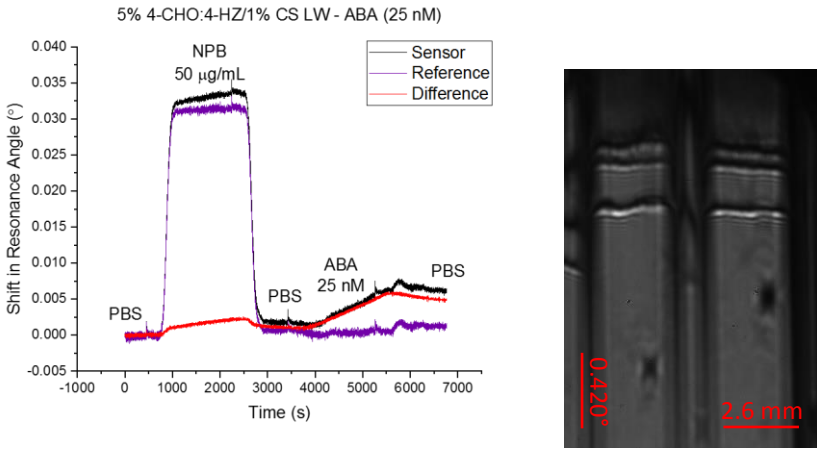

Figure 5.41. 5% 4-CHO:4-HZ/1% CS stacked LW treated with the ABA protein immobilisation strategy (left). Output image of the treated 5% 4-CHO:4-HZ/1% CS stacked LW (right). Left channel = reference, right channel = sensor.

Despite having excellent and reproducible response, this method is not without its flaws when considering POC use. Problems with this method are as follows:

- It is again a lengthy method with the 5 h conditioning. This cannot be done prior to testing the film as longer exposure to the PBS will damage the CS LW.
- It is designed for ABA, but this is not a biologically relevant molecule such as procalcitonin (PCT). Any other antibody needs to contain the anti-biotin moiety for this to work and will likely need pre-treatment to work.

In conclusion, this method has provided reproducible results and is an excellent step towards showing the usability of these LW films, but translation to POC does not seem likely at this stage.

5.4 Lactoferrin, LF

The major focus of this work thus far has been with regard to misdiagnosed acute respiratory infections (ARIs). Whilst this remains an important and necessary venture, the issue of misdiagnosed infections isn't limited to just ARIs and it is hoped that these LW devices will be able to help detect a range of other infections in the same way. Therefore, this section explores a different biomarker to prove the suitability of LW devices to detect and quantify the severity of urinary tract infections (UTIs).

UTIs are a common ailment, particularly prevalent in females of reproductive age. Despite being so common, many of the main symptoms are not solely indicative of UTIs; dysuria (painful urination), polyuria (excessive urination), haematuria (blood in urine), and cloudy/uncharacteristic urine are all major symptoms of a UTI yet can also be present in multiple other diseases and infections [40].

The most common method currently used to diagnose a UTI is the dipstick test; this is a quick and non-invasive test that is often relied upon both at home and at a GP surgery, and tests for the presence of: nitrites, blood, ketones, urobilinogen, leukocyte esterase etc. [40, 41]. However, the accuracy of such tests has been questioned as these tests are typically qualitative and not quantitative. For example, a nitrite-only test has a sensitivity of just 23.31% [40]. Highly accurate results are available from lab-based culture testing, which involves sending a sample of urine to a lab and can therefore take days before the patient receives a diagnosis and subsequent treatment [42]. During this time, the infection may have grown worse and more painful for the patient. In severe cases, the infection may have spread to the kidneys or bloodstream and will require much more vigorous treatment.

Incidentally, antibiotics have been linked to an increased risk of Candidiasis [43], a fungal infection more commonly known as thrush; an incorrect initial diagnosis leading to antibiotic prescription can therefore cause further infections with near-identical symptoms and hence significantly increase complications of treatment and discomfort to the patient.

The glycoprotein lactoferrin (LF), also called lactotransferrin, is a marker of UTIs. LF has been shown to increase in concentration up to 1000-fold for a patient with a UTI, thus a quick LF urine test could provide a suitable way for doctors to diagnose a patient and provide the correct treatment. LF is reported at concentrations of 30.4 ± 2.7 ng/mL in healthy patients, while it presents at 3300.0 ± 646.3 ng/mL in those suffering from UTI infections [44].

For this reason, LF has been detected on 1% CS LW films at concentrations ranging from 1 nM – 100 nM *via* the glycine method reported in **Section 5.2.6**. The first stage of this was attaching the anti-LF to the CS LW film (**Figure 5.42**). To do this, a 0.25% (v:v) solution of glutaraldehyde was applied to the film for 1 hour. 1 mg/mL anti-LF was reacted for a further hour, and finally 5% (w:v) glycine was used for 5 hours to block any remaining glutaraldehyde.

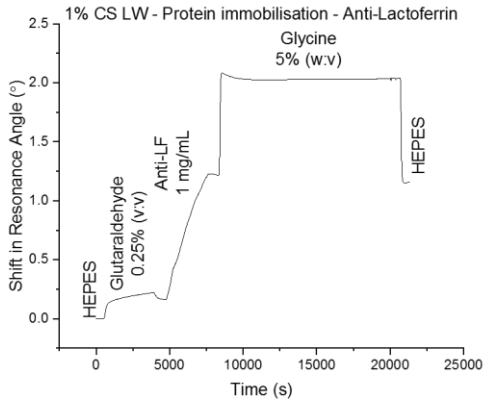

Figure 5.42. 1% CS LW treated with the lactoferrin-glycine protein immobilisation strategy.

After successful binding of the anti-LF and blocking of remaining glutaraldehyde, LF in concentrations from 1 nM to 100 nM was subsequently added to the flow cell for 2 hours each. As we can see in **Figure 5.43** the 1 nM LF did not produce visible binding and instead remained at the same plateau as the HEPES buffer. 5 nM was the next concentration applied, which did show an increase in resonance angle, suggesting that these films are able to detect 5 nM of LF using this immobilisation strategy.

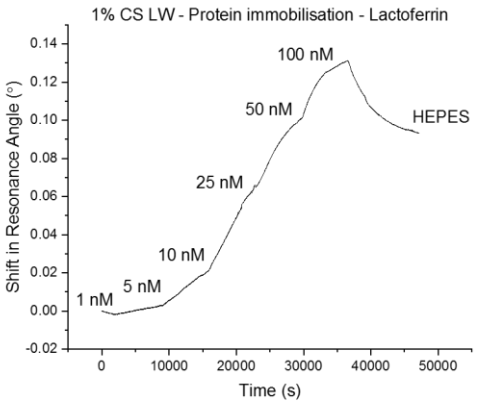

Figure 5.43. 1% CS LW treated with the lactoferrin-glycine protein immobilisation strategy from 1 nM to 100 nM LF.

Additionally, there is a clearly visible shift in the dip on the output image after reaction with the anti-LF, followed by a much smaller but still trackable shift after LF immobilisation (**Figure 5.44**).

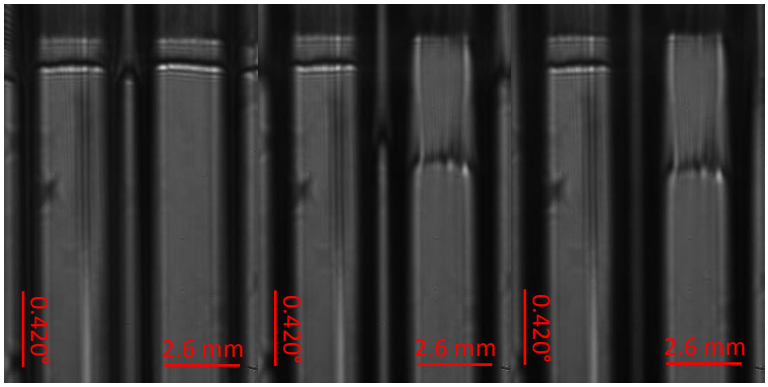

Figure 5.44. Output images of the treated 1% CS LW at different stages of the protein immobilisation. Left = start, middle = after glutaraldehyde, anti-LF, and glycine, right = After LF. Left channel = reference, right channel = sensor.

This method is very exciting and implies that LF can be detected at 5 nM, equivalent to 400 ng/mL. While this is not low enough to detect LF in healthy patients, it is able to detect patients suffering with a UTI which causes an increase of LF in the urine. Further work may be able to improve the sensitivity to detect down to the concentrations seen in healthy patients, but this has not been explored at this time.

5.5 Detection in spiked samples

The samples presented so far have all been carried out in buffer. Of course, real samples will contain a large mixture of interferents [45]. Interferents can be either endogenous or exogenous, meaning they come from within the specimen itself or are introduced into the specimen respectively. There are a significant number of ways interferents can be introduced, including *via* [45-47]:

- Haemolysis, icterus, lipaemia
- Medication or recreational drugs
- Sample preservatives, stabilisers, anticoagulants etc.
- Poor sample handling
- Ingested substances
- Antibodies
- Proteins, including paraproteins such as IgM and IgG
- Metabolites

Any protein detection method must be able to eliminate the effects of these interferents; at the current stage of this project, the focus is on elimination of endogenous interferents such as proteins and metabolites within the sample matrix.

For this reason, we have tested the effect of synthetic urine and human serum on the films and where possible we have attempted protein immobilisation within these matrices to simulate endogenous interferents.

5.5.1 Human serum

Human serum is the main fluid component of human blood which can be obtained upon removal of any blood clotting factors. It is therefore an important biological serum and can contain many clues as to the health of the patient.

Originally a solution of 100% human serum was applied to a 1% CS LW. This resulted in major damage to the film, destroying the waveguiding ability. Therefore, we diluted the serum to 50%, and then to 10%. 10% serum bound significantly to the CS but tracking was still possible, while 50% again damaged the film too quickly and strongly to track.

Figure 5.45 shows this binding, with an extremely high value of up to 3.0°. This change was rapid, and the software used to track the mode struggled to keep up with the change. At higher serum concentrations the tracking is lost on the mode due to the fast movement. As the 10% serum causes a permanent change to the film of such a significant amount it indicates that serum samples will not be suitable for use with these films at the current time, and certainly not at higher concentrations than 10%. This could be addressed in the future by making changes to the film to reduce any NSA before the application of the serum.

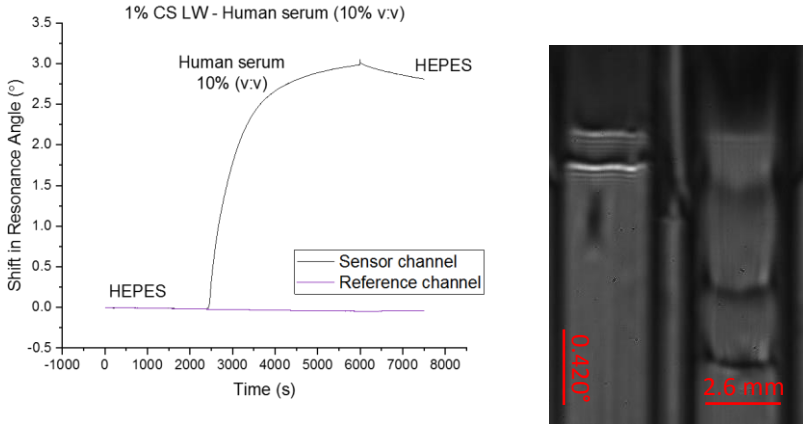

Figure 5.45. 1% CS LW treated with 10% (v:v) human serum (left). Output image of the 10% human serum-treated 1% CS LW (right). Left channel = reference, right channel = sensor.

5% 4-CHO:4-HZ LWs (1:1) also respond to 10% human serum with a small negative shift in resonance angle (**Figure 5.46**). But when returning to buffer, there is no overall change in baseline since before application of the serum. This shows that the 4-CHO:4-HZ films are resistant to NSA from the serum components.

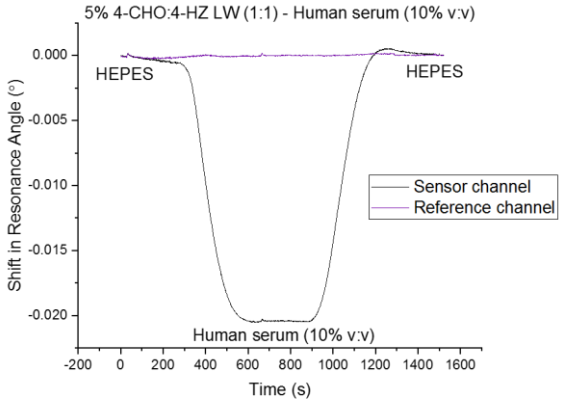

Figure 5.46. 5% 4-CHO:4-HZ (1:1) LW treated with 10% (v:v) human serum.

0.96% PAAm LWs also gave no permanent shift in resonance angle when exposed to 10% human serum, while at 100% serum there is a permanent shift (**Figure 5.47**).

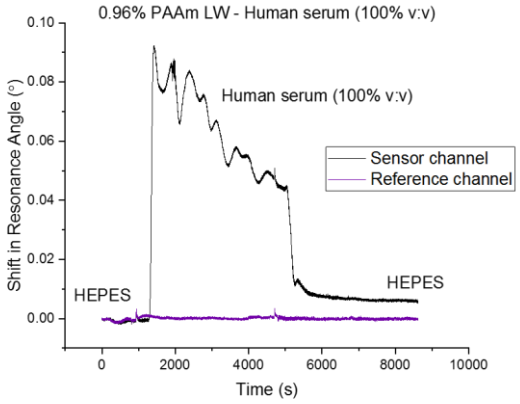

Figure 5.47. 0.96% PAAm LW treated with 100% (v:v) human serum.

For both the 4-CHO:4-HZ and PAAm LWs, the lack of permanent response to 10% serum is not ideal. This is because the reference layer needs to respond to the interferents in the same way the sensor layer does, which will allow for removal of these effects from the final response. As these films are unable to provide this response it calls into question their suitability as references for 1% CS LWs. This highlights the need for a reference layer which is as structurally similar to the sensor layer as possible.

Tests were carried out on single layer LWs in 10% serum to study the effect on protein binding within the serum matrix. A 1% CS LW was tested *via* the ABA method with 10% serum added after the NPB. Serum was added to both the sample and reference channel, giving a large negative shift in resonance angle, and when returning to PBS the channel containing ABA had a higher permanent change than the reference channel which had only been exposed to serum without ABA (**Figure 5.48**).

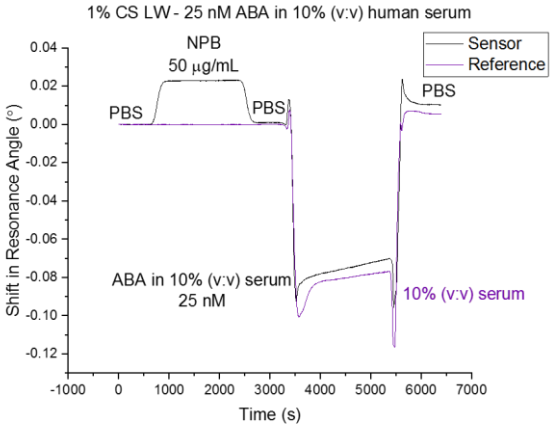

Figure 5.48. 1% CS LW treated with the ABA protein immobilisation method in 10% (v:v) human serum.

It was however unclear whether the serum was interacting differently with the sensor channel to the reference channel as the reference channel did not contain NPB; for this reason, we used a fresh CS LW where both channels were treated with NPB, followed by 10% serum again in both channels but only ABA in the sensor channel (**Figure 5.49**).

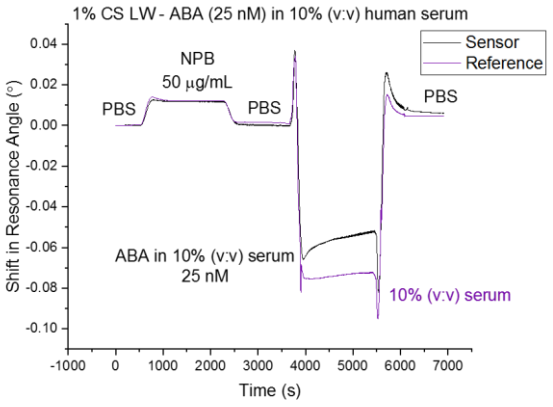

Figure 5.49. 1% CS LW treated with the ABA protein immobilisation method in 10% (v:v) human serum.

The results of this showed a much closer response between the sensor and reference at the end of the experiment. This implies that the serum is interacting differently with the NPB-treated CS compared to untreated. It also suggests that some of the ABA has bound in the sensor channel as the response is higher than that of the reference by 0.001453°. This is

significantly smaller than the response from the buffer samples which gave an average response across three LWs of 0.007266° ± 0.000643° which suggests the 10% serum is restricting the binding from ABA by adsorbing to the LW and blocking the binding sites.

5.5.2 Urine

Urine is another abundant and useful matrix that can be used to detect analytes such as LF. Like blood, urine is also made of various components which could interfere with sensing. For these experiments we used a synthetic urine diluent composed of: calcium chloride, magnesium chloride, potassium chloride, sodium chloride, sodium phosphate, sodium sulfate, urea, creatinine, sodium azide [48].

The 1% CS LWs have a negative shift in resonance angle in response to 10%, 50% and 100% urine. The shift is significantly lower than seen for human serum, and the shift was easily tracked *via* the software at all concentrations. **Figure 5.50** shows how little the mode has visibly moved.

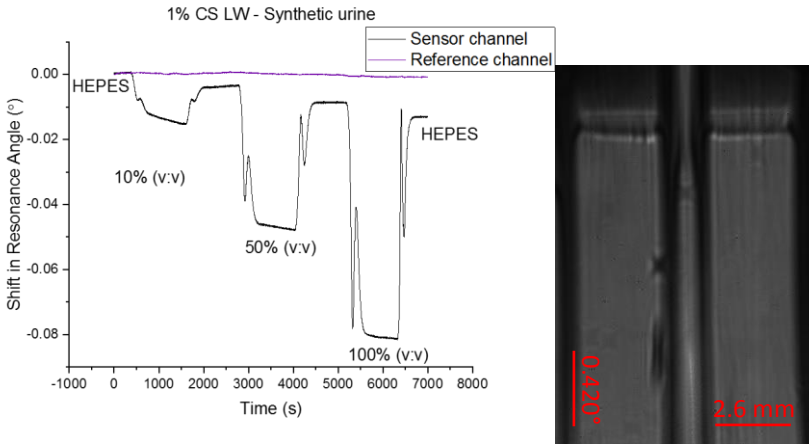

Figure 5.50. 1% CS LW treated with synthetic urine (left). Output image of the 100% synthetic urine-treated 1% CS LW (right). Left channel = reference, right channel = sensor.

Both the 4-CHO:4-HZ and PAAm LWs have positive responses to all the concentrations of urine, without any permanent damage caused to the film (**Figure 5.51**). Again, these responses have the same issues as seen with the serum, making these reference layers less than ideal for working with 1% CS LWs.

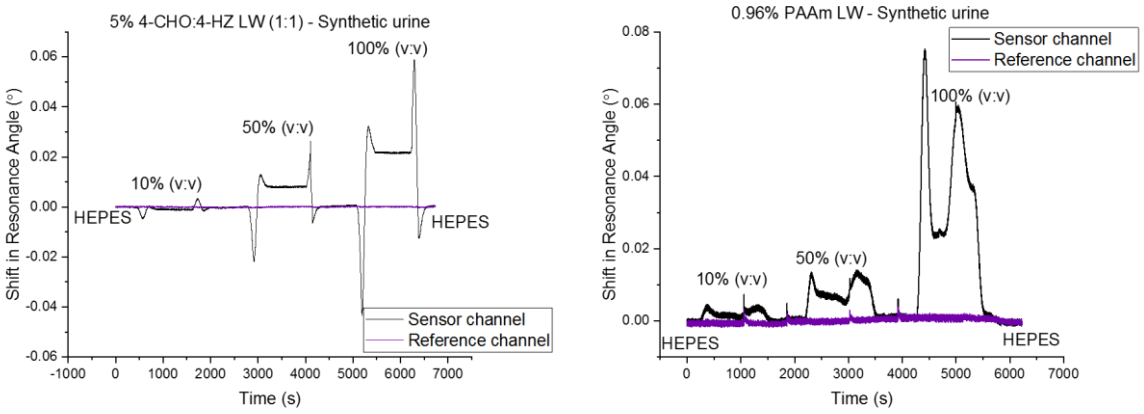

Figure 5.51. 5% 4-CHO:4-HZ (1:1) (left) and 0.96% PAAm (right) LWs treated with synthetic urine.

5% 4-CHO:4-HZ (1:1)/1% CS LWs were tested *via* a shortened NPB method to test the effect of the urine on streptavidin binding. For this, a two-channel flow cell was used in which both channels were treated with NPB as usual. Following this, one channel was treated with streptavidin prepared in buffer, and the other channel was treated with streptavidin prepared in 10% urine. This allowed for a direct comparison of the two channels across the same device. The results are presented in **Figure 5.52**.

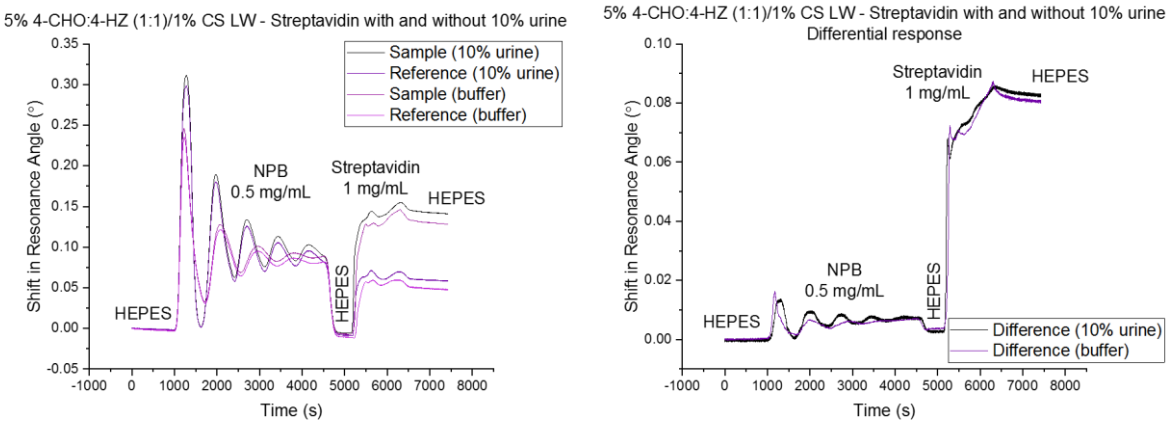

Figure 5.52. 5% 4-CHO:4-HZ:1% CS stacked LW treated with the shortened NPB streptavidin immobilisation strategy, with and without 10% urine.

The results show that the channel with 10% urine gives a slightly increased response to streptavidin compared to the buffer channel. This is expected as the additional content of the urine-containing streptavidin will cause NSA. When the differential response is taken for both channels and compared, there is only a very slight increase in binding in the urine-containing channel in comparison to the buffer channel. This is hopeful, as it shows that most of the NSA and any other fluctuations have been nearly completely negated in both channels. The slight increase in the urine-containing channel is attributed to the urine binding to the CS and not the 4-CHO:4-HZ layers, which was expected as we previously concluded that the 4-CHO:4-HZ will struggle to fully compensate for this due to structural differences between the two channels.

Following this, the same experiment was repeated using 100% urine instead of 10% (**Figure 5.53**).

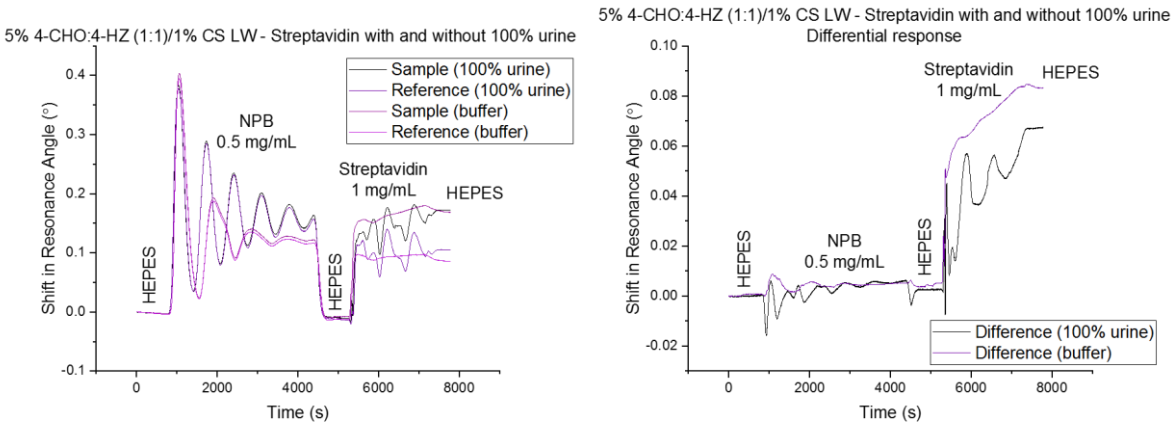

Figure 5.53. 5% 4-CHO:4-HZ:1% CS stacked LW treated with the shortened NPB streptavidin immobilisation strategy, with and without 100% urine.

The results for this were less ideal but were expected. The channel containing 100% urine gives a significantly increased differential response to streptavidin of approximately 0.02° in comparison to the buffer channel. This solidifies the need to develop a reference layer capable of negating NSA due to matrix differences.

5.6 Summary

Taking the LW films developed in **Chapters 3** and **4**, we have applied various protein immobilisation strategies in an attempt to acquire reproducible results for both IgG and LF samples. Based on the current data the best methods are the oxidised antibody, glycine, and LF methods, but all present significant issues when considering their use at POC. Nevertheless, it is still important to explore these methods to find a solution to the POC issue.

While we are not yet able to detect IgG at a level comparable to ELISA, this is not a major issue as we are able to detect IgG in quantities observed in the human body. While a lower LOD would be ideal, when used for IgG this is not necessary.

Differences in response for the reference and sample layers to interferents such as serum and urine call into question the suitability of the reference layers. Ideally the reference layer should respond in the same way as the sensing layer to any interferents, with the only difference being a lack of binding with the desired analyte. As we can see this is not the case, and therefore different reference layers may need to be investigated. By using a reference layer which has high structural similarity to the sensor layer, but without the functionality, the response of both layers should be very similar if not identical to interferents.

5.7 References

1. Mohamad, N.R., et al., *An overview of technologies for immobilization of enzymes and surface analysis techniques for immobilized enzymes.* Biotechnology, biotechnological equipment, 2015. **29**(2): p. 205-220.
2. Liébana, S. and G.A. Drago, *Bioconjugation and stabilisation of biomolecules in biosensors.* Essays in biochemistry, 2016. **60**(1): p. 59-68.
3. Kim, D. and A.E. Herr, *Protein immobilization techniques for microfluidic assays.* Biomicrofluidics, 2013. **7**(4): p. 41501-41501.
4. Zhang, Y.H.P., et al., *Toward low-cost biomanufacturing through in vitro synthetic biology: bottom-up design.* Journal of Materials Chemistry, 2011. **21**(47): p. 18877-18886.
5. Mokhtar, N.F., et al., *The Immobilization of Lipases on Porous Support by Adsorption and Hydrophobic Interaction Method.* Catalysts, 2020. **10**(7): p. 744.
6. CD Bioparticles. *Streptavidin Modification*. 2021 [cited 02-06-2022]; Available from: https://www.cd-bioparticles.com/support/streptavidin-modification.html.
7. Ahluwalia, A., G. Giusto, and D. De Rossi, *Non-specific adsorption on antibody surfaces for immunosensing.* Materials Science and Engineering: C, 1995. **3**(3): p. 267-271.
8. Lichtenberg, J.Y., Y. Ling, and S. Kim, *Non-Specific Adsorption Reduction Methods in Biosensing.* Sensors (Basel, Switzerland), 2019. **19**(11): p. 2488.
9. Sheikh, S., C. Blaszykowski, and M. Thompson, *Sacrificial BSA to block non-specific adsorption on organosilane adlayers in ultra-high frequency acoustic wave sensing.* Surface and Interface Analysis, 2013. **45**(11-12): p. 1781-1784.
10. Riquelme, M.V., et al., *Optimizing blocking of nonspecific bacterial attachment to impedimetric biosensors.* Sensing and Bio-Sensing Research, 2016. **8**: p. 47-54.
11. Sabaté del Río, J., et al., *An antifouling coating that enables affinity-based electrochemical biosensing in complex biological fluids.* Nature Nanotechnology, 2019. **14**(12): p. 1143-1149.
12. Zhang, B., et al., *Effective Reduction of Nonspecific Binding by Surface Engineering of Quantum Dots with Bovine Serum Albumin for Cell-Targeted Imaging.* Langmuir, 2012. **28**(48): p. 16605-16613.
13. Tacha, D.E. and L. McKinney, *Casein Reduces Nonspecific Background Staining in Immunolabeling Techniques.* Journal of Histotechnology, 1992. **15**(2): p. 127-132.
14. Reimhult, E. and F. Höök, *Design of surface modifications for nanoscale sensor applications.* Sensors (Basel, Switzerland), 2015. **15**(1): p. 1635-1675.
15. abcam. *Sheep IgG ELISA Kit (ab190546)*. 2022 [cited 05-07-2022]; Available from: https://www.abcam.com/sheep-igg-elisa-kit-ab190546.html.
16. abcam. *Human IgG ELISA Kit (ab195215)*. 2022 [cited 05-07-2022]; Available from: https://www.abcam.com/human-igg-elisa-kit-ab195215.html.
17. Sigma Aldrich. *Normal Rabbit IgG*. [cited 28-04-2022]; Available from: https://www.sigmaaldrich.com/GB/en/product/mm/12370.
18. RCSB Protein Data Bank. *2VUO Crystal structure of the rabbit IgG Fc Fragment*. 2008 [cited 29-04-2022]; Available from: https://www.rcsb.org/structure/2VUO.
19. Sigma Aldrich. *Protein G and Protein A Bind to Different IgG*. [cited 03-05-2022]; Available from: https://www.sigmaaldrich.com/GB/en/technical-documents/technical-article/protein-biology/protein-pulldown/protein-a-g-binding.
20. Tsai, B., et al., *Poly(Poly(Ethylene Glycol) Methyl Ether Methacrylate) Grafted Chitosan for Dye Removal from Water.* Processes, 2017. **5**(1): p. 12.
21. Xiao, Y. and S.N. Isaacs, *Enzyme-linked immunosorbent assay (ELISA) and blocking with bovine serum albumin (BSA)--not all BSAs are alike.* J Immunol Methods, 2012. **384**(1-2): p. 148-51.

22. Silin, V., H. Weetall, and D.J. Vanderah, *SPR Studies of the Nonspecific Adsorption Kinetics of Human IgG and BSA on Gold Surfaces Modified by Self-Assembled Monolayers (SAMs).* Journal of Colloid and Interface Science, 1997. **185**(1): p. 94-103.
23. Ahirwar, R., et al., *BSA blocking in enzyme-linked immunosorbent assays is a non-mandatory step: a perspective study on mechanism of BSA blocking in common ELISA protocols.* RSC Advances, 2015. **5**(121): p. 100077-100083.
24. RCSB Protein Data Bank. *3V03 Crystal structure of Bovine Serum Albumin*. 2012 [cited 29-04-2022]; Available from: https://www.rcsb.org/structure/3v03.
25. University of California San Francisco Health. *Albumin blood (serum) test*. [cited 04-05-2022]; Available from: https://www.ucsfhealth.org/medical-tests/albumin-blood-(serum)-test#:~:text=The%20normal%20range%20is%203.4,vary%20slightly%20among%20different%20laboratories.
26. Babcock, J.J. and L. Brancaleon, *Bovine serum albumin oligomers in the E- and B-forms at low protein concentration and ionic strength.* International journal of biological macromolecules, 2013. **53**: p. 42-53.
27. Gupta, R. and N.J. Goddard, *A study of diffraction-based chitosan leaky waveguide (LW) biosensors.* Analyst, 2021. **146**(15): p. 4964-4971.
28. ThermoFisherScientific. *Pierce™ Sulfo-NHS-Acetate*. [cited 04-07-2022]; Available from: https://www.thermofisher.com/order/catalog/product/26777#:~:text=Thermo%20Scientific%20Pierce%20Sulfo%2DNHS,prevent%20specific%20interactions%20or%20conjugations.
29. Hermanson, G.T., *Chapter 3 - The Reactions of Bioconjugation*, in *Bioconjugate Techniques (Third Edition)*, G.T. Hermanson, Editor. 2013, Academic Press: Boston. p. 229-258.
30. Wu, W.J., B. Vrhovski, and A.S. Weiss, *Glycosaminoglycans Mediate the Coacervation of Human Tropoelastin through Dominant Charge Interactions Involving Lysine Side Chains*.* Journal of Biological Chemistry, 1999. **274**(31): p. 21719-21724.
31. Bax, D.V., et al., *Linker-free covalent attachment of the extracellular matrix protein tropoelastin to a polymer surface for directed cell spreading.* Acta Biomaterialia, 2009. **5**(9): p. 3371-3381.
32. ThermoFisherScientific. *Avidin-Biotin Interaction*. [cited 03-05-2022]; Available from: https://www.thermofisher.com/uk/en/home/life-science/protein-biology/protein-biology-learning-center/protein-biology-resource-library/pierce-protein-methods/avidin-biotin-interaction.html.
33. Luong, J.H.T. and S.K. Vashist, *Chemistry of Biotin-Streptavidin and the Growing Concern of an Emerging Biotin Interference in Clinical Immunoassays.* ACS Omega, 2020. **5**(1): p. 10-18.
34. BroadPharm. *DBCO Azide Ligation Protocol*. 2022 [cited 02-06-2022]; Available from: https://broadpharm.com/web/protocol_files/DBCO-Azide%20Click%20Chemistry.pdf.
35. Trilling, A.K., et al., *Orientation of llama antibodies strongly increases sensitivity of biosensors.* Biosensors and Bioelectronics, 2014. **60**: p. 130-136.
36. Zhang, C., et al., *Site-Selective Cysteine-Cyclooctyne Conjugation.* Angew Chem Int Ed Engl, 2018. **57**(22): p. 6459-6463.
37. Liu, H. and K. May, *Disulfide bond structures of IgG molecules: structural variations, chemical modifications and possible impacts to stability and biological function.* MAbs, 2012. **4**(1): p. 17-23.
38. Oshige, M., et al., *Immobilization of His-Tagged Proteins on Various Solid Surfaces Using NTA-Modified Chitosan.* Open Journal of Polymer Chemistry, 2013. **3**(1).
39. Martin, N.C., et al., *The use of phosphate buffered saline for the recovery of cells and spermatozoa from swabs.* Sci Justice, 2006. **46**(3): p. 179-84.
40. Mambatta, A.K., et al., *Reliability of dipstick assay in predicting urinary tract infection.* Journal of family medicine and primary care, 2015. **4**(2): p. 265-268.
41. Patel, H.D., et al., *Can urine dipstick testing for urinary tract infection at point of care reduce laboratory workload?* Journal of clinical pathology, 2005. **58**(9): p. 951-954.

42. Pan, Y., et al., *Electrochemical immunosensor detection of urinary lactoferrin in clinical samples for urinary tract infection diagnosis.* Biosensors & bioelectronics, 2010. **26**(2): p. 649-654.
43. Homei, A. and M. Worboys, *Chapter 3 - Candida: A Disease of Antibiotics*, in *Fungal Disease in Britain and the United States 1850-2000: Mycoses and Modernity*. 2013, Palgrave Macmillan: Basingstoke, UK.
44. Arao, S., et al., *Measurement of urinary lactoferrin as a marker of urinary tract infection.* Journal of clinical microbiology, 1999. **37**(3): p. 553-557.
45. Clinical and Laboratory Standards Institute. *Clinical Laboratory Testing Interference*. 2019 [cited 20-05-2022]; Available from: https://clsi.org/about/blog/clinical-laboratory-testing-interference/.
46. Dimeski, G., *Interference testing.* The Clinical biochemist. Reviews, 2008. **29 Suppl 1**(Suppl 1): p. S43-S48.
47. Cornell University College of Veterinary Medicine. *Interferences*. 2020 [cited 20-05-2022]; Available from: https://eclinpath.com/test-basics/interferences/.
48. Sigma Aldrich. *Sigmatrix Urine Diluent*. [cited 08-05-2022]; Available from: https://www.sigmaaldrich.com/GB/en/product/sigma/sae0074.

6 Chapter 6 – Portability

6.1 Introduction

To achieve effective point-of-care (POC) diagnosis, it is imperative that the instrumentation and software used for testing and analysis is portable and easy to use. A sensor cannot be described as POC if it is unable to be easily transported and operated outside of a dedicated clinical laboratory and by highly skilled technicians. This is of particular importance when considering the use of such instruments in low-resource countries. It is estimated that around 6.6 million children younger than 5 years old die each year [1], with 5.2 million dying from treatable diseases in 2019 [2]. Of this, 95% of these children are from low-resource countries, with at least a third of the deaths occurring due to acute respiratory infections (ARIs) [1]. Sub-Saharan Africa has a death rate of 1 in 13 in children below 5 years old [2], and while these cannot all be attributed to disease, an improvement in health care, diagnostics and treatments will undoubtedly reduce this extreme mortality rate.

To achieve an improvement in health care it is essential that patients are diagnosed rapidly and provided timely access to appropriate treatment. One way to achieve this is using POC instrumentation which can be used outside of a clinical laboratory without a decrease in result accuracy. Often this involves the miniaturisation and simplification of current instrumentation to make it portable and durable, hence suited to travel and for use by those with minimal training. While modern analytical instrumentation continues to develop and include more components to improve usage, adaptability, sensitivity, and accuracy, there is the issue presented by making an instrument “too complicated”. POC biosensors must be accessible for use by healthcare workers who do not have significant experience operating

and troubleshooting that specific device. It is therefore crucial to strike a balance between maintaining the accuracy of the instrument while ensuring it is straightforward to the end user.

Over the past decade three-dimensional (3D) printing with plastic resins has risen in popularity as 3D printers have become increasingly accessible and affordable. More expensive printer models can be used for dedicated industrial purposes while cheaper printer models are available as personal devices. 3D printing technology has improved to the point where 3D printed scientific instruments can be designed and developed for a lower cost than traditional instruments, e.g., those made of expensive and heavy metals [3, 4]. 3D printing is also known as additive manufacturing, referring to the fact that the end-product is built layer by layer from a starting material [5, 6]. This is in direct comparison to subtractive manufacturing often used in metal-based instrumentations, in which a block of starting material is shaped by removing sections and producing a significantly higher amount of waste than additive manufacturing [6].

Not only can some devices be made for a lower cost, but they can also be designed to be more portable by reducing the size and weight of the instrument. Smartphone-based applications can also be developed to further improve portability by removing the requirement for a dedicated computer [4, 7-9].

Metal 3D printing can be achieved by laser sintering, but such products tend to be expensive, heavy, and rough. Meanwhile plastic waveguiding structures have already been 3D printed, such as those designed by Chahal *et al.* which incorporates a 3D printed plastic waveguide base coated in metal, making the waveguide lighter and smoother [3]. This

waveguide was designed for use in antennas and was suggested to have applications in everyday life such as in vehicles. While this is not a biosensor, it does highlight the adaptability of 3D printed instruments for use in everyday life.

3D printed microfluidic chips are becoming more prevalent, and an optical biosensor comprising of a 3D printed microfluidic chip and gold-platinum nanocatalysts was developed by Zheng *et al.* with the ability to detect down to 17 colony forming unit (CFU)/mL of *Salmonella typhimurium*, an important biomarker in food safety, and the authors suggest that it is easily adaptable to the sensing of other bacteria by simply changing the target antibody [10]. In comparison a previous study published 10 years prior by Kim *et al.* was able to detect *Salmonella* at a LOD of 10^6 CFU/mL [11], showing the clear improvement achieved by Zheng *et al.* by using a 3D printed microfluidic chip with integrated micromixer to enhance bacteria separation.

Somarapalli *et al.* developed a 3D printed surface plasmon resonance (SPR) optical transducer for approximately $600 [12]. This device comprises of multi-channels for internal referencing, along with two light sources, two polarisers, and two optical fibres. The low cost of the instrument is extremely impressive when compared to the high cost of modern laboratory-based SPR sensors which typically start at $50,000 for a basic model [13], but the inclusion of multiple components such as two separate light sources does increase the chances of channel-to-channel variability. Nevertheless, this is an excellent example of a portable optical sensor developed through 3D printing techniques, with a sensitivity in the order of 10^{-4} refractive index units (RIU).

To achieve the portability aspect of this project, a miniature 3D printed waveguide was designed and produced by a collaborator. This device was kindly donated to this project and was used to test leaky waveguides (LWs) [14]. This instrument has significant portability improvements over the traditional laboratory-based instrumentation (**Figure 6.1**).

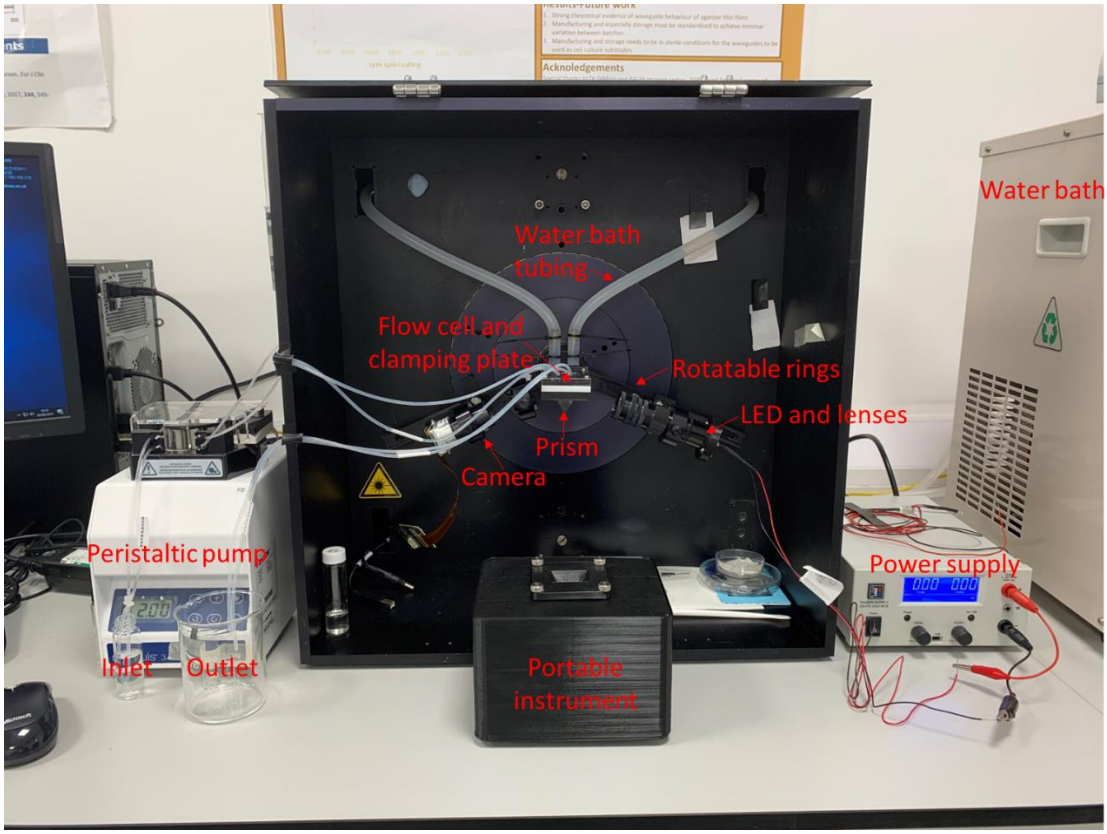

Figure 6.1. Comparison of the laboratory-based instrumentation (rear) and the portable instrumentation (front).

Typically, a laboratory-based waveguide such as the one seen in **Figure 6.1** consists of a heavy metal casing produced *via* subtractive milling techniques, mounted with a prism holder and rotatable rings to control the positioning of the attached light emitting diode (LED) light source and camera [15]. In addition, a power source is required to power the LED, a water bath to control the temperature, and a peristaltic pump to control sample flow. The instrument is then connected to a computer, where data is collected *via* a specialist program. This instrumentation contains multiple moveable components which increases the versatility

of the instrument but also increases the risk of introducing significant mechanical fluctuations. This setup is also not suitable for use by untrained technicians, as there are multiple adjustments that can be made to change the output. Overall, this instrument is suitable for laboratory-based testing, but the size (~60x60x35 cm), weight (~25 kg), and complexity all prevent this from being suitable for POC applications.

In comparison, the 3D printed instrument is produced from lightweight carbon fibre-filled polylactic acid (CF-PLA), and the optical components are all contained within the chassis. This instrument requires a power socket, peristaltic pump, and computer, making it significantly more portable than the bulky traditional instrument.

A drawback of this instrument is the inability to regulate temperature. While the lab instrument can be connected to a water bath to maintain a consistent temperature, or a secondary channel used to negate temperature fluctuations, the portable instrument is unable to use either of these techniques due to practicality issues. Therefore, any LW tested using this instrument is exposed to signal fluctuations due to temperature changes. While this is an issue for single-layer LW films, incorporation of an internal referencing system *via* stacked LWs will allow for the removal of such undesirable effects.

Figure 6.2 shows the internal setup of the 3D printed instrument. A mirror is employed to reduce the size of the instrument and allow the camera to be placed further from the prism. Additionally, both the mirror and camera positions can be shifted *via* the computer software, therefore can be tailored to each LW. By containing the moveable components within the chassis of the instrument it is much less likely to be subjected to accidental movement by untrained technicians.

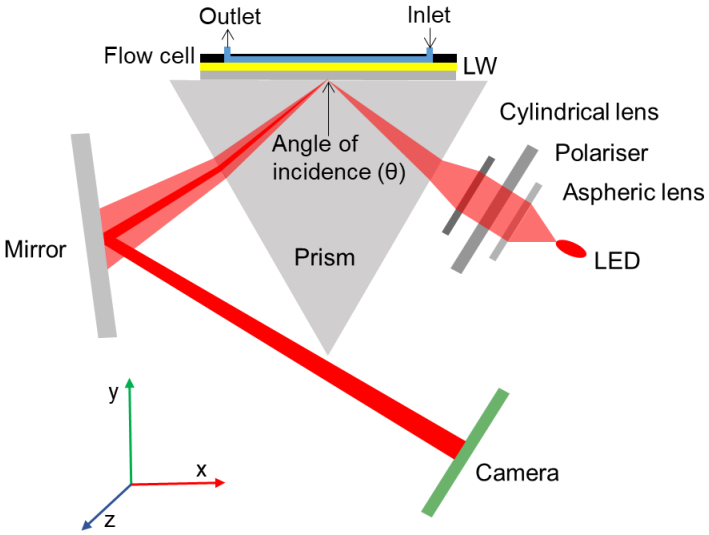

Figure 6.2. Schematic of the internal setup of the 3D printed waveguide instrument.

This chapter will explore the testing of the portable instrument using both single and stacked waveguide films. Some of this work was carried out in parallel to the work on the laboratory instrument and therefore there is some crossover between sensing strategies.

In all cases the results obtained on the portable instrument have been displayed alongside the results for the same type of films on the laboratory instrument to allow for direct comparison of the instrumentation. This comparison consists mainly of glycerol and PEG calibration sensorgrams, allowing for clear assessment between the instruments based on refractive index sensitivity (RIS) and porosity.

The portable device was not produced as a part of this project and was donated by a collaborator. All data reported in this thesis using the portable instrument has been carried out as part of this project and not by the collaborator.

6.2 Flow cell design

Due to limitations in the camera distance and angle, the portable instrument was unable to support the two-channel flow cell as only one channel was visible on the output image for tracking. This highlighted the need for an internally referenced waveguide biosensor that does not rely on separate channels. For this system the circular flow cell was initially used as per the laboratory-based instrument, but phased out and replaced with the Y-shaped flow cell presented in **Chapter 3** (**3.3.3**). This proved to be an improvement over the circular flow cell but did not offer enough flexibility on placement. Therefore, a simple short straight channel flow cell was employed (**Figure 6.3**). This was an improvement over the circular flow cell and less prone to dead zones, while allowing multiple areas of a single film to be tested consecutively as the short nature of this flow cell provides more placement options.

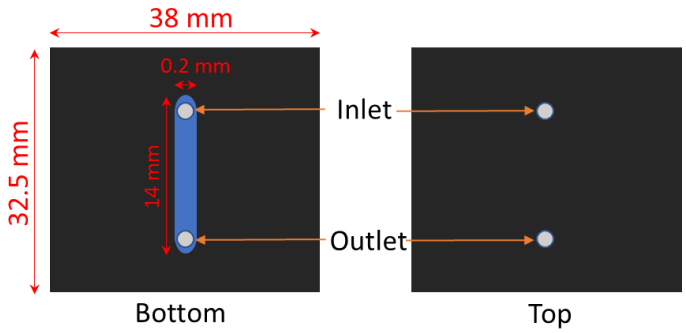

Figure 6.3. A single channel flow cell.

Throughout this chapter the single channel flow cell has been used except where the circular or Y-shaped flow cell has been stated.

6.3 Single layer leaky waveguides

Due to the lack of temperature regulation in this instrument, single layer LWs were tested within a temperature-controlled room at 22.0 °C. This helped to maintain the consistency of results without a two-channel flow cell or water bath.

6.3.1 Chitosan DDLW, CS (doped)

As with the laboratory instrument, the first films tested on this instrument were the dye-doped leaky waveguide (DDLW) 1% chitosan (CS) films. **Figure 6.4** shows the typical output of such a film on this instrument. Like with the laboratory instrument, the dip is dark and broad due to the Reactive Blue 4 (RB4). It is also close to the total internal reflection (TIR) boundary which is just visible at the top of the image.

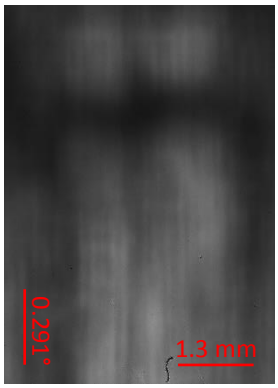

Figure 6.4. Output image of a 1% CS DDLW on the portable instrument under a single channel flow cell.

The response from the glycerol and poly(ethylene glycol) (PEG) solutions are comparable to the laboratory instrument reported in **Chapter 3** (**3.2.2**), indicating that this instrument is operating on a similarly high level to the laboratory instrument (**Figure 6.5**).

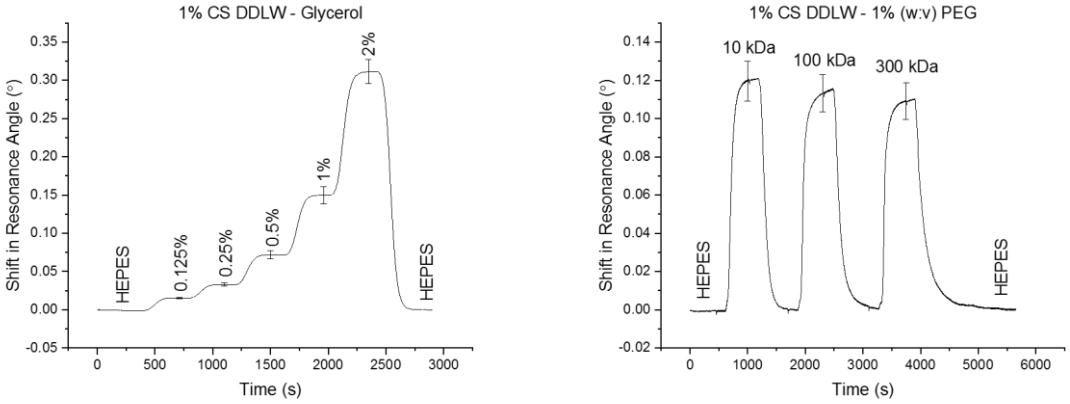

Figure 6.5. Glycerol (left) and PEG (right) runs on 1% CS DDLW films using the portable instrument. Error bars were calculated as 1σ across three different DDLWs.

For comparison purposes, the average responses are recorded below in **Table 6.1**. Any variation can be attributed to slight device-to-device variation rather than instrumental differences.

Table 6.1. Comparison of the average responses of 1% CS DDLWs to 1% PEG solutions of different molecular weights (MWs) on the laboratory and portable instruments.

1% PEG SIZE	LABORATORY RESPONSE (°)	PORTABLE RESPONSE (°)
10 kDa	0.110360	0.112691
100 kDa	0.087345	0.103936
300 kDa	0.076586	0.098794

The RIS is found as the gradient of the line produced from plotting the refractive index (RI) against the shift in resonance angle (**Figure 6.6**).

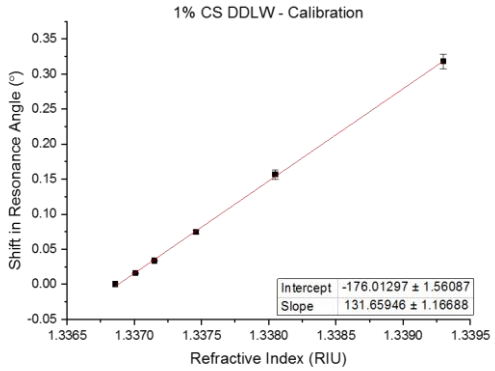

Figure 6.6. Calibration curve for 1% CS DDLWs on the portable instrument. Error bars were calculated as 1σ across three different DDLWs.

As reported in **Table 6.2**, the RIS of the portable instrument is not far from the RIS of the laboratory instrument for the same films. This, along with the glycerol and PEG data, suggests that these films are highly reproducible across different devices, and the laboratory and portable instruments can detect RI changes in these films to a very similar level.

Table 6.2. Comparison of the RIS values for 1% CS DDLWs on the laboratory and portable instruments.

LABORATORY INSTRUMENT RIS (°/RIU)	PORTABLE INSTRUMENT RIS (°/RIU)
140.43 ± 1.53	131.70 ± 1.17

For protein testing, a primitive version of the glutaraldehyde method reported in **Chapter 5** (**5.2.2**) was used, referred to as GA-v1 (**Figure 6.7**). This was carried out before the optimisation of the method.

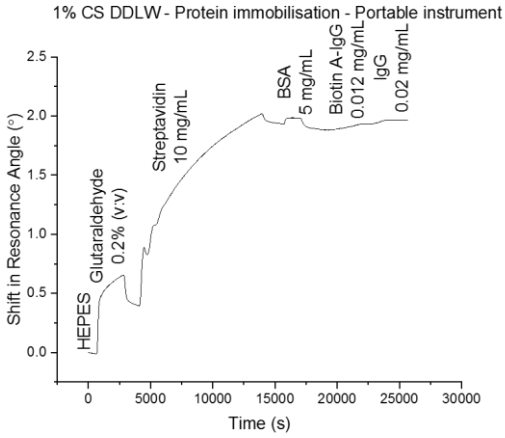

Figure 6.7. 1% CS DDLW treated with the GA-v1 glutaraldehyde protein immobilisation strategy on the portable instrument.

This method involved using a very high concentration of streptavidin, followed by bovine serum albumin (BSA) to block any remaining glutaraldehyde. Biotin anti-immunoglobulin G (biotin A-IgG) was then used to bind sheep IgG at 0.02 mg/mL.

This method worked well and provided a strong response for the IgG. It was further modified in **Chapter 5** to improve binding and reproducibility, but in this case has been reported to show the clear binding that can be seen on the portable instrument. This gave good results which were subsequently reported in [14].

6.3.2 Chitosan LW, CS

As the development of the purified 1% CS films continued, they were also tested using this instrument. As expected, the output image of these films such as that in **Figure 6.8** shows a dip that is much brighter and thinner than the one in **Figure 6.4**.

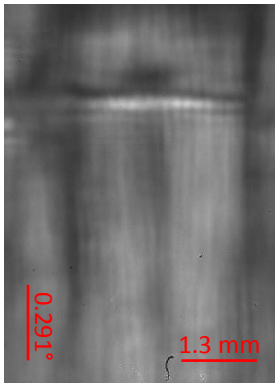

Figure 6.8. Output image of a 1% CS LW on the portable instrument under a single channel flow cell.

There is a strong response to both glycerol and PEG solutions, with the PEG response reducing as the molecular weight (MW) increases (**Figure 6.9**).

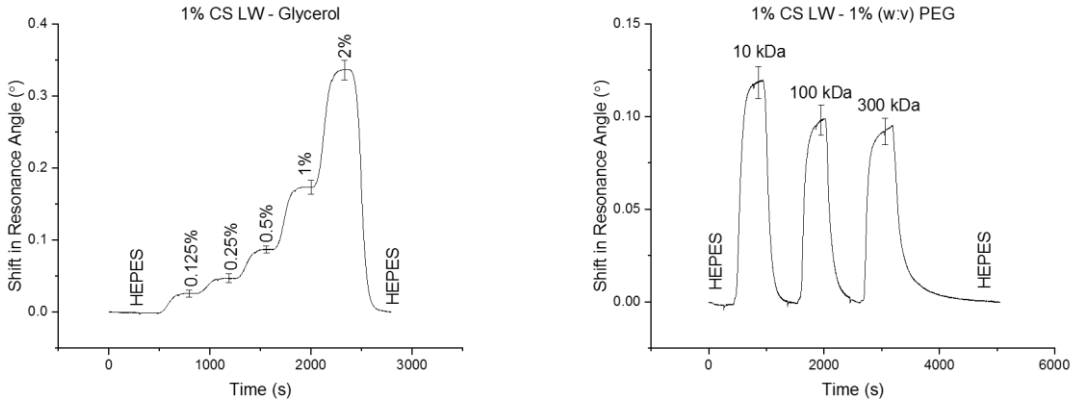

Figure 6.9. Glycerol (left) and PEG (right) runs on 1% CS LW films using the portable instrument. Error bars were calculated as 1σ across three different LWs.

As with the doped CS films, these undoped CS films are highly similar to the results obtained on the laboratory instrument (**Table 6.3**), providing further evidence that the two instruments produce comparable data.

Table 6.3. Comparison of the average responses of 1% CS LWs to 1% PEG solutions of different MWs on the laboratory and portable instruments.

1% PEG SIZE	LABORATORY RESPONSE (°)	PORTABLE RESPONSE (°)
10 kDa	0.116419	0.116523
100 kDa	0.091583	0.096954
300 kDa	0.080598	0.092745

The RIS is excellent with a value of 133.41 ± 1.55 °/RIU, again attesting to the sensitivity of both the films and the instrument (**Figure 6.10**).

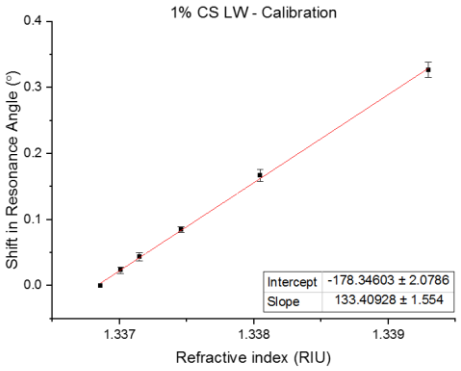

Figure 6.10. Calibration curve for 1% CS LWs on the portable instrument. Error bars were calculated as 1σ across three different LWs.

The RIS of these films is lower than that obtained on the laboratory instrument but is still high (**Table 6.4**). These films show excellent sensitivity to RI changes, suggesting that not only are the LWs reproducible as already discussed in **Chapter 3** (**3.2.2**), but also that the portable instrument produces a response very similar to the laboratory instrument for both the doped and purified CS.

Table 6.4. Comparison of the RIS values for 1% CS LWs on the laboratory and portable instruments.

LABORATORY INSTRUMENT RIS (°/RIU)	PORTABLE INSTRUMENT RIS (°/RIU)
144.23 ± 1.21	133.41 ± 1.55

Protein testing was carried out *via* the NHS-PEG_{12}-biotin (NPB) method reported in **Chapter 5** (**5.2.3**). The results for this method were excellent, with a clear response from IgG binding (**Figure 6.11**). As discussed in **Chapter 5**, this method is susceptible to non-specific adsorption (NSA) despite the inclusion of sulfo NHS acetate (SNA) and the use of streptavidin makes it irreproducible and hence this method will not be used in the long term; regardless,

it does show that the portable instrument is comparable to the laboratory instrument in terms of binding.

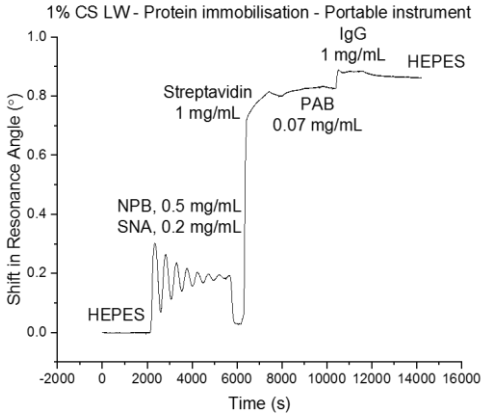

Figure 6.11. 1% CS LW treated with the NPB protein immobilisation strategy on the portable instrument.

Unfortunately, the difference in response between films of the same composition is striking; two 1% CS LWs were prepared on the same day and tested consecutively. The responses for each step of the immobilisation are reported below for each film (**Table 6.5**).

Table 6.5. Comparison of the response of two different 1% CS LWs to each stage of the immobilisation strategy using the portable instrument.

	EXPOSURE TIME	**FILM 1**	**FILM 2**
NPB (0.5 mg/mL) & SNA (0.2 mg/mL)	1 h	0.038252°	0.028832°
STREPTAVIDIN (1 mg/mL)	20 min	1.010622°	0.759225°
PAB (0.07 mg/mL)	30 min	0.166984°	0.025742°
RABBIT IgG (1 mg/mL)	20 min	0.667044°	0.042257°

Film 1 provided a higher response at each step of the immobilisation strategy, particularly when considering the binding of protein A biotin (PAB) and IgG. This extreme difference in response further proves the irreproducibility of this technique and emphasises the reasons why it was replaced in **Chapter 5**. Despite the difference in response, this does prove that both the instrument and films are sensitive to changes in RI.

6.3.3 N-(3-aminopropyl)methacrylamide, APMA

While the N-(3-aminopropyl)methacrylamide (APMA) films were ultimately confirmed to be less ideal for sensing than the 1% CS films, they were still tested in parallel on the portable instrument. **Figure 6.12** shows an excellent example of an APMA film on the portable instrument; the dip is uniform and clear, highly suited to tracking.

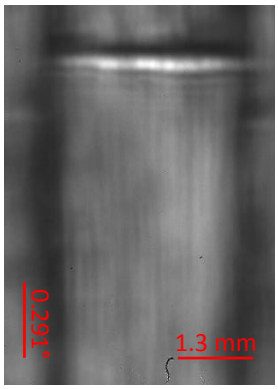

Figure 6.12. Output image of a 4.5% APMA LW on the portable instrument under a single channel flow cell.

Despite the excellent output, the response to the PEG solutions is less ideal (**Figure 6.13**). While the pattern behaves as expected with the lower MW PEG giving the highest response and vice versa, the actual responses are much lower than anticipated.

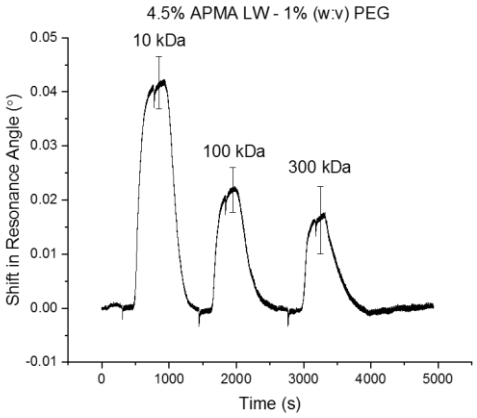

Figure 6.13. PEG run on a 4.5% APMA LW film using the portable instrument. Error bars were calculated as 1σ across three different LWs.

The porosity of these films appears to have dropped significantly in comparison to the laboratory instrument (**Table 6.6**). The response to each PEG has approximately halved, and this is expected to be due to the fabrication inconsistencies discussed in **Chapter 3** (**3.2.4**). This is backed up by the large error bars which indicate device-to-device inconsistencies. While we cannot rule out the difference being related to the instrument, it is much more likely due to the LWs themselves which lack uniformity and reproducibility.

Table 6.6. Comparison of the average responses of 4.5% APMA LWs to 1% PEG solutions of different MWs on the laboratory and portable instruments.

1% PEG SIZE	LABORATORY RESPONSE (°)	PORTABLE RESPONSE (°)
10 kDa	0.070383	0.037010
100 kDa	0.041621	0.025169
300 kDa	0.032506	0.025381

Protein immobilisation was also attempted with these films *via* the NPB method reported in **Chapter 5** (**5.2.3**) (**Figure 6.14**).

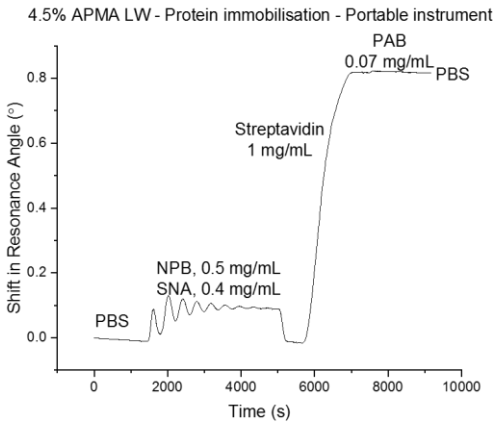

Figure 6.14. 4.5% APMA LW treated with the NPB protein immobilisation strategy on the portable instrument.

No binding was seen for PAB, suggesting that the streptavidin was unable to react with it. This could be due to the low film porosity preventing the PAB from entering the film and

reacting with the streptavidin. It is also possible that the streptavidin has too few binding sites available in this particular case due to binding excessively to the NPB. The SNA concentration had also been increased in this test to prevent further NSA, meaning it could also be possible that not enough NPB had bound to the film in the first place to bind enough streptavidin.

Further research on these films was not carried out on the portable instrument due to the issues with film fabrication. While more investigation could be done into these films, this was determined not to be a conducive use of time as discussed in **Chapter 3**. Nevertheless, these LWs have been useful to help compare the laboratory and portable instruments.

6.3.4 Polyacrylamide, PAAm

0.96% Poly(acrylamide) (PAAm) films were also tested on the instrument in preparation for stacked films. **Figure 6.15** shows such a film, with a bright and clear dip that can easily be tracked. The dip itself is not entirely uniform as seen by the waving formation and is discussed in relation to the results below.

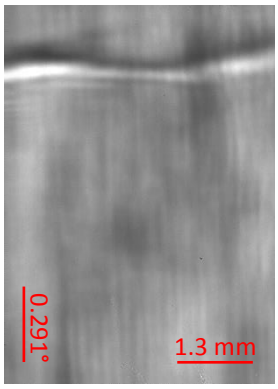

Figure 6.15. Output image of a 0.96% PAAm LW on the portable instrument under a circular flow cell.

The PEG behaviour was as anticipated, although the shift in resonance angle for each MW was slightly lower than expected (**Figure 6.16**).

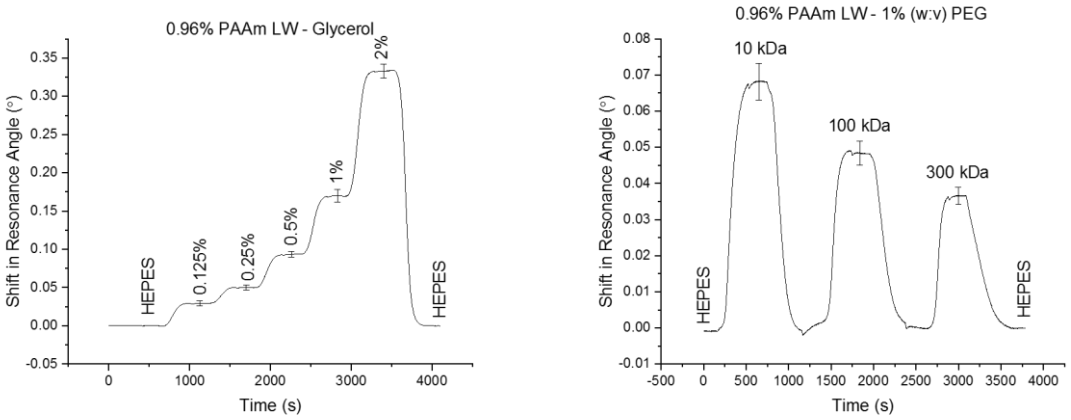

Figure 6.16. Glycerol (left) and PEG (right) runs on a 0.96% PAAm LW film using the portable instrument. Error bars were calculated as 1σ across the width of one LW.

The PEG results are all approximately 0.02° lower than the comparative results on the laboratory instrument reported in **Chapter 4** (**4.2.1**) (**Table 6.7**).

Table 6.7. Comparison of the average responses of 0.96% PAAm LWs to 1% PEG solutions of different MWs on the laboratory and portable instruments.

1% PEG SIZE	LABORATORY RESPONSE (°)	PORTABLE RESPONSE (°)
10 kDa	0.088122	0.068012
100 kDa	0.068089	0.048342
300 kDa	0.057916	0.036539

This could be due to fabrication differences as previously discussed. There is high variability in these films from device-to-device, shown by the large error bars on the laboratory instrument data. The data collected on the portable instrument was only able to be procured using one PAAm film due to issues with the fabrication, therefore it is likely that the difference between the laboratory and portable instrument responses is due to device-to-device variability rather than due to instrumentation changes. The lack of strong uniformity of this film in particular also indicates fabrication challenges.

The RIS for these films on the portable instrument is good, with a value of 112.63 ± 2.27 °/RIU (**Figure 6.17**). While this is still approximately 20 °/RIU below the RIS of CS on the same instrument, it is higher than seen for the same type of films on the laboratory instrument.

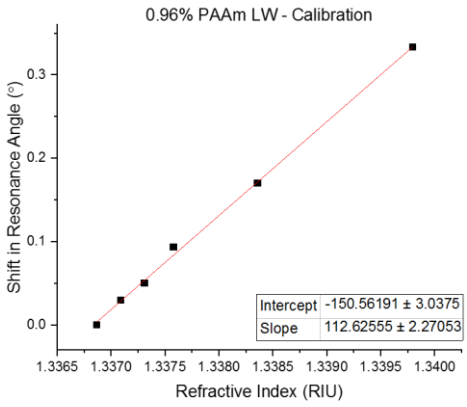

Figure 6.17. Calibration curve for the 0.96% PAAm LW on the portable instrument.

The RIS is much higher for the portable instrument, which again could be explained by the fabrication issues (**Table 6.8**). It is possible that the single film tested on the portable instrument was not a good example of these films. To make this test more reliable it should be repeated at minimum a further two times, but this was not possible at this time as the films were not reproducible enough. This implies that these films are not ideal for use as LWs without further development.

Table 6.8. Comparison of the RIS values for 0.96% PAAm LWs on the laboratory and portable instruments.

LABORATORY INSTRUMENT RIS (°/RIU)	PORTABLE INSTRUMENT RIS (°/RIU)
73.94 ± 2.77	112.63 ± 2.27

6.4 Stacked leaky waveguides

6.4.1 Poly(acrylamide)/Chitosan DDLW, PAAm/CS (doped)

PAAm films were prepared at 0.96% (w:v) and 1% (w:v) CS was spin coated on top. The films were doped with RB4 to form DDLWs and tested on the portable instrument. Two dark but clearly visible and relatively uniform dips are seen in the output image, suggesting that these films will be easy to track and have good layer separation (**Figure 6.18**).

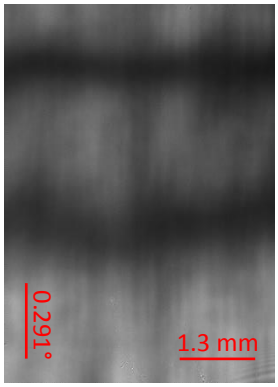

Figure 6.18. Output image of a 0.96% PAAm/1% CS stacked DDLW on the portable instrument under a circular flow cell.

The porosity of these films is excellent, but the large error bars suggest high film-to-film variability (**Figure 6.19**). This was expected as the exposure to glutaraldehyde for CS crosslinking will also affect the PAAm layer and the degree of further crosslinking caused will be uncontrollable. Additionally, the issues with preparing uniform PAAm films will also contribute to the large error bars. Despite this, the films give good results and there is clear definition between each mode.

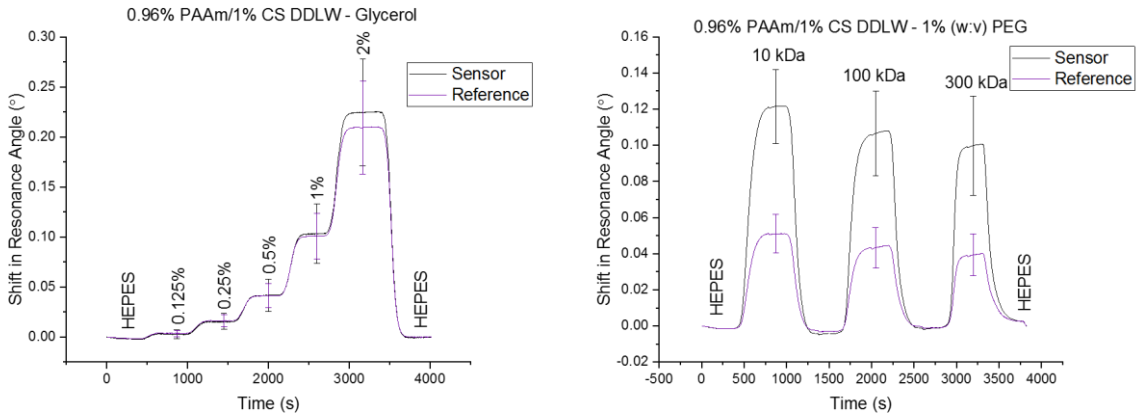

Figure 6.19. Glycerol (left) and PEG (right) runs on 0.96% PAAm/1% CS stacked DDLWs films using the portable instrument. Error bars were calculated as 1σ across three different LWs.

The responses are also very similar to those gained on the laboratory instrument for both layers; in fact, the portable instrument has higher responses for the 1% CS that again can be attributed to the fabrication variations (**Table 6.9**).

Table 6.9. Comparison of the average responses of 0.96% PAAm/1% CS stacked DDLWs to 1% PEG solutions of different MWs on the laboratory and portable instruments.

1% PEG SIZE	1% CS RESPONSE (°)		0.96% PAAM RESPONSE (°)	
	Laboratory	Portable	Laboratory	Portable
10 kDa	0.087199	0.114802	0.063889	0.058333
100 kDa	0.083325	0.103025	0.050719	0.051857
300 kDa	0.082658	0.093402	0.047130	0.046244

The RIS values for each layer do vary but are not significantly different. The RIS for the 1% CS DDLW layer is 102.87 ± 2.67 °/RIU, while the 0.96% PAAm LW layer is just 8.74 ± 2.66 °/RIU lower (**Figure 6.20**).

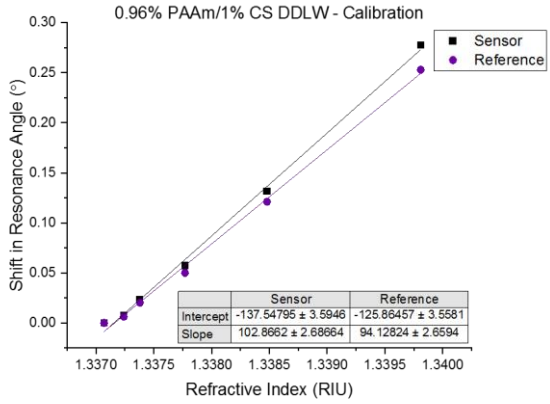

Figure 6.20. Calibration curve for 0.96% PAAm/1% CS stacked DDLWs on the portable instrument. Error bars were calculated as 1σ across three different DDLWs.

Compared with the laboratory instrument, the portable instrument appears to have an increased sensitivity (**Table 6.10**). This again could be due to film-to-film variation caused by the fabrication; regardless of the reason, the high sensitivity is desirable for these films and for POC and thus this is a positive outcome.

Table 6.10. Comparison of the RIS values for 1% CS and 0.96% PAAm stacked DDLWs on the laboratory and portable instruments.

	LABORATORY INSTRUMENT RIS (°/RIU)	**PORTABLE INSTRUMENT RIS (°/RIU)**
1% CS (DOPED)	86.22 ± 1.64	102.87 ± 2.67
0.96% PAAm	87.15 ± 0.95	94.13 ± 2.66

Finally, protein immobilisation *via* the same method as reported for the 1% DDLW in **Section 6.3.1** was performed, with the removal of the BSA step (**Figure 6.21**).

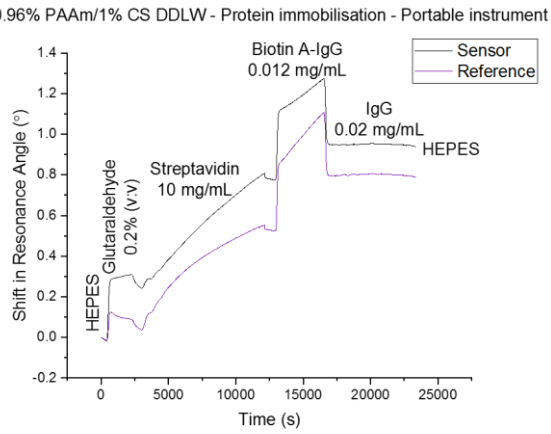

Figure 6.21. 0.96% PAAm/1% CS stacked DDLW treated with the GA-v1 protein immobilisation strategy on the portable instrument.

Here it can be seen that both layers give a different response at each stage, but both follow the same pattern. This is to be expected as the PAAm layer should not be able to bind with any of the analytes but will still show a reduced response as it will also respond to changes in the sensor layer above. Unfortunately, in this case the IgG did not bind strongly to the film and cannot be seen on the graph. This may be attributable to the issues we had with biotin A-IgG and IgG not binding as expected; this was an ongoing issue that may have been due to degraded proteins. This ultimately led to the replacement of biotin A-IgG and sheep IgG with PAB and rabbit IgG, but this experiment was not repeated at this stage.

6.4.2 Poly(acrylamide)/Chitosan LW, PAAm/CS

As discussed previously, the purified CS does not need to be dye-doped to visualise the mode. Therefore 0.96% and 1.2% (w:v) PAAm films were prepared, followed by spin coating 1% (w:v) CS on top.

6.4.2.1 0.96% PAAm/1% CS

The 0.96% PAAm/1% CS stacked LW shows two clear modes with good separation (**Figure 6.22**). The top mode is partially broken which could be due to either fabrication issues or handling issues.

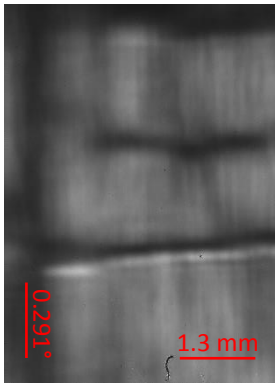

Figure 6.22. Output image of a 0.96% PAAm/1% CS stacked LW on the portable instrument under a Y-shaped flow cell.

The glycerol data shows equal responses for both layers, while the PEG data shows that both layers are equally porous to 10 kDa PEG, but the porosity of the reference layer decreases earlier than the sensor layer for higher MWs (**Figure 6.23**).

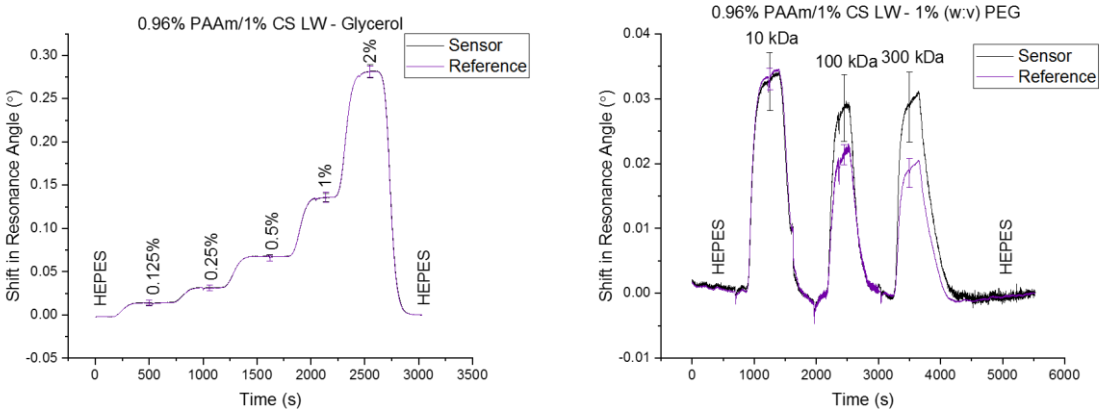

Figure 6.23. Glycerol (left) and PEG (right) runs on 0.96% PAAm/1% CS stacked LWs films using the portable instrument. Error bars were calculated as 1σ across three different LWs.

The CS layers showed significantly lower porosity than expected; when compared to the laboratory instrument, the response to 10 kDa PEG has decreased by approximately

0.055°. The PAAm layers have instead increased, with an improvement of 0.053° for 10 kDa PEG (**Table 6.11**).

Table 6.11. Comparison of the average responses of 0.96% PAAm/1% CS stacked LWs to 1% PEG solutions of different MWs on the laboratory and portable instruments.

1% PEG SIZE	1% CS RESPONSE (°)		0.96% PAAM RESPONSE (°)	
	Laboratory	Portable	Laboratory	Portable
10 kDa	0.086415	0.030706	0.018982	0.033642
100 kDa	0.083936	0.022120	0.011253	0.018782
300 kDa	0.076812	0.020436	0.009238	0.015117

Despite the films visually having two separate modes there is not a strong gap between the modes when responding to PEG, suggesting that these films may not have been prepared to the same standard as those tested on the laboratory instrument. The two layers may have partially merged, leading to a reduction in CS sensitivity and a slight increase in PAAm sensitivity.

A direct comparison between the sensitivities on each instrument is not available as this data was not collected on the laboratory instrument due to time constraints; however, the CS has a RIS of 142.95 ± 4.38 °/RIU while the PAAm is 142.14 ± 3.99 °/RIU (**Figure 6.24**). Both values are excellent and are higher than the equivalent response gained on the portable instrument for these films as single layer LWs. But due to the issues with porosity and the likelihood of film merging, this cannot be taken as standard.

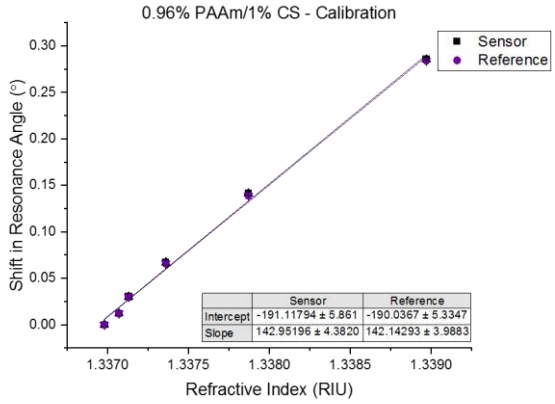

Figure 6.24. Calibration curve for 0.96% PAAm/1% CS stacked LWs on the portable instrument. Error bars were calculated as 1σ across three different LWs.

Protein immobilisation was performed using the NPB method (**Figure 6.25**).

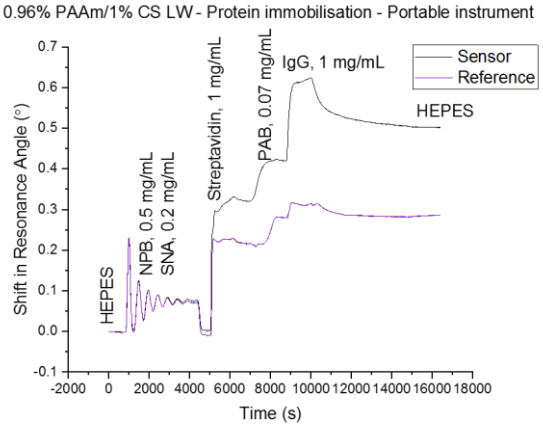

Figure 6.25. 0.96% PAAm/1% CS stacked LW treated with the NPB protein immobilisation method on the portable instrument.

This method showed both excellent IgG binding and a good separation of the modes. This shows that the two layers have good separation without leaching and additionally that the PAB/rabbit IgG combination provides much stronger results than the biotin A-IgG/sheep IgG combination.

Again, this experiment was unable to be repeated and cannot be taken as representative of these films but can be used to show the ability of the portable instrument to accurately track throughout a protein run.

6.4.2.2 1.2% PAAm/1% CS

The 1.2% PAAm/1% CS films were visually similar to the 0.96% PAAm/1% CS films, but the 1.2% PAAm dip was further separated from the 1% CS dip and TIR (**Figure 6.26**). This was expected as the 1.2% PAAm should be less porous than the 0.96% equivalent.

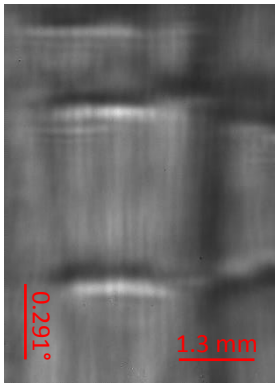

Figure 6.26. Output image of a 1.2% PAAm/1% CS stacked LW on the portable instrument under a Y-shaped channel flow cell.

The 1.2% PAAm/1% CS LWs had much better porosity than seen in the 0.96% PAAm/1% CS LWs. Much better separation of the modes is seen, but again the large error bars suggest a lot of device-to-device variability (**Figure 6.27**).

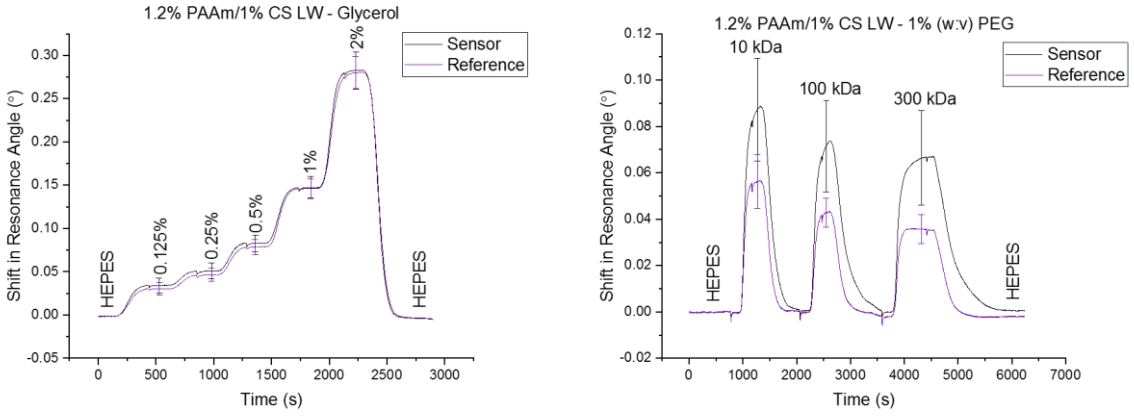

Figure 6.27. Glycerol (left) and PEG (right) runs on 1.2% PAAm/1% CS stacked LWs films using the portable instrument. Error bars were calculated as 1σ across two different LWs.

As with the 0.96% PAAm/1% CS LWs no direct laboratory comparison could be made, but the excellent RIS values of 131.18 ± 6.32 °/RIU and 128.23 ± 5.77 °/RIU for the 1% CS and

1.2% PAAm respectively suggest that this instrument is operating on a high level with a good sensitivity (**Figure 6.28**).

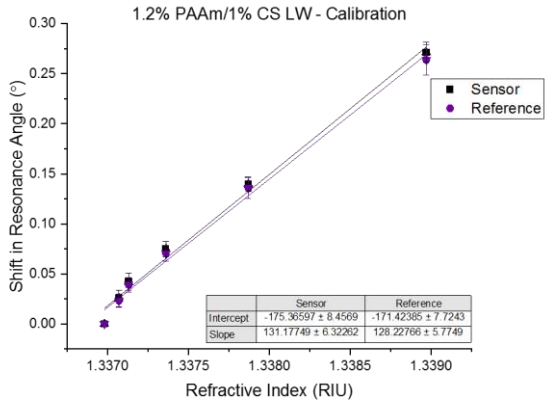

Figure 6.28. Calibration curve for 1.2% PAAm/1% CS stacked LWs on the portable instrument. Error bars were calculated as 1σ across two different LWs.

6.4.3 4-arm-PEG$_{20,000}$-aldehyde:4-arm-PEG$_{2000}$-hydrazide/Chitosan, 4-CHO:4-HZ/CS

The last stacked LWs tested were the 5% 4-arm-PEG$_{20,000}$-CHO:4-arm-PEG$_{2000}$-HZ/1% chitosan (5% 4-CHO:4-HZ/1% CS) LWs. Two modes are present on the output, but there does appear to be some distortion down the centre of the image (**Figure 6.29**). This may be due to not fully rehydrating the film before placing it under the flow cell which would lead to the modes shifting as it slowly rehydrates.

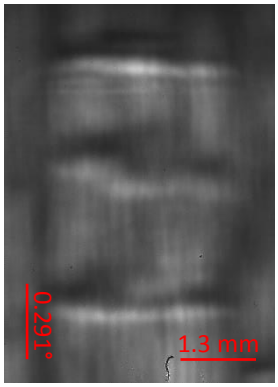

Figure 6.29. Output image of a 5% 4-CHO:4-HZ (1:1)/1% CS stacked LW on the portable instrument under a single channel flow cell.

The PEG run shows outstanding separation between the response of the two modes, although the error bars do suggest a high degree of device-to-device variability (**Figure 6.30**).

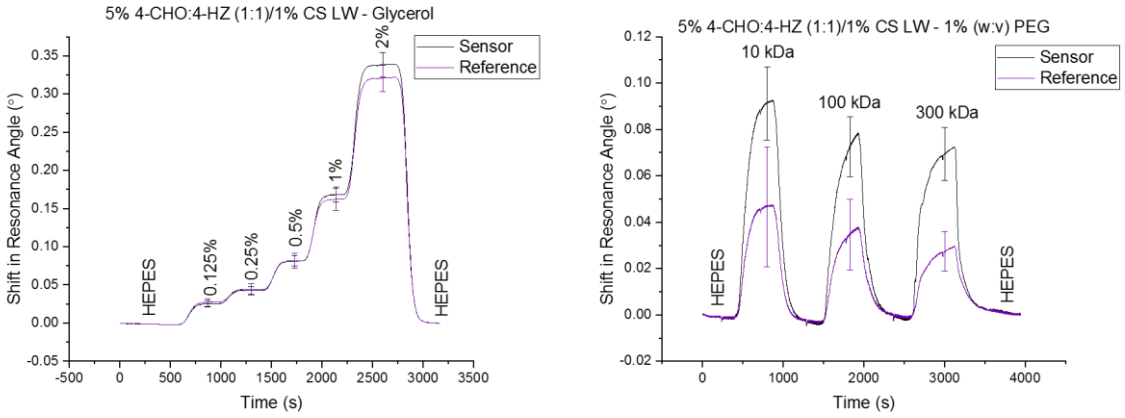

Figure 6.30. Glycerol (left) and PEG (right) runs on 5% 4-CHO:4-HZ (1:1)/1% CS stacked LWs films using the portable instrument. Error bars were calculated as 1σ across three different LWs.

These films show a similar porosity to that observed on the laboratory instrument (**Table 6.12**). This is an excellent sign, suggesting that not only are these films reproducible, but also that they are responding in the same manner across both instruments.

Table 6.12. Comparison of the average responses of 5% 4-CHO:4-HZ/1% CS stacked LWs to 1% PEG solutions of different MWs on the laboratory and portable instruments.

1% PEG SIZE	1% CS RESPONSE (°)		5% 4-CHO:4-HZ RESPONSE (°)	
	Laboratory	Portable	Laboratory	Portable
10 kDa	0.097639	0.075467	0.035514	0.052977
100 kDa	0.077673	0.058973	0.023679	0.035376
300 kDa	0.066507	0.050766	0.018120	0.024408

The RIS values are again close in value to each other, with the CS having an RIS of 118.46 ± 2.02 °/RIU and the 4-CHO:4-HZ an RIS of 111.66 ± 2.44 °/RIU (**Figure 6.31**). This suggests both layers have similar sensitivities.

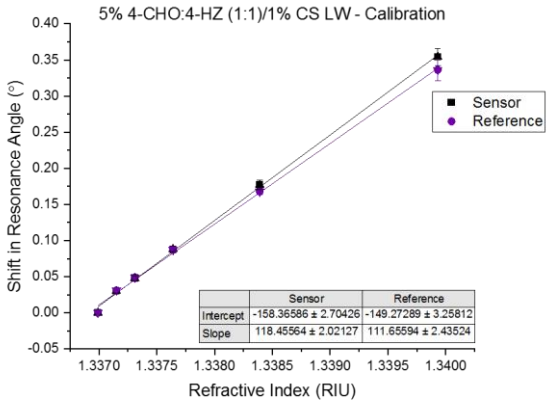

Figure 6.31. Calibration curve for 5% 4-CHO:4-HZ (1:1)/1% CS stacked LWs on the portable instrument. Error bars were calculated as 1σ across three different LWs.

Unfortunately, the RIS on the portable instrument appears to have dropped fairly significantly compared to the laboratory instrument (**Table 6.13**). This may be due to fabrication issues or instrumental issues and will need further exploration.

Table 6.13. Comparison of the RIS values for 1% CS and 5% 4-CHO:4-HZ (1:1) stacked LWs on the laboratory and portable instruments.

	LABORATORY INSTRUMENT RIS (°/RIU)	PORTABLE INSTRUMENT RIS (°/RIU)
1% CS	145.69 ± 3.39	118.46 ± 2.02
5% 4-CHO:4-HZ (1:1)	148.73 ± 3.25	111.66 ± 2.44

As discussed in **Chapter 4** (**4.4**) the batch-to-batch inconsistencies in the 4arm-PEG-CHO prevented further work being carried out on these films. While the LWs are very promising when considering the characterisation data, protein studies could not be performed.

6.4.4 Poly(acrylamide-*co*-acrylic acid)/Poly(acrylamide), PAAm-Ac/PAAm

The poly(acrylamide-*co*-acrylic acid)/poly(acrylamide) (PAAm-Ac/PAAm) films were already discussed in **Chapter 4** (**4.3.1**), where it was concluded that these films are hopeful due to their clear difference in response between the sensor and reference layers and the similarity of the RIS values, but low porosity could cause problems.

An output image of one PAAm-Ac/PAAm film shows two modes close together and with varying brightness (**Figure 6.32**). The dips are also not entirely uniform, indicating fabrication difficulties.

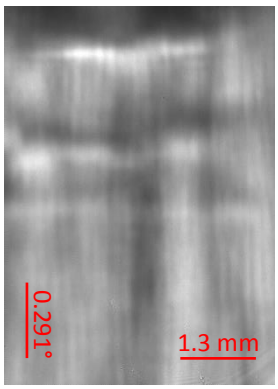

Figure 6.32. Output image of a 2.88% PAAm-Ac/0.96% PAAm stacked LW on the portable instrument under a Y-shaped flow cell.

There is good separation between the sensor and reference modes in the PEG run, while the glycerol response for each layer is very similar (**Figure 6.33**).

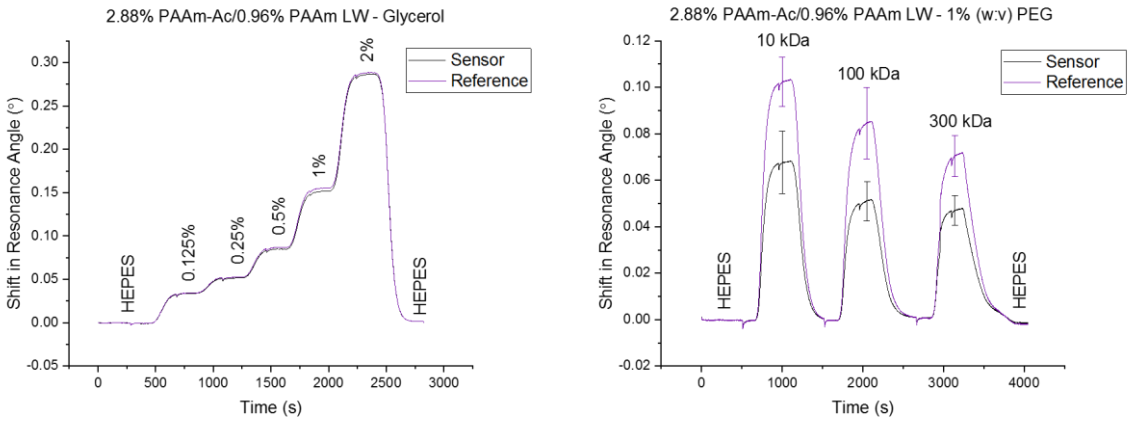

Figure 6.33. Glycerol (left) and PEG (right) runs on for 2.88% PAAm-Ac/0.96% PAAm stacked LWs films using the portable instrument. Error bars were calculated as 1σ across three different LWs.

The response to both glycerol and PEGs has increased drastically compared to the laboratory results, which could be due to instrumental differences but is thought to be due to fabrication differences instead (**Table 6.14**). These films are difficult to reproduce, therefore inconsistencies are highly likely. Even so, this porosity is ideal for protein immobilisation and is promising.

Table 6.14. Comparison of the average responses of 2.88% PAAm-Ac/0.96% PAAm stacked LWs to 1% PEG solutions of different MWs on the laboratory and portable instruments.

1% PEG SIZE	2.88% PAAM-AC RESPONSE (°)		0.96% PAAM RESPONSE (°)	
	Laboratory	Portable	Laboratory	Portable
10 kDa	0.025778	0.062502	0.046337	0.094298
100 kDa	0.023217	0.041909	0.037341	0.068403
300 kDa	0.018728	0.039264	0.030061	0.060014

The RIS for both layers are extremely similar, with values of 136.74 ± 6.65 °/RIU for the PAAm-Ac and 137.06 ± 6.66 °/RIU for the PAAm (**Figure 6.34**).

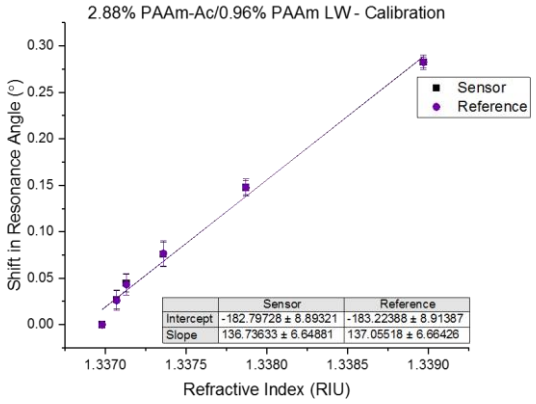

Figure 6.34. Calibration curve for 2.88% PAAm-Ac/0.96% PAAm stacked LWs on the portable instrument. Error bars were calculated as 1σ across three different LWs.

In direct contrast to the 5% 4-CHO:4-HZ/1% CS films, these films have drastically increased in sensitivity between instruments, as have the errors, again due to the fabrication issues (**Table 6.15**). Further work would be needed to understand where the cause for this lies and how best to fix it.

Table 6.15. Comparison of the RIS values for 2.88% PAAm-Ac and 0.96% PAAm stacked LWs on the laboratory and portable instruments.

	LABORATORY INSTRUMENT RIS (°/RIU)	**PORTABLE INSTRUMENT RIS (°/RIU)**
2.88% PAAm-Ac	40.41 ± 0.79	136.74 ± 6.65
0.96% PAAm	41.91 ± 2.03	137.06 ± 6.66

6.5 Summary

This chapter has introduced a 3D printed portable waveguiding instrument and compared the results obtained to those gained from the laboratory-based instrument. Calibration of each film has been carried out on both instruments via glycerol and PEG tests, along with some basic protein immobilisation.

From this we can see that while the sensitivity of the portable instrument varies from that of the laboratory instrument in certain cases, this is likely due to LW fabrication variations and not the instrument itself. There are no significant differences between the results when comparing films which have already proven to have high uniformity and reproducibility on the laboratory instrument with the portable instrument; this is particularly visible in the case of 1% CS LWs, in which the response on both instruments is very similar.

While this instrument is unable to regulate temperature internally, the portability aspect of it make it much more suited to POC than the laboratory instrument. When in a consistent environment where temperature fluctuations are minimal the instrument provides excellent results. Combination of this instrument with an internal referencing system such as the stacked waveguides should negate the issues raised by an unstable environment.

Further development of the stacked films is necessary before more testing is carried out using this instrument. At the current stage, the 5% 4-CHO:4-HZ/1% CS stacked films are once again providing the most reliable results in regard to the results obtained on both instruments.

6.6 References

1. Tazinya, A.A., et al., *Risk factors for acute respiratory infections in children under five years attending the Bamenda Regional Hospital in Cameroon.* BMC Pulmonary Medicine, 2018. **18**(1): p. 7.
2. World Health Organization. *Children: improving survival and well-being*. 2020 [cited 25-05-2022]; Available from: https://www.who.int/news-room/fact-sheets/detail/children-reducing-mortality.
3. Ghazali, M.I.M., et al., *3D Printed Metalized Plastic Waveguides for Microwave Components.* Advancing Microelectronics, 2018. **45**(2): p. 12-16.
4. Roda, A., et al., *Integrating Biochemiluminescence Detection on Smartphones: Mobile Chemistry Platform for Point-of-Need Analysis.* Analytical Chemistry, 2014. **86**(15): p. 7299-7304.
5. Remaggi, G., A. Zaccarelli, and L. Elviri, *3D Printing Technologies in Biosensors Production: Recent Developments.* Chemosensors, 2022. **10**(2): p. 65.
6. Muñoz, J. and M. Pumera, *3D-printed biosensors for electrochemical and optical applications.* TrAC Trends in Analytical Chemistry, 2020. **128**: p. 115933.
7. Roda, A., et al., *Smartphone-based biosensors: A critical review and perspectives.* TrAC Trends in Analytical Chemistry, 2016. **79**: p. 317-325.
8. Kenyon, J.I., R. Poropatich, and M.R. Holtel, *Cell Phones in Telehealth and Otolaryngology.* Otolaryngologic Clinics of North America, 2011. **44**(6): p. 1351-1358.
9. Zhang, D. and Q. Liu, *Biosensors and bioelectronics on smartphone for portable biochemical detection.* Biosensors and Bioelectronics, 2016. **75**: p. 273-284.
10. Zheng, L., et al., *Optical Biosensor for Rapid Detection of Salmonella typhimurium Based on Porous Gold@Platinum Nanocatalysts and a 3D Fluidic Chip.* ACS Sensors, 2020. **5**(1): p. 65-72.
11. Kim, G.-Y., et al., *Detection of Pathogenic Salmonella with a Composite Quantum Dot.* Journal of Biosystems Engineering, 2010. **35**(6): p. 458-463.
12. Somarapalli, M., R. Jolivot, and W. Mohammed, *Realization of Low-Cost Multichannel Surface Plasmon Resonance Based Optical Transducer.* Photonic Sensors, 2018. **8**(4): p. 289-302.
13. Thoren, K. *The Role of Surface Plasmon Resonance in Clinical Laboratories*. 2019.
14. Goddard, N.J., et al., *3D Printed Instrumentation for Point-of-Use Leaky Waveguide (LW) Biochemical Sensor.* IEEE Transactions on Instrumentation and Measurement, 2020: p. 1-1.
15. Gupta, R. and N.J. Goddard, *A proof-of-principle study for performing enzyme bioassays using substrates immobilized in a leaky optical waveguide.* Sensors and Actuators B: Chemical, 2017. **244**: p. 549-558.

7 Chapter 7 – Conclusions and Future Outlook

7.1 Conclusion

This work has investigated and assessed the suitability of different hydrogels as optical leaky waveguide (LW) biosensors, in both the single and stacked form. This has involved the optimisation of hydrogels and protein immobilisation methods with the successful detection of 5 nM lactoferrin (LF). We have also compared bulky laboratory-based instrumentation to three-dimensional (3D) printed portable instrumentation, along with reporting the development of different flow cells.

The ultimate goal of this work going forwards is to detect procalcitonin (PCT). This project has identified the best single layer waveguide studied as chitosan (CS), which has successfully detected immunoglobulin G (IgG) and LF down to nM levels. PCT is present in pM levels and this level of sensitivity has not yet been achieved, but with further work this may be possible. Additionally, the incorporation of either a two-channel flow cell or a second hydrogel film to form a stacked waveguide has allowed for internal referencing, enabling the simple identification of inaccuracies that can occur throughout a measurement.

7.1.1 Single layer leaky waveguides

While synthetic polymers were expected to perform better as sensing waveguides, CS has proven to be much more porous, consistent, and durable than all of the synthetic polymers studied thus far. The bonus of CS is the ease of procurement and low cost. A summary of all the LWs tested as sensors can be found in **Table 7.1**. Reproducibility and

uniformity have been qualitatively ranked according to the success criteria stipulated in **Chapter 3** (**3.1.2**), alongside porosity which is ranked in comparison to 1% CS LWs as the standard.

Table 7.1. Comparison of all the hydrogels tested as sensor LWs.

HYDROGEL	PERCENT	REPRODUCIBILITY	UNIFORMITY	POROSITY	SENSITIVITY (°/RIU)	LONGEVITY	STORAGE
CS	1% (w:v)	High	High	High	144.23 ± 1.21	≥6 months	Wet
CS (DOPED)	1% (w:v)	High	High	High	140.43 ± 1.53	≥2 months	Wet
CS (HMW)	1% (w:v)	Low	Medium	High	117.28 ± 8.12	≥2 months	Wet
PAAm-Ac WITH 4.8% (V:V) GLYCEROL	2.88% (w:v)	Medium	High	Medium	118.94 ± 1.29	≥4 months	Dry
APMA	4.5% (molar)	Low	Medium	Medium	116.86 ± 8.70	5 days	Dry
4-ARM-PEG-NH_2	6% (w:v)	Low	Low	Unknown	Unknown	Unknown	Unknown
4-SH:4-MAL (1:1.5)	5% (molar)	Low	Low	Low	116.39 ± 3.80	≥2 weeks	Wet or dry
4-SH:2-MAL (1:1)	5% (molar)	Low	Low	Low	Unknown	≥2 weeks	Wet or dry
4-SH:4-MAL (1.5:1) WITH 5% (V:V) GLYCEROL	5% (molar)	Medium	High	Low	109.27 ± 2.99	≥2 weeks	Wet or dry
4-SH:4-MAL (1.5:1) WITH 5% (W:V) BSA	5% (molar)	Medium	Medium	Medium	228.61 ± 10.20	≥2 weeks	Wet or dry
4-SH:4-MAL (1.5:1) WITH 5% (W:V) BSA AND 2.5% (V:V) GLYCEROL	5% (molar)	Low	Low	Low	Unknown	≥2 weeks	Wet or dry
4-CHO:4-HZ (1:1.5)	5% (molar)	Medium	High	Medium	115.88 ± 3.06	≥2 weeks	Dry
4-CHO:4-HZ (2:1)	5% (molar)	Low	Medium	Medium	121.96 ± 3.59	≥2 weeks	Dry

7.1.2 Reference leaky waveguides

For the internal referencing aspect of the project, the focus centred on the development of stacked LWs comprised of a sensor and reference layer. To achieve this, different polymers were tested as reference layers and are summarised in **Table 7.2**. The best results were obtained from 5% 4-arm-$PEG_{20,000}$-aldehyde:4-arm-PEG_{2000}-hydrazide (4-CHO:4-HZ) films, which produced consistently uniform films with sensitivity close to that of 1% CS LWs. The longevity is reported as ≥2 months as these films showed no degradation by 2 months, but longer time periods were not tested at this stage.

An unfortunate consequence of using synthetic polymers such as the 4-CHO:4-HZ is the risk of batch-to-batch differences. This was regrettably an issue we ran into, discussed in more detail in **Chapter 4** (**4.4**). The high cost and batch differences make using synthetic polymers risky. Unless a method can be developed to produce these polymers reproducibly and affordably, and ideally in-house, they will not be suited for use as mass-produced biosensor chips regardless of the impressive features this particular batch produced.

Table 7.2. Comparison of all the hydrogels tested as reference LWs.

HYDROGEL	PERCENT	REPRODUCIBILITY	UNIFORMITY	POROSITY	SENSITIVITY (°/RIU)	LONGEVITY	STORAGE
PAAm (HMW) WITH 4.8% (V:V) GLYCEROL	0.96% (w:v)	Medium	High	Medium	73.94 ± 2.77	≥4 months	Dry
PAAm (LMW) WITH 4.8% (V:V) GLYCEROL	0.96% (w:v)	Low	Medium	Unknown	Unknown	Unknown	Dry
AAm	3% (molar)	Low	Medium	Unknown	Unknown	Unknown	Wet or dry
AGAROSE	2% (w:v)	Low	High	Medium	125.53 ± 1.45	≥2 weeks	Dry
AGAROSE	2.5% (w:v)	High	High	Low	116.09 ± 1.52	≥2 weeks	Dry
4-SH:4-MAL (1:1) WITH 5% GLYCEROL	5% (molar)	Medium	Medium	Low	162.26 ± 6.78	≥1 month	Wet or dry
4-CHO:4-HZ (1:1)	5% (molar)	High	High	Low	134.07 ± 3.35	≥2 months	Dry

7.1.3 Stacked leaky waveguides

Whilst the initial thought was to place the reference layer on top of the sensor layer to create an internal filtration system, this could not be achieved when using CS for practical reasons. The CS hydrogels will collapse when allowed to dry out leading to loss of the pores. The synthetic polymers tested so far such as poly(acrylamide-*co*-acrylic acid) (PAAm-Ac) do not experience this issue and can be dehydrated overnight before application of the reference layer on top. From a practical standpoint the ability to dry these films out without damage is highly desirable for fabrication, transport, and storage purposes. Yet, CS consistently provided superior results to any of the synthetic polymers tested for sensors. This led to the flipping of the stacked structure, with the reference layer attached directly to the glass substrate followed by the CS layer on top. While this was not the original aim, this configuration did give excellent results particularly when combined with 4-CHO:4-HZ as the reference layer.

It is expected that the use of the reference layer along with non-specific adsorption (NSA) agents such as sulfo NHS acetate (SNA) will be able to compensate for the lack of internal filtration system.

All of the stacked LWs tested are summarised in **Table 7.3**.

Table 7.3. Comparison of all the hydrogels tested as stacked LWs.

HYDROGEL	PERCENT	REPRODUCIBILITY	UNIFORMITY	POROSITY	SENSITIVITY (°/RIU)	LONGEVITY	STORAGE
PAAm-Ac WITH 4.8% (V:V) GLYCEROL/PAAm (HMW) WITH 4.8% (V:V) GLYCEROL	2.88% (w:v)/0.96% (w:v)	Medium	Medium	Medium	40.41 ± 0.79/ 41.91 ± 2.03	≥3 months	Dry
PAAm WITH 4.8% (V:V) GLYCEROL/CS (DOPED)	0.96% (w:v)/1% (w:v)	Medium	Medium	High	87.15 ± 0.95/ 86.22 ± 1.64	≥3 months	Wet
PAAM WITH 4.8% (V:V) GLYCEROL/CS	0.96% (w:v)/1% (w:v)	Low	Low	High	Unknown	≥3 months	Wet
AGAROSE/CS	2.5% (w:v)/1% (w:v)	Medium	High	Low	106.77 ± 3.12/ 111.66 ± 2.99	≥1 month	Wet
4-SH:4-MAL (1:1) WITH 5% (V:V) GLYCEROL/CS	5% (molar)/1% (w:v)	Low	Medium	Low	107.80 ± 1.58/ 109.02 ± 1.87	≥1 month	Wet
4-CHO:4-HZ (1:1)/CS	5% (molar)/1% (w:v)	High	High	High	148.73 ± 3.25/ 145.69 ±3.39	≥3 months	Wet

7.1.4 Internal referencing

Both a two-channel flow cell and a stacked waveguide formation were investigated. Currently the best results were obtained using the two-channel flow cell. This is for the following reasons:

1. The reference channel is directly parallel to the sensing channel, therefore is mostly exposed to the same environmental conditions as the sensing channel.
2. When CS is used as the sensing layer the LW has high uniformity across the width of the film. This further ensures the sensing and reference channels are as identical as possible.
3. Higher sensitivity and uniformity are achieved with single layer LWs compared to stacked LWs, meaning a two-channel flow cell produces higher quality and more reproducible results.

In spite of these advantages, a two-channel flow cell is not the most ideal form of internal referencing. Despite the close proximity of the two channels and the simplicity of the setup, there is still the possibility of temperature gradients between the two channels, or fluctuations caused by improperly mixed sample solutions, air bubbles introduced into just one channel, seepage between channels due to an imperfect seal etc. Equally, the use of a two-channel flow cell was not possible with the portable instrument and indicates that this method of internal referencing isn't feasible in a point-of-care (POC) scenario without further instrumental modification.

These disadvantages highlight the need for a better internal referencing system, which has been addressed in this project as stacked LWs. Even though the two-channel flow cell is

currently producing better results, this is not to say that the stacked waveguides will never be suitable for internal referencing purposes. Instead, we suggest that more work is needed to accurately prepare reproducible stacked films. This may be achieved by changing fabrication methods or by changing the polymers involved, but at the point of writing the two-channel flow cell is the best technique for internal referencing with these waveguides. Alternatively, other methods of internal referencing may be explored such as photopatterned hydrogels [1].

7.1.5 Portability

The issues with stacked waveguides calls into question the suitability of the portable instrument for POC use when combined with these stacked LWs. While the portable instrument holds much potential for POC use, the current lack of internal referencing system is a major barrier to prevent this. This could be solved by redesigning the instrument to allow for a wider output image and therefore allow for the use of the two-channel flow cell as a short-term fix, or alternatively by continuing to work on stacked waveguides.

Despite the internal referencing issues with this instrument, the instrument itself is highly portable and has a sensitivity nearly equal to that of the larger laboratory-based instrument. In addition to the improved portability, this instrument is significantly cheaper to produce and would be suitable for use by a non-specialist with only minimal training.

7.1.6 Protein immobilisation

Various protein immobilisation strategies have been studied and optimised throughout this project. This includes the testing of NSA agents such as bovine serum albumin (BSA) and SNA.

All of the reported strategies are based on immobilisation of proteins from free amine groups available in the hydrogel film. This was based primarily on the fact that CS has free amine groups which are readily available for reacting. Some work was performed on the PAAm-Ac films with the hope of exploiting the free carboxylic acid groups, but this was not successful at this time.

When investigating the thiol:maleimide and aldehyde:hydrazide hydrogels as potential sensing layers it was expected that these films could be tailored to provide free thiol/maleimide or aldehyde/hydrazide groups to open up new routes of protein immobilisation *via* these functional groups. As these films did not behave as expected this was not explored further, but with more research into these films it may be possible to improve their sensitivity and reactivity.

There were many setbacks when developing immobilisation methods, be it due to lack of reactivity, non-specific binding, or uncontrollable reagents such as glutaraldehyde and streptavidin-biotin reactions. Ultimately the best results were achieved using one of three methods: glycine, anti-biotin antibody (ABA), and lactoferrin. These methods had the lowest degree of variation and seem to hold potential for future research.

Additionally, some testing was done to investigate the effects of human serum and synthetic urine on the hydrogel films. At this stage the human serum is causing too much

damage to the CS films to provide any useful results without significant pre-dilution, while synthetic urine is more hopeful. Differences in permanent response of the sensor and reference LWs to these matrices has introduced a further issue when considering internal referencing, suggesting that using a sensor and reference layer of similar structure would be more suited to this application.

7.1.7 Reusability

Something not touched upon in this work, but which may be relevant for future work is the concept of reusability. Single-use tests tend to be more expensive and wasteful than reusable tests, and this has been seen on a huge scale due to the COVID-19 pandemic. The World Health Organisation (WHO) estimates over 140 million single-use COVID tests were shipped within the United Nations between March 2020 and November 2021, which is the equivalent of approximately 2600 tonnes of mostly plastic waste and 731,000 litres of chemical waste. While some of this can be recycled, much is incorrectly handled and incinerated or placed in landfill [2]. This places a huge burden upon the environment; therefore, reusability or recyclability is of great importance.

7.1.8 Final conclusion

Regardless of the problems associated with these stacked devices, the project has explored various fabrication and immobilisation methods, and successfully detected nM levels of proteins and provided a strong basis for future work. CS has been identified as the current best sensor layer, with 4-CHO:4-HZ as the most suitable reference layer. Preliminary work has

also been done into sensing in the presence of synthetic urine and human serum in different concentrations to investigate the effect of interferents.

7.2 Future work

Future work is envisaged to continue the development of the stacked LWs, ideally improving the film-to-film reproducibility and the limit of detection (LOD). Upon improvement of the LOD, PCT will be detected on these films firstly in buffer and then in spiked samples to prove the suitability of the devices for POC applications. To improve the LOD we suggest the incorporation of electro-focusing techniques, allowing for concentration of the analyte into one region and subsequent detection. This is an advantage of using LWs which do not require metal layers to work, allowing for the combination with electro-focusing.

More work is needed into the protein immobilisation strategies, ideally with the aim of producing a reusable test. Elimination of the use of streptavidin and glutaraldehyde would be ideal if they can be replaced by reagents with a similar selectivity and finer control.

Further development of the software used to run the portable instrumentation could potentially see additional improvements in portability, such as the development of a mobile phone application as opposed to a computer application.

Additionally, the portable instrument may be modified to allow for a two-channel flow cell to achieve internal referencing on single layer LWs.

7.3 References

1. Pal, A.K., et al., *A Self-Referenced Diffraction-Based Optical Leaky Waveguide Biosensor Using Photofunctionalised Hydrogels.* Biosensors, 2020. **10**(10): p. 134.
2. World Health Organization, *Global analysis of health care waste in the context of COVID-19*. 2022.

8 Chapter 8 – Experimental

8.1 Materials

Anti-Lactoferrin antibody (*anti-LF*) (ab112968) was bought from Abcam (Cambridge, UK). Chitosan (*CS*) 100K-300K (349050500) and 600K-800K (428850500), and Toluene anhydrous (10354113) were purchased from Acros Organics (Geel, Belgium). Sodium acetate trihydrate 99% (A16230) and Polyethylene oxide (*PEG*) 100 kDa (42236) and 300 kDa (42237) were purchased from Alfa Aesar (Ward Hill, Massachusetts, US). Nitrile o-rings (01-08-01901) were obtained from Ashton Seals (Brampton, UK). 4-ArmPEG-CHO (*4-CHO*) (A44004-20K) and 4-ArmPEG-HZ (*4-HZ*) (A44019-2K) were bought from Biopharma PEG Scientific (Watertown, Massachusetts, US). Azido-PEG_4-hydrazide HCl salt (BP-23874), DBCO-PEG_4-NHS ester (BP-21855) and Mal-PEG_3-NHS ester (NPM) were purchased from BroadPharm (San Diego, California). Goat anti-biotin antibody (*ABA*) (A150-111A) was purchased from Cambridge Bioscience (Cambridge, UK). 4-Arm PEG-Amine, molecular weight (*MW*) 10K (PSB-431) and 4-Arm PEG-Amine, MW 20K (PSB-435) were procured from Creative PEGWorks (Research Triangle Park, North Carolina, US). SUNBRIGHT® DE-200MA (*2-MAL*), SUNBRIGHT® DE-200SH (*2-SH*), SUNBRIGHT® PTE-400MA (*4-MAL*), and SUNBRIGHT® PTE-200SH (*4-SH*) were purchased from NOF Europe GmbH (Frankfurt am Main, Germany). Sodium hydroxide solution (*NaOH*) (1 M) (35256) was supplied by Honeywell Fluka (Charlotte, North Carolina, US). Streptavidin (2-02-03) was bought from IBA Lifesciences (Göttingen, Germany). Bootlace ferrules (211-4252) were procured from RS Components (Corby, UK). Acetic acid (1 M) (160305), Acrylamide (*AAm*) solution (40%) (A4058), Acrylamide/Bis-acrylamide (*AAm/BAAm*) (40%) 29:1 (A7802), Amicon Ultra-0.5 Centifugal Filters (UFC503024), N-(3-

Aminopropyl)methacrylamide hydrochloride (*APMA*) (731099), (3-Aminopropyl)triethoxysilane (*APTES*) (A3648), Ammonium persulfate (*APS*) (A3678), anti-human Immunoglobulin (Fc specific)-biotin antibody (*biotin A-IgG*) (B3773), Bovine serum albumin (*BSA*) (A2153), Chloro(dimethyl)vinylsilane (CDMVS) (395439), Ethanol (1.00983), Fluoresceinamine isomer I (201626), N-(5-Fluoresceinyl)maleimide (*F5M*) (38132), Glutaraldehyde solution 25% (G5882), Glycine (50046), Hexamethyldisilazane (*HMDS*) (440191), Human serum (H6914), Immunoglobulin G (*IgG*) from rabbit serum (I5006), IgG from sheep serum (I5131), Inhibitor removers (322332), Lactoferrin Human (*LF*) (L1294), Latex beads, polystyrene (1.1 µm mean particle size) (LB11), Methanol (34860), N,N'-Methylenebis(acrylamide) (*BAAm*) 99% (146072), Polyacrylamide (*PAAm*) MW: 5,000,000-6,000,000 (92560), Poly(acrylamide-*co*-acrylic acid) (*PAAm-Ac*) partial sodium salt ~80 wt. % MW: 520,000, Mn: 150,000 (511471), Poly(ethylene glycol) diacrylate (*PEGDA*) Mn: 575 (437441), Poly(ethylene glycol) diacrylate Mn: 700 (455008), Poly(ethylene glycol) diacrylate Mn: 10,000 (729094), Poly(ethylene glycol) diglycidyl ether (*PEGDGE*) Mn: 500 (475696), Poly(ethylene glycol) methyl ether acrylate (*PEGMEA*) Mn: 480 (454990), Polyethylene oxide 6 kDa (8.07491), Polyethylene oxide 10 kDa (81280), Protein A-Biotin (*PAB*) from Staphylococcus aureus (P2165), Reactive Blue 4 (*RB4*) (244813), Sigmatrix Urine Diluent (SAE0074), Sodium (meta)periodate (1.06597), Sodium phosphate dibasic heptahydrate (S9390), Sodium phosphate monobasic dihydrate (71505), Sodium sulfite (S4672), Toluene (32249), Trimethoxy(3,3,3-trifluoropropyl)silane (*TMTFS*) (91877), Tris(2-carboxyethyl)phosphine hydrochloride (*TCEP-HCl*) (646547), and Trypsin-ethylenediaminetetraacetic acid (*trypsin-EDTA*) (T4049) were purchased from Sigma Aldrich/Merck (Gillingham, UK). 1.2-1.5 mm thick glass slides (MIC2154) and Sartorius Minisart

Syringe Filters NML 5 µm Luer Lock (FIL6602) were bought from Scientific Laboratory Supplies Ltd. (SLS) (Nottingham, UK). 2,2'-Azobis[2-(2-imidazolin-2-yl)propane] Dihydrochloride (*AIP*) (A3012), Biotin-PEG_6-maleimide (*BPM*) (B5563), Genipin (G0548), (3-Mercaptopropyl)trimethoxysilane (*MPTMS*) (M0928), and N,N,N',N'-Tetramethylethylenediamine (*TEMED*) (T2515) were bought from Tokyo Chemical Industry (TCI) (Tokyo, Japan). Agarose (165200), Cargille Immersion Oil Type A (11328113), Decon 90 (10335650), Glycerol (G/0650/17), (4-(2-hydroxyethyl)-1-piperazineethanesulfonic acid) (*HEPES*) (BP310), Hydrazide-Biotin (21339), NHS-PEG_{12}-Biotin (*NPB*) (21312), SnakeSkinTM Dialysis Tubing (10K MWCO, 22 mm), Sodium chloride (*NaCl*) (S/3120/60) and Sulfo NHS acetate (*SNA*) (26777) were procured from Thermo Fisher Scientific (Waltham, Massachusetts, US). Hydrochloric acid (*HCl*) (1 M) (30024.290) was purchased from VWR (Radnor, Pennsylvania, US).

8.2 Substrate preparation

8.2.1 Standard cleaning

Plain glass slides, 25 mm x 25 mm x 1.5 mm, were cleaned by sonication for 30 minutes in Decon 90, deionised (DI) water, and ethanol respectively, for a total of 90 minutes.

8.2.2 Ozone cleaning

Glass slides were first prepared *via* the standard cleaning method reported in **Section 8.2.1**. The clean slides were then placed in an Ossila UV Ozone Cleaner E511 for between 2-10 minutes.

8.2.3 Plasma cleaning

Glass slides were first prepared *via* the standard cleaning method reported in **Section 8.2.1**. The clean slides were then placed in a PDC-002-CE expanded plasma cleaner (Harrick) for 30 minutes.

8.3 Leaky waveguide fabrication

8.3.1 Single layer LWs

8.3.1.1 Poly(ethylene glycol) methyl ether acrylate and Poly(ethylene glycol) diacrylate, PEGMEA/PEGDA

A solution of AIP (0.225% w:v) was dissolved in degassed DI water using a vortex. Inhibitor removers (~0.01 g) were mixed with PEGMEA (1 mL) and PEGDA (1 mL) for 10 minutes. The PEGMEA and PEGDA solutions were centrifuged to separate the inhibitor remover beads. PEGMEA, PEGDA, and AIP were mixed together in the correct ratios to prepare 40, 20, 15, 10% (w:v) gels at ratios of 4:1 8:1, 16:1, 32:1 of PEGMEA:PEGDA. The resulting solution was mixed before exposing to 365 nm UV light for between 5 – 60 minutes.

8.3.1.2 Chitosan, CS

8.3.1.2.1 Purification

CS was first purified *via* a method we previously reported by Goddard *et al.* [1], adapted from Filho and Signini [2]. Briefly, the CS was dissolved in 0.1 M acetic acid with stirring for 18 hours, forming a 1% (w:v) solution. The resulting solution was filtered through 5 µm syringe filters. 1 M NaOH(aq) was added in excess to form an off-white precipitate, which was collected *via* centrifugation. The precipitate was dialysed against DI water for 5 days, after which it was collected and washed a further 4 times *via* centrifugation, at the following ratios of methanol to DI water: 75:25, 50:50, 25:75, 0:100. Any remaining methanol was removed *via* rotary evaporation, and water was removed by freeze drying the product for 48 hours. The purified CS was collected in a ~80% yield.

8.3.1.2.2 Fabrication

Purified CS was dissolved as a 1% (w:v) solution in 0.1 M acetic acid, with stirring for 18 hours. 100 µL of this solution was spin coated onto clean glass slides at 900 rpm, 100 rpm/s, for 30 s. The slide was immediately placed in an incubator at 25^{o}C with a humidity of 75-80% for 3 minutes, before crosslinking *via* immersion in a 0.03125% (v:v) glutaraldehyde solution in 100 mM HEPES buffer, pH 7.4 for 10 minutes. The slide was then immersed in 100 mM HEPES buffer, pH 7.4, and covered with aluminium foil and stored in a dark, cool cupboard until use.

Dye-doped films were produced by immersing the CS films in a 0.1 mM solution of RB4 in 100 mM HEPES, pH 7.4, for 5 minutes. The films were then rinsed in HEPES before storing in HEPES as described above.

8.3.1.3 Poly(acrylamide-*co*-acrylic acid), PAAm-Ac

8.3.1.3.1 Glass functionalisation

Glass petri-dishes were functionalised with a 1% (v:v) solution of HMDS in toluene for 10 minutes, then washed with toluene and allowed to air dry.

A 1% (v:v) solution of APTES in toluene was added to the glass petri-dishes and briefly stirred. Clean glass slides were added to the solution and allowed to react for 30 minutes. The slides were then washed with toluene for 5 minutes and allowed to air dry. They were then placed in an oven at 60 ^{o}C for 45 minutes.

8.3.1.3.2 Fabrication

PAAm-Ac was dissolved as a 3% (w:v) solution in 1 M HCl/5% (v:v) glycerol with stirring for 18 hours. 96.0 µL of the PAAm-Ac solution and 4.0 µL of 0.625% (v:v) glutaraldehyde in 1

M HCl were mixed and immediately spin coated on to clean glass slides at 2000 rpm, 200 rpm/s, for 30 s, producing a 2.88% (w:v) PAAm-Ac film containing 0.025% (v:v) glutaraldehyde and 4.8% (v:v) glycerol. The slides were allowed to crosslink overnight before testing and were stored dry.

8.3.1.4 N-(3-aminopropyl)methacrylamide, APMA

8.3.1.4.1 Glass functionalisation

Glass petri-dishes were functionalised with a 1% (v:v) solution of HMDS in toluene for 10 minutes, then washed with toluene and allowed to air dry.

A 0.2% (v:v) solution of (CDMVS) in toluene was added to half of the petri-dishes, and a 0.2% (v:v) solution of TMTFS in toluene was added to the other half of the petri-dishes. The solutions were briefly stirred, before adding clean glass slides to each solution and leaving for 30 minutes. The slides were then washed with toluene for 5 minutes and allowed to air dry.

On the TMTFS-functionalised slides, 1 µL (0.005% w:v) of 1.1 µm latex bead solution was pipetted to give 8 evenly spaced spots around the outer edge of the slide, and allowed to air-dry.

8.3.1.4.2 Fabrication

A 4.5% total monomer gel was prepared by vortexing together a solution of 0.42% (w:v) APMA, 4.08% (w:v) AAm 40% solution, 0.61% (v:v) PEGDA, 1.25% (w:v) APS, and 1.25% (v:v) TEMED in degassed DI water. 100 µL of the solution was immediately pipetted onto a CDMVS-functionalised slide, before carefully covering with the TMTFS spacer slide. A 500 g weight was placed on top of each for 10 minutes, before removing and soaking the slides in DI water for a further 10 minutes. The slides were carefully prised apart, and the spacer slide

discarded. Depending on the use of the film, they were either stored in DI water, 100 mM HEPES buffer, pH 7.4, 100 mM phosphate buffered saline (PBS) buffer, pH 7.4, or stored dry.

8.3.1.5 4-arm-PEG-NH_2

A 10% (w:v) solution of the required 4-arm-PEG-NH_2 (PEG-10K or -20K) was dissolved in 100 mM PBS, pH 7.4. An 88 mM solution of genipin was prepared by dissolving 0.0199 g of genipin in 1 mL of 100 mM PBS, pH 7.4. Appropriate volumes of each solution were mixed together to achieve 100 µL solutions of PEG:genipin, at 15 mM, 17.6 mM 25 mM, 35.2 mM of genipin. The solutions were allowed to react on a rocker for 12-24 hours. To increase the speed of the reaction, solutions could be heated to 50 °C on a hot plate with stirring. The reaction was considered complete when the solutions had turned from clear to a dark blue.

8.3.1.6 PEG-thiol and PEG-maleimide, SH:MAL 4- or 2-arm

8.3.1.6.1 Glass functionalisation

Glass troughs were functionalised with a 1% (v:v) solution of HMDS in toluene for 10 minutes, then washed with toluene and allowed to air dry.

Clean glass slides were then treated with MPTMS by one of the following methods:

Method 1: Under nitrogen atmosphere, a 5% (v:v) solution of MPTMS in anhydrous toluene was allowed to pre-hydrolyse for 12 hours. Clean glass slides were subsequently added to the pre-hydrolysed solution and allowed to functionalise for between 8 and 14 hours. The functionalised slides were then sonicated in toluene:methanol (1:1), methanol, and DI water for 15 minutes each.

Method 2: Under nitrogen atmosphere, a 2.5% (v:v) solution of MPTMS was prepared and the clean slides were immersed for 2 hours for functionalisation. The slides were then rinsed with toluene for 5 minutes, before placing in an oven at 110 °C for 2 hours. Disulfide bonds were reduced using a 10 mM solution of TCEP-HCl in DI H_2O under nitrogen atmosphere for 30 minutes before use.

8.3.1.6.2 Fabrication

The following compounds were used: 4-arm-$PEG_{20,000}$-thiol (4-SH) or 2-arm-$PEG_{20,000}$-thiol (2-SH); 4-arm-$PEG_{40,000}$-maleimide (4-MAL) or 2-arm-$PEG_{20,000}$-maleimide (2-MAL).

5% total monomer gels were prepared at a 2:1, 1.5:1, 1.25:1, or 1:1 molar ratio, with addition of 5% (v:v) glycerol or BSA solution. Gelation was carried out in either 100 mM acetate buffer, pH 5.0, or 100 mM PBS, pH 5.0. The solution was spin coated onto the MPTMS-functionalised slides at 1500 rpm, 75 rpm/s, 30 s. The films were then allowed to gel in air for 15 minutes, before immersion in pH 7.4 PBS for storage, or stored dry.

8.3.1.7 4-arm-$PEG_{20,000}$-aldehyde and 4-arm-PEG_{2000}-hydrazide, 4-CHO:4-HZ

Glass slides were functionalised with either APTES or CDMVS as described in **Sections 8.3.1.3.1** and **8.3.1.4.1** respectively.

5% total monomer gels were prepared at a 1.5:1, 1.25:1, or 1:1 molar ratio. Gelation was carried out in 100 mM acetate buffer, pH 4.0, or 100 mM PBS, pH 5.0. The solution was spin coated onto the MPTMS-functionalised slides at 1200 rpm, 200 rpm/s, 30 s. The films were then allowed to gel in air for 15 minutes, before either storing dry or wet in a solution of 100 mM PBS, pH 7.4, depending on the application.

8.3.1.8 Poly(acrylamide), PAAm

PAAm was dissolved as a 1%, 1.25%, or 1.5% (w:v) solution in 1 M HCl/5% glycerol with stirring for 18 hours.

96.0 µL of the PAAm solution and 4.0 µL of 0.625% (v:v) glutaraldehyde in 1 M HCl were mixed and immediately spin coated on to clean glass slides at 1500 rpm, 100 rpm/s, for 30 s, producing 0.96% (w:v), 1.2% (w:v), or 1.44% (w:v) PAAm films respectively, containing 0.025% (v:v) glutaraldehyde and 4.8% (v:v) glycerol. The slides were allowed to crosslink overnight before testing and were stored dry.

8.3.1.9 Acrylamide, AAm

Glass slides were prepared with TMTFS and CDMVS as reported in **Section 8.3.1.4.1**.

A 3% total monomer gel was prepared by vortexing together a solution of 3.33% (w:v) AAm/BAAm 40% solution (29:1 ratio), 0.083% (w:v) APS and 0.083% (v:v) TEMED in degassed DI water. 50 µL of the solution was immediately pipetted onto a CDMVS-functionalised slide, before carefully covering with the TMTFS-functionalised spacer slide. A 500 g weight was placed on top of each for 10 minutes, before removing and soaking the slides in DI water for a further 10 minutes. The slides were carefully prised apart, and the spacer slide discarded. The films were then stored dry.

8.3.1.10 Agarose

A 2% or 2.5% (w:v) solution of agarose was prepared by dissolving agarose powder in DI water at 100 °C with stirring on a hot plate. After a uniform solution had formed, the heat was reduced to 70 °C. Clean glass slides and pipette tips were heated to 70 °C on the same hot plate. Using the heated apparatus, the agarose solution was quickly pipetted onto the slides

and spin coated at 2000 rpm, 100 rpm/s, 60 s. The films were then allowed to dry for 30 minutes before storage, either as dry films or hydrated in DI water.

8.3.2 Stacked leaky waveguides

8.3.2.1 Poly(acrylamide-*co*-acrylic acid)/Poly(acrylamide), PAAm-Ac/PAAm

2.88% (w:v) PAAm-Ac films were prepared as reported in **Section 8.3.1.3** and allowed to dry out. 0.96% (w:v) or 1.44% (w:v) PAAm was spin coated on top as reported in **Section 8.3.1.8**.

Films were stored dry.

8.3.2.2 Poly(acrylamide)/Chitosan, PAAm/CS

0.96% (w:v) PAAm films were prepared as reported in **Section 8.3.1.8** and allowed to dry out. 1% (w:v) purified CS was spin coated on top as reported in **Section 8.3.1.2**.

Films were stored in 100 mM HEPES, pH 7.4, protected from light.

Dye-doped films were produced by immersing the films in a 0.1 mM solution of RB4 in 100 mM HEPES, pH 7.4, for 5 minutes. The films were then rinsed in HEPES before storing in HEPES as described above.

8.3.2.3 Agarose/Chitosan, Agarose/CS

2.5% (w:v) agarose films were prepared as reported in **Section 8.3.1.10** and allowed to dry out. 1% (w:v) purified CS was spin coated on top as reported in **Section 8.3.1.2**.

Films were stored in 100 mM HEPES, pH 7.4, protected from light.

8.3.2.4 4-arm-arm-$PEG_{20,000}$-thiol:4-arm-$PEG_{40,000}$-maleimide/Chitosan, 4-SH:4-MAL/CS

Glass slides were functionalised with MPTMS as reported in **Section 8.3.1.6.1**, Method 1.

5% 4-SH:4-MAL (1:1) films were prepared as reported in **Section 8.3.1.6** with the addition of 5% (v:v) glycerol. Gelation was carried out in pH 100 mM PBS buffer, pH 5.0. The films were then allowed to dry out. 1% purified CS was spin coated on top as reported in **Section 8.3.1.2**.

Films were stored in 100 mM HEPES, pH 7.4, protected from light.

8.3.2.5 4-arm-$PEG_{20,000}$-aldehyde:4-arm-PEG_{2000}-hydrazide/Chitosan, 4-CHO:4-HZ/CS

Glass slides were functionalised with APTES as reported in **Section 8.3.1.3.1**.

5% 4-CHO:4-HZ (1:1) films were prepared as reported in **Section 8.3.1.7**. Gelation was carried out in 100 mM acetate buffer, pH 4.0. The films were then allowed to dry out. 1% (w:v) purified CS was spin coated on top as reported in **Section 8.3.1.2**.

Films were stored in 100 mM HEPES, pH 7.4, protected from light.

8.4 Characterisation

8.4.1 Glycerol tests

Using either 100 mM HEPES or 100 mM PBS, pH 7.4, a solution of 10% (v:v) of glycerol was prepared. Serial dilutions were performed to obtain glycerol solutions of 2%, 1%, 0.5%, 0.25%, and 0.125% (v:v).

To test the leaky waveguides (LWs), the LW was first flushed with the relevant buffer solution. Glycerol solutions were then introduced in sequence from 0.125% - 2% (v:v), allowing each concentration to plateau before adding the next. After 2% glycerol had plateaued, the relevant buffer was then reintroduced into the flow cell and allowed to plateau.

8.4.2 PEG test

Using either 100 mM HEPES or 100 mM PBS, pH 7.4, 1% (w:v) solutions of 10 kDa, 100 kDa, and 300 kDa PEGs were prepared by stirring at room temperature for 1 hour.

To test the LWs, the LW was first flushed with the relevant buffer solution. The 10 kDa PEG was introduced and allowed to plateau, before replacing with the buffer. This was repeated for the 100 kDa and 300 kDa PEGs.

8.4.3 Calculation of error bars

The standard deviation has been calculated using the entire population at plateau for each characterisation graph. This is then reported as error bars at 1σ from the average population.

Equation 8.1. Standard deviation calculation.

$$\sigma = \sqrt{\frac{\sum(x_i - \bar{x})^2}{n}}$$

Where:

x = each value from the sample population

x = mean value of the population

n = sample size.

8.4.4 4-SH:2-MAL (1:1) testing

8.4.4.1 Fabrication

5% 4-SH:2-MAL (1:1) thiol-containing hydrogel solutions were prepared as reported in **Section 8.3.1.6** and cast using slide holders. A poly(methyl methacrylate) (PMMA) slide holder was prepared, with a cavity of 1.2-1.5 mm to match the thickness of the glass substrates. A glass slide was functionalised with MPTMS as reported in **Section 8.3.1.6.1**, Method 1 and placed into the cavity. A spacer of 100 µm thickness was outlined with silicone oil to provide an air-tight seal with the glass, then placed on top of the slide. A final PMMA sheet was placed on top with two cavities to allow solution to be injected into the mould and secured with screws.

150 µL of gel solution was injected into the mould and allowed to gel for 10 minutes. The mould was disassembled, and the resulting 100 µm thick gel was removed and soaked in 100 mM PBS, pH 7.4.

8.4.4.2 Free thiol testing

Method 1: The hydrated gel was soaked in a solution of NHS-PEG_3-maleimide (NPM) for 20 minutes. After washing with 100 mM PBS, pH 7.4, the gel was stained with 0.1 mg/mL fluoresceinamine for 3 hours. Gels were soaked for a further 25 hours in PBS, and ultraviolet-visible (UV-Vis) spectroscopy spectra were recorded periodically.

Method 2: The hydrated gels were tested either immediately, 2 days, or 7 days after fabrication and were soaked in 1 mM F5M for 2 hours and then soaked in DI water for up to 11 days. UV-Vis spectra were recorded periodically.

8.4.5 4-SH:4-MAL (1.5:1) testing

8.4.5.1 Fabrication

5% 4-SH:4-MAL (1.5:1) LWs were prepared with 5% BSA as reported in **Section 8.3.1.6**.

8.4.5.2 BSA removal

Testing was carried out in 100 mM PBS, pH 7.4. LWs were heated to 37 °C *via* a water bath and trypsin-EDTA (0.25% v:v) was heated continuously on a hotplate to the same temperature and exposed to the film for 1 hour. BPM (0.4 mg/mL) was exposed to the film for 1 hour after trypsin treatment followed by streptavidin (1 mg/mL) for 20 minutes. This was followed by a final wash with PBS.

8.4.6 4-CHO:4-HZ (1:1.5) testing

8.4.6.1 Fabrication

5% 4-CHO:4-HZ (1:1.5) LWs were produced as reported in **Section 8.3.1.7**.

8.4.6.2 Free hydrazide testing

LWs were treated with 100 mM PBS, pH 7.4. Glutaraldehyde (0.2% v:v) was exposed to the LW for 30 minutes followed by PBS.

8.4.7 4-CHO:4-HZ (2:1) testing

8.4.7.1 Fabrication

5% 4-CHO:4-HZ (2:1) LWs were produced as reported in **Section 8.3.1.7**.

8.4.7.2 Free aldehyde testing

LWs were treated with 100 mM PBS, pH 7.4. Hydrazide-biotin (1 mg/mL) was allowed to react with the LW for 1 hour, followed by PBS. Streptavidin (1 mg/mL) was reacted for a further 20 minutes before a final PBS wash.

8.4.8 4-CHO NMR

The data presented below was not collected as part of this project. It was kindly supplied by the manufacturer Biopharma PEG Scientific Inc. and is presented with their permission to show the differences between the two batches of 4-CHO used during this project.

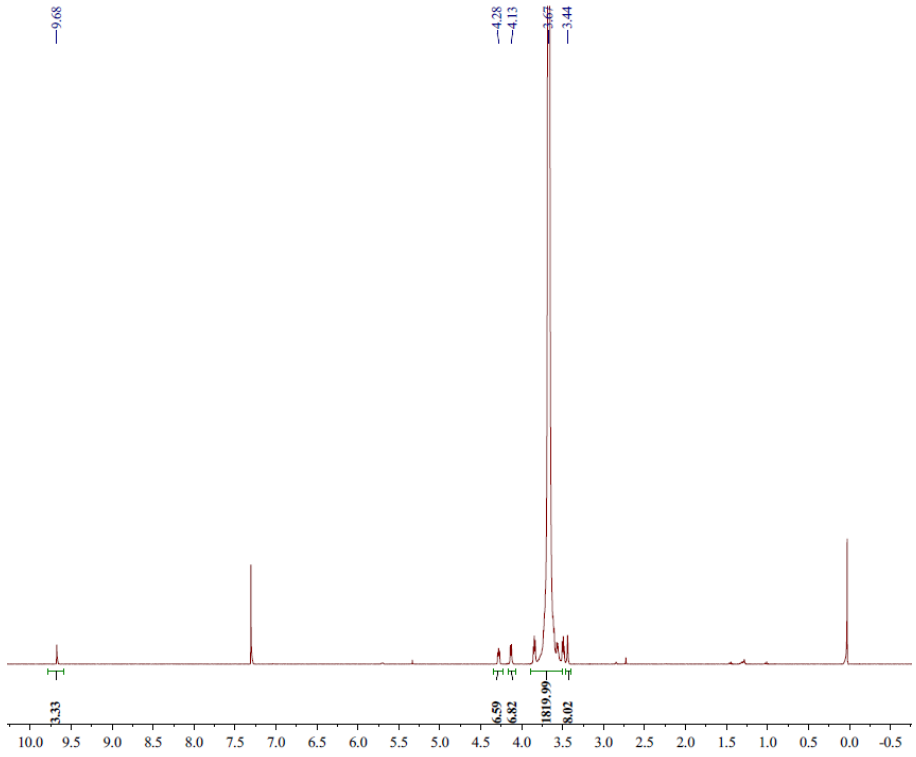

Figure 8.1. NMR spectrum of 4-arm-PEG-CHO, batch 1, performed in $CDCl_3$. Data collected by Biopharma PEG Scientific Inc.

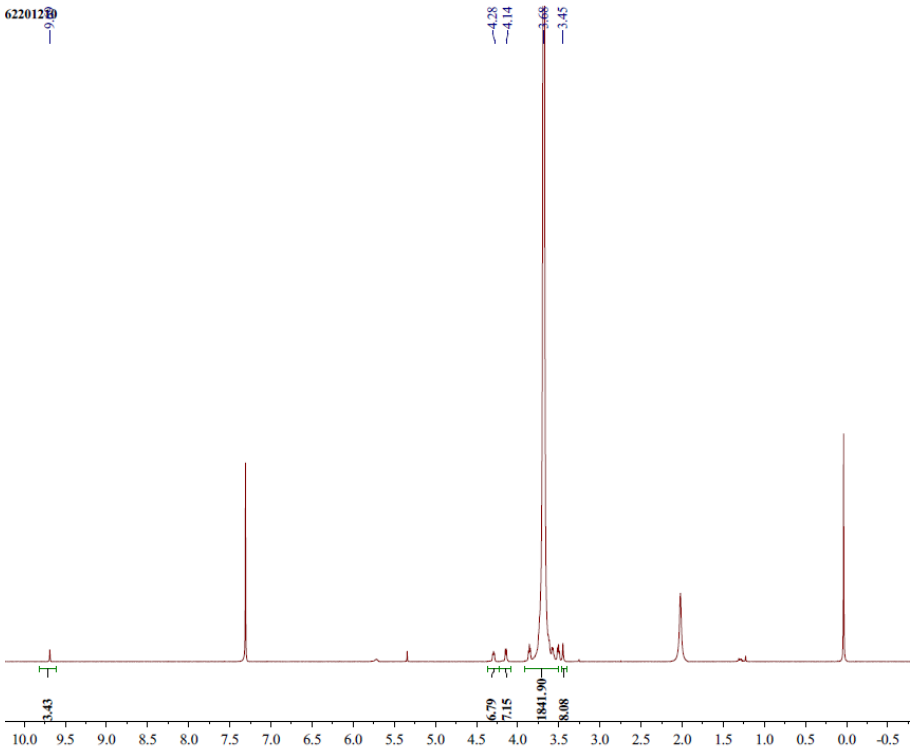

Figure 8.2. NMR spectrum of 4-arm-PEG-CHO, batch 2, performed in $CDCl_3$. Data collected by Biopharma PEG Scientific Inc.

8.5 Protein detection

8.5.1 Glutaraldehyde method

8.5.1.1 Version 1 (GA-v1)

A 1% (w:v) CS LW was reacted with glutaraldehyde (0.2% v:v) for 30 minutes. This was followed by streptavidin (10 mg/mL) for 2.5 hours, BSA (5 mg/mL) for 20 minutes, biotin A-IgG (0.012 mg/mL) for 1 hour, and sheep IgG (0.1 mg/mL) for 2 hours. All solutions were prepared in 100 mM HEPES, pH 7.4, and the same buffer was used to flush the film between each step to remove any unreacted molecules.

8.5.1.2 Version 2 (GA-v2)

A 1% (w:v) CS LW was reacted with glutaraldehyde (0.2% v:v) for 30 minutes. This was followed by SNA (1 mg/mL) for 15 minutes, streptavidin (1 mg/mL) for 1 hour, PAB (0.07 mg/mL) for 1 hour, and rabbit IgG (1 mg/mL) for 30 minutes. All solutions were prepared in 100 mM HEPES, pH 7.4, and the same buffer was used to flush the film between each step to remove any unreacted molecules.

8.5.1.3 Version 3 (GA-v3)

A 1% (w:v) CS LW was reacted with glutaraldehyde (0.05% v:v) for 30 minutes. This was followed by streptavidin (1 mg/mL) for 30 minutes, PAB (0.07 mg/mL) for 30 minutes, and rabbit IgG (1 mg/mL) for 30 minutes. All solutions were prepared in 100 mM HEPES, pH 7.4, and the same buffer was used to flush the film between each step to remove any unreacted molecules.

8.5.2 NHS-PEG_{12}-biotin (NPB) method

A 1% (w:v) CS LW was reacted with a mixture of NPB (0.5 mg/mL) and SNA (0.2 mg/mL) for 1 hour. This was followed by streptavidin (1 mg/mL) for 20 minutes, PAB (0.07 mg/mL) for 30 minutes, and finally rabbit IgG (1 mg/mL) for 20 minutes. All solutions were prepared in 100 mM HEPES, pH 7.4, and the same buffer was used to flush the film between each step to remove any unreacted molecules.

8.5.3 Strain-promoted alkyne-azide cycloaddition (SPAAC) method

100 mM HEPES buffer, pH 5.0 and pH 7.0, were prepared by dissolving HEPES (2.38 g), sodium acetate (0.164 g), and NaCl (0.8766 g), in DI water (90 mL), and pH adjusted using acetic acid and NaOH (1 M). The final volume was made up to 100 mL using DI water.

Sheep IgG (2 mg) was dissolved in 100 mM HEPES, pH 5.0 (1 mL). Sodium periodate (0.107 g) was dissolved in the same buffer (25 mL). The sodium periodate solution (1 mL) was added to the IgG solution (1 mL) in an Eppendorf, wrapped in aluminium foil, and placed on a rocker for 1 hour. The reaction was quenched with sodium sulfite (0.01 g) for 10 minutes. The solution was then evenly separated into dialysis centrifuge filters and centrifuged at 14,000 xg for 10 minutes. The filtrate was discarded, and the sample mixed with 100 mM HEPES, pH 7.0, and centrifuged again. This was repeated 4 times, and the sample was then collected by centrifuging the collection filters upside down at 70 xg for 5 minutes. The resulting solution was 0.5 mg/mL of oxidised IgG in 100 mM HEPES, pH 7.0.

The oxidised IgG (2 mL) was then reacted with a 40 mM azido-PEG_4-hydrazide HCl salt solution (250 µL) at pH 7.0. The reaction was incubated at room temperature for 2 hours. Centrifuge dialysis was then performed, increasing the pH to 7.4.

In parallel a 1% (w:v) CS LW was functionalised by mixing DBCO-PEG_4-NHS (50 µL) with 100 mM HEPES, pH 8.0 (450 µL) and running this solution across the LW for 2 hours. The film was then flushed with 100 mM HEPES, pH 7.4.

Following this, the functionalised IgG was run across the LW for 2 hours.

8.5.4 Oxidised IgG method

Sheep IgG or rabbit IgG was oxidised *via* the method reported above in **Section 8.5.3**.

This sample was then run across the 1% (w:v) CS LW film for between 1 and 2 hours before flushing with 100 mM HEPES, pH 7.4.

8.5.5 Glycine method

A 1% (w:v) CS LW was reacted with glutaraldehyde (0.25% v:v) for 1 hour. This was followed by rabbit IgG (0.1 mg/mL) for 1 hour. Glycine (1% - 5% w:v) was reacted with the film for between 1 and 5 hours, followed by PAB (0.07 mg/mL) for 20 minutes. All solutions were prepared in 100 mM HEPES, pH 7.4, and the same buffer was used to flush the film between each step to remove any unreacted molecules.

8.5.6 Anti-biotin antibody (ABA) method

A 1% (w:v) CS LW was conditioned by running 10 mM PBS, pH 7.4, across the film for 5 hours. NPB (50 µg/mL) was introduced *via* the flow cell for 30 minutes before flushing with PBS. This was followed by ABA (25 nM) for a further 30 minutes, before a final buffer wash. All solutions were prepared in 10 mM PBS, pH 7.4, and the same buffer was used to flush the film between each step to remove any unreacted molecules.

8.5.7 Lactoferrin (LF) method

A 1% (w:v) CS LW was reacted with glutaraldehyde (0.25% v:v) for 1 hour, followed by anti-LF (1 mg/mL) for 1 hour, and glycine (5% w:v) for 5 hours. LF solutions (1 nM, 5 nM, 10 nM, 25 nM, 50 nM, 100 nM) were introduced in sequence for 90 minutes each.

All solutions were prepared in 100 mM HEPES, pH 7.4, and the same buffer was used to flush the film between each step except for lactoferrin steps to remove any unreacted molecules.

8.6 Interferent tests

8.6.1 Human serum

1% (w:v) CS, 5% 4-CHO:4-HZ (1:1), and 0.96 (w:v) PAAm LWs were exposed to 10%, 50%, and 100% (v:v) human serum prepared in 100 mM HEPES, pH 7.4 for between 15 and 60 minutes each.

1% (w:v) CS LW was then tested as in **Section 8.5.6**, with ABA prepared in 10% (v:v) human serum.

8.6.2 Urine

1% (w:v) CS, 5% 4-CHO:4-HZ (1:1), and 0.96 (w:v) PAAm LWs were exposed to 10%, 50%, and 100% (v:v) synthetic urine prepared in 100 mM HEPES, pH 7.4 for 15 minutes each.

5% 4-CHO:4-HZ (1:1)/1% (w:v) CS LWs were tested with NPB (0.5 mg/mL) for 1 hour followed by streptavidin (1 mg/mL) prepared in 10% or 100% synthetic urine for 20 minutes. 100 mM HEPES, pH 7.4 was used to flush the film between each step to remove any unreacted molecules.

8.7 Instrumentation

8.7.1 Laboratory waveguide

A laboratory based waveguiding instrument was used, with an approximate weight of 25 kg and dimensions of 60x60x35 cm. This was fabricated *via* subtractive milling techniques using robust metals such as aluminium and steel. This setup combines a 650 nm light emitting diode (LED) and EA Elektro-Automatik Bench Power Supply (EA-PS 2042-06 B) with a BK7 equilateral prism and a USB camera (Daheng Imaging MER-2000-19U3M-L 20 Mpixel CMOS USB3 camera or Pixelink PL-B781 6.6 Mpixel CMOS USB2 camera), alongside a peristaltic pump and water bath.

8.7.2 Portable waveguide

A portable three-dimensional (3D) printed waveguiding instrument was developed in [1] by a collaborator. This instrument weighs 825 g with dimensions of 162x130x107 mm. Most of the instrument was constructed *via* 3D printing with the exception of optical components and electronics, which were purchased from specialist suppliers. The camera used in this setup was the IDS Imaging UI-1492-LE 10 Mpixel USB2 camera.

8.7.3 Flow cells

Flow cells were prepared from 3 mm thick black PMMA sheets. Computer numerical control (CNC) machining was used to create the microfluidic channels at a depth of 0.2 mm, surrounded by recessed grooves 0.75 mm deep and 1 mm wide. Nitrile o-rings were mounted in the grooves, while bootlace ferrules were glued into holes at either end of the flow cell

cavity to produce inlets/outlets. Different shapes of microfluidic channels were prepared and are discussed in more detail in **Chapter 3** (**3.3**).

8.7.4 Refractometer

A Bellingham and Stanley RFM970-T Refractometer was used throughout the project to measure the refractive index (RI) of all buffer, glycerol, and PEG solutions prepared to 6 d.p. To do this, the refractometer prism was thoroughly cleaned with ethanol and allowed to dry, followed by setting a zero sample with DI water. The sample solution was then pipetted (~1 mL) onto the prism and the lid shut. The RI was measured by the instrument, followed by removal of the sample and cleaning. This was repeated two additional times per sample to allow for an average response to be taken.

8.7.5 Other instrumentation

Additionally, the following instruments were employed throughout the project: Hanna instruments HI 2210 pH meter, Laurell WS-650MZ-23NPPB spin coater, PDC-002-CE expanded plasma cleaner (Harrick), PS-20A Digital ultrasonic Jakansonic cleaner, Ossila UV Ozone Cleaner E511, Buchi Rotavapor R-100, Benchmark MyTemp mini digital incubator H2200-H, Eppendorf Centrifuge 5702, Grant Instruments LT ecocool 100 recirculating water bath, Gilson F155001 minipuls 3 peristaltic pump, Jenway 6715 UV/Vis Spectrophotometer, Sigma 1-14 centrifuge, Benchmark scientific M2100 Tube Rocker, Mettler Toledo MS205DU analytical balance, Fisher Scientific Mini Vortex Mixer.

8.8 References

1. Goddard, N.J., et al., *3D Printed Instrumentation for Point-of-Use Leaky Waveguide (LW) Biochemical Sensor.* IEEE Transactions on Instrumentation and Measurement, 2020: p. 1-1.
2. Signini, R. and S.P. Campana Filho, *On the preparation and characterization of chitosan hydrochloride.* Polymer Bulletin, 1999. **42**(2): p. 159-166.